N° d'ordre :

THÈSE

PRÉSENTÉE A

L'UNIVERSITÉ BORDEAUX 1

ÉCOLE DOCTORALE DES SCIENCES CHIMIQUES

par Matthias Heim

POUR OBTENIR LE GRADE DE

DOCTEUR

SPÉCIALITÉ : Chimie-Physique

ELABORATION, CHARACTERISATION AND APPLICATIONS OF POROUS ELECTRODES

Directeur de recherche : Prof. Alexander Kuhn

Soutenue le : 05.12.2011

Devant la commission d'examen formée de :

M. VELEV, Orlin D	Professeur NC State University	Rapporteur
M. LACROIX, Jean-Cristophe	Professeur Université Paris Diderot	Rapporteur
M. RAVAINE, Serge	Professeur Université de Bordeaux I	Examinateur (Président)
M. ALLONGUE, Philippe	Directeur de recherche Paris Tech	Examinateur
M. KUHN, Alexander	Professeur Université de Bordeaux I	Directeur de thèse
M. SOJIC, Neso	Professeur Université de Bordeaux I	Invité
M. YVERT, Blaise	Directeur de recherche INSERM Bordeaux	Examinateur (Directeur de soutenance)

Abstract

In the present work template-assisted electrodeposition was used to produce highly ordered macro- and mesoporous electrodes. Colloidal crystals obtained by the Langmuir-Blodgett (LB) technique were infiltrated using potentiostatic electrodeposition of metals and conducting polymers followed by removal of the inorganic template. In the resulting macroporous electrodes, the pore diameter was controlled by the size of the silica spheres, while the thickness could be controlled by temporal current oscillations caused by a periodic change of the electroactive area in the template. Various colloidal superstructures were produced in this way leading to electrodes with on purpose integrated planar defects or well-defined gradients in terms of pore size. Furthermore we showed that alternating multilayers of different metals could be deposited with high accuracy into a colloidal monolayer altering the optical properties of the material. Successful miniaturization of the process was demonstrated by elaborating macroporous gold microcylinders showing besides higher active surface areas also increased catalytic activity towards the reduction of oxygen compared to their flat homologues. In this context a miniaturized electrochemical cell composed of two macroporous gold electrodes was also proposed.

Finally, mesoporous platinum films were deposited on microelectrode arrays (MEAs) using lyotropic liquid crystals as templates. The increased surface area of mesoporous compared to smooth electrodes led to improved performance in the recording of neuronal activity with MEAs owing to a reduced noise level.

Keywords: Porous electrodes; Colloidal crystals; Electrocatalysis; Pore gradient; MEA; Neuronal recording.

Resumé

Dans ce travail des électrodes macro- et mesporeuses hautement organisées ont été fabriquées grâce à l' électrodéposition dans différents types de template. Des cristaux colloïdaux obtenus par la technique de Langmuir-Blodgett ont été infiltrés par des métaux ou des polymères conducteurs en utilisant l'électrodéposition potentiostatique suivi par la dissolution du template. La taille des pores, ainsi que l'épaisseur du film macroporeux pouvaient être contrôlée respectivement par le diamètre des billes de silice et par des oscillations temporelles du courant. Différentes superstructures colloïdales ont également été produites menant à des électrodes avec des défauts artificiels ou des gradients bien définis en termes de taille des pores. Des couches alternantes de différents métaux ont été déposées avec grande précision dans une monocouche de particules

entrainant une modification des propriétés optiques du matériau. La miniaturisation a pu être démontrée par l'élaboration des microcylindres d'or macroporeux qui disposent non seulement d'une plus grande surface active mais aussi d'une plus grande activité catalytique envers la réduction de l'oxygène en comparaison avec leurs homologues non poreux. Dans ce même contexte une cellule électrochimique miniaturisée composé de deux électrodes macroporeuses a été proposée.

Par ailleurs du platine mesoporeux a été électrodéposé en présence d`un template de type cristaux liquides lyotropes sur des réseaux de microélectrodes. Grâce à une plus grande surface active par rapport à leurs homologues non poreux des microélectrodes mesoporeuses ont montré une meilleure performance dans l'enregistrement de l' activité neuronale due à un niveau de bruit plus faible.

Mots de clés: Electrodes poreuses; Cristaux colloïdales; Electrocatalyse; Gradient de pore; MEA; enregistrement de l'activité neuronale.

Contents

List of abbreviations:

AC	alternating current
AIROF	activated iridium oxide
ALD	atomic layer deposition
bcc	body centerd cubic
CE	counter electrode
CNT	carbon nanotube
CP	conducting polymer
CVD	chemical vapor deposition
CV	cyclic voltammetry
DC	direct current
EIROF	electrodeposited iridium oxide
fcc	face centered cubic
FOM	figure of merit
hcp	hexagonal close packed
LB	Langmuir-Blodgett
LC	liquid crystal
LLC	lyotropic liquid crystal
NIR	near infra-red (light)
NIM	negative index material
MEA	microelectrode array, multielectrode array
PANi	polyaniline
PBT	polybithiophene
PC	photonic crystal
PECVD	plasma-enhanced CVD
PEDOT	poly(3,4-ethylenedioxythiphene)
PPy	polypyrrole
PVD	physical vapor deposition
RE	reference electrode
RIE	reactive ion etching
SDS	sodium dodecyl sulfate
SEM	scanning electron microscopy
SERS	surface enhanced raman spectroscopy
SNR	signal-to-noise ratio
SPP	surface plasmon polariton
SRR	split-ring resonator

SWCNTs	single-walled carbon nanotubes
TEOS	tetraethyl orthosilicate
UV	ultraviolet (light)
VACNTs	vertically aligned carbon nanotubes
VD	vertical deposition
Vis	visible (light)
WE	working electrode

1 Introduction

Electrochemical devices occupy an important part of our life. Among the most well-known and broadly used electrochemical cells are batteries or fuel cells allowing to store and convert energy, respectively.[1, 2] Electrochemical sensors allow the concentration of various biological or chemical species to be determined.[3, 4] These are just some of the numerous examples in which electrochemical reactions serve for useful purposes. In many respects the characteristics of the electrode plays a crucial role, affecting the performance of these devices. By exchanging electrons with the electrolyte, the electrode is directly involved in the reaction process. Hence, specific electrode parameters including the size, the constituting materials and the surface properties can have a major effect on the global reaction scheme.

A strategy to improve the efficiency of electrochemical setups in different fields of applications consists in using electrodes with a nanostructured surface.[5, 6] Scaling down the characteristic dimensions of matter to very small scales is in many cases associated with the emergence of new and unprecedented properties, which cannot be obtained with macroscopic features. A good example for size-dependent properties in the domain of electrochemistry is the enhanced mass transport observed in (ultra-)microelectrodes due to the more efficient radial diffusion.[7] In analytical measurements the use of microelectrodes allowed to increase the sensitivity and/or to decrease the detection limits. Furthermore they allowed to perform electrochemical measurements at single cells.[8, 9] Improvement of the performance of macroscopic electrodes can be achieved by modifying their surface with particles of nanoscopic dimensions, e.g. metal nanoparticles or carbon nanotubes. The high surface-to-volume ratio of nanoparticles provides an efficient way to increase the active surface area of electrodes. Another approach for achieving the same goal consists in using porous electrodes.

The concept of porous electrodes dates more than a century, as the first flow through porous electrode was introduced.[10] Since then, many efforts have been made to develop new synthesis procedures allowing to control the microstructure and the organization in porous materials. In this regard the use of templates has proved to be particularly well-suited to generate porous materials with a well-defined morphology. Owing to the structure directing property of the different types of templates, porous materials can be produced, which are a cast of the template. The possibility to use a wide range of different materials for the infiltration of a template also makes it a very versatile method.

Up to date various templates, which can be divided into hard and soft templates, have been employed to create porous films on electrodes surfaces. Hard templates include track etched or

anodized alumina and polycarbonate membranes, which were among the first templates that have been successfully used to produce nanostructured conductive films on the surface of an electrode.[11] Furthermore also mesoporous silica membranes or colloidal microspheres assembled to colloidal crystals belong to this category. Examples for soft templates are surfactant molecules, block-copolymers, polymer gels and emulsions. The particular benefit in using templates rather than other nanofabrication techniques, e.g. chemical dealloying,[12] resides in the high level of control over the microstructure in the porous material offered by the template based approach.

In the present work highly-ordered porous electrodes will be produced using template-assisted electrodeposition. The main focus is on the controlled elaboration and characterisation of the macro- and mesoporous materials by showing also their potential applications in different fields including catalysis, optics and neurobiological analysis.

At first we present different methods from the literature allowing to create colloidal crystals by using microspheres as the building blocks. Among these, the Langmuir-Blodgett (LB) technique offers specific advantages over concurrent techniques. We used LB to produce colloidal crystals, because the number of deposited sphere layers can be perfectly controlled in these crack-free templates. The optical properties of colloidal crystals are further discussed and their particular significance in the field of photonic crystals is pointed out. Still focusing on the optical properties of periodically nanostructured materials, we introduce metamaterials by illustrating the state of the art in terms of the fabrication and the applications of this group of materials.

The following chapter deals with the infiltration of colloidal crystal templates using electrodeposition in order to generate macroporous electrodes. Therefore the different infiltration techniques together with the corresponding microstructures in the porous material are compared. We show that electrodeposition is a very suitable technique to control the filling level in the template and thus the thickness of the porous film on the electrode. Besides the characterization of the macroporous structure in the SEM, the increase of active surface area in the porous compared to the flat metal electrodes is determined using electrochemical techniques. The broad field of applications, in which macroporous electrodes can be used for, is presented in the last section of this chapter.

Macroporous materials with complex pore architectures are elaborated in Chapter 4. The generation of a desired sphere layer stacking sequence in a colloidal template imposes a "layer-by-layer" transfer technique like LB. Thus, we examine the possibility to create different types of template architectures containing on purpose integrated defect layers or gradients in term of sphere size. Our goal consists in producing inverse replicas of the templates by infiltrating them with different materials using electrochemical deposition.

Another aspect being covered in the next chapter of this work concerns the fabrication and the optical characterization of colloidal sphere monolayers, in which layers of conductive materials with a corresponding thickness in the subwavelength range are alternatively deposited. This strategy presents a new approach towards the realization of a metamaterial by electrodepositing multilayers of either a conducting polymer and a metal, or two different metals in a colloidal template. The optical properties are characterized by comparing simulated to measured data using reflectance spectroscopy.

In Chapter 6 we focus on miniaturized macroporous electrodes with a cylindrical geometry. Instead of using planar substrates, the transfer of sphere layers and the subsequent electrochemical infiltration of the template is evaluated on gold microwires. Despite the multiple benefits of using such electrodes in confined volume for analytic or catalytic measurements, only very few examples exist in the literature that deal with templated microcylinders. After the characterization of the active surface area and the microstructure of macroporous gold wires, we tested their utility for the catalytic reduction of oxygen. By depositing two different metals in a 3-layer structure into the colloidal template, of which the central layer can be dissolved, we also present a strategy to develop a miniaturized electrochemical cell which is composed of macroporous electrodes.

Finally, we discuss the benefits of highly ordered mesoporous films which are electrodeposited on the microelectrodes of microelectrode arrays (MEAs). MEAs are used in the field of neurobiology for the recording and stimulation of neuronal activity in electrogenic tissues. An actual trend in MEAs consists in miniaturizing the microelectrodes in order to increase the electrode density on the array and hence the available information density. However, an increased thermal noise and a lower charge injection during the recording and stimulation, respectively, limit the perfomance in MEAs when the size of the microelectrodes is reduced. A detailed overview over existing strategies to improve the performance of MEAs using nanostructured electrodes is presented. Our approach aims at overcoming existing limitations in MEAs by artificially increasing the active surface area of the microelectrodes. Therefore lyotropic liquid crystal templating is used to deposit highly ordered mesoporous overlayers on the microelectrodes of MEAs. After comparing the thermal noise and the impedance of flat and mesoporous microelectrodes in physiological solution we demonstrate the utility of the mesoporous coating for the end user by recording neuronal activity from an embryonic mouse spinal cord.

2 Colloidal Crystals

In crystalline materials the atoms or molecules are arranged in defined locations building up a highly ordered crystal lattice. The same degree of order is found in colloidal crystals (see Figure 2.1b). Here the building blocks represent colloidal spheres with dimensions typically three orders of magnitude larger than atoms. A natural form of colloidal crystals represent gem opals attracting one's attention by their intense coloration (see Figure 2.1a) that changes when the opal is observed under different angles. This phenomenon known as opalescence is caused by a diffraction of light at the periodic crystal lattice generally being composed of sub-µm sized spherical particles. Even though colloidal crystals can be used directly for different kind of applications, several others arise from the possibility to fabricate inverse opals of various materials. Infiltration followed by a dissolution of the colloidal template is employed in order to produce negative replicas of colloidal crystals. Those inverse opals resemble "honeycomb structures" and are characterized by a 3-dim periodic arrangement of interconnected voids in a host material (see Figure 2.1c). Inverse opals offer great potential in application fields including photonic crystals, metamaterials or macroporous materials.

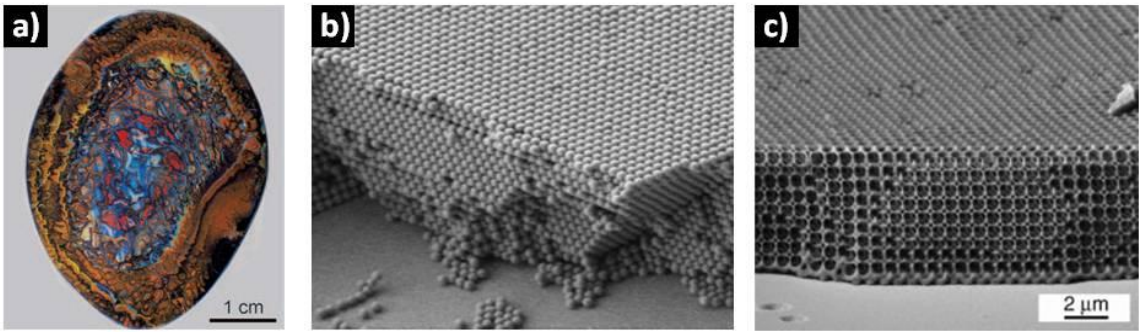

Figure 2.1: a) Top view of a natural iron oxide-containing matrix opal.[13] b) Cross-sectional SEM image of a colloidal crystal made up from silica spheres with a diameter of 1000nm.[14] c) Silicon inverse opal obtained from a colloidal crystal like the one shown in b). Those structures show optical properties consistent with a photonic bandgap.[14]

2.1 Synthesis of colloidal microspheres as starting material

Colloidal crystals are generally build-up from spherical building blocks that can be of organic or inorganic nature. These particles may have metallic, semiconducting or electrical isolating character. As the colloidal crystals synthesized in this work are used as an inert template for a subsequent electrodeposition, the focus will be directed on electrically isolating particles. A

crucial parameter in the assembly of colloidal crystals represents the monodispersity of the colloidal building blocks. The narrower the size distribution of the colloids, the better the resulting quality and the lower the number of stacking faults in the colloidal crystal.[15] The key feature in particle synthesis therefore consists in controlling the process in such a way that nucleation on one side and the growth of the nuclei on the other are distinct processes that are well separated from each other.[16]

In the literature several well-known synthesis routes are described allowing to achieve this goal for various different materials. Focusing on organic matter, it is mainly poly(methylmethacrylate) (PMMA) and polystyrene (PS) that are employed in order to produce colloidal particles. Monodisperse polymer spheres are obtained by several techniques, the most widely used represents the emulsion polymerization. Here an insoluble monomer is dispersed in a medium (generally water) by the aid of an emulsifier. The surfactant is present in forms of micelles that contain most of the added monomer. Adding a radical initiator starts the polymerization and leads to a nucleation burst of small particles. These initial particles are generated by the reaction of radicals with the monomer which is present in the aqueous phase. Once the particles formed their growth will continue very slowly due to the limited amount of monomer that can be dissolved in the aqueous phase with the micelles acting as a reservoir to provide the monomer for the polymerization. The growth of the particles will continue until all the monomer stocked in the micelles has been consumed. In this way particles with diameters ranging from 20nm to 1 µm can easily be produced.[17]

The most widely used and studied material for the synthesis of monodisperse particles in inorganic systems represents silica. In 1968 Fink and Stöber found that hydrolysis and polycondensation of a dilute siloxane precursor in an alcoholic solution under basic conditions results in silica particles with a very narrow size distribution.[18] The precursor generally is tetraethyl orthosilicate (TEOS) which is hydrolyzed in the presence of ethanol and water with ammonia acting as a catalyst. At high pH the silica spheres are surface charged which keeps them separated due to electrostatic repulsion. Lowering the pH value below 2, corresponding to the isoelectric point of silica, would favor the formation of a silica gel instead of individual particles. The final size of the particles was shown to depend on several parameters. Besides the pH, also the temperature, the method used for mixing the reactants and their concentration affect the result. The increase of the ammonia concentration was reported to lead to bigger particles whereas higher amounts of water resulted in rather narrow size distributions and spheres with a more uniform spherical shape.[19] Higher reaction temperatures generally resulted in smaller particles.[20] By choosing the right parameters the size of the silica particles can be adjusted to values between 50nm and 1µm. For the synthesis of bigger particles a two step process can be

used. In a first step, silica colloids of sub-micrometer dimensions are produced by the Stöber method. These "seeds" can be grown to their final size by a controlled addition of the precursor. Here the addition rate of the precursor was shown to be the dominant factor for producing monodisperse silica particles up to sizes of 2µm.[21] By using a semi-batch instead of the Stöber batch approach, broad particle size distributions that were observed by several authors can be avoided.[21, 22]

In Figure 2.2 the characterization of silica beads employed in this work is shown. The SEM images in Figure 2.2a) - Figure 2.2f) reveal the high degree of monodispersity for the different particle diameters. The size distributions of three different samples obtained by dynamic light scattering experiments are illustrated in Figure 2.2g). The results show single populations of beads expressed by the different peaks that are centered around the mean diameter of the particles.

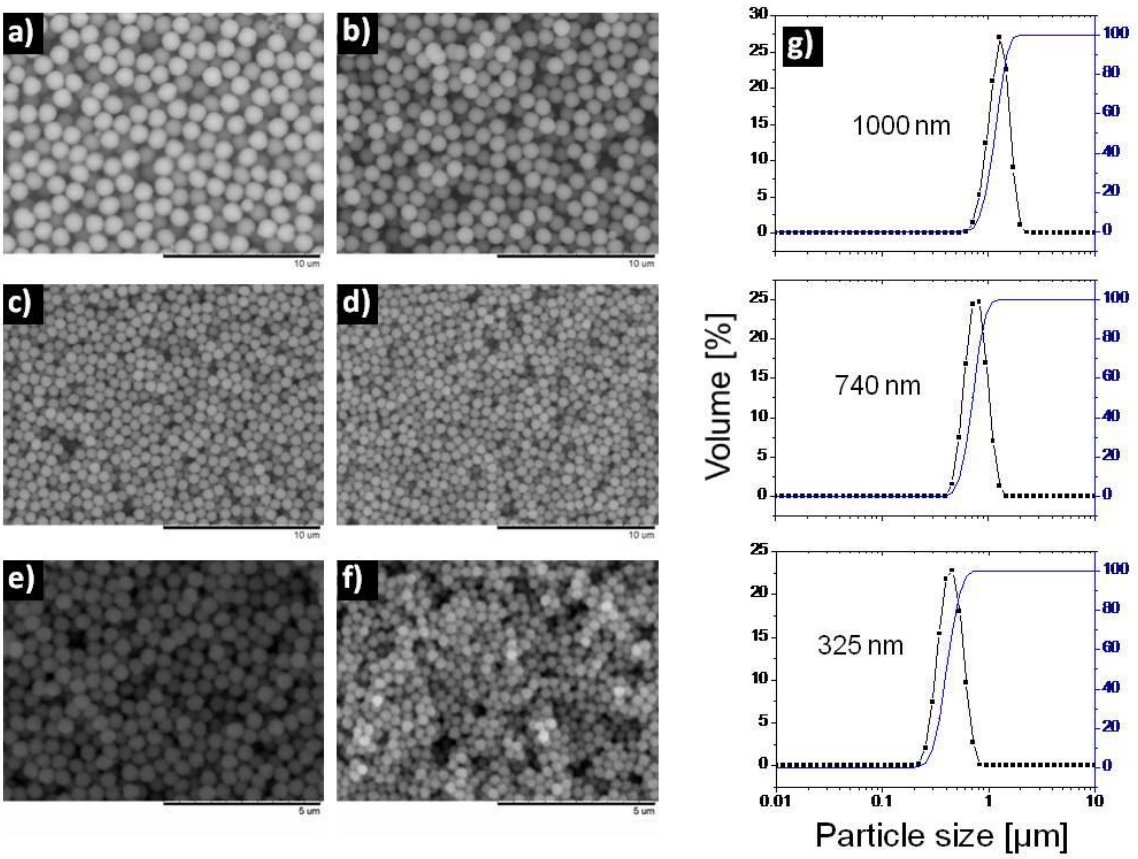

Figure 2.2 Characterization of silica beads that have been synthesized by batch or semi-batch processes inspired by the Stöber method. a)-f): SEM -images of particles crystallized on a substrate with diameters of a) 1200nm b) 1000nm c) 740nm d) 600nm e) 470nm f) 325nm. g): Size distribution of the samples b), c) and f) in suspension obtained by dynamic light scattering (DLS).

Silica offers the convenience that the surface properties can be changed relatively easily and in a wide range by using siloxane chemistry.[23, 24] In this work the silica spheres were functionalized with aminopropyltriethoxysilane which was added during or after the synthesis of the particles.[25]

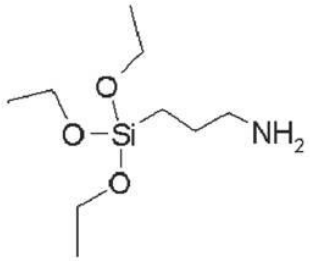

Aminopropyltriethoxysilane

This step was necessary to allow the formation of stable Langmuir films from silica particles. Without modification the silica spheres would be too hydrophilic and directly sink into the water after they are spread on the surface of the water. A modification with aminopropyltriethoxysilane allowed to render the particles more hydrophobic compared to bare silica due to the NH_2-terminated alkyl chain.

2.2 Self-assembly techniques of colloidal particles

Self-assembly represents a process where structures organize into ordered patterns without human intervention. It can be found at all scales in the natural or the artificial domain of our world. Examples for self-assembly are living cells, molecules, self-assembled monolayers (SAMs), liquid and colloidal crystals, bacterial colonies and even animal swarms (ants).[26] Self-assembly of colloidal particles represents an area with considerable interest for the fabrication of ordered nanostructures. The different forces present in this size regime therefore should be identified to be able to understand and to direct the process in a desired direction.

A condition which has to be fulfilled in order to form stable aggregates in colloidal systems presents the establishment of a balance between attractive and repulsive forces that act on the particles. The internal forces that are present in colloidal systems can be assigned to two different groups.

Van der Waals attraction being based on dipole interactions and the electrostatic repulsion resulting from an interaction of counterions in the electric double layer represent basic colloidal forces. In the DLVO theory (Derjaguin, Landau, Verwey, Overbeek) the balance between these two forces determines the stability of colloidal solutions. Even if the particle interaction can be predicted in a wide range of distances by considering the ratio of electrostatic to van der Waals

forces, other colloidal forces including steric, hydrophobic and solvation forces should be considered especially when particles are in proximity to each other.

The second group of forces is rather induced by different colloidal phenomena and does not directly result from intermolecular interaction. These induced forces exhibit particular importance in the colloidal regime as the magnitude and length scale is comparable to that observed in colloidal forces. As will be shown in the next chapters, capillary forces and surface tension are crucial in colloidal self-assembly. The wetting behaviour and adhesion on colloids or interfaces equally can affect the force balance in the assembly process. For sub-micrometer sized colloidal spheres also the influence of gravity, diffusion and Brownian motion are in comparable scales meaning that slight changes in experimental conditions can favor either one or the other to be the dominant effect. Osmotic pressure, force by flow as well as electrokinetic and magnetophoretic forces equally represent forces that are induced by colloidal phenomena.

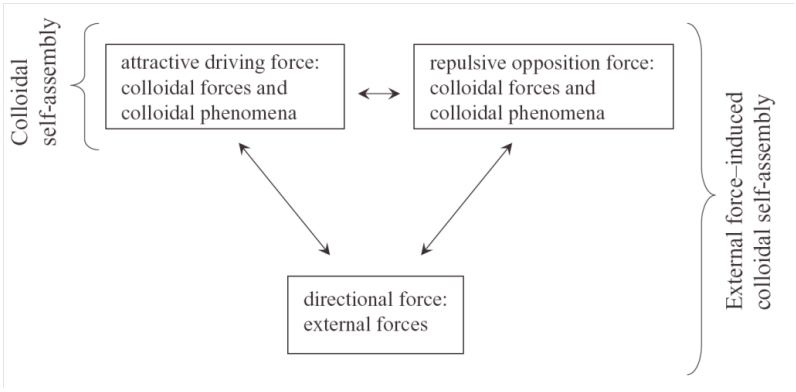

Figure 2.3 Scheme showing the relation of the different forces involved in colloidal self-assembly.[27]

In order to assemble colloidal spheres into a 3-dim colloidal crystal a highly directional process is required that allows to gain control over the involved forces. Self-assembly however that relies strictly on the internal forces described above presents a rather random process in colloidal systems.[27] External forces enable to change the force balance in such a way that the assembly can become directional and highly controllable (see Figure 2.3).

Many effort has been dedicated to exploring various routes allowing a self-assembly of colloidal crystals via the involvement of different external forces. A considerable part of the research performed in this field focused on achieving high quality colloidal crystals with a low number of defects. Especially for an application in the field of photonic crystals big interest consists in controlling the assembly in such a way that defects can be integrated into the colloidal crystal structure in a highly controlled manner. In the same context, colloidal crystal structures with various patterns may yield new solutions for applications that demand a special design of

assembled crystals. Finally a scale-up and an acceleration of the self-assembly process represent important goals in order to allow an economic manufacturing at the industrial scale. In recent works detailed overviews are given over principal methods used for the self-assembly of colloidal spheres into colloidal crystals.[13, 28, 29]

2.2.1 **Evaporation and sedimentation techniques**

Using sedimentation of colloidal microspheres in suspensions is probably the most straight forward technique in order to produce colloidal crystals.[30] Forces acting on the particles are gravity, Brownian motion and also the electrostatic repulsion in the case that particles are charged. Colloidal crystals obtained by sedimentation were shown to possess a face centered cubic (fcc) lattice structure.[31] Regardless of the employed self-assembly method fcc tends to be a more favorable configuration in opals than the hexagonally closed packed (hcp) arrangement.[28] This finding was further supported by theoretical considerations, reporting fcc to be slightly more stable than the hcp lattice when the assembly occurred in thermodynamic equilibrium conditions.[32] However, sedimentation represents only a well adapted method for a very limited range of particle sizes. Using big particles leads to a very fast sedimentation which prevents well ordered colloidal crystal from being formed.[33] On the other hand this technique can not be employed when the particle size is getting too small to allow an efficient settling of the particles to take place in a reasonable amount of time. Adding centrifugal forces allowed to accelerate the sedimentation process,[34] whereas electrophoretic forces could be used to either slow down or speed up the natural sedimentation of charged particles depending on the bias of an electric field with respect to the gravitational force.[35] The ordering and the structural quality in colloidal crystals could be improved by using prestructured substrates[36] or oscillatory shear.[37]

Colloidal spheres also self-assemble while solvent evaporates from a colloidal suspension. In the horizontal deposition method, a small amount of a colloidal suspension is spread onto a hydrophilic, horizontally arranged substrate and is allowed to slowly evaporate.[38, 39] Ordering of the beads was found to start as soon as the thickness of the liquid layer during evaporation became equal to the particle diameter which is schematically illustrated in
Figure 2.4.[40] At first some particle clusters start to grow arising from a deformation of the liquid meniscus around the particles. Evaporation of solvent from these particle clusters causes liquid to flow towards them, a process induced by capillary forces, which drags further spheres along for the self-assembly. This flow-induced assembly of colloidal particles starts at the outside of a drop

moving continually towards its center. As a result the thickness of the colloidal crystal is not homogeneous throughout the sample showing thicker deposits in the outer than in central regions. With a controlled air flow it was possible to guide the self-assembly and to achieve a more homogeneous thickness throughout the sample.[41] Sonication assisted evaporation resulted also in a better crystal quality by equally speeding up the evaporation process.[42]

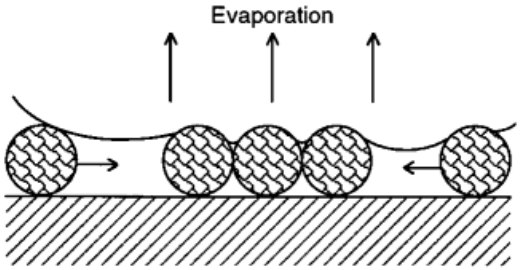

Figure 2.4 Self-assembly of colloidal spheres on a horizontal substrate due to evaporation induced capillary forces.[17]

The vertical deposition method (VD) was introduced by Jiang et al.[43] and is schematically shown in Figure 2.5a). Here a hydrophilic substrate is placed vertically or slightly tilted in a beaker containing a colloidal suspension. During evaporation of the solvent well arranged colloidal crystals form at the surface of the substrate. The colloidal crystal is formed in a very similar way than described for the horizontal deposition, although gravity acting on the particles is now pulling them away from the growth interface of the crystal.

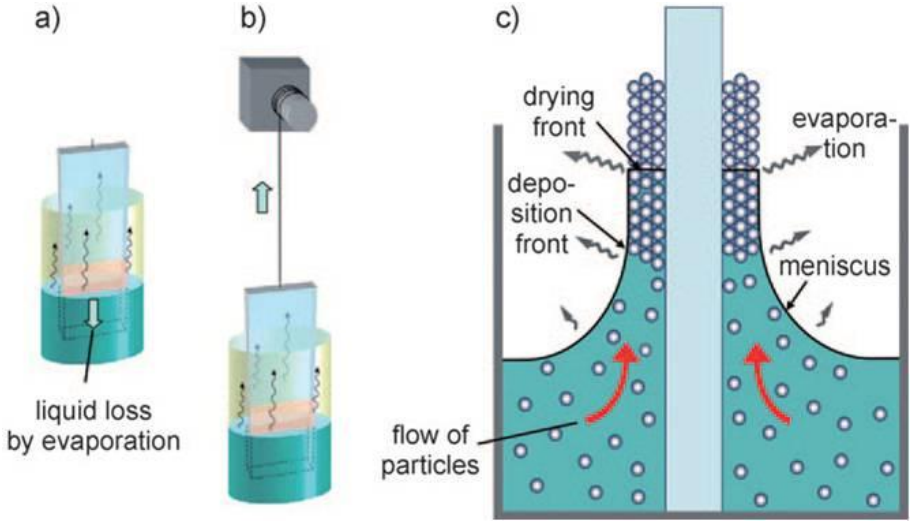

Figure 2.5 The vertical deposition (VD) method. a) Original configuration of the VD method. b) Additional slow lifting of the sample. c) Illustration of the processes happening at the air-liquid-substrate interface during solvent evaporation.[13]

As illustrated in Figure 2.5c) the solvent evaporation occurring in already deposited opal layers induces a flow of liquid towards the meniscus that steadily transports new particles from solution

towards the growth front of the colloidal crystal. Opposite to this flow the gravitational force is acting on the colloidal particles. In its original configuration this method was therefore not adapted for assembling big colloidal particles into colloidal crystals as the sedimentation rate of these spheres was too high. This limitation could be overcome by introducing a permanent flow in the solution by heating[44, 45] or mechanical agitation[46] keeping the spheres in suspension. The influence of a range of different process parameters on the assembled colloidal crystals were studied and optimized including temperature[47], sphere size[48], volume fraction of particles in solution[49], relative humidity[50] and also the pH and the ionic strength of the solution.[51] Simultaneous application of negative pressure during the evaporation of solvent was shown to further improve the film quality.[52] In terms of the structural quality of the assembled colloidal crystals VD leads to better results compared to the sedimentation or the horizontal deposition. Well ordered crystals with a low number of defects can be obtained in that way, an example of that is given in Figure 2.6a). Residual defects as the ones illustrated in Figure 2.6b) are mostly due to insufficient monodispersity in the size distribution of the colloidal spheres. The intrinsically slow process of the natural evaporation of aqueous solutions could be accelerated by using ethanol instead of water as the solvent.[52, 53] The thickness of the deposited film can roughly be adjusted by controlling the particle concentration of the suspension. Also a change in the tilt angle of the substrate could serve the same purpose.[54] However the film thickness generally was found to vary throughout the sample, as particle concentration increases with proceeding evaporation of solvent. By pulling the substrate slowly out of the solution (see Figure 2.5b), the method was accelerated and variations in film thickness throughout the sample could be avoided. [55, 56]

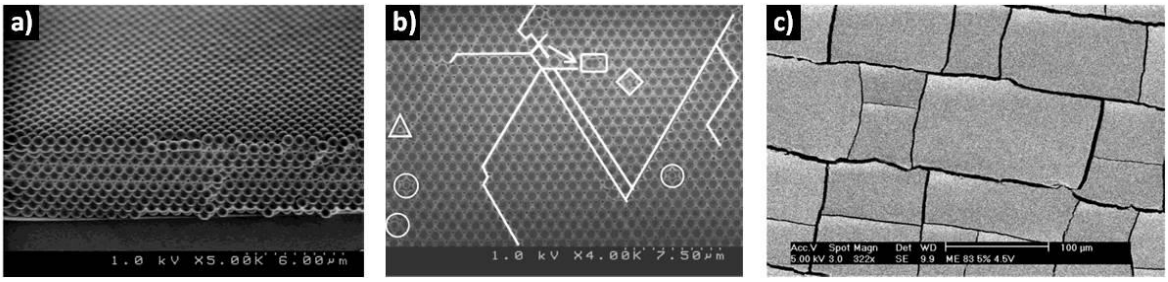

Figure 2.6: SEM images of colloidal crystals produced by VD under isothermal heating (a) + (b) or horizontal deposition (c). In (b) different kind of defects are shown including bigger or smaller particles, doublet or missing spheres. (c) shows the typical crack formation that is observed in colloidal crystal assembly based upon solvent evaporation.[45, 57]

A general issue of colloidal crystals formed from particle suspensions represents the cracking of the structure that occurs during the drying process (see Figure 2.6c).[56, 58] Here, the shrinking of individual particles and/or the solvent evaporation between the spheres leads to a stress in the lattice domains of the colloidal crystal adhering to the substrate. This stress is released in form of

cracks splitting the colloidal crystal into different crystalline domains. Only very few techniques exist that allow producing crack-free colloidal crystals directly from a particle suspension. A way of avoiding the stress appearing during the drying process consists in using flexible substrates. Molten metals as Ga or Hg can provide fluid substrates that are free to move in order to compensate a shrinkage in the colloidal crystal.[57] Another possibility of producing crack-free colloidal crystals presents the use of prestructured substrates that are meant to keep the particles in a fixed position and so preventing cracks in the structure.[59]

2.2.2 **Colloidal self-assembly driven by electric fields**

The self-assembly of colloidal particles can also be controlled by using electric fields.[60] When colloidal suspension are exposed to an electric field a movement of particles results from forces that either act directly on them or cause a liquid flow that drags the particles along. An overview of the different forces and the underlying mechanism is given in Figure 2.7.

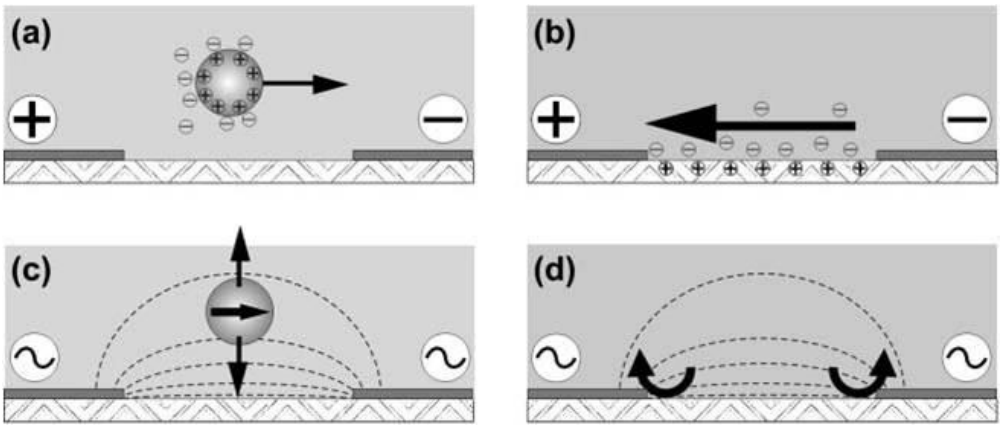

Figure 2.7: Different forces acting on a colloidal particle upon application of a DC (a) + (b) or an AC (c) +(d) electric field. (a) DC electrophoresis. (b) DC electroosmosis. (c) AC dielectrophoresis. (d) AC electro-hydrodynamics.[60]

The principle of DC electrophoresis is shown in Figure 2.7a). The cloud of negative counterions around the positively charged particle is attracted by the anode and slightly sheared away into this direction. This local charge imbalance creates an electrophoretic force that causes an acceleration of the particle towards the electrode that exhibits opposite polarity with respect to the particle, in our present case towards the cathode . The velocity u of the particle will depend on the electrophoretic mobility μ of the particle and the strength of the applied electric field E, which is shown in equation 2.1.

$$u = \mu E \quad (2.1)$$

The electrophoretic mobility can be expressed as a function of the zeta-potential ζ of the particle(s), the viscosity η of the solution and the dielectric permittivity ε and ε_0 of the medium and the vacuum, respectively (see equation 2.2).

$$\mu = \frac{\varepsilon\varepsilon_0\zeta}{\eta} \quad (2.2)$$

μ increases when the zeta-potential ζ of the particle increases or the viscosity η of the solution decreases in a given solution.

By applying a constant DC electric field between two electrodes in a suspension containing colloidal spheres with a charged surface, colloidal crystals can be assembled on the electrode surface. Colloidal crystals have been assembled from silica[61, 62] and latex[63-65] beads using electrophoresis as the driving force. In order to understand which effect leads to the creation of ordered particle arrays, the kinetics during electrophoretic assembly has been studied[66, 67] and a hydrodynamic model has been proposed.[68] The counterionic atmosphere around the particles was shown to disturb the polarization layer of the electrode surface, which as a result caused electrohydrodynamic flow around the particles pulling them together to form 2- or 3-dim colloidal crystals. A colloidal crystal with a body centered cubic (bcc) lattice orientation could be obtained by using a patterned substrate for the electrophoretic deposition which was slowly withdrawn from the colloidal suspension[69] Application of a DC electric field however may result in effects disturbing the assembly process of colloidal particles including electroosmotic flow and faradaic reactions happening at the electrode surface. If ethanol was added to aqueous solutions, water decomposition could be avoided enabling higher electric fields to be applied without emergence of parasitic reactions.[64] The origin of the electroosmotic flow is illustrated in Figure 2.7b). Here, the layer of counterions which is formed close to a non conducting charged surface moves towards the electrode with opposite polarization and causes a liquid flow near that surface. In Figure 2.8a) a colloidal crystal obtained by electrophoretic deposition with a low density of stacking faults is shown.

In contrast to DC, AC electric fields offer the advantage that higher electric fields can be applied without causing electrolysis or electroosmotic water motion, given that the employed frequency is high enough. The continuous change of polarization in AC fields prevents charged particles from being attracted to an electrode due to electrostatic interactions. As shown in Figure 2.7c) the dielectrophoretic force F_{DEP} attracts colloidal particles to areas of higher electric field intensity. F_{DEP} results from the interaction of induced dipoles with a nonuniform electric field and is expressed by equation 2.3.

$$F_{DEP} = 2\pi\varepsilon_1 Re|\underline{K}(\omega)|r^3\nabla E^2 \quad (2.3)$$

F_{DEP} depends strongly on the gradient of the electric field squared, ∇E^2, and the particle radius r cubed, with ε_1 being the dielectric constant of the medium. The real part of the Clausius-Mossotti function K describes the effective polarizability of the particle and influences the magnitude and also the sign of F_{DEP}. As illustrated in Figure 2.7c), particles are attracted to the regions of high field intensities by the dielectrophoretic force. This behavior is observed for highly polarizable particles, e.g. metal particles, resulting in a Re(K) > 0 in the whole frequency range. If less polarizable particles, e.g. polymer beads are exposed to an AC electric field, it will depend on the frequency whether the attraction occurs towards the regions of higher (Re(K) > 0, at low frequencies) or lower (Re(K) < 0, at high frequencies) electric field intensities. The first report dealing with the assembly of colloidal particles by an AC electric field was provided by Richetti et al. [70] Here, and in following works with a similar objective,[71-76] electrodes were separated by a thin gap of the order of the particle diameter. Upon application of an AC electric field the particles could be organized into 2-dim colloidal crystals. Parameters, that allow for a tuning of the interparticle distance and therefore the shape of a colloidal assembly, are the frequency,[74] the applied field intensity and the temperature.[76] Using basically the setup shown in Figure 2.7c) in a thin cell, 3-dim colloidal crystals could be assembled from polymer[77, 78] or silica particles,[79] the latter possessing a fluorescent core in order to facilitate the evaluation of the bead arrangement in the crystal structure.

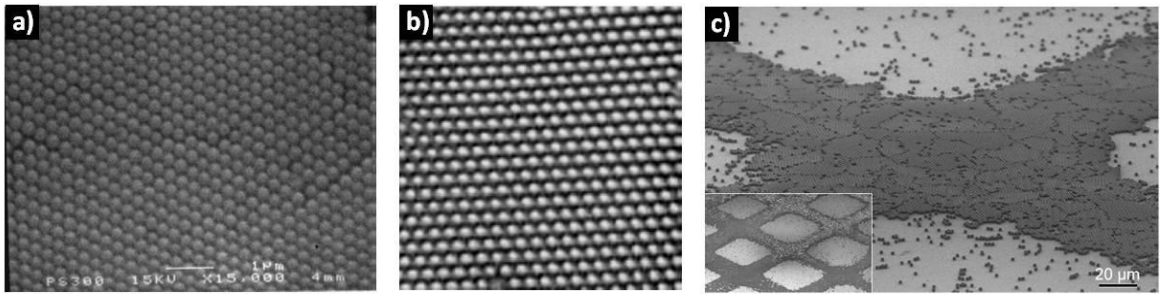

Figure 2.8: SEM images of colloidal crystals obtained by applying electric fields. a) Colloidal assembly obtained by DC electrophoretis.[64] b) Colloidal crystal formed by AC dielctrophoresis from latex spheres with a diameter of 1,4µm.[77] c) Colloidal crystal patterns on ITO obtained by applying a DC electric field with simultaneous illumination of the ITO through a mask.[80]

Electric fields are also well adapted for producing different colloidal crystal patterns on electrode surfaces. Therefore the conductivity of the electrode surface first was locally modified in order to give rise to non-uniform electric fields inducing fluid flows around the patterned areas. Non conducting photoresist- [81, 82] and gold-patterns deposited on an ITO electrode[83] allowed to assemble colloidal particles into crystalline patterns onto the electrode surface by either applying a DC [81, 83] or an AC [82, 84] electric field. Another very sophisticated technique uses an electric field

with UV light to reversibly assemble and disperse colloidal particles at an ITO electrode surface (see Figure 2.8c).[80] The electric field could be locally changed by illuminating ITO in certain areas by means of a mask, leading to a formation of colloidal crystal patterns in the regions of higher electric fields.

2.2.3 **Langmuir-Blodgett (LB) technique**

In its original concept the Langmuir-Blodgett technique was conceived to transfer molecular films from the water surface onto solid samples. As research interests of Irving Langmuir rather focused on studying the assembly of amphiphilic molecules at the air-water interface,[85] it was by the collaboration with Katherine Burr Blodgett, who explored the transfer of these monomolecular films onto solid substrates,[86] that this technique finally got its name. The basic principle is illustrated in Figure 2.9a). A molecular film, the polar head groups pointing into the water and the hydrocarbon tails towards the air, can be transferred to a solid substrate upon its immersion into the water. When the sample is lifted up again, another layer of molecules is transferred onto the previously deposited one, the hydrophilic head groups oriented towards one another. By repeating the dipping process multilayered molecular films can be produced on bulk samples.

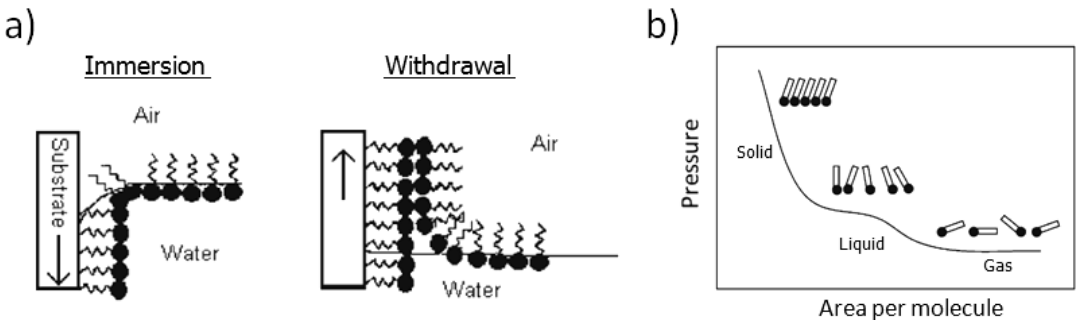

Figure 2.9: a) Principle of transferring a molecular Langmuir film onto a bulk substrate.[87] b) Schematic representation of a compression isotherm for a molecular Langmuir film. The surface pressure is plotted over the area per molecule.[88]

Before a Langmuir film is transferred to a substrate it is compressed by means of movable barriers in order to obtain dense and well ordered monolayers. The degree of film compression can be controlled by monitoring the surface pressure of the water as a function of film area or area per molecule. A typical compression isotherm for a molecular film is shown in Figure 2.9b). Here, three distinct states can be distinguished that are classified in analogy to the different phases of matter into a solid, a liquid and a gaseous state. At the onset of the compression the molecules are far from each other, so that they do not exhibit any kind of interaction resulting in a constantly low value of surface pressure. With further compression, beginning electrostatic or

steric interactions between the molecules cause an increase of the surface pressure denoting the liquid state. The steep rise of the pressure corresponds to the molecules getting in close contact by forming a well compressed monolayer on the water surface. Any further compression would lead to a collapse of the film with layers being stacked on top of each other.

The use of the LB technique in combination with colloidal particles necessitates the formation of stable colloidal Langmuir films on the water surface. This issue could be resolved by silylation of silica beads in order to change their surface chemistry from a hydrophilic to a more hydrophobic state.[23, 24] Surface functionalized beads in this way were prevented from sinking into the aqueous subphase when they were spread onto the water surface (see Figure 2.10a). However recently it could be shown that silica particles in a limited size range from 180 to 360nm do not explicitly have to be surface functionalized in order to form stable colloidal monolayers on the water surface.[89] The compression of colloidal films (see Figure 2.10b) can be followed by controlling the surface pressure of the water in a similar way as shown in Figure 2.9b). In contrast to the transfer process of molecular Langmuir films that is shown in Figure 2.9a), a colloidal Langmuir film is transferred exclusively during the upstroke of the sample (see Figure 2.10c), which was reported to require less energy than forcing the particles into the aqueous subphase.[90] Consequently, the number of dipping events, involving one down and one up cycle, corresponds to the number of deposited particle layers. LB therefore represents a technique allowing the assembly of colloidal crystals within a precision of a single monolayer. Langmuir films can be transferred successfully onto substrates that are hydrophilic enough to allow wetting and the formation of a meniscus at the interface of substrate and liquid. The first works on this topic reported the fabrication of 2D colloidal crystals consisting of a monolayer of silica[91] or titania[92] spheres. Shortly after 3D colloidal crystals were successfully built up onto glass microscope slides by a successive deposition of particle monolayers.[93-95]

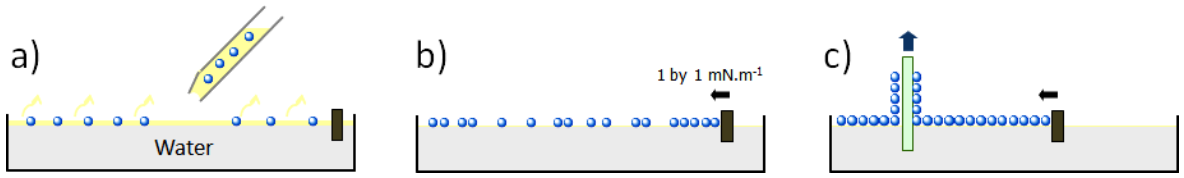

Figure 2.10: Different steps involved in the Langmuir-Blodgett process together with colloidal particles. a) Spreading of the particles on the water surface. b) Compression of the Langmuir film. c) Transfer of the colloidal film to a hydrophilic substrate at constant surface pressure

The Langmuir trough used in our experiments is shown in Figure 2.11. A trough area of 1200 cm^2 enabled to prepare Langmuir films of a good quality covering a surface area ranging from 180 to 600 cm^2. The movable barriers A and B in combination with the balances A and B allowed to

compress the film and simultaneously measure the surface pressure of the water. Once the film was in a well compressed state, the surface pressure was kept constant and a sample was introduced into the dipping mechanism onto which the film was transferred during the upstroke (v = 1mm/min). The compression and film transfer could be controlled by a computer equipped with the software Nima TR 7.8. A PMMA cover was kept closed immediately after spreading of the film in order to prevent the film quality to be degraded by dust particles from the atmosphere.

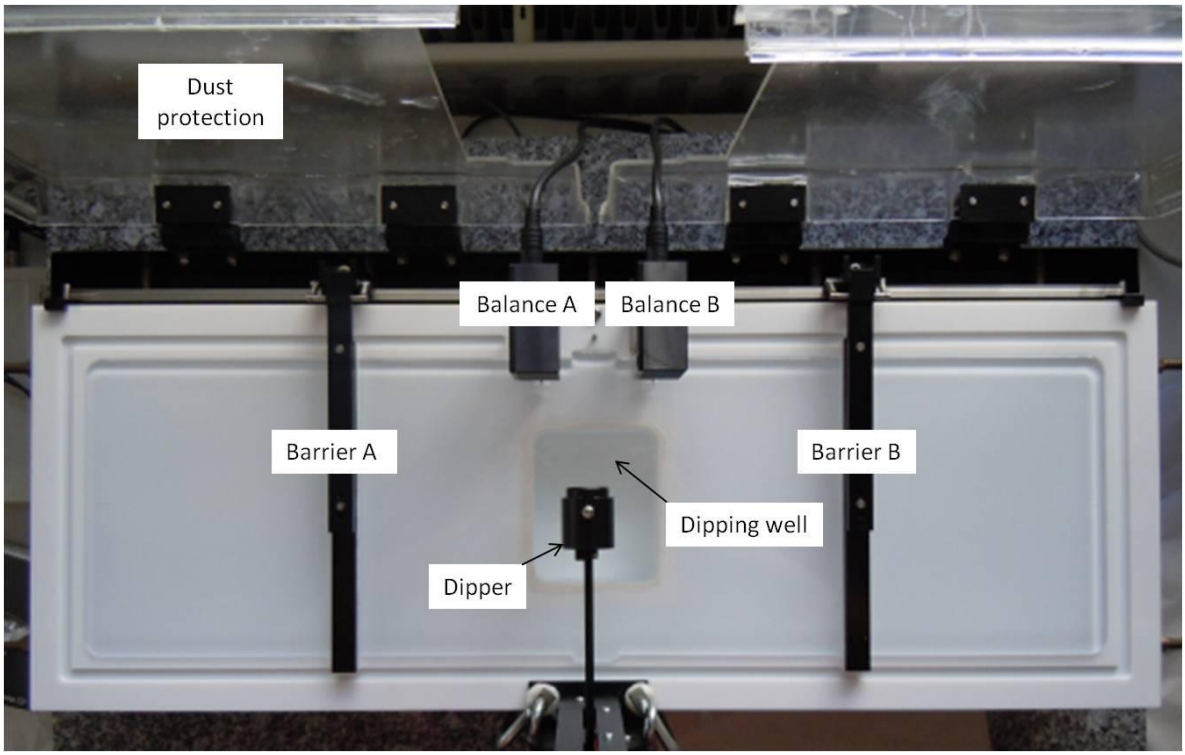

Figure 2.11: Top view of the alternate Nima Langmuir trough (L ×W: 60cm × 20cm) with two independent movable barriers A and B, two surface pressure sensors (balance A and B) and a dipping mechanism.

Side views of the LB setup during or after film deposition is provided in Figure 2.12a) and Figure 2.12b). The surface pressure of the water could be measured by means of a piece of paper, the Wilhelmy plate, which was immersed into the water being attached at the same time to a balance. Increasing the surface pressure would sligthly lift the Wilhelmy plate. This difference in weight could be translated into a change in surface pressure. In Figure 2.12a), multiple monolayers of silica spheres have been transferred onto the gold substrate by fast immersion (v= 63mm/min) followed by slow withdrawing (v= 1mm/min) cycles. Figure 2.12b) shows the transfer of the first particle monolayer onto a gold substrate (sample size 48cm^2) during the upstroke. Although being less apparent than the multilayer LB film of Figure 2.12a), the deposited monolayer still can be discriminated from the blank gold substrate. In this way uniform mono- and multilayer colloidal crystals could be produced over an area of up to 20 to 30 cm^2. The maximal film size that can be

transferred onto a sample is only limited by the dimensions of the Langmuir-trough, in particular the dipping well, and not by the process itself.

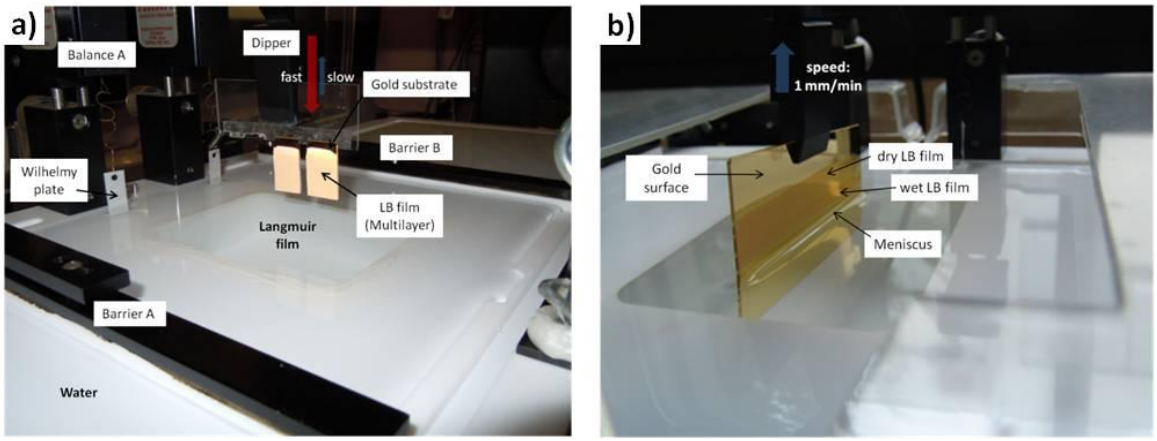

Figure 2.12: a) Side view on a Langmuir-Blodgett experiment. Several monolayers of silica beads have been transferred onto the gold coated glass substrate (ca. 1,5cm × 2,5cm). b) Transfer of the first monolayer on a gold coated substrate (8cm × 6cm). The meniscus that forms at the substrate-liquid interface confirms good wetting of the gold surface which was modified with a self-assembled monolayer (SAM) of cysteamine.

A typical example of a compression curve of a colloidal Langmuir film is illustrated in Figure 2.13a). Compared to the compression of molecular films seen in Figure 2.9b) the corresponding liquid state in the compression curve misses here. This represents a general feature observed in colloidal Langmuir films.[93] The film transfer occurs at constant surface pressures with values ranging from 5...10 mN/m. While the film is transferred to a sample, the movable barriers will reduce the area occupied by the Langmuir film in order to keep the surface pressure constant.

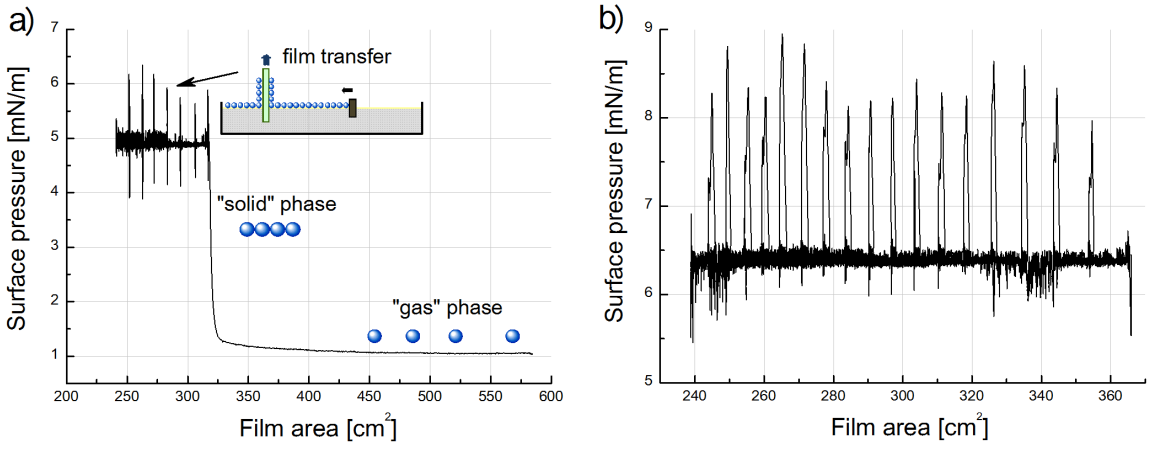

Figure 2.13: Surface pressure over the area occupied by the particle film in the LB trough. a) Compression of the particle film (silica, 470nm diameter) to a surface pressure of 5mN/m and subsequent transfer of 7 layers onto a bulk sample. b) Graph showing the transfer of 18 layers (silica, 600nm diameter) of a Langmuir film at a surface pressure of 6.4mN/m.

This feature can be seen in Figure 2.13a) and b), where the area occupied by the film decreases during the transfer. The peaks observed after every deposited layer are due to the sample leaving or reentering the water surface which creates a short peak in the measured surface pressure. They represent a convenient feature to follow the transfer process and to control the successful deposition of the desired number of monolayers on the sample. Figure 2.14 shows SEM images of colloidal crystals that have been produced using the LB technique. Figure 2.14a) and b) give a top view on a monolayer of silica spheres deposited on gold, whereas Figure 2.14c) and d) show the cross-sections of two multilayer samples of different sphere diameter. Figure 2.14a) illustrates a zone where a perfect crystalline array of close packed silica spheres is found. However, examining the LB film under a lower magnification reveals that well ordered domains are perturbed by several defects including grain bounderies, missing spheres or empty space between the spheres (see Figure 2.14b). The cross section of multilayer samples in Figure 2.14 c) and d) confirm that the thickness of the colloidal crystal is uniform throughout the sample. It is found that the actual number of layers found on the samples corresponds to the programmed ones.

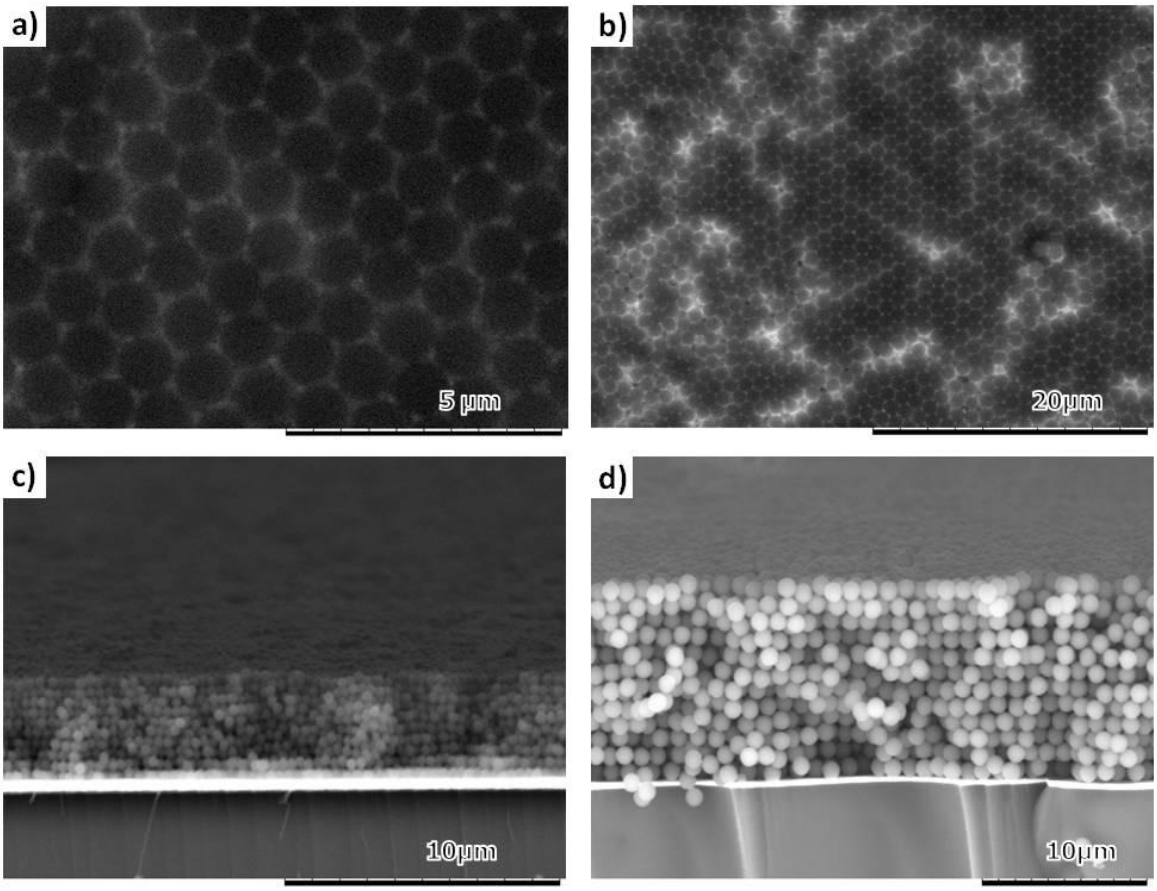

Figure 2.14: SEM images of colloidal crystals produced by the LB technique. a) + b): Top view of a monolayer of silica spheres (diameter 1µm) deposited onto a gold substrate in different magnifications. c) + d): Cross section of colloidal crystals composed of c) 10 layers of silica beads (d = 325nm) and d) 12 layers of silica beads (d = 1µm).

The high level of control that offers the LB technique is accompagnied by inferiour structural quality compared to colloidal crystals that have been obtained by other methods e.g. vertical deposition (VD). In the Langmuir-Blodgett technique 3D colloidal crystals are produced by stacking sphere monolayers onto one another which before have been assembled on a water surface. This results in a different packing and less ordered sphere layers than in colloidal crystals obtained from evaporation or sedimentation methods. The packing factor c in colloidal crystals obtained by LB is higher ($\geq$ 0.9) than in a perfect fcc lattice (0.816).[90] The enlarged layer spacing in the z-direction is accompagnied by optical properties that are different from those observed in fcc colloidal crystals.[96-98] Despite this drawback the LB technique offers several advantages over competing methods used for assembling colloidal crystals. As mentioned in chapter 2.2.1, colloidal crystals assembled from colloidal suspensions suffer from cracks that occur during the drying process. In this regard the LB technique offers a serious advantage. Building up colloidal crystals by a transfer of single monolayers from the air-water interface leaves enough time to dry for the individually deposited layers avoiding stresses in the colloidal crystal leading to crack formation. Therefore colloidal crystals produced by LB do not contain any cracks in their structure. Furthermore very few techniques are reported in the literature allowing to deposit only a single monolayer of particles onto different substrates.[99] This approach being of particular interest for applicatiions in nanosphere lithography.[100] Finally, LB allows a perfect control over the number of deposited layers including the possibility to combine spheres of a different diameter or chemical composition in the different layers of a colloidal crystal. This characteristic will be taken advantage of in chapter 4 to assemble colloidal templates that consist of very sophisticated architectures including sphere gradients or defect layers.

2.2.4 **Other techniques for colloidal sphere assembly**

Besides the basic techniques there are several other methods that can be used to assemble colloidal crystals and that may offer particular benefits over those discussed so far. The first that will be presented in this section relies on the assembly of colloidal spheres in capillaries. A straight forward setup is shown in Figure 2.15a). Here, two glass plates that are separated by thin spacers are placed into a colloidal suspension. Capillary forces will transport spheres into the cell towards the edges where evaporation of solvent and the crystallization of particles takes place. The thickness of the growing crystal is defined by the distance between the two plates. An SEM image of a sample produced with this setup can be seen in Figure 2.15c).[101] The crystal is very homogenous over large distances with a very low number of defects. For bigger particle

diameters less well ordered structures resulted which is probably due to the influence of gravity acting opposite to the capillary force.

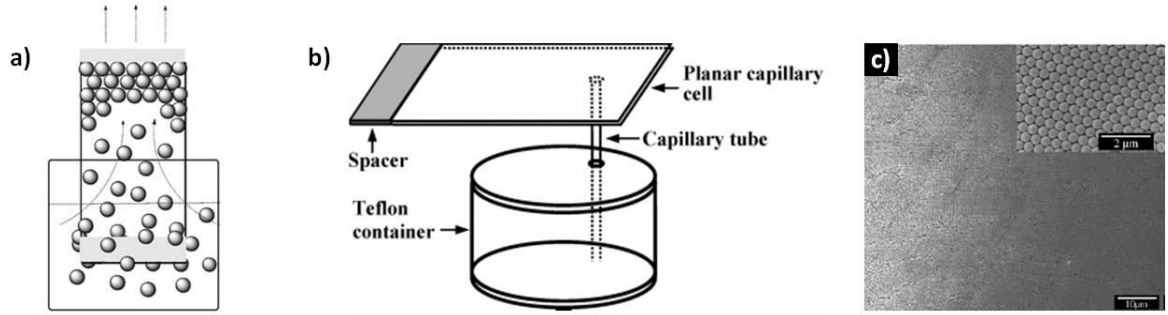

Figure 2.15: Capillary method. a) Schematic representation of the vertical capillary cell.[101] b) Setup containing a capillary tube for the transport and a capillary cell for the crystallization of colloidal spheres.[102] c) Colloidal crystal fabricated with the setup shown in a); particle diameter was 423nm.[101]

An alternative setup for this method illustrates Figure 2.15b).[102] In this bi-capillary deposition method particle suspension is transported first from a reservoir via a capillary tube into a secondary capillary cell. The crystallization of spheres in this planar cell is analogue to the process shown in Figure 2.15a) involving transport of suspension towards the edges of the cell followed by particle crystallization. The method was reported to allow for a good control over thickness and crack arrangements in colloidal crystals. Very similar setups to the ones shown in Figure 2.15 are used when colloidal crystals are formed by confinement. Park et al. were the first presenting a confinement cell in order to assemble colloidal crystals from particle suspensions.[103] However, in their configuration the particle flow was driven by the application of positive pressure transporting the particles to the cell edges. Microstructured membranes at the cell edges allowed the solvent to evaporate by retaining the particles in the cell.

Another group of techniques employs shear forces in order to produce ordered colloidal crystal arrays. The spin-coating process represents an example for shear induced ordering. Therefore colloidal silica particles were suspended in non-volatile triacrylate monomers and the mixture was spin-coated onto different substrates.[104] Ordering of the spheres is observed due to shear forces occurring when the suspensions smears on the rotating substrate. The photopolymerization of the monomer gave stable composite films where individual particles however were not necessarily in contact with each other. The use of volatile solvents as suspension medium enabled to produce colloidal crystals with touching spheres that did not have to be enclosed in a polymer matrix.[105] Apart from spin coating different setups can be employed to apply shear forces to a colloidal assembly.

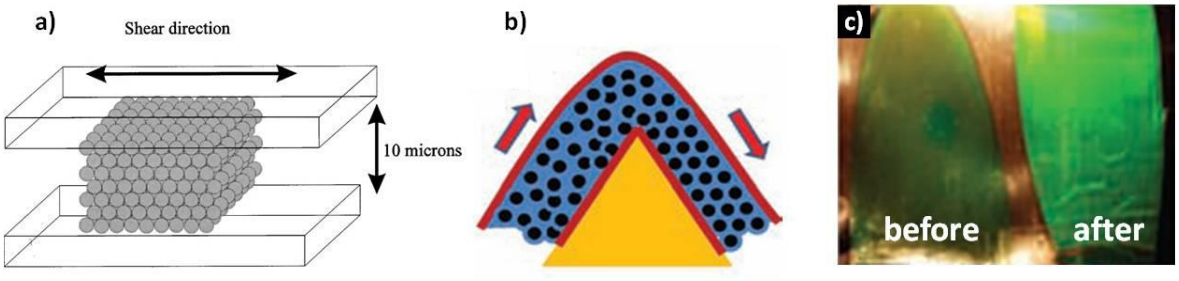

Figure 2.16: Ordering of colloidal assemblies by shear forces. a) Scheme of the shear alignement based process.[106] b) Ordering in opaline films by edge-induced shearing. c) Opal films before and after edge induced shearing [107]

In Figure 2.16a), a colloidal film is confined in a thin cell composed of two parallel plates, of which one is sheared against the other.[106] The resulting shear forces produce well ordered colloidal crystal arrays. Generally core-shell particles with a soft polymer shell grafted on a hard silica or polymer core are employed in techniques based on a shear alignment. By using polymer core-shell particles well established processing methods in polymer fabrication including extrusion or hot pressing can be employed to fabricate colloidal crystals.[107, 108] Recently, a possibility was presented to enhance the crystalline quality in these core-shell opaline films. First crystalline films out of polymer particles composed of a polystyrene core and a soft polyethylacrylate shell have been produced by extrusion followed by a rolling procedure of the produced ribbons. In a second step these films were drawn over a heated edge, which is schematically shown Figure 2.16b). This process resulted in significant improvements in terms of the crystalline order of these films. This finding is supported by the brighter colors seen for the opaline film shown in Figure 2.16c) on the right, where edge-induced shearing has been performed.

Some insight of what is possible in the field of colloidal assembly is given by Figure 2.17 and Figure 2.18. By confinement or patterning of substrates the crystallization in colloidal systems can be controlled leading to interesting new structures.

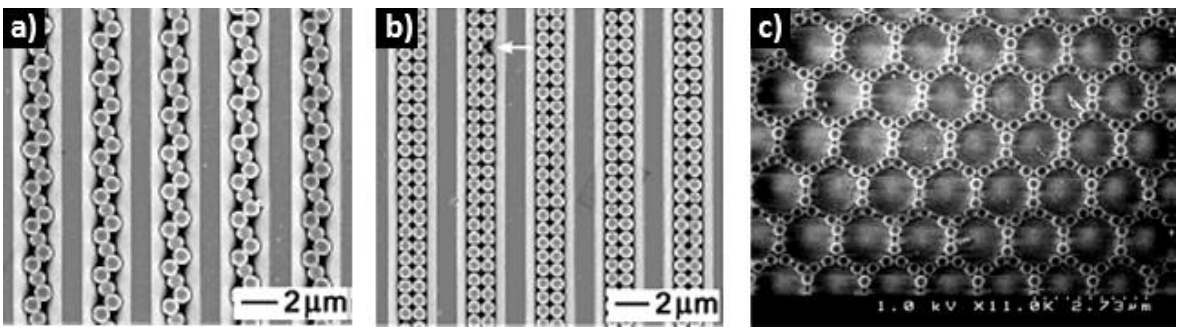

Figure 2.17: Aligned crystallization of colloidal spheres in V-shaped grooves into a) helical chains and b) straight chains. The arrow in b) denotes a missing sphere.[109] (c) Colloidal crystallization of a bi-modal sphere suspensions (diameter of the particles 1.28µm and 260nm).[53]

In Figure 2.17a) for example, the sphere diameter and the dimension of a V-shaped groove have been matched in order to lead to a helical chain of colloidal particles. When the same geometry is used in combination with a different bead diameter, the particles assemble into straight lines, as shown in Figure 2.17b). Achieving order in multi-modal systems equally is a very challenging task. Figure 2.17c) shows the crystallization of big particles in the presence of smaller ones forming a regular crystalline colloidal network. Here, choosing the right volume and size ratios between the two particle distributions are important parameters for a successful co-crystallization. Although the example shown in Figure 2.17c) relies on a 2D colloidal assembly, also 3D multimodal structures with long range periodicity can be fabricated.[110] By controlling the surface properties of the substrate, colloidal crystallization can also lead to very complex crystalline objects as illustrated in Figure 2.18.[111]

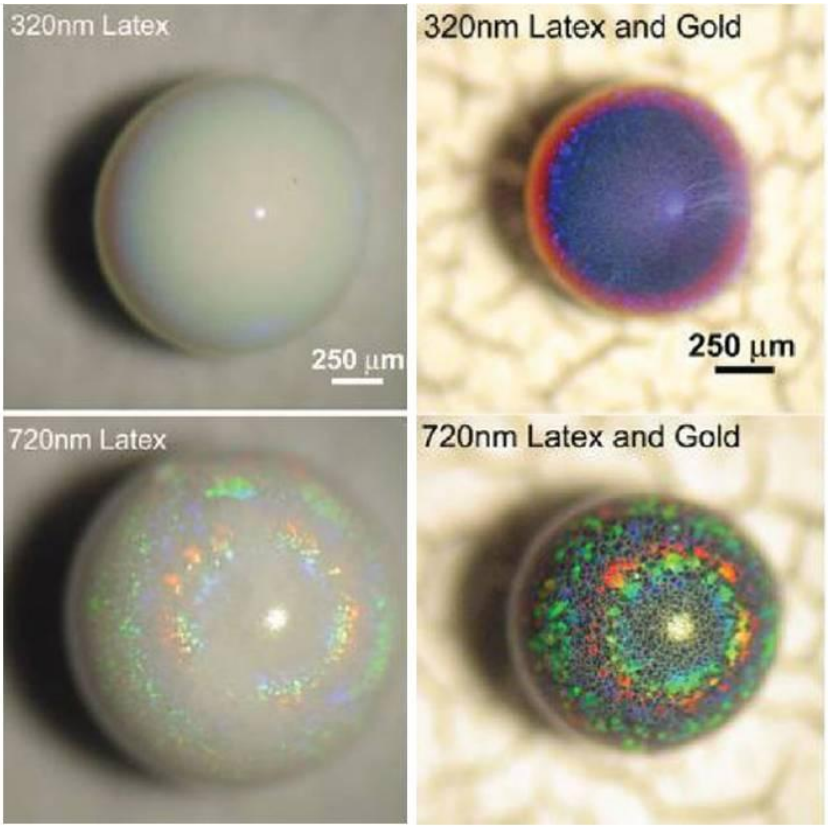

Figure 2.18: Colloidal crystal spheres obtained by crystallization on super-hydrophobic substrates. Spheres containing crystallized latex particles (*left*) and co-crystallized spheres of latex and gold nanoparticles (*right*).[111]

Superhydrophobic substrates ensured a minimal contact area between the colloidal droplet and the surface of the substrate leading to a spherical geometry. By changing the wettibility of the substrate also other forms including hemispherical shapes can be produced. The pictures at the left of Figure 2.18 show homogenous latex "microballs" of two different diameters. The opalescence in these structures already can be regarded as a proof for an ordered crystalline

particle arrangement. Co-crystallization of colloidal particles in presence of gold nanoparticles (d ~ 20nm) resulted in objects that are shown in the images at the right of Figure 2.18. At these objects the colors owing to Bragg diffraction are even more pronounced than in the latex "microballs", which was attributed to an increased reflectance and suppressed backscattering caused by the gold nanoparticles. By using electric fields these free floating colloidal droplets could be manipulated[112] enabling to produce various anisotropic structures including eyeballs and striped particles.[113]

2.3 Optical properties of colloidal crystal

The 3-dim periodic organization of spheres leads to a diffraction of light at the lattice of colloidal crystals. The characteristic coloration in artificial opals hence can be regarded as a proof for a high order of the constituting particles. Figure 2.19 shows gold coated glass slides with a deposit of either one (a and b) or two (c and d) layers of silica spheres. As mentioned in chapter 2.2.3, LB allows colloidal crystals to be fabricated on large sample areas which is illustrated by Figure 2.19a) showing a uniform monolayer film of silica spheres of more than 30cm^2 transferred on a gold electrode. The different colors observed in Figure 2.19b) - c) are due to the angular dependence of the Bragg diffraction and demonstrate the high quality of colloidal crystals obtained by LB.

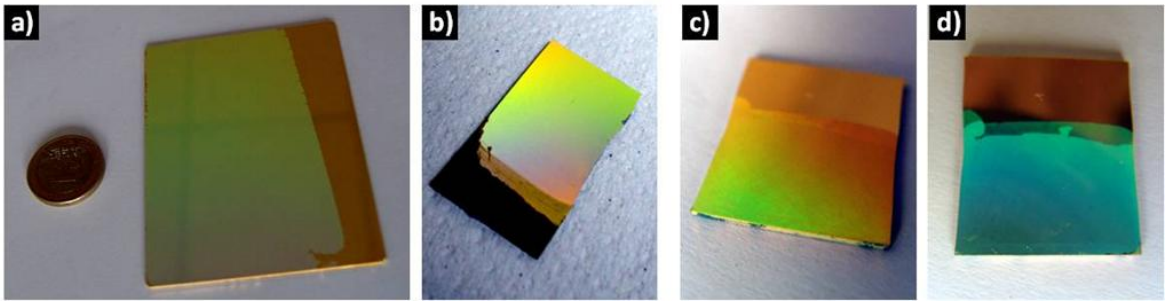

Figure 2.19: Optical photographs of different silica colloidal crystals transferred on gold coated glass slides by LB. One sphere layer with a diameter of a) 395 and b) 1200nm. c) and d): A sample composed of two sphere layers with a diameter of 440nm observed under different angles.

Bragg's law (see equation 2.4) describes the condition for which constructive interference of light occurs at the successive planes in the crystalline lattice.

$$m \cdot \lambda = 2 \cdot n_e \cdot d_{hkl} \cdot \sin\varphi \quad (2.4)$$

The integer m indicates the order of the diffraction, λ the wavelength of the Bragg peak, φ the scattering angle being equal to 90° for normal incidence and d_{hkl} the spacing between the planes in the lattice, which is given for the (111) plane in equation 2.5.

$$d_{111} = \sqrt{\frac{2}{3}} \cdot d \quad (2.5)$$

d corresponds to the diameter of the spheres in equation 2.5. n_e mentioned in equation 2.4 is the effective refractive index, which can be calculated from the refractive indices of the constituting materials n_{Si} = 1.43 and n_{Air} = 1 and their respective volume fraction Ø in the colloidal crystal (Ø = 0.74 for fcc), shown in equation 2.6.

$$n_e = \sqrt{\emptyset \cdot n_{Si}^2 + (1 - \emptyset) \cdot n_{Air}^2} \quad (2.6)$$

Spectroscopic measurements performed in the UV-Vis-NIR wavelength range are usually employed to characterize the optical properties of colloidal crystals.[45, 95, 114-116] In this non-destructive method different characteristics including the degree of order in colloidal crystals and their thickness can be obtained. Since colloidal crystals have been assembled on gold substrates, reflectance spectroscopy was carried out using a microspectrophotometer working at normal incidence in the UV-Vis-IR range between 250 and 1650 nm. Figure 2.20a) compares the spectra obtained for three colloidal crystals each comprising ten sphere layers with different particle sizes. In each curve the Bragg peak is characterized by a minimum of the reflected light intensity (indicated by the black arrows), shifting towards higher wavelength when the sphere size becomes bigger, as theoretically expected from equation 2.4.

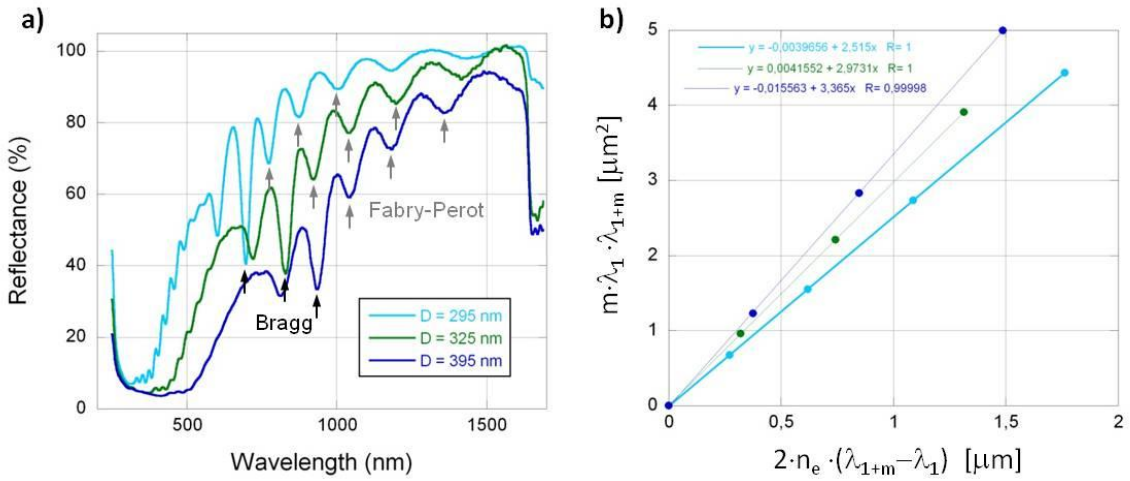

Figure 2.20: a) UV-Vis-NIR reflectance spectra of three colloidal templates consisting of 10 sphere layers of silica particles of either 295, 325 or 395nm diameter. Arrows indicate the positions of the Bragg peak and the Fabry-Pérot fringes. b) Plot for the determination of the thickness of each sample given by the slope of the linear fits by taking into account the peak positions of the different Fabry-Pérot fringes.

In addition to the Bragg peaks regular oscillations are observed in the different curves (here, between 700 and 1500 nm) which are known as Fabry-Pérot fringes. They originate from multiple

scattering processes of light at the gold/silica and silica/air interfaces causing interference phenomena.[25, 95] The wavelength positions of consecutive reflectance maxima (indicated by the gray arrows) allow to estimate the thickness Θ of a colloidal crystal,[95] using equation 2.7.

$$m \cdot \lambda_1 \cdot \lambda_{1+m} = 2 \cdot n_e \cdot (\lambda_{1+m} - \lambda_1) \cdot \Theta \quad (2.7)$$

λ_1 here is the wavelength position of the first visible fringe taken into account and n_e is given in equation 2.6, assumed to be close to 1.33. For each sample, Θ is therefore equal to the slope of the linear fits plotted in Figure 2.20b). By assuming a fcc packing of sphere layers the theoretical thickness e of a colloidal crystal with N sphere layers with a diameter d can be calculated from equation 2.8.

$$e = \left[1 + (N-1) \cdot \sqrt{\frac{2}{3}}\right] \cdot d \quad (2.8)$$

The theoretical thickness e and the experimental value Θ are compared in Table 2.1, showing a very good agreement for the colloidal crystals obtained with 295 and 395nm spheres. It is likely that the 325nm-spheres are slightly bigger than assumed causing the observed deviation between e and Θ.

d [nm]	N	e [µm]	Θ [µm]
295	10	2.46	2.51
325	10	2.71	2.97
395	10	3.30	3.36

Table 2.1: Comparison of the theoretical and experimentally determined thickness e and Θ, respectively, for three different colloidal crystals composed of N = 10 sphere layers of different sphere diameters d.

The fact that well defined Bragg peaks and Fabry-Pérot fringes are visible in the reflectance spectra confirmed that well-ordered colloidal crystals of uniform thickness had been fabricated by the LB technique. As shown by equation 2.4 the wavelength position of the Bragg peak depends on several parameters including the sphere size, the distance of the sphere planes and the refractive index of constituting materials allowing to use colloidal crystals and their inverse replicas as photonic sensors (see chapter 3.4). In the next section we will discuss which standards have to be met that colloidal crystals can be used as photonic crystals with a complete photonic bandgap.

2.4 Photonic crystals (PCs)

The term photonic crystals stands for a class of materials in which dielectrics or metallo-dielectrics with different refractive index are alternately arranged forming a crystalline structure. The refractive index throughout the material varies with a periodicity equal to the wavelength of light that may range from the visible up to the microwave region.

The basic concept of PCs has been introduced in the late 80's by Yablonovitch[117] and John[118] who predicted that photons of a certain wavelength could be prevented from propagating in PCs. They claimed the existence of allowed bands and forbidden gaps for photons in PCs. This may be considered in analogy to semiconductors, where the band structure determines the probability distribution of electrons in the material.[119] In semiconductors the periodic potential of the atomic lattice leads to the formation of a bandgap. Instead of atoms, a photonic crystal consists of a periodically structured dielectric media. If the dielectric constants of this media are different enough, Bragg scattering occurs at the dielectric interfaces resulting in a formation of a photonic band gap. [120] This leads to the case that photons with energies lying in the range of this forbidden band gap are not allowed to exist in the PC any longer. In a complete photonic bandgap a broad range of frequencies of light can be prevented from propagating in the photonic crystal.

The concept of the photonic band gap may also be used to guide the light in a photonic crystal. Therefore the perfect crystalline structure of a PC can very locally be interrupted by intentionally integrating a defect into the material. When this PC additionally possesses a complete photonic band gap for a certain range of frequencies, light within the wavelength of the gap only can propagate along the direction of the defect. Depending on the nature of the defect (line or point defect), light can be either guided through or localized in the crystal. Producing materials that would be able to guide or mold the flow of light represents the most exciting vision of how PCs could be used in future applications. Due to the fact that photons travel much faster in dielectric materials than electrons do in integrated circuits based on semiconductors, a new generation of optical circuits would allow to transport information faster and with lower energy losses due to the nondissipative interaction between light and dielectric media.[120]

Photonic crystals are characterized by different parameters. First of all they do exist as 1, 2 or 3D structures as illustrated in Figure 2.21. A one-dimensional PC structure (see Figure 2.21 *left*) consists of a periodic stack of alternating layers of different materials. In order to satisfy the condition for Bragg diffraction, the thickness of the different layers should be in the range of the wavelength λ of the light. By varying thickness and/or dielectric constants in the different layers the interference can be adjusted to be either constructive, which results in high reflection e.g. in a Bragg mirror, or destructive which can be taken advantage of in antireflective coatings.

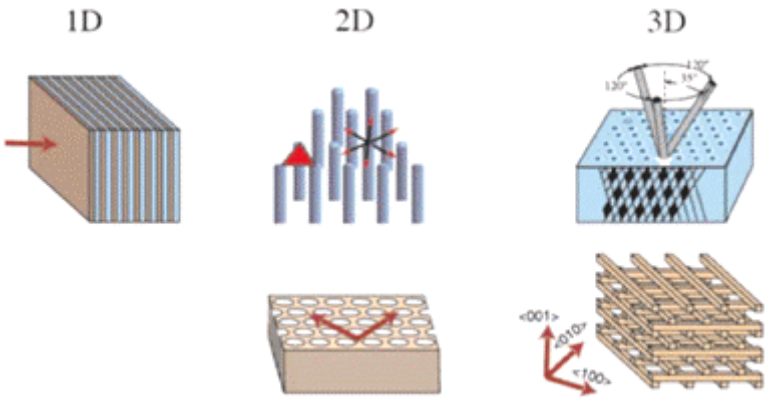

Figure 2.21: Photonic crystals of different dimensionality. *From left to right:* One dimensional structure: Bragg mirror. Two-dimensional structures: Hexagonal lattices formed by rods or pores. Three-dimensional structures: "Yablonovite" and "woodpile" structures [121]

However, as the material is anisotropic, total reflection of the irradiated light will be observed only for a single angle of incidence, making it impossible to achieve an omnidirectional photonic band gap with these 1D structures. In contrast 2D structures (see Figure 2.21 *middle*) are more complex to produce but comprise the possibility to be used in planar integrated optics.[121] The only structures which are isotropic, therefore allowing for a complete photonic band gap to open up irrespective of the angle of incidence of the irradiated light, are 3D PC structures (see Figure 2.21 *right*). The topology and the structural layout equally represent important parameters in PCs. For example, the distance between the basic building blocks in a PC directly has an influence on the spectral position of the photonic gap. Finally, a crucial parameter in PCs are the refractive indices n of the constituting materials. It can be distinguished between the effective refractive index n_{eff} and the refractive index contrast n_c of a PC. n_{eff} is calculated from the refractive indices n_1 and n_2 of the different constituents and their respective volume fraction φ in the crystal by equation 2.9.

$$n_{eff} = \sqrt{\varphi n_1^2 + (1-\varphi)\, n_2^2} \qquad (2.9)$$

The refractive index contrast n_c is defined by the ratio n_1 / n_2, where the higher of both values corresponds to n_1, therefore leading to values for $n_c \geq 1$. The higher n_c, the larger the spectral extension of the photonic band gap in PCs. It can be shown in simulations that n_c has to exceed a threshold value before a photonic band gap will appear in a given crystal lattice.[122] The influence of n_c on the band structure of a material is illustrated in Figure 2.22 for 1D structures. In bulk GaAs (*left*) no photonic bandgap exists due to the complete lack of a refractive index change in the homogeneous material. In a multilayer structure of GaAs and GaAlAs (*middle*) a photonic

bandgap opens up, which however is very small owing to the relatively low n_c (dielectric constants ε are 13 and 12). The photonic gap considerably widens when GaAlAs is replaced by air leading to a GaAs/Air multilayer structure (*right*) with a high n_c (with ε being 13 and 1).

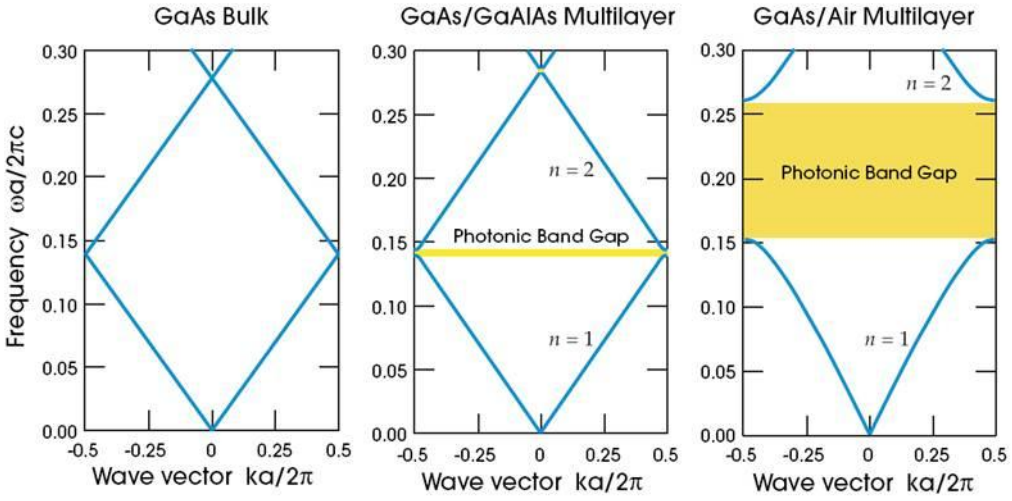

Figure 2.22: The photonic band structures for on-axis propagation, as computed for three different materials. *Left: bulk GaAs,* the dielectric constant is ε=13. *Center:* multilayer (similar to the structure shown in Fig left) alternating between ε of 13 and 12. *Right:* multilayers alternating between ε of 13 and 1. [122]

The first 3D photonic crystal with a complete photonic band gap could be realized in 1991 by Yablonovitch et al.[123] The bandgap was located in the microwave region of the electromagnetic spectrum and was attained with a Yablonovite structure corresponding to the one shown in Figure 2.23a). It was fabricated by drilling three sets of holes under a certain angle into the material as shown in the top right scheme of Figure 2.21.

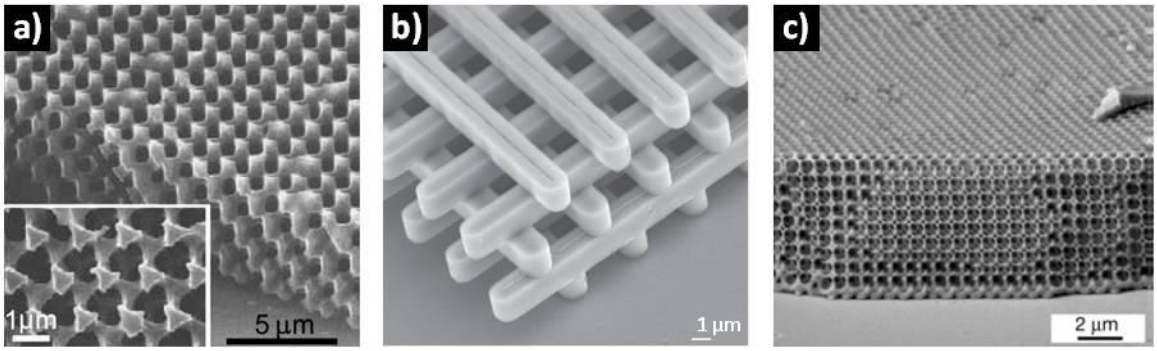

Figure 2.23: SEM images of 3D photonic crystals. a) Yablonovite structure produced in PMMA by a cylinder with a diameter of 650nm. [124] b) Woodpile PC structure made of silicon with a complete band gap at a wavelength of around 12µm. [122, 125] c) Silicon inverse opal with a photonic band gap around 1.3µm [44]

The woodpile structure, illustrated in Figure 2.23b) was introduced shortly after by Ho et al. [126] Compared to the previous method it offered the advantage that the "logs" could be added layer by layer using standard lithographic methods. This allowed for a more convenient integration of

defects in the crystal structure (see Figure 2.24b). Further miniaturization of the unit cell in the woodpile structure enabled to shift the photonic band gap towards the technologically interesting regions around a wavelength of 1.55µm which is used in optical communication technology.[125, 127-129]

Complete omnidirectional bandgaps also can be produced using a bottom-up approach based on the self-assembly of colloidal crystals. For this objective, colloidal crystals but especially their replicas come into consideration. The benefits of a colloidal approach, relying on readily available self-assembly techniques, consists in low fabrication costs combined with relatively big achievable sample areas. However for an application in PC, colloidal assemblies need to fulfill high standards concerning the crystal quality assuring a low number of stacking faults. A low percentage of disorder in the crystalline array was shown to restrict photonic band gap formation.[130] A complete photonic bandgap can be attained in colloidal crystals when the assembled spheres form a diamond crystal lattice, which is hard to realize with existing assembly techniques yielding mostly fcc or hcp packed orientations. [122, 131] However inverse opals with a fcc lattice orientation can exhibit complete photonic band gaps. This has been theoretically predicted in 1992 by Sözüer et al. [132, 133] and experimentally verified roughly ten years later, first by Blanco et al. and later by Vlasov et al. [44, 134] In Figure 2.23c) the perfect fcc alignment of air spheres in a silicon matrix is seen which gave rise to a complete photonic bandgap in the near-infrared region of the electromagnetic spectrum.

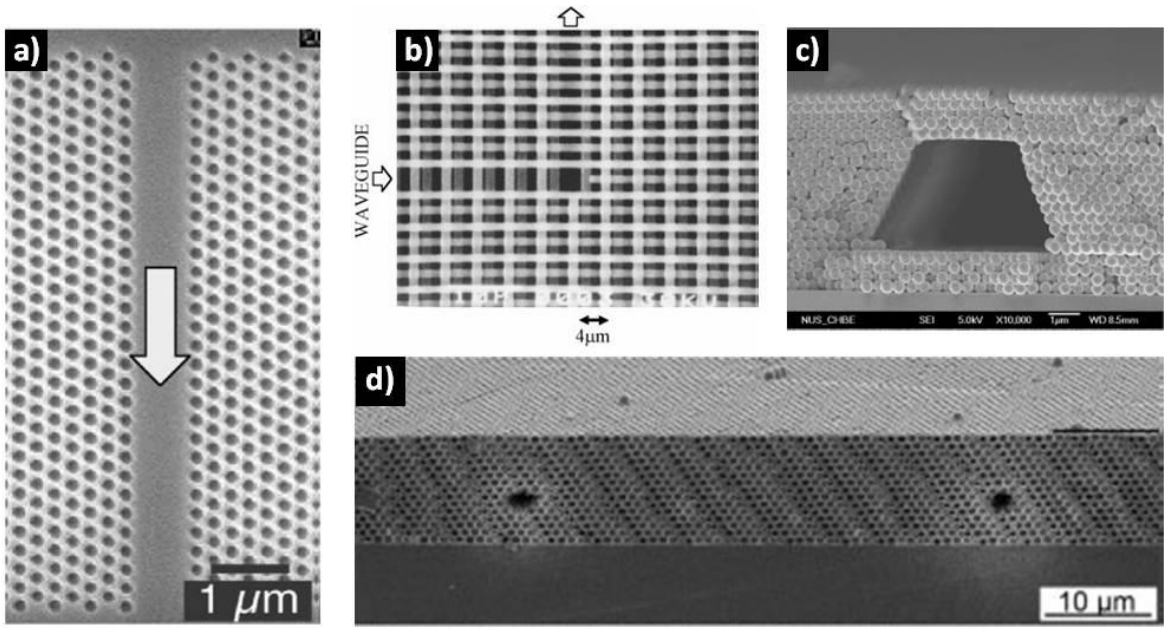

Figure 2.24: SEM images of defect structures integrated in photonic crystals. a) Principle of waveguiding in 2D photonic crystal structure. [121] b) Top view on a woodpile PC structure with a sharp bend (90°) waveguide.[128] c) Colloidal crystal containing a line defect. [135] d) Silicon inverse opal showing two air line defects. [136]

The objective to control the flow of light in a PC includes besides fabrication of the crystalline structure also its interruption in a defined area. Similar to the doping of semiconductors, the integration of defects can provide additional energy levels in the photonic gap where photons of a certain energy are permitted. Different kinds of defects can be integrated in PCs including 1D-point, 2D-line or 3D-planar defects. The principle of waveguiding in a two-dimensional PC is illustrated in Figure 2.24a). Here two arrays of holes are separated by a line defect out of dielectric material. The arrow represents light whose respective wavelength lies within the band gap of the photonic crystal. Thus it can not penetrate into the ordered array of holes. Instead its propagation direction is confined to the line defect situated in the middle of the PC. Defects can be integrated into a PC already during its fabrication or afterwards by top-down modifications of the structure. Figure 2.24b) gives an example where a waveguide structure has been integrated into a woodpile PC during its fabrication by using lithographic methods. A detailed overview over the various approaches to integrate different kinds of defects in colloidal photonic crystals is given by Yan et al. [137] For example, the line defect shown in the colloidal crystal in Figure 2.24c) could be produced by a deposition of photoresist in a two step assembly process of colloidal spheres. Among bottom-up techniques spin coating,[138, 139] transfer-printing[140] and the Langmuir-Blodgett technique [141, 142] have been successfully employed to build defects in PCs. Top down techniques comprise reactive ion etching[143] and multi-photon polymerization,[136, 144, 145] with the latter being employed to produce the air defects in the silicon inverse opal seen in Figure 2.24d).

2.5 Metamaterials

Metamaterials often are referred to as materials with properties that do not occur in nature. These artificially structured materials gain their properties from the unit structure rather than the constituent materials, a concept which is also found in photonic crystals. However, the inhomogenity scale which corresponds to the lattice parameter in periodic structures, is much smaller in metamaterials than the wavelength of interest. Its electromagnetic response is still expressed in terms of homogenized material parameters. [146] The research in metamaterials is a very new and interdisciplinary field where physicists work on the modelisation and the establishment of the theoretical background while chemists and material scientists provide techniques to fabricate these materials. The most important field in the area of metamaterials focuses on the research of materials with a negative refractive index.

In all naturally occurring materials the refractive index n of a material has a positive value typically greater than unity for electromagnetic radiation excluding x-rays. This is described by equation 2.10 where c denotes the velocity of light in vacuum and v_m the velocity in the material.

$$n = \frac{c}{v_m} \quad (2.10)$$

Based on Snell's law, a light beam will be refracted when entering and leaving materials with a refractive index contrast. The angle of refraction with respect to the normal, θ, depends on the ratio of the refractive indices of both media. For materials with a positive refractive index, θ is always positive leading to a refraction of a light beam which is qualitatively shown in Figure 2.25a). In materials with a negative refractive index the light beam will bend in the direction opposite to the normal resulting in a negative θ, as illustrated in the simulation of Figure 2.25b).

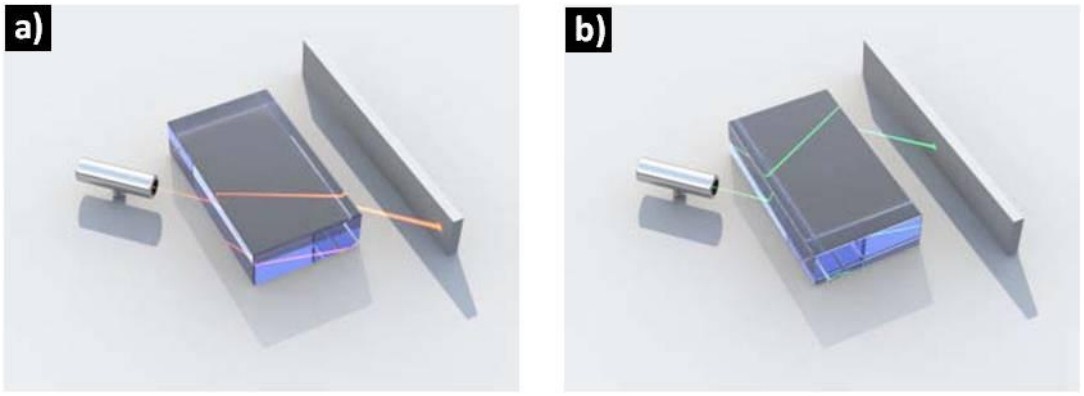

Figure 2.25: Simulation of a light beam that is refracted by a material with a) positive and b) negative index of refraction. Simulations are based on the raytracing method. [147]

Alternatively n can be defined by the relative permittivity ϵ and the relative permeability μ which are material parameters defining how the material is affected by an electric and a magnetic field, respectively. The relation between n, ϵ and μ is shown in equations 2.11 and 2.12.

$$n^2 = \epsilon \cdot \mu \quad (2.11)$$

$$n = \pm\sqrt{\epsilon \cdot \mu} \quad (2.12)$$

In order to classify the existing forms of matter by their value for ϵ and μ, a diagram with the real part of the relative permittivity and the relative permeability which are plotted in x and y direction is shown in Figure 2.26. Common transparent materials are situated in the quadrant where ϵ and μ both are positive. In the grey quadrants one of the parameters, either ϵ or μ is negative. Here, no propagating waves can be found in materials when the index of refraction

becomes purely imaginary. Furthermore this condition is fulfilled in plasmas, in metals at optical wavelengths (ϵ < 0) and in ferromagnetic media near resonance (μ < 0). The majority of the materials however that are used in optics are situated in a narrow zone, which corresponds to a value for μ = 1 represented by the dotted green line. To obtain a negative index material (NIM) with both, negative permittivity and permeability, situated in the remaining light blue quadrant, the coupling of a material with the magnetic field component of light has to be increased to achieve a negative value for the permeability. [146]

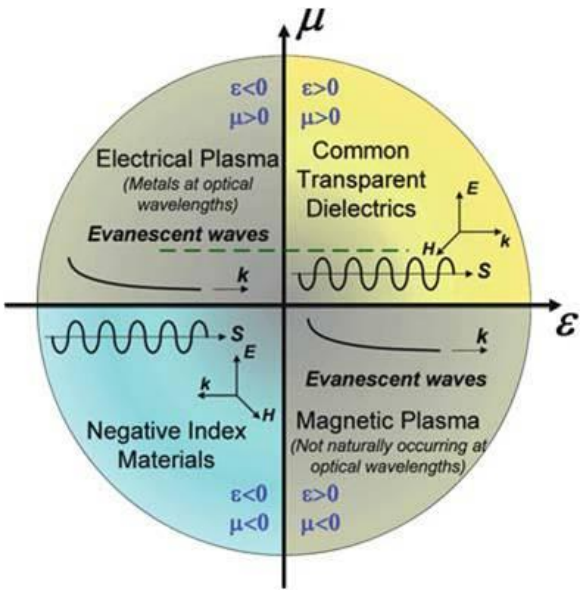

Figure 2.26: The parameter space for ϵ and μ. The two axes correspond to the real part of the permittivity and the permeability. The dashed green line denotes non magnetic materials with $\mu = 1$. [146]

The theoretical description of media with simultaneously negative permittivity and permeability has been provided by Veselago in 1968. [148] However it took more than 30 years to provide experimental evidence for this effect. In the year 2000 the first NIM with an operating frequency in microwave region was reported by Smith et al.[149] They used a composite medium consisting of periodic arrays of interspaced nonmagnetic copper split-ring resonators (SRRs). The illustration of their SRR design is shown in Figure 2.27.

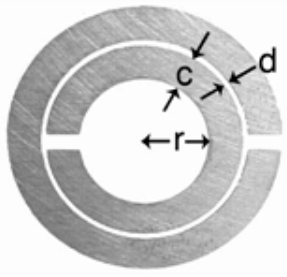

Figure 2.27: Split-ring resonator with two open concentric rings facing in opposite directions. In this first demonstration of a NIM the dimensions of the SRR were relatively big (c = 0.8mm, d = 0.2mm and r = 1.5mm) resulting in a resonance frequency of 4.845 GHz.[149]

The SRR structure can be regarded as an electronic circuit composed of inductive and capacitive elements. The rings form the inductive elements whereas the two slits with a gap between the rings act as capacitors. According to Lenz's law a magnetic field oriented perpendicular to the rings induces circulating and oscillating electrical currents in the rings that give rise to an opposing magnetic field in the loop. In consequence, this leads to diamagnetic response of the material which results in a negative real part of the permeability.[150, 151]

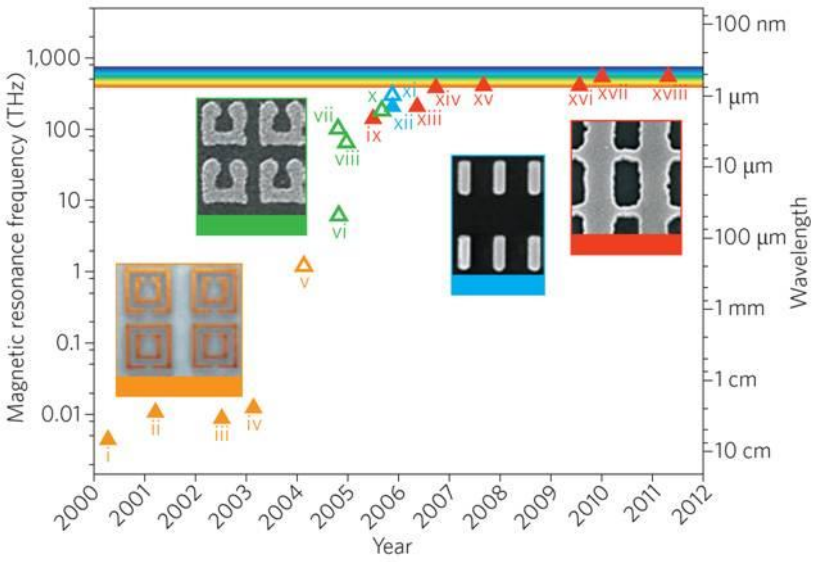

Figure 2.28: Progress in operating frequency of NIMs. The different colors refer to the different design employed in the metamaterial. Orange: SRRs; green: U-shaped SRRs; blue: Metallic cut-wire pairs; red: Negative-index double-fishnet structures. Empty triangles denote a negative permeability, solid triangles a negative index of refraction.[151]

Figure 2.28 illustrates the progress that has been achieved over the last 10 years in NIMs concerning the increase in operating frequency. By decreasing the unit size and slightly changing the design in SRRs, negative refraction was first verified at telecommunication[152] and subsequently at optical wavelengths (see Figure 2.29b).[153] Besides SRRs several other metamaterial designs have been developed till today that showed a negative refractive index. Among those are periodic arrangements of metallic cut wire pairs (see Figure 2.29c),[154] elliptical and cylindrical holes in metal-dielectric stacks,[155, 156] metallic nanowires,[157] and double-fishnet structures (see Figure 2.29a).[158] The latter, which was proposed theoretically in 2005,[159] helped to push the operating regime in NIMs towards optical wavelengths, as can be seen from Figure 2.28.[160-162] The pairs of broader metal strips in double-fishnet structures provide negative permeability, whereas pairs of narrower metal strips give negative permittivity.[150] In simulations the influence of different parameters, including the interlayer distance or the total number of layers, on the refractive index and the losses in the material were examined.[163]

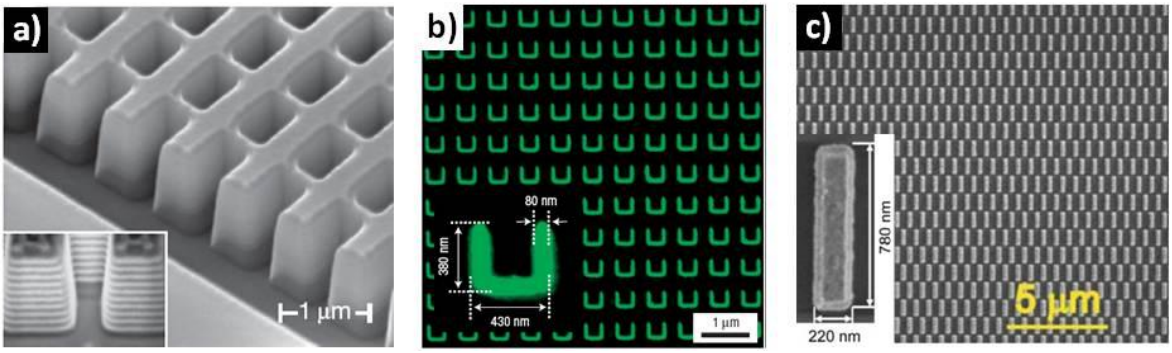

Figure 2.29: Images showing basic metamaterial designs. a) SEM image of a double fishnet structure consisting of alternating layers (see inset) of 30nm of Ag and 50nm of MgF_2.[160] b) FESEM image of a U-shaped SRR structure consisting of aligned gold rings.[153] c) FESEM image of a gold nanorod array.[146]

As can be seen from the different metamaterials illustrated in Figure 2.29, the single features as well as the distance between them are significantly smaller than the wavelength of visible light. Therefore the fabrication of these structures represents a critical issue in metamaterial research. Most of the methods employed in order to realize such small features rely on top-down approaches. Among them, e-beam lithography,[160, 162] interference lithography[155] and direct laser writing[164] represent the most commonly used techniques. Recently, a very convenient method to fabricate large areas (up to 75cm^2) of double-fishnet structures has been proposed.[165] This process is based on nanotransfer printing and uses a lithographically patterned stamp to deposit a metamaterial onto a desired substrate with the possibility to reuse the stamp for subsequent depositions. Bottom-up techniques however could provide a serious advantage over the state of the art techniques in terms of lower fabrication costs and a higher throughput. Electrochemical deposition into anodized alumina templates has proved to be a feasible strategy to fabricate NIMs resulting in periodically ordered arrays of metal nanowires.[157]

The first fabricated NIMs consisted of a single or a very low number of active layers with thicknesses in the sub-micrometer range making it difficult to measure material parameters in this thin 2D material. These metamaterial structures are also too small to serve in real world applications. Therefore a goal in metamaterial research consists in fabricating thicker 3D structures which would justify the use of the term "bulk" metamaterial. However, a general problem encountered in metamaterials represent the losses. All the different structures discussed so far rely on the use of metals in combination with a dielectric material. The basic problem with metals is their strong absorption of light especially in the near-infrared and optical domain of the electromagnetic spectrum. The relative permittivity ϵ as well as the permeability μ and consequently also the refractive index n can be expressed by a real and an imaginary part, as shown in equation 2.13.

$$n = n' + in'' = \sqrt{\epsilon \cdot \mu} \quad (2.13)$$

The imaginary part describes the loss of electromagnetic radiation in the material. The figure of merit (FOM), defined as n'/n'', represents a measure of the efficiency of metamaterials concerning its radiation loss. A metamaterial exhibiting low losses will show a high FOM. For example, a value of FOM = 3 is equivalent to a loss of more than 35% of the initial light intensity after passing a distance of a quarter of the wavelength inside the material (for λ = 600nm this corresponds to a distance of d = 150nm).[151] In this context it is important to know that a value of three for the FOM is among the best values achieved in metamaterials,[158, 161] even though very recently a value of eight was reported in the literature.[165] For practical applications of metamaterials these losses are still too high. Besides the possibility to reduce the losses by further optimization of the metamaterial design,[163] one can also introduce gain into the structure. As recently shown the incorporation of fluorescent dye molecules into a NIM can lead to a significant increase of the transmitted light intensity and so to higher FOMs.[166] Therefore the intermediate alumina layers in a double fishnet structure first were etched away in order to be replaced by an epoxy composite which contained the dye. Care had to be taken that the emission wavelength was matched to the operating frequency of the NIM. Although in this case researchers were able to increase the FOM from one to a value of 26, the pulses needed to pump the dye resulted in photobleaching after a short period of time, which still demands the search for sustainable solutions.

When research based on metamaterials would succeed to produce sufficiently big bulk structures with low radiation losses, some remarkable applications could be realized using these materials. The most appealing among them represents the realization of a superlens, which first was theoretically described in the year 2000 by Pendry[167] In classical optical lenses the smallest feature that still can be resolved is of the order of half of the wavelength of the incident light. When a planar slab of a NIM is used as the lens, not only the propagating waves but also evanescent waves can contribute to resolve the fine details of the object.[146] As shown in Figure 2.30a) the details of small objects such as DNA could be resolved by using negative index metamaterials. These superlenses however are limited to near-field imaging and work only at a single wavelength which represents a considerable drawback. Imaging beyond the diffraction limit already has been reported using thin silver slabs[168] or a superlens based on SiC,[169] although these materials did not exhibit a negative refractive index.

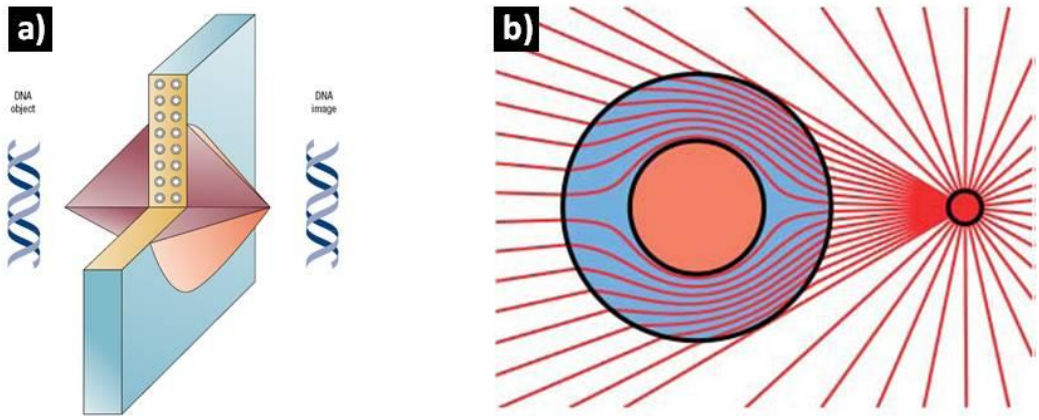

Figure 2.30: Applications of metamaterials. a) A superlens could perform high resolution of an image.[150] b) Principle of the cloaking of an object.

Another application in the field of transformation optics represents the realization of cloaking devices based on metamaterials. In 2006, two publications showed theoretically, that being able to design the permeability and the permittivity of a material at will would allow to bend light around an object without being absorbed or reflected by it.[170, 171] As the cloaked object shows no interaction with the electromagnetic radiation it would appear invisible to an observer (see Figure 2.30b). Five months after the theoretical prediction the first cloaking device based on SRR was experimentally shown for microwave frequencies.[172] Up to now several other demonstrations of successful cloaking with NIMs were provided in the near infrared regime of the electromagnetic spectrum with 2D[173, 174] and 3D structures.[175] Although many scientists predicted this effect to be restricted to a single wavelength, broadband cloaking over a range of frequencies was observed.[174-176] However, the spot size that effectively could be hidden from interacting with electromagnetic radiation was very small, in the order of some μm^2. And there is considerable doubt among the scientific community if one will ever be able to cloak macroscopic objects using metamaterials.[177]

In the following we`ll explain how the templates obtained by LB can be infiltrated with different materials and finally can lead to interesting devices not only in the context of metamaterials but also for many other applications including electrochemical or optical sensors, displays, energy conversion and storage devices, miniaturized cells or plasmon-enhanced metallic nanostructures.

3 Macroporous electrodes by infiltration of colloidal templates

In many cases colloidal crystals are not used directly for a certain application, they rather serve as templates for the fabrication of 3-dim ordered macroporous materials. There are several reasons which account for this. Inverse opals represent a mechanically more robust material than colloidal crystals. In the latter cohesion between the assembled spheres may get lost simply by plunging them into a liquid medium. The transformation of colloidal crystals into their inverse replicas also offers the possibility for new functionality. As discussed in chapter 2.4, it is not possible to achieve complete photonic band gaps with colloidal crystals except if the spheres are arranged in the diamond lattice. In inverse opals, however, the situation is different, owing to the lower filling ratio being with 26% instead of 74% for the ideal fcc lattice considerably lower. Choosing high refractive index materials ($n \geq 2.85$, e.g. silicon) for the formation of the inverse structure therefore allows complete photonic bandgaps in these materials.[44, 134] Besides multiple applications in the optical domain, these 3-dim ordered macroporous materials are also interesting as electrode materials which offer a high active surface area required in sensors, catalytic and energy-related applications. A structure is considered as macroporous, when the pore size exceeds 50nm, pores with 2-50nm are considered as mesopores whereas pores smaller than 2nm are termed microporous.

The general steps involved in transforming a colloidal crystal into its inverse structure are shown in Figure 3.1.

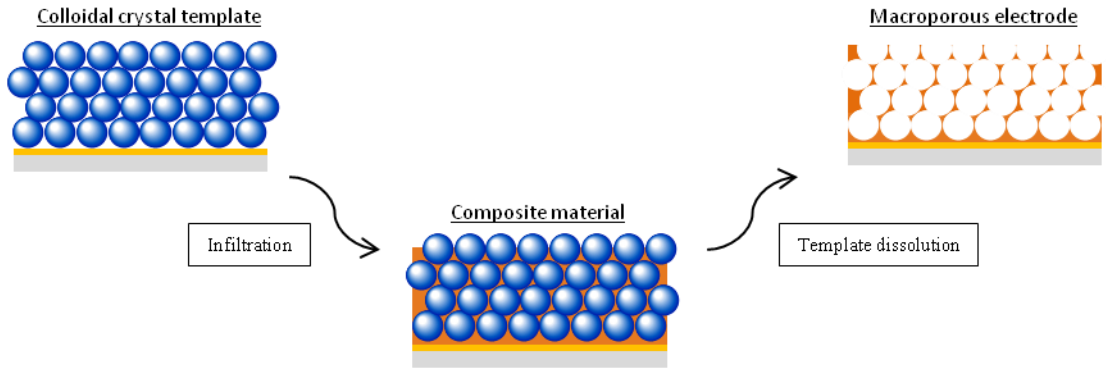

Figure 3.1: Fabrication steps in colloidal crystal templating. The void space in a colloidal crystal is infiltrated with another material. Removal of the template is achieved by calcination or dissolution of the colloidal spheres. As a result an inverse opal structure composed of interconnected air spheres which are embedded in the infiltrated material is obtained.

After assembling an ordered array of spheres on a substrate the void space present in the colloidal template can be filled with another material. Different techniques exist that allow efficient infiltration relying on precursors either in liquid or gaseous form. The choice of the adequate technique here is crucial for the final properties of the inverse structure as it will depend strongly on the employed infiltration method. Once the infiltration is terminated, the template can be removed by calcination or dissolution revealing a 3-dim ordered macroporous material.

Some general points regarding colloidal crystal templating may be addressed before discussing the different infiltration techniques. It has to be assured that the colloidal sphere template provides enough stability to allow its infiltration in liquid environments. To further stabilize the template structure it may be sintered. This results in a neck formation between neighboring spheres driven by surface energy minimization and eventually to a merging of the spheres. It is important to control this step by adapting the temperature and sintering time, because otherwise the void space can get too reduced to allow infiltration of the template. Combining sintering with a subsequent etching step also allows to fabricate non closed packed opals.[178] In order to allow the spheres to be removed after the infiltration, the etching solution has to be able to access the beads. Therefore the colloidal crystal should only be partly filled with material not exceeding the top layer of the template. This may be difficult to control in certain top-down based infiltration methods. The removal of the template generally occurs in dilute hydrofluoric acid for silica spheres and in appropriate solvents (e.g. toluene, dichloromethane or acetone) or by calcination for latex spheres.

In

Figure 3.2 two different inverse opal structures, that are obtained by colloidal templating, are schematically shown.

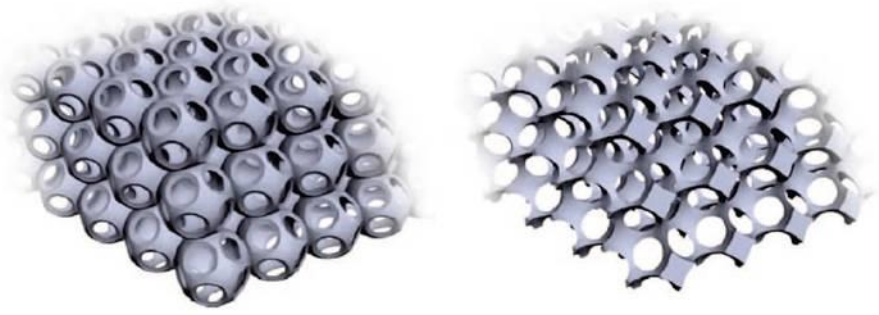

Figure 3.2: Schematic diagrams of a surface-templated material (*left*) and a volume-templated material (*right*).[179]

The structure on the left shows a surface-templated structure. Here the precursor interacts strongly with the spheres during the infiltration resulting in skeletal walls that follow the curvature of the original spheres.[179] In this case only part of the template is filled by the infiltrated material. On the right of

Figure 3.2 a typical example for a volume-templated material is depicted. Contrary to surface templating, all the available void space is filled by the infiltrating material so that the inverse structure is the exact cast of the original colloidal template. Which of both structures is present in inverse opals depends on both, the employed infiltration method and the degree of interaction of the precursor with the sphere material. Also mixtures of both cases are possible. For a given infiltration technique, one may switch from one structure to the other by changing either the precursor or the chemical nature of the spheres. These small structural differences also have influence on the optical properties of inverse opals e.g. the band structures in photonic crystals and hence have been subject of detailed research.[179-181]

3.1 Overview over different infiltration techniques

3.1.1 **Gaseous precursor infiltration**

Among the techniques that employ precursors in gaseous form the standard method for the infiltration of opals represents chemical vapor deposition (CVD). CVD is widely used in semiconductor processing to deposit thin coatings of silicon, metals and insulation layers on silicon on semiconductor wafers. In order to deposit thin films by CVD at least one gaseous precursors is introduced into a reaction chamber and condenses at the surface of a heated substrate. Substrate temperatures typically are in the range of 500 - 1000°C. CVD equally is known to result in uniform deposits even on complex 3-dim cavities, which makes it a suitable technique for the infiltration of colloidal crystals. In contrast standard physical vapor deposition (PVD) methods including sputtering or e-beam evaporation would result only in film deposition on top of the colloidal crystal which were used in the fabrication of 2D nanostructured metal films.[182] CVD generally is performed under reduced pressure in order to avoid undesirable reactions to take place in the gas phase including condensation reactions of gas molecules before they reach the surface of the substrate. The high temperatures involved in the process necessitate a temperature stability of the substrates. This excludes polymer particle assemblies from being infiltrated by CVD and bringing into focus silica based colloidal crystals. A variation of the process employs a plasma to increase the chemical reaction rates of the precursors enabling to lower the

reaction temperatures in plasma enhanced CVD (PECVD). Figure 3.3 shows some examples for inverse opals that were produced by chemical vapor deposition methods. Figure 3.3a) - c) all reveal the typical structure observed for surface-templated inverse opals (see also

Figure 3.2 *left*).

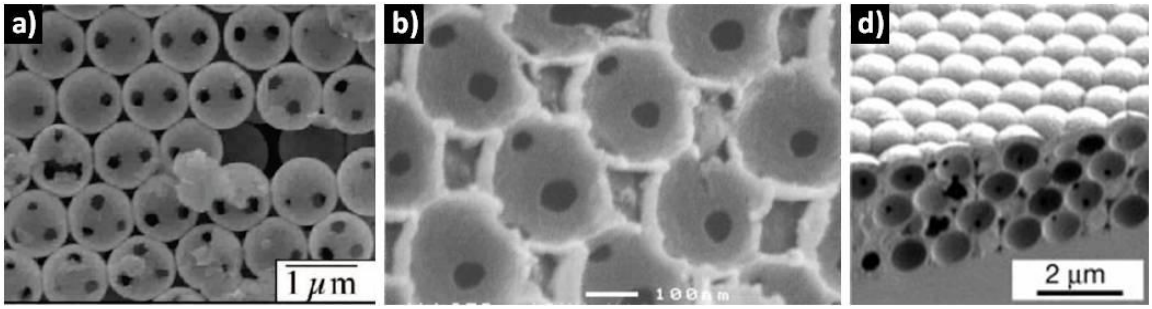

Figure 3.3: SEM images of inverse opal structures produced by CVD. a) Tungsten inverse opal showing the typical surface-templated structure.[179] b) Graphitic replica of an opal prepared by PECVD.[183] c) Si inverse opal obtained by low pressure CVD at temperatures slightly below 580°C.[44]

Gaseous precursor flows through the substrate and reacts at the surface of the spheres leading to a uniform coating. However colloidal templates are not filled completely by CVD, as access to the void space in the template gets restricted for the gas flow as soon as a certain deposition thickness is reached. Figure 3.3a) shows an example in which only a thin tungsten film has been deposited onto the colloidal template. After removal of the latter a crystalline assembly of hollow spheres with air cavities at the points where the colloidal spheres have been in contact is obtained. Figure 3.3b) depicts a graphitic inverse opal with similarly low filling fractions, showing the inner surface of a hollow sphere array. High filling ratios using CVD are generally accompanied by an overgrowth of material covering the top layer of the colloidal template which is illustrated in Figure 3.3c). This makes the removal of the template difficult as the access for the etching solution to reach the spheres is blocked. The excessively deposited material therefore first has to be removed. Ion milling using a focused ion beam provides a costly but well suited technique to ablate nanometer thick films in a controlled manner.[184] The materials deposited by CVD are amorphous, which requires heat treatment for several hours at temperatures where recrystallization in the material occurs.[44] Using CVD a range of materials can be infiltrated into opals including semiconductors (Si, Ge, InP, etc.), [13, 44] carbon based materials,[183, 185] or oxides.[186, 187] Recently, a variation of the CVD process has been applied for the infiltration of colloidal crystals permitting high control over the thickness of the deposited material.[184, 188, 189] In atomic layer deposition (ALD) different gaseous precursors are alternatively applied by a pulsed deposition. In between of the pulses a purging step allows to remove non-chemisorbed material. For example, a $TiCl_4$ layer, which has been chemisorbed at the surface of the substrate in a

previously applied pulse will react with the H_2O precursor provided by a second pulse, resulting in an atomic layer of TiO_2.[184] In this way the desired thickness is reached by a layer-by-layer deposition. As the process is self-limiting, ALD allows to deposit materials including TiO_2, WN and ZnS at a resolution of atomic layers.[13]

3.1.2 **Liquid precursor infiltration**

Inverse opals of various materials can also be obtained by infiltrating opals with liquid precursors. One can distinguish the different techniques by the type of medium used to infiltrate the opal including molecular precursors, sols, nanoparticle suspensions and molten media. The sol-gel process represents a versatile and commonly used technique in order to infiltrate opals. Here, metal alkoxide precursors infiltrate the void space of the opal and start a sol-gel process.[190, 191] Alternatively, the sol can be prepared before the infiltration and the sol-gel process is completed in the opal.[13, 192] The infiltration and reaction mechanism can be repeated several times in order to increase the filling fraction in the opal.[191] Once the infiltration is terminated the polymer template is removed by calcination which eliminates eventual remains of solvent and stabilizes the inverse opal structure. This process is accompanied by shrinkage of the structure (up to 40%)[13] and mass transport leads to a reorganisation of material in the structure. Typical inverse opal structures obtained by a sol-gel based infiltration technique are shown in Figure 3.4 a) and b). In these examples volume-templating in combination with material reorganisation during the sintering produced a skeletal structure with nearly rod-like struts.[179] Volume-templated inverse opal structures also could be obtained using sol-gel based infiltration.[193] The electrostatic interactions between the colloidal template and the precursor solution as well as the conditions during hydrolysis, drying and condensation represent important parameters influencing the final structure of the inverse opal.[179] Despite considerable drawbacks of the process involving the roughness of the inverse structure (~10nm), low filling fractions (about 12%) and the volume loss associated with the shrinkage, sol-gel based infiltration represents a very versatile technique. Besides the well studied oxide systems including TiO_2, ZrO_2, SiO_2 and Al_2O_3[116, 190, 191] also carbides[194] and even inverse opal doped with metals can be realized.[194, 195]

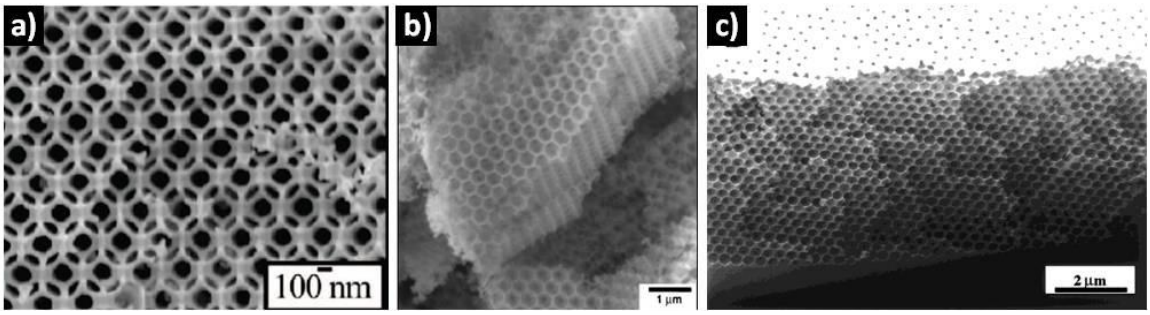

Figure 3.4: SEM images of inverse opals produced by infiltration with liquid precursors. a) Tungsten inverse opal with skeletal structure.[179] b) Inorganic skeleton of a macroporous zirconium oxide sample after calcination.[190] c) PMMA inverse opal with 24 layers after monomer infiltration, UV-polymerization and removal of the silica template.[196]

Polymer inverse opals can be fabricated by infiltrating colloidal crystals with monomers followed by a polymerization of the monomers by exposure to UV light [196, 197] , heating [198] or catalyzed polymerization.[199] Using this approach different polymers including PU (polyurethane), PMMA and PS can easily be fabricated.[196-199] The same strategy was employed to produce inverse opals of conjugated polymers leading to electrochromic devices with enhanced switching times.[200] A simplification towards a one step process was proposed by Yan et al., who mixed the precursor directly with the colloidal suspension in order to form an ordered crystalline assembly of the mixture on a water surface.[201] The cross section image of a PMMA polymer inverse opal is depicted in Figure 3.4c). A shrinkage of 20 to 30% was reported to result from polymerization of the monomers.[196]

Alternatively metallic or semiconducting materials can be infiltrated in the molten state into opals when the melting temperature is low enough. The infiltration of molten selenium into a colloidal crystal led to an inverse opals with a high refractive index contrast interesting for an application in photonic crystals.[202]

Another strategy consists in using nanoparticles to infiltrate colloidal crystals. The nanoparticles have to be sufficiently small to allow the infiltration of the void channels in the opal (about a tenth of the diameter of the void channels).[13] In this way the shrinkage was considerably reduced, as the nanoparticles already were in their final chemical form. This approach enables inverse opals to be fabricated from a variety of materials including metals, oxides or semiconductors. [116, 203, 204] Recently transparent macroporous electrodes from antimony doped tin oxide (ATO) have been fabricated in this way.[204] This technique may further be simplified by mixing colloidal spheres with nanoparticle suspensions in order to co-assemble "filled" opals from bi- or multimodal dispersions.[205, 206] A heating step may provide structural stability to the crystalline assembly prior to the template removal. With this method very complex metallodielectric inverse opals can be obtained by using core shell nanoparticles possessing a metallic core and a dielectric

shell or the other way round.[207] The use of microfluidic devices allowed to break bi-modal suspensions of polystyrene and silica spheres into separate droplets resulting in very uniform porous microspheres after the drying and calcination of the samples.[208]

3.1.3 **Infiltration via electrochemical deposition**

The void space in a colloidal crystal template equally may be filled using electrochemical deposition. A typical setup for electrodeposition experiments consists of three electrodes, a working (WE), a counter (CE) and a reference electrode (RE) that are connected to a direct current power supply. The electrodes are immersed into an electrolyte solution which contains species that may be deposited by reduction (e.g. metal ions) or oxidization (e.g. monomers) on the working electrode. The driving force for the redox process is provided by a potential or a current which is applied to the working electrode in potentiostatic or galvanostatic mode, respectively. The substrate containing the colloidal template serves as the WE and thus needs to be electrically conductive. The application of adequate potentials at the working electrode leads to a film growth at the surface of the electrode. Contrary to the methods described in the chapters 3.1.1 and 3.1.2, the filling of the void space here starts at the bottom of the template proceeding towards the surface. This is quite convenient as it allows to stop the electrodeposition at the desired filling level and avoids overgrowth of material over the top surface of the template. In most cases, the entire void space of a colloidal crystal is filled by the electrodeposited material, hence leading to volume-templated inverse opal structures (see
Figure 3.2 *right*). As a consequence, high filling fractions are achieved during in the electrochemical infiltration of opals. Additionally, the shrinkage, if involved in the process, is insignificantly small compared to sol-gel techniques, as the electrodeposited material already is in its final chemical form. This results in inverse opals with a good mechanical stability.

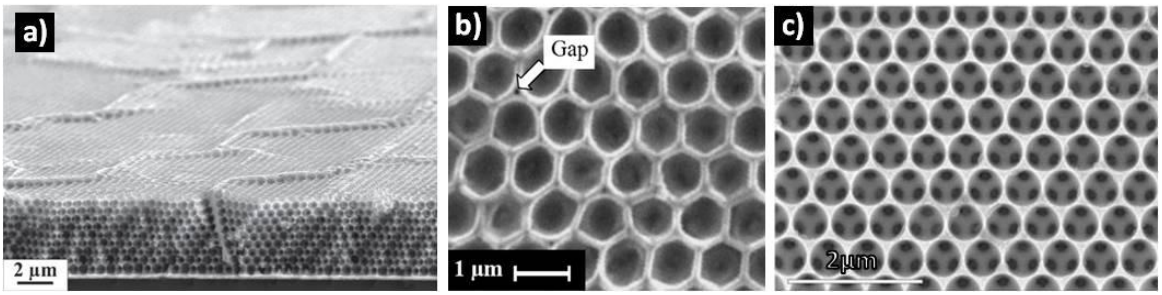

Figure 3.5: Inverse opals produced by electrochemical deposition. a) Cross-section of a nickel inverse opal with nine and a half-layers. [209] b) Top-view of a conducting polymer inverse opal produced by electrodeposition of poly(3,4-ethylenedioxythiphene) (PEDOT). [210] c) Top-view of a germanium inverse opal fabricated by electrochemical deposition in an ionic liquid. [211]

In some conducting polymer inverse opals also surface-templated structures were observed. [210, 212] Figure 3.5b) shows a poly(3,4-ethylenedioxythiphene) (PEDOT) inverse opal possessing small air gaps at the connecting points between neighboring air cavities. These gaps are due to the growth of the polymer happening preferentially around the sphere template guiding the film deposition. This guiding effect was attributed to the electrostatic interactions between the radicals formed during the polymerization and the surface groups of the colloidal spheres.[210] Figure 3.5c) gives an example of a volume-templated inverse opal structure in which the electrodeposition was stopped exactly at a half height of a sphere layer. The three dark spots inside of each macropore correspond to the areas where spheres of an underlying layer were in contact with the top layer spheres. Here the colloidal template has been completely filled with germanium. Figure 3.5a) shows the cross-section of macroporous nickel electrode with highly interconnected pores.

A wide range of materials can be electrodeposited and was used to infiltrate colloidal crystals. The biggest group among them represents metallic deposits owing to the commercial availability of ready-to-use plating solutions providing a uniform film deposition in the colloidal template. Inverse metallic opals have been prepared by electrochemical deposition from platinum,[213-215] gold,[203, 206, 215-218] silver,[219, 220] copper,[213] nickel,[209, 213, 221-226] cobalt,[214, 222] palladium,[214] bismuth,[227] antimony,[228] and iron.[222] Conducting polymers also can be grown into a colloidal template by electrochemical deposition. Inverse opals of conducting polymers were obtained from polypyrrole (PPy),[212, 229, 230] polyaniline (PANi),[212, 231] polythiophene (PT) [212, 230] and PEDOT. [210] Some semiconducting materials including Ge,[211] CdS [232] and CdSe [232] have also used to infiltrate opals by electrodeposition. Additionally a range of metal oxide inverse opals has been fabricated by electrodeposition including ZnO,[233, 234] WO_3,[235] PbO_2,[236] IrO_2,[237] RuO_2,[238] MnO[239] and NiO,[240] completed by some inorganic/organic hybrid derivatives.[241]

3.2 Electrodeposition of metals in colloidal templates

The gold coated glass slides onto which colloidal crystals had been previously assembled by the LB technique, were used in the following to fabricate macroporous metal electrodes.

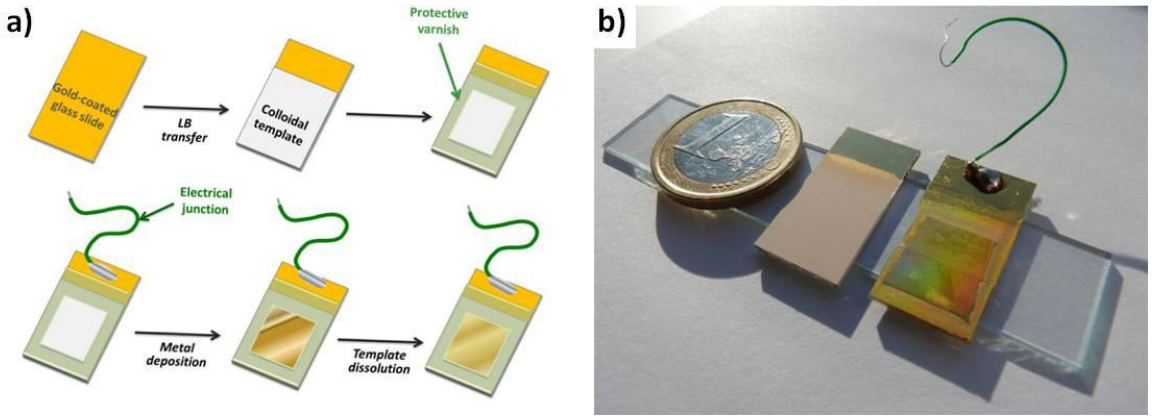

Figure 3.6: a) Schematic representation of the different steps involved in the fabrication of macroporous metal electrodes. Varnish is used in order to delimit the accessible area for the electrochemical deposition on the sample. b) Optical photograph of the gold coated glass slides after deposition of the colloidal template (*middle)* and at the end of the whole process (*right)*.

The fabrication steps including colloidal template assembly, metal electrodeposition and removal of the inorganic template are schematically illustrated in Figure 3.6a). Here, the sides and the parts on the gold coated glass slides where no colloidal template has been deposited, were covered with varnish in order to exclude these regions from participating in the electrodeposition process. A conductive wire was soldered to the gold surface in order to facilitate the electrical connection of the sample. The setup which was used for the electrochemical deposition is schematically illustrated in Figure 3.7. In a classic three electrode setup the gold substrate with the colloidal template served as WE. A silver-silverchloride electrode (Ag/AgCl, sat. KCl) was used as RE and a platinum plate or mesh as CE. All electrodes were connected with a µ-Autolab Type III which provided a DC current supply and which was controlled by the software GPES. A counter electrode with a big surface area, at least double the size of the WE, was used in order to avoid a limitation of the electrodeposition process at the anodic part of the reaction. Both, working and counter electrode were placed parallel to each other at a defined distance in order to ensure homogeneous deposition rates throughout the whole sample area.

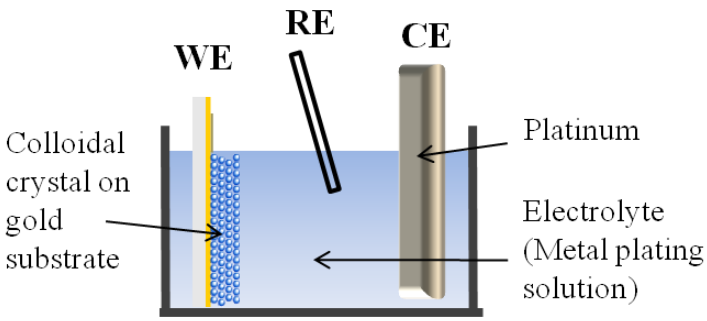

Figure 3.7: Scheme of the setup used for the infiltration of colloidal crystals with various metals by electrochemical deposition. WE: working electrode; RE: reference electrode (Ag/AgCl); CE: counter electrode.

By applying a sufficiently negative potential to the WE the electrodeposition process was initiated, provoking the reduction of metal ions accompanied by metallic film growth at the surface of the WE. The metallic deposit consequently filled the void space in the colloidal template. Once the desired thickness of the deposit was reached, the electrodeposition was stopped. The inorganic template was removed by immersing the sample for 5 minutes in dilute hydrofluoric acid (HF; 5% aqueous solution) resulting in a macroporous metal electrode. The picture in Figure 3.6b) shows a gold coated glass slide with the colloidal template (*middle*) and the macroporous gold electrode after electrodeposition and removal of the silica template (*right*).

3.2.1 **Gold electrodeposition into colloidal templates**

For the electrodeposition of gold into the void space of colloidal templates the commercial gold bath ECF 60 (Metalor) was used. In Figure 3.8 the different plating baths together with aqueous solutions of metal ions employed in this work have been compared using cyclic voltammetry. In the cyclic voltammograms (CVs) the onset potentials for the reduction of the different metal ions can be determined. By comparing the CVs of the aqueous gold chloride solution and ECF 60, one notices, that considerably more negative potentials have to be applied to the commercial gold solution in order to reduce the gold ions than in the case of the solution containing the gold salt. The reason for this high overpotential is the presence of different additives in the plating solution aiming to inhibit uncontrolled 3D growth and to favor a smooth 2D growth process. As described in previous works, we used a potential of -660mV vs. Ag/AgCl in order to reduce $AuSO_3^{2-}$ ions, contained in the plating solution, to metallic gold.[217, 218, 242]

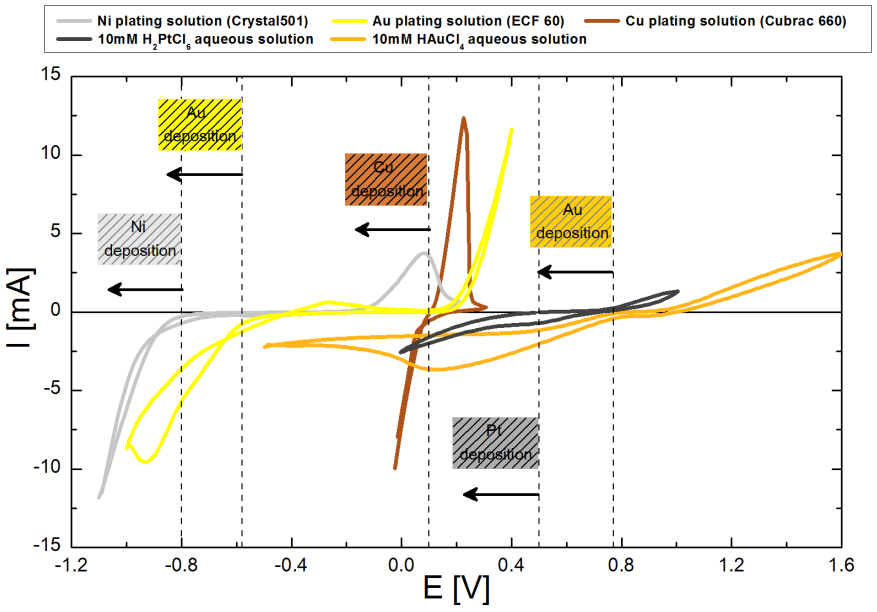

Figure 3.8: Cyclic voltammograms performed in commercial plating solutions and aqueous solutions containing a metal salt with a gold coated glass slide as WE. The different onset potentials for the electrodeposition of metallic films are illustrated by the dashed vertical lines.

The intensity of the faradaic current during amperometric deposition was measured as a function of the electrodeposition time and is shown in Figure 3.9. Here, we were able to observe very regular current oscillations during the infiltration of the colloidal templates with gold. The main parameters, which affect the current intensity during potentiostatic deposition, are the applied electrode potential, the composition and temperature of the plating solution and the active area of the WE. As the potential was kept constant during the electrodeposition and the electrolyte composition and temperature changed only insignificantly in the course of an experiment, the faradaic current response depends exclusively on the active surface area of the WE. Deposition performed on a smooth electrode without a colloidal crystal on its surface hence is expected to result in a constant response of the current intensity. The presence of a colloidal template on the surface of the electrode however leads to current oscillations (see Figure 3.9) that are caused by a periodic variation of the surface area that is available for the electrodeposition in the colloidal template.

During the early stages of the electrodeposition in Figure 3.9, the metal film nucleation adds a certain amount of surface roughness to the electrode and hence increases its active area. The absolute value of the current therefore increases and reaches a maximum, corresponding to the first local minimum in the plot since the current is negative. The value of the absolute current decreases in the following as the metal film begins to fill the void space of the first bead layer. Here, the surface area accessible for the growing film gets more and more restricted in the

colloidal template and finally reaches a minimum, when the growth front attains the half height of the first bead layer. Consequently also the absolute current attains a minimum at this point, corresponding to the first local maximum in Figure 3.9. The half-layer gold filling level in the colloidal template is illustrated by the corresponding inset in Figure 3.9. From this point on, the upper half of the first bead layer in the template will be filled with electrodeposited gold.

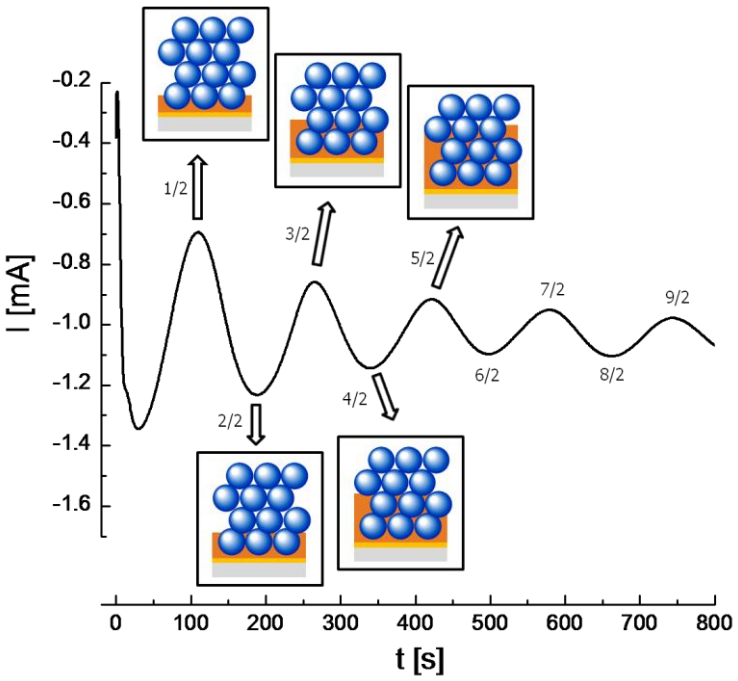

Figure 3.9: Current oscillations observed during potentiostatic gold deposition at E = -660mV into a colloidal crystal template with a sphere size of 395nm. Absolute current minima corresponding to different half-layer gold filling levels in the template and absolute current maxima to full-layer filling levels with gold.

Contrary to the previously described period, the space between the neighbouring spheres here continually increases providing a greater surface area for the growing metal film. The absolute value of the current consequently increases, up to the point, where the film reaches the bottom of the second sphere layer in the template. This results in an absolute current maximum which corresponds to the second local minimum in Figure 3.9. The void space of the first bead layer here is completely filled with gold (see corresponding inset in Figure 3.9). The whole process, here described in detail for the infiltration of the first bead layer, continues for the filling of succeding sphere layers and results in well pronounced oscillations of the recorded current response. Infiltration into colloidal crystals therefore can be regarded as an electrochemical deposition where the surface area of the WE periodically changes througout the experiment.

These oscillatians represent a very convenient feature because they allow to perfectly control the filling of the void space in colloidal crystals with an accuracy that can reach a few nanometers. Obviously, as illustrated by the different insets in Figure 3.9, one can stop the electrodeposition at

half- or full-layer filling levels which results either in completely open or almost fully closed pore structures, respectively, after removal of the colloidal template. As the electrodeposition can be stopped at any time between the local extrema, very good control is provided over the final structure of the inverse opal. In order to ensure best possible access of the solution to the macroporous structure, the electrodeposition generally was stopped at a half-layer filling level resulting in a complete opening of the pore mouths at the electrode surface.

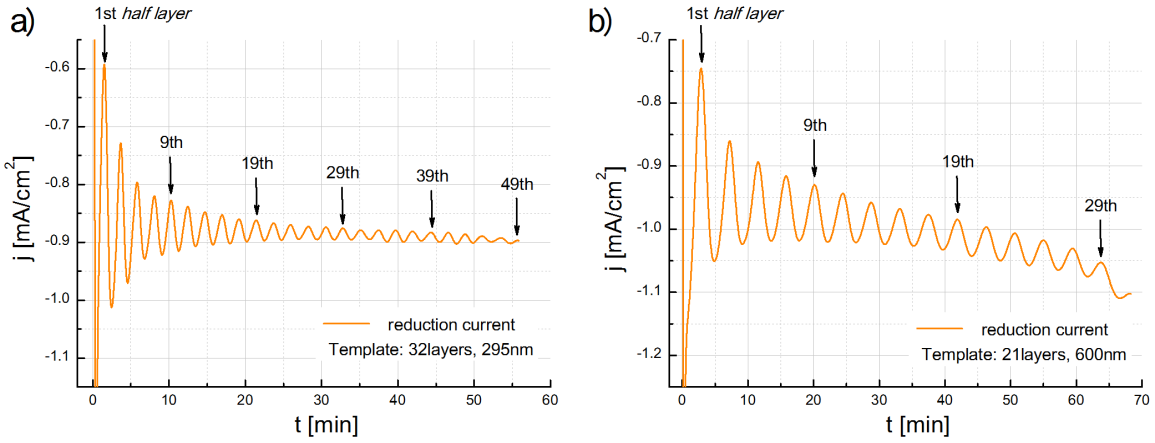

Figure 3.10: Amperometric electrodeposition of gold into colloidal crystal templates at E = -0,66V. Oscillations obtained for the infiltration of a) 49 half-layers (bead size 295nm) and b) 31 half-layers (bead size 600nm) of gold into the templates.

Oscillating currents during amperometric electrodeposition into colloidal crystal templates have been reported before by several authors including preceding works performed in our group. [209, 217, 221, 224, 242] The appearance of this phenomenon is coupled to two crucial parameters requiring both, a well organized colloidal crystal structures combined with the uniform growth of the electrodeposited material. As shown by the oscillations in Figure 3.9, the intensity decreases the longer the electrodeposition time and the more void space in the template gets filled by the metal. The cause for the gradual decrease of the oscillation amplitude can be twofold. A lack of organization in the sphere layers and electrodeposited material not growing homogeneously throughout the template are both leading to the situation, that the synchronization between the factors increasing or decreasing the global current response gets lost in the course of the infiltration so that the oscillations finally are "canceled out". Nevertheless, we were able to observe an oscillating current response during the infiltration of colloidal templates for up to 25 sphere layers and deposition times exceeding one hour (see Figure 3.10a and b). Such results confirm that the packing of sphere layers in colloidal templates produced by the LB technique is very regular. In the corresponding literature the oscillations cancel out much faster and could be observed in the best case only up to a filling level of 10 sphere layers. [209] In Figure 3.10 the current

density j, which corresponds to the measured current intensity divided by the geometric surface area of the sample, has been plotted as a function of the electrodeposition time facilitating the comparison of the results obtained for samples with different surface areas.

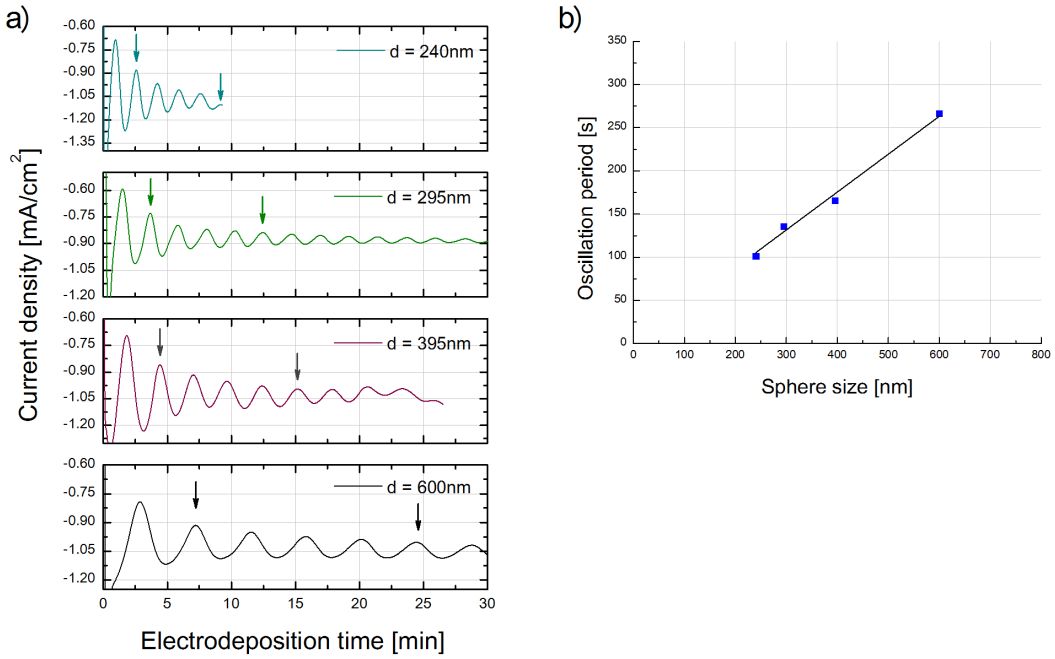

Figure 3.11: a) Chronoamperometric curves for the electrodeposition of gold into colloidal crystals with a different sphere size. The two arrows represented in each curve correspond to the filling of 3/2 (*1st arrow*) and 11/2 layers (*2nd arrow*) of the template with gold. b) Plot of the oscillation period obtained from the results shown in a) as a function of the colloidal sphere size of the template.

By comparing Figure 3.10a) and b), one notes that the frequency of the current oscillations changes when the sphere size of the colloidal template changes. By geometrical considerations the oscillation frequency should be doubled when spheres with a two times smaller diameter form the template, supposing a constant metal deposition rate during different template infiltrations. In Figure 3.11a) four different chronoamperometric curves are compared showing the infiltration of gold into different colloidal templates, that are composed of different sphere diameters. It is found that the frequency of the oscillations decreases when templates composed of bigger spheres are infiltrated. The arrows added in Figure 3.11a) indicate that three (*first arrow*) and eleven (*second arrow*) half-layers of the template have been filled with gold. For bigger sphere sizes the corresponding arrows are shifted towards longer times, the frequency decreases and the oscillation period increases. Based on the data of Figure 3.11a), one can plot the oscillation period as a function of the sphere size in the template shown in Figure 3.11b). A linear relation is found between sphere size and oscillation period (or frequency) in accordance with theoretical considerations.

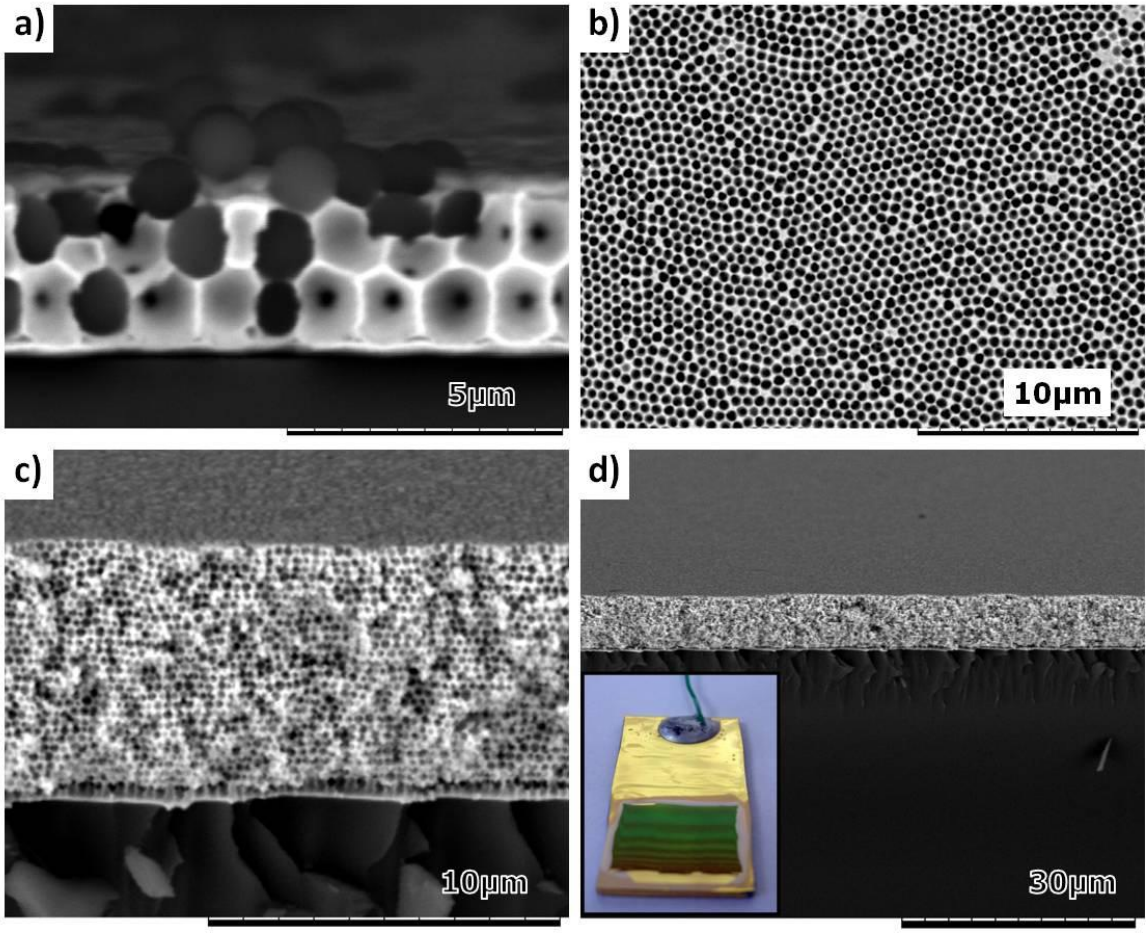

Figure 3.12: SEM images of macroporous gold electrodes obtained by electrochemical deposition. a) Cross section of a colloidal structure (d=1200nm) where two layers have been filled with gold. b) Top view onto three half-layers of macroporous gold (d=600nm). c) Cross section of a macroporous gold electrode with 49 half-layers (d=295nm); The corresponding amperometric curve is shown in Figure 3.9a). d) Larger view of c) with the inset showing a picture of the sample (geometric area of the macroporous deposit ~1cm^2).

Figure 3.12 illustrates SEM images of several macroporous gold electrodes. In Figure 3.12a) an electrode cross section of a two-layer template is shown which has been filled with gold. As expected, the whole volume in the template has been filled with gold resulting in volume-templated structures. At the black spots which lie inside the macropores, no metal was deposited because touching spheres prevented the electrolyte solution from accessing these areas. After template removal these spots will become the interconnection points between neighbouring macropores. Figure 3.12b) provides a top view of a macroporous gold electrode with a thickness corresponding to one and a half pore layers. Here, macroporous domains with a perfect organization are disturbed by some defects in the structure which is in accordance with the colloidal template structure discussed previously in Figure 2.14b). Figure 3.12c) and d) show the cross section of the macroporous gold electrode which corresponds to the amperometric deposition curve in Figure 3.10a). Both SEM images confirm the uniform thickness of the electrode which consists of 49 half-layers of macroporous gold.

3.2.2 **Electrodeposition of copper, nickel and platinum in colloidal templates**

Besides gold also other metals including copper, nickel and platinum have been deposited into colloidal templates. For the electroposition of copper and nickel, commercially available plating solutions have been employed (Copper: Cubrac 660, Nickel: Crystal 501; both Coventya). Platinum was electrodeposited from an aqueous solution containing 60mM hexachloroplatinic acid (H_2PtCl_6) and 0.1 wt-% of the anionic surfactant sodium dodecyl sulfate (SDS).[243] Cycling voltammetry experiments gave a first indication of the potentials required to reduce the corresponding metal ions in these electrolytes (see Figure 3.8). Additionally, electrodeposition at different applied potentials was performed for each electrolyte solution in order to find the adequate potential leading to smooth and homogeneous film growth. For nickel and platinum, straight forward conditions were found for applied potentials of - 0.93V and + 0.142V [244] vs. Ag/AgCl, respectively. In contrast to Pt and Ni deposits, electrodeposited copper films (applied potential: + 0.05V) showed a very rough surface structure. It was therefore not possible to observe current oscillations during the amperometric deposition of copper into colloidal templates. The film growth of nickel and platinum in the colloidal template however proceeded homogeneously and smoothly enough that oscillations in the current response could be observed. In Figure 3.13a) a colloidal template composed of 10 layers with a sphere diameter of 325nm was filled with 17 half-layers of platinum. The measured current here showed similarly regular oscillation profiles as the ones previously observed during potentiostatic gold infiltration. As a consequence the filling level of the colloidal template with platinum could be perfectly controlled. Figure 3.14a) shows the cross section image of the same electrode after platinum had been deposited into the template. It turns out, that exactly eight and a half-layers of the template have been infiltrated with platinum which is in perfect agreement with the results shown in Figure 3.13a). In Figure 3.14b) the silica template has been etched away resulting in the macroporous platinum film electrode. The thickness of the film is perfectly uniform and the pore layers are well organized in the sample. By looking closely one can see black air spots inside the macropores that interconnect adjacent pores.

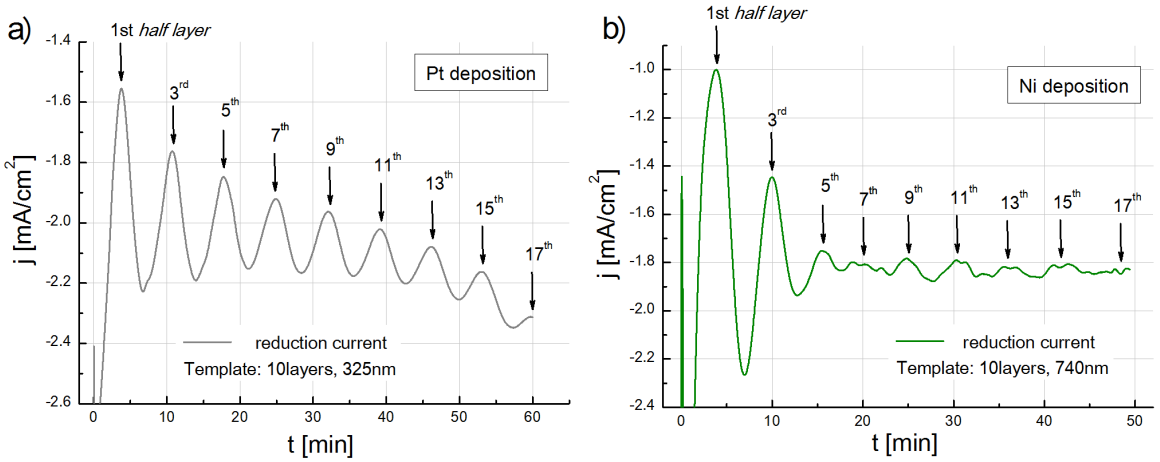

Figure 3.13: Amperometric electrodeposition of a) platinum into a colloidal crystal template (10 sphere layers, diameter 325nm) at an applied potential of E = 0.142V. b) nickel into a colloidal template (10 sphere layers, diameter 738nm) at an applied potential of E = -0,93V.

In Figure 3.13b) the current oscillations observed during the nickel infiltration into a colloidal template is illustrated. Here, as in the case of Pt, 17 half-layers of the template should be filled with nickel. The sphere size in the colloidal template however was with 740nm more than double the size of the one used in Figure 3.13a). At the beginning of the electrodeposition the first and second oscillations show a very regular form with high amplitudes. Already the third oscillation is less pronounced and a big part of the oscillation amplitude is lost. Nevertheless, oscillations are visible until the deposition process is stopped corresponding to a filling level of slightly more than eight sphere layers. The relatively fast loss in the oscillation amplitude during the electrochemical infiltration may be due to an irregular sphere layer stacking in the colloidal template. Figure 3.14c) shows the electrode cross section after the filling of the template with nickel. The top surface of the template here is found to be very uniform providing no direct evidence of irregular packing of the sphere layers in the colloidal crystal. In order to identify the reason for the less regular oscillations observed in the case of nickel infiltration further electrodeposition experiments are necessary. In Figure 3.14d) the macroporous nickel electrode is shown. The thickness as well as the organisation of the pore layers here seem less uniform than in the case of porous platinum films. As the gold coated glass electrodes are broken in order to allow cross-section images to be made, the fracture surface may be more or less intact after the breaking process providing rarely a view on a single plane in the sample. In the case of the macroporous nickel film shown in Figure 3.14d) the cross-section image seems to contain different planes of the sample pretending the structure to be less ordered.

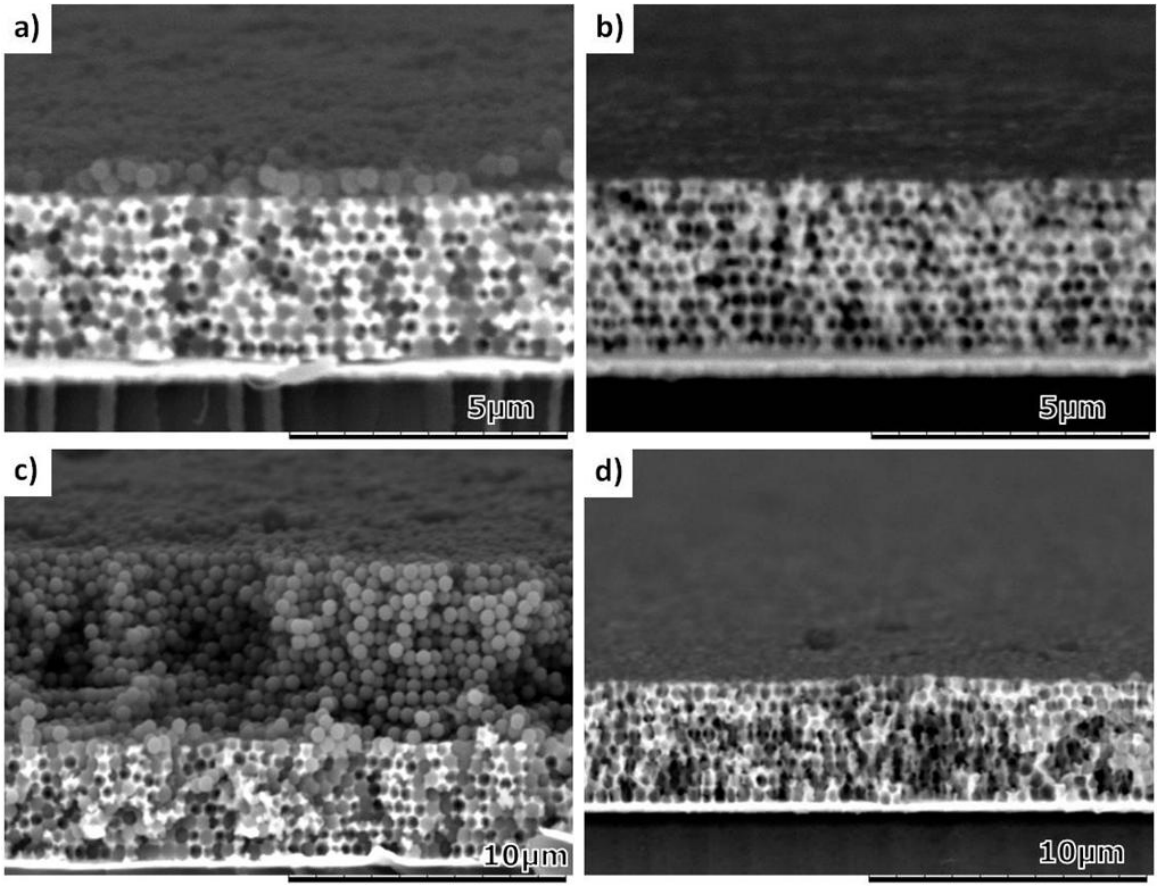

Figure 3.14: SEM cross section images of nickel and platinum films electrodeposited in colloidal templates. a) Platinum film infiltrated into a colloidal crystal (10l. of 325nm). b) Same structure as in a) but without the colloidal template. c) Nickel film electrodeposited into a colloidal crystal (20l. of 738nm). d) Same as in c) but without colloidal template.

3.2.3 **Electrochemical characterization of macroporous metal electrodes**

Macroporous metal electrodes possess a greater surface area than their non porous analogues. It is this gain in active electrode surface which makes macroporous materials interesting for different kind of applications including energy storage and conversion, electrocatalysis and electroanalysis. Some examples for the application of macroporous electrodes will be given in chapter 3.4. In this context the determination of the active surface area presents an important property in order to characterize the macroporous material. There are different ways to determine the real surface area of metal electrodes by using electrochemical techniques. [245] The choice of the most appropriate method depends on the type of metal that is characterized. For metals including Pt, Rh and Ir, hydrogen adsorption is typically used to determine the real electrode area. Prior to H_2 evolution at sufficiently negative applied potentials a monolayer of hydrogen atoms is adsorbed onto the electrode surface. Assuming the adsorption of one hydrogen atom on each metal atom, the charge associated to the hydrogen ad- or desorption

peak allows to calculate the number of metal ions at the surface of the electrode hence its active surface area. In a similar way oxide monolayer formation and its reduction on electrode surfaces can be used to determine active electrode areas. This represents the standard method that is used for the electrochemical characterization of gold electrodes. The potential here is cycled in between fixed values leading during the anodic scan to the formation of a complete oxide layer on the gold surface which then is fully reduced in the cathodic cycle. The charge which is associated with the reduction of the oxide layer allows to calculate the real surface area of the electrode, assuming a value of 390 $\pm$ 10 µC/cm^2 for a smooth polycrystalline gold surface. [245]

Cyclic voltammograms performed in 0.5M sulfuric acid with smooth and macroporous gold electrodes are shown in Figure 3.15a). Macroporous electrodes with the same pore size but a different number of pore layers have been compared with a smooth gold electrode in this plot. The potential was cycled in between limits of 0V and 1.5V. Gold oxide formation started above 1.1V and the reduction peak in the cathodic scan was situated around 0.9V. The measured current has been divided by the geometric surface area of the sample in order to be able to compare the obtained results quantitatively.

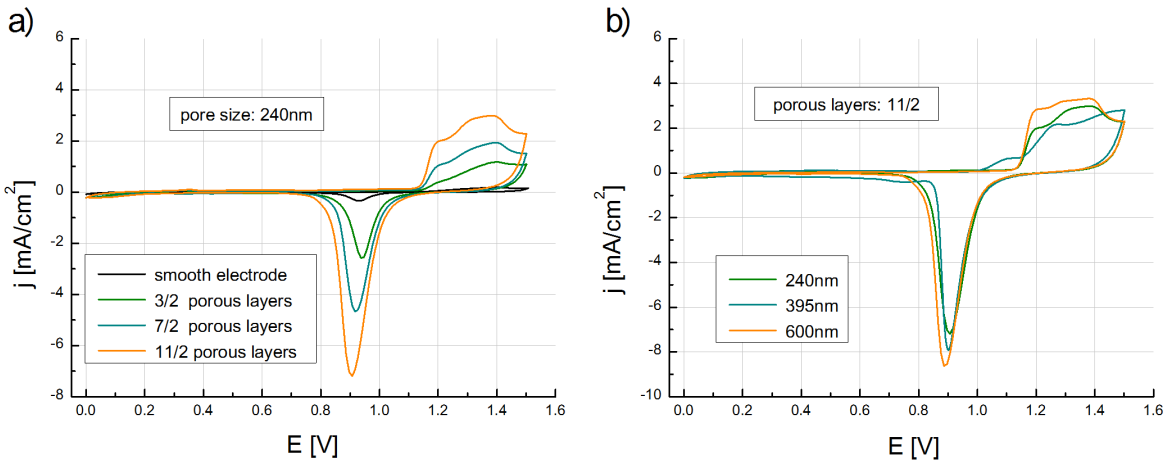

Figure 3.15: Characterization of macroporous gold electrodes by cyclic voltammetry in 0.5M sulfuric acid. a) Comparison of macroporous gold electrodes with increasing number of pore layers (3, 7 and 11 half-layers) with a non porous gold electrode. b) Three macroporous electrodes with the same number of pore layers (11 half-layers) but different pore sizes are compared.

As one would expect, the intensity of the oxidation and the reduction peaks are considerably higher for the macroporous electrodes compared to the flat gold sample and are gradually increasing as the number of pore layers in the sample increases. In Figure 3.15b) the CVs of three macroporous gold electrodes with the same number of pore layers but different pore sizes are compared. Although the absolute film thickness is by more than a factor two higher for the sample with 600nm pores compared to the one with 240nm pores, the observed peak intensities

in the different curves all are approximately at the same level. But it also has to be considered that the pore density and hence the gain in surface area in a given volume of porous material is increased when the pore size decreases. By geometrical considerations the factor by which the active surface area is increased in macroporous materials can be determined.[218] This factor will be referred as to the theoretical roughness factor R_{th}, which is given in equation 3.1.

$$R_{th} = \sqrt{\frac{4}{3}} \cdot \pi \cdot n \quad (3.1)$$

As n in equation 3.1 corresponds to the number of pore layers in the macroporous material, the increase of surface area in macroporous materials consequently only depends on the number of porous layers and not on the pore size. This is in perfect agreement with the results shown in Figure 3.15b). The active surface area of samples with a higher number of porous layers (31 and 49 half-layers) also was determined as shown in Figure 3.16a). Here the peak currents are further increased for the macroporous samples, which results in barely visible peaks for the bare gold sample at this scale (see inset Figure 3.16a).

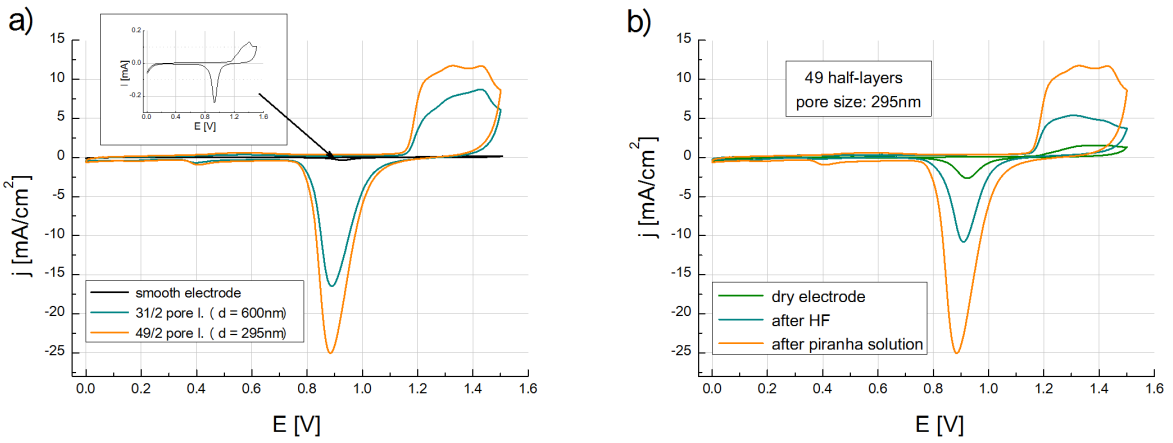

Figure 3.16: Characterization of macroporous gold electrodes by cyclic voltammetry in 0.5M sulfuric acid. a) Compared are a smooth electrode and two macroporous electrodes composed of 31 and 49 pore half-layers. b) Wetting effect in macroporous electrodes: CVs of the sample composed of 49 half-layers after storage for more than a month in air (*dry*), after immersion for five minutes in HF (5 vol-%) and for one minute in piranha solution (75 vol-% H_2SO_4, 25 vol-%H_2O_2).

In order to evaluate the increase in active surface area in a quantitative way, the roughness factor R and the active surface area has been determined for the different samples and is shown in Table 3.1. For a 49 half-layers thick macroporous gold film the roughness factor reached a value of 88, meaning that the initial geometric surface area of 0.64cm^2 has been multiplied by this value resulting in an active surface area of more than 55cm^2 in the macroporous gold electrode.

Pore layers on the sample (pore size)	Geometric sample area $\boldsymbol{A}$ [cm^2]	Charge of the gold oxide reduction peak $\boldsymbol{Q}$ [µC]	Roughness factor **R** $= \frac{Q}{A} \div 390 \frac{\mu C}{cm^2}$	Real active surface area $S_r = A \cdot R$ [cm^2]
3/2 (240nm)	0.7	1800	6.6	4.6
7/2 (240nm)	1.68	8470	12.9	21.7
11/2 (240nm)	1.68	14200	21.6	36.4
31/2 (600nm)	0.96	21500	57.4	55.1
49/2 (295nm)	0.64	22000	88.1	56.4

Table 3.1: Calculation of the roughness factor R and the real active surface area S_r for macroporous gold samples with different number of pore layers.

In Figure 3.17 the experimentally determined roughness factors are plotted as a function of pore layers in the material. An excellent correlation is found between the experimental and the theoretical values, the latter being represented by a straight line derived from equation 3.1.

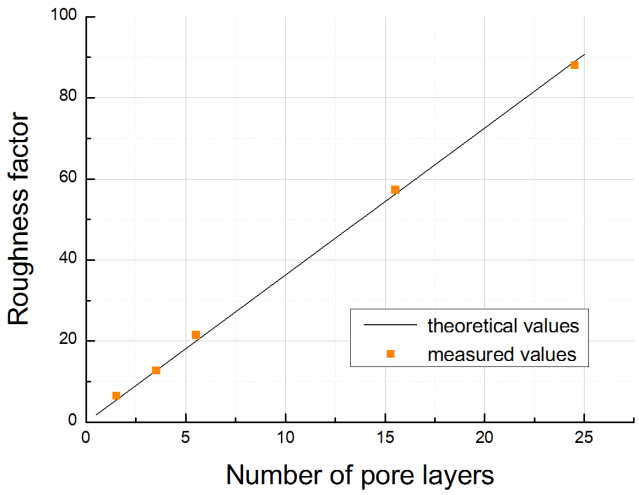

Figure 3.17: The roughness factor as a function of the number of pore layers for macroporous gold electrodes. Correlation between the theoretical expected value (from purely geometric consideration) and the measured values.

In some cases during our measurements the electrolyte solution did not penetrate into the whole existing pore volume and we obtained lower values for the active surface area than theoretically would have been expected (see Figure 3.16b). The rather hydrophobic nature of gold here might complicate the wetting of the interior pore volume. The air that is present in dry macroporous samples hence is "entrapped" inside the pores and a considerable part of the pore volume remains inaccessible to the solution. As illustrated in Figure 3.16 only a very small percentage of the real surface area is detected by CV in samples that have been stored in air for longer periods of time. Exposing these samples to hydrofluoric acid solution leads to a partial wetting of the inner pore structures and the redox peaks in the CV increase. Immediate wetting of the whole

pore structure is attained by immersing the samples into piranha solution so that peak amplitudes in the CV reach the theoretically expected values. It was also found during the CV measurements that the template not necessarily had to be removed in order to measure the active surface area in the sample. Silica spheres synthesized by the Stöber method contain a certain microporosity that allows the electrolyte solution to reach the gold surface by passing through these pores. The CV shown for a sphere size of 395nm in Figure 3.15b) actually was obtained for a composite structure of gold deposited into the silica template. Despite the silica template still being present it was possible to determine the correct surface area by CV. For thick composite structures composed of gold and silica spheres the redox peaks of gold were found to be shifted, indicating that diffusion through the pores in the silica can become a limiting factor in the reaction. Additionally the amount of porosity present in silica spheres is a function of synthesis conditions and generally is the lower the bigger the size of the spheres.

The active surface area of macroporous platinum films equally has been determined using cyclic voltammetry. In Figure 3.18 the CVs of a smooth and a macroporous platinum electrode composed of 17 half-layers are compared. The CV obtained for the macroporous electrode shows typical features of polycrystalline platinum with well defined hydrogen ad- and desorption peaks for potentials lower than 0.1V. In order to resolve the peaks on the flat platinum sample, the scale had to be adapted for this curve which is shown in the inset of Figure 3.18. Somehow surprising is that the current intensities for the redox peaks of macroporous platinum are higher compared to the gold sample with 49 pore half-layers. When the roughness factor is determined by the charge associated to the platinum oxide reduction similarly as for the gold samples, we obtain a value for R equal to 186, assuming 420µC/cm^2 for a smooth polycrystalline platinum surface.[245] An even higher value of 267 is obtained by calculating the roughness factor from the charge for the hydrogen adsorption, using 210µC/cm^2 as the conversion factor.[245] In a macroporous electrode composed of 17 pore half-layers the active surface area however should be increased only by a factor of roughly 30. This difference between theoretical and experimental value may be explained by the presence of additional (smaller) pores in the macroporous structure.

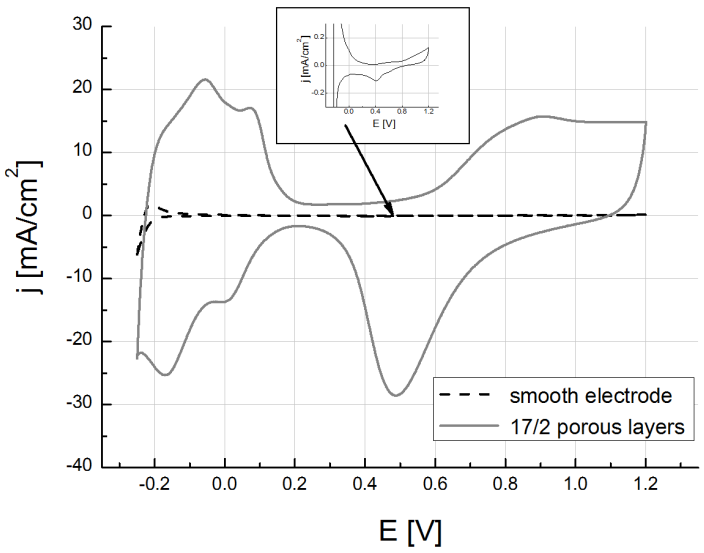

Figure 3.18: CV of a smooth (see also inset) and a macroporous platinum electrode with 17 pore half-layers (pore size: 325nm). It is believed that a hierarchical porosity is present in the sample with mesopores penetrating the walls of the macroporous platinum.

The composition of the plating solution that has been used for the platinum electrodeposition (see chapter 3.2.2) was adopted from a work by Choi et al., who reported a mesoporous structure in platinum electrodeposits.[243] The authors supposed that surfactant molecules being present in the plating solution arrange to micelles at the electrode surface around which platinum is deposited. This resulted in mesoporous platinum films on smooth substrates after the surfactant had been dissolved in aqueous solutions. Typically, these mesoporous films have been produced by electrochemical deposition in highly viscous plating mixtures with surfactant concentrations around 30 - 45 wt-%.[246] Choi et al. however used a solution containing only 0.1 wt-% SDS and supposed that the arrangement of the surfactant molecules into ordered micelle structures was controlled by the applied potential during the electrodeposition. A more detailed insight in the formation of mesoporous structures from surfactant molecules will be given in chapter 7.2. The potential that was applied in this work in order to deposit platinum into the colloidal templates however did not correspond to the one that was employed in the original report.[243] Nevertheless our results strongly indicate the presence of a mesoporous structure in the macroporous platinum film. Materials with both, macro- and mesopores, have been reported before by several authors using colloidal crystal templating.[247-249] A macroporous Pt electrode with two pore layers produced under the same experimental conditions showed a roughness factor of 61 and 96, depending if R was determined according to the oxide reduction or the hydrogen absorption peak, respectively. These values also were by a factor of 8 - 13 higher than theoretically expected for a macroporous material composed of two pore layers. In order to provide further evidence of the hierarchical porosity obtained by this process, additional studies including a variation of the

deposition potential and transmission electron microscopy (TEM) images of thin platinum film deposits might be performed in future works.

3.3 Electrodeposition of conducting polymers in colloidal crystals

Conducting polymers (CPs) cover a wide spectrum of conductivities ranging from isolating over semiconducting up to a metal-like behavior. CPs are produced by oxidization of the corresponding monomers. The removal of electrons from the conjugated backbone during the oxidation of the polymer allows for the remaining delocalized electrons to move along the conjugated structure. In this "doped" state the conductivity of conjugated polymers is increased by several orders of magnitude compared to the "undoped" state. A conversion to the less conducting state is obtained by reducing the polymer, where electrons are reinserted into the structure of the polymer. Analogue to semiconductors this type of conductivity promoted by non existing electrons or positive "holes" in the band structure refers to p-type conductivity. Principally, also n-type conductivity is possible in conducting polymers, which however, is much less common than the p-type conduction. Polyaniline (PANi), polypyrrole (PPy) and poly(3,4-ethylenedioxythiphene) (PEDOT) are among the most widely used conducting polymers. They are employed for different kinds of applications in fields including electroanalysis,[250] electrochromism,[251] actuators,[252-254] energy storage,[255] bioelectrochemistry,[256] electrocatalysis,[257, 258] neural engineering,[259] corrosion protection[260] and sensors.[256] The fabrication of a macroporous structure by colloidal templating can add new functionalities [261-264] or improve the performance in existing applications, which are based on conducting polymers. [200, 265, 266]

3.3.1 **Polypyrrole deposition**

The electrochemical polymerization of pyrrole is schematically illustrated in Figure 3.19. The polymer is formed by the oxidation of the pyrrole monomer whereas counterions (A^-) are incorporated in between the polymer chains to guarantee charge neutrality in the polymer. Figure 3.19 represents a simplified presentation of the electropolymerization process, showing only the educt and the idealized structure of the polymer product. In reality the polymerization process is more complex and can be divided into several steps.[267] When sufficiently positive potentials are applied to the electrode, the monomer will be oxidized and radicals are formed. Radical-radical coupling now occurs and the growth of the polymer chain proceeds until the charge is such that a counterion is incorporated. When experimental conditions are favorable, the chain length reaches

a critical length so that the solubility limit is exceeded and the polymer precipitates on the electrode surface.

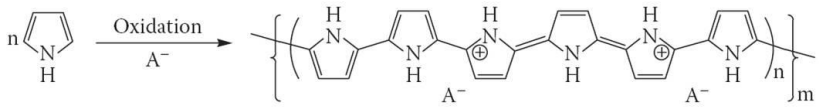

Figure 3.19: Simplified illustration of polypyrrole formation by oxidation of the pyrrole monomer. A^- is the counterion incorporated into the polymer ensuring charge balance, m corresponds to the polymer chain length and n to the molecular weight. [267]

The aim was to control the electropolymerization in such a way, that smooth polymer film growth would be attained, which eventually could lead to similar current oscillations during the potentiostatic infiltration of colloidal crystals that previously have been observed for metallic deposits. In Figure 3.20a) the electropolymerization of polypyrrole by potential cycling onto a smooth gold electrode is shown. An aqueous solution containing the monomer (0.1M pyrrole) and a supporting electrolyte (1M KCl, counterion incorporated in the PPy film: Cl^-) was used for the PPy deposition, which was slightly changed with respect to a report found in the literature.[268]

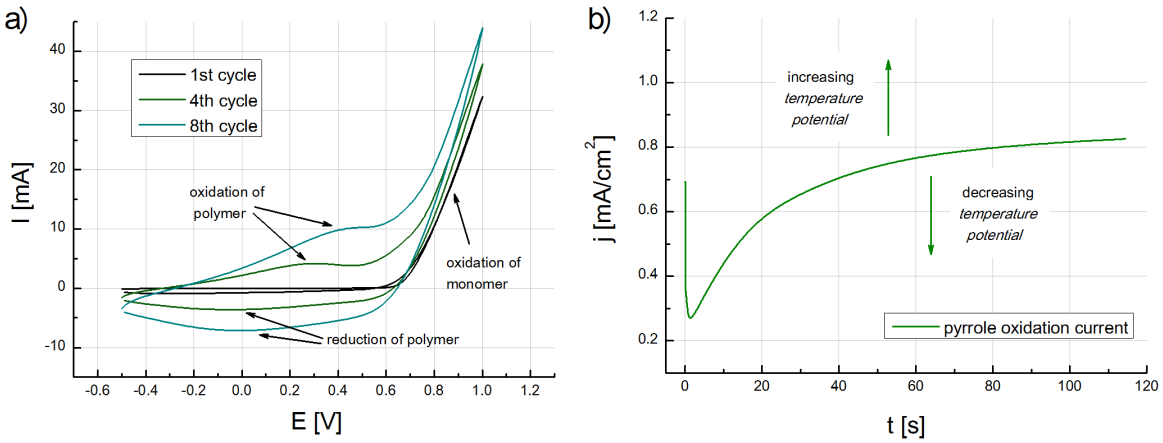

Figure 3.20: Electropolymerization of pyrrole by a) cyclic voltammetry (scan rate: 100mV/s) and b) in potentiostatic mode from an aqueous solution containing 0.1M pyrrole and 1M KCl. In b) a constant potential of +600mV vs. Ag/AgCl was applied.

The potential here was cycled between -0.5V and +1.0V. In the first cycle PPy is deposited on the pristine gold surface with an onset potential of about +600mV in the anodic scan. The resulting polymer film is reduced during the cathodic scan. In subsequent cycles different peaks corresponding to the redox peaks of the polymer and the oxidation of the monomer are observed. As the amount of polymer on the electrode increases with each cycle, the intensity of the corresponding redox peaks also increase. The onset potential for the oxidation of the monomer was found to shift towards lower potentials in the course of the deposition, combined with

increasing peak intensities. This effect is due to the polymerization occurring more readily on already deposited PPy than on the electrode substrate.[267]

However, using cyclic voltammetry for the electropolymerization into colloidal crystals does not allow us to control the filling level of the template with sufficient precision. Therefore potentiostatic deposition was performed at different applied potentials and the resulting polymer films were characterized by their optical aspect and corresponding SEM images. In Figure 3.20b) the current response for potentiostatic deposition of PPy on a smooth gold sample is shown. A potential of +600mV vs. Ag/AgCl was applied, resulting in smooth polymer films at reasonable deposition rates. Using lower potentials resulted in inhomogeneous film deposition and lower efficiencies. In fact, radicals and polymer chains can diffuse away before they are deposited at the electrode surface so that part of the totally applied charge is "lost" in this case. For certain conditions it is therefore possible that no film growth is observed although a considerable amount of charge is applied during the electropolymerization.[267] PPy films deposited at higher potentials than +600mV (e.g. +700mV) showed a higher surface roughness in the SEM images.

At the start of the deposition process shown in Figure 3.20b) charging of the double-layer capacity at the electrode leads to a steep decrease of the current. In the following the current increases during polymer film growth at the electrode. In initial stages of the deposition process the substrate exerts a dominating influence on the kinetics of the electropolymerization. With increasing thickness of the polymer film the influence of the underlying electrode material decreases and the polymerization occurs more readily, hence leading to continually increasing currents which may reach a plateau for very thick polymer film deposits. When the applied potential or the temperature of the electrolyte solution were changed, the curve principally exhibited a similar shape but was shifted to higher or lower current densities, as indicated in the plot. The quality of the PPy films and the reproducibility in the experiments were found to depend strongly on the purity of the monomer, which hence has to be distilled before use.

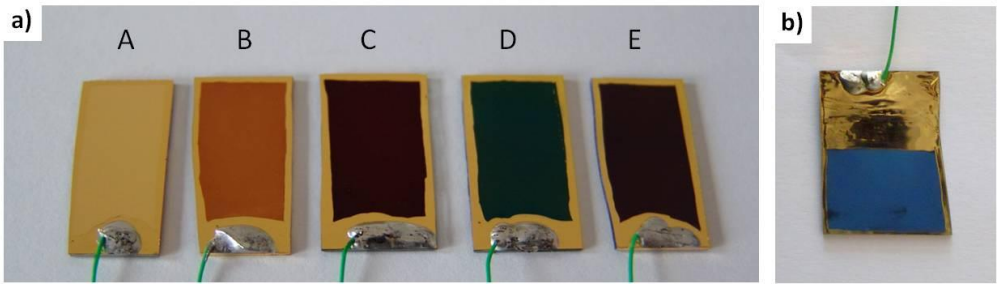

Figure 3.21: a) Polypyrrole films electropolymerized at an applied potential of +600mV a) onto smooth gold electrodes with applied charge densities corresponding to (A) 0, (B) 20, (C) 40, (D) 80, (E) 120mC/cm^2. b) into a colloidal crystal template (Template: 395nm sphere size with 8 sphere layers; PPy filling level: seven half-layers).

The film thickness of the polymer could be controlled by the charge applied during the electropolymerization. Applied charge densities of 400mC/cm^2 have been reported to result in 1µm thick PPy films.[269] Figure 3.21a) shows gold samples coated with PPy films by applying different charge densities during the electropolymerization. Sample A is the uncoated gold electrode and from sample B (50nm) to E (300nm) the thickness of the PPy films increases. As a function of the thickness the color of the PPy film deposits on gold changed. Continuous color change was observed up to applied charge densities of about 150-200mC/cm^2, higher values resulted in black PPy film deposits. Thus the optical aspect is a measure of the thickness and the uniformity of PPy thin films. Cross-section SEM images of the samples B and C are shown in Figure 3.22a) and confirmed that the PPy films exhibited the expected thickness and were uniform throughout the sample.

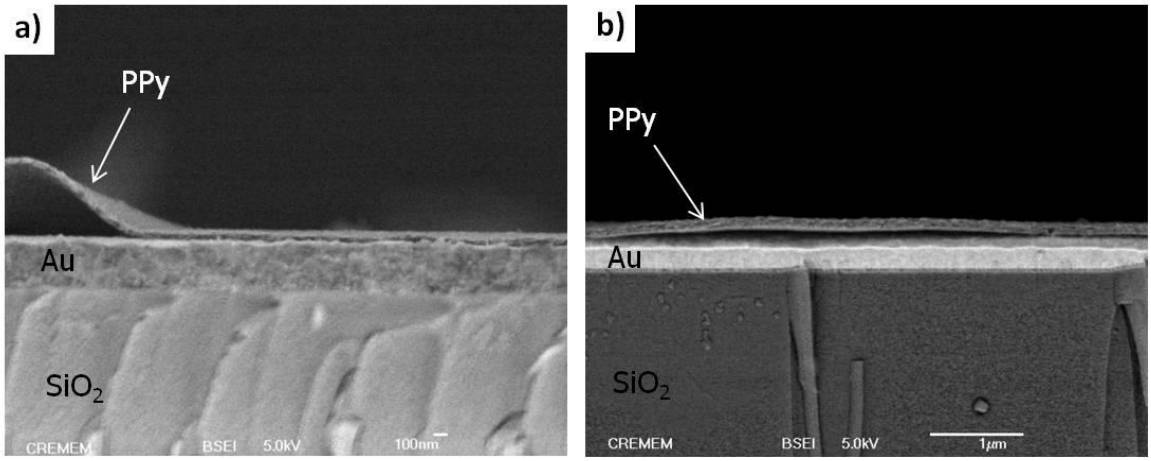

Figure 3.22: SEM cross-section images of polypyrrole films electrodeposited on gold slides. a) and b) correspond to the samples B and C from Figure 3.21, respectively. The thickness of the PPy-films was found to be a) ~50nm and b) ~100nm.

In the following, colloidal crystal templates were electrochemically infiltrated with PPy. Similarly as shown for metal deposits in colloidal templates, we were able to observe regular current oscillations during potentiostatic electropolymerization of PPy, illustrated in Figure 3.23. However, since the formation of polypyrrole results from an oxidation process, the faradaic current has a positive sign. As a consequence, each current density minimum in the plots now corresponds to a minimum of the electroactive surface, equal to a half-layer filling level in the colloidal template.
In Figure 3.23a) a colloidal template composed of 20 sphere layers with a bead size of 240nm has been infiltrated with PPy. Well defined minima and maxima in the recorded current allowed us to stop the electrodeposition at different half- or a full-layer filling levels in the template, respectively, similarly as for the metal deposition. In the present case 23 half-layers of the template have been filled with PPy.

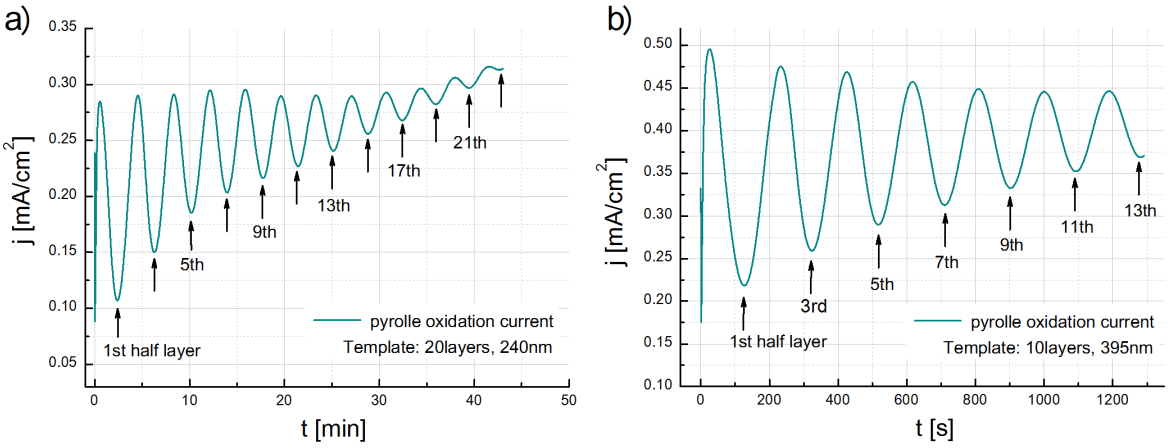

Figure 3.23 Current oscillations observed during potentiostatic electropolymerization (E = +0,6V) of pyrrole into colloidal templates. The templates were filled with polypyrrole up to a) 23 and b) 13 half-layers.

In Figure 3.23b) the observed current oscillations were even more regular than in Figure 3.23a) as a template composed of 395nm spheres was filled with PPy up to 13 half-layers. Figure 3.21b) shows a digital photograph of a colloidal crystal template which has been partly infiltrated with PPy.

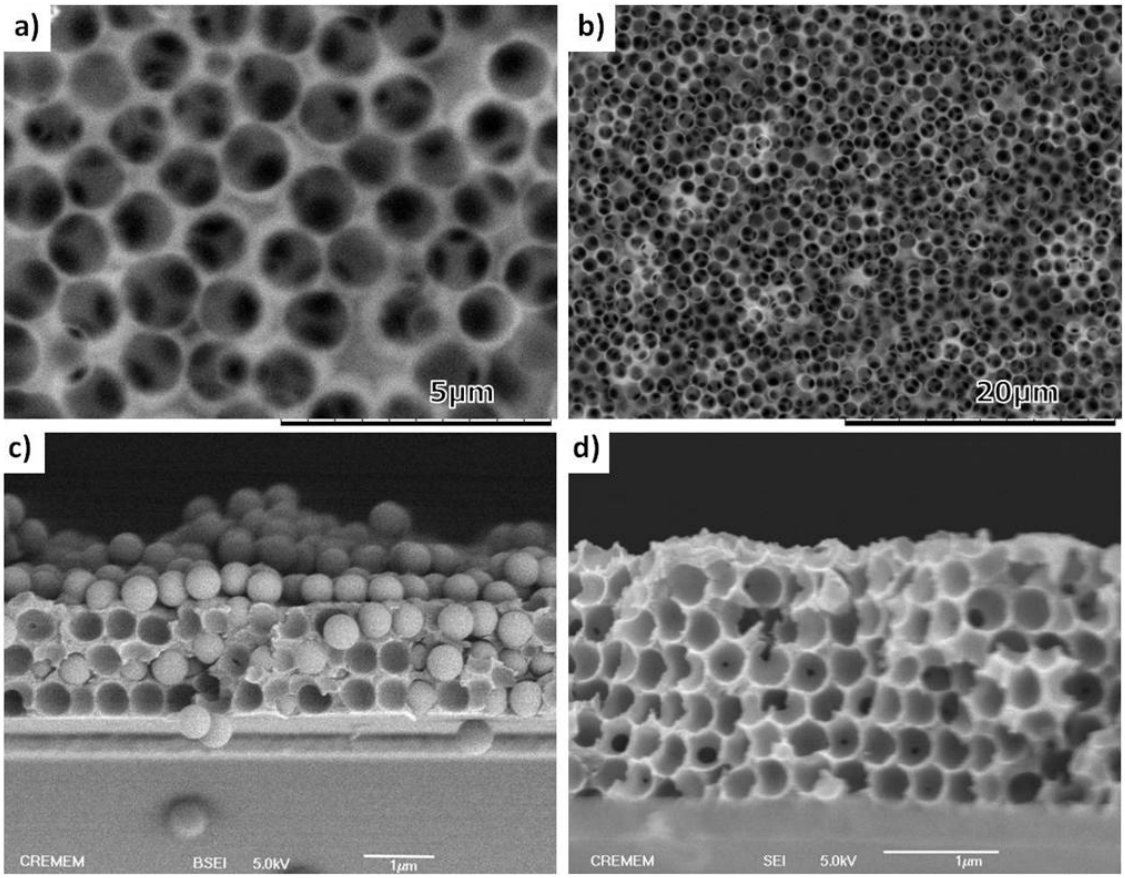

Figure 3.24: SEM images of macroporous and composite polypyrrole films. a) and b): Top view of a macroporous PPy-film electrode with a pore size of 1200nm and a thickness of 13 half-layers in different magnifications. c) Cross-section of a colloidal template (sphere size 470nm) in which 3 layers have been infiltrated with polypyrrole. d) Cross-section of a macroporous PPy film with a thickness 13 half-layers and a pore size of 395nm.

The characterization of different macroporous PPy films by SEM is illustrated in Figure 3.24. The top surface of a macroporous polymer film with a pore size of 1200nm is shown in different magnifications in Figure 3.24a) and b). The windows interconnecting the top to the underlying pore layers appear as black spots and are clearly visible in both figures. The PPy struts have different thickness indicating that the silica spheres in this case have not been in a completely close packed arrangement. In Figure 3.24c) a cross section image of a colloidal template composed of 470nm beads is shown after the infiltration with PPy. Slightly more than three sphere layers have been filled by the PPy film, which revealed a very uniform growth front throughout the template. Figure 3.24d) shows the cross-section of a macroporous PPy film with six and a half pore layers.

3.3.2 **Polybithiophene deposition**

In this work polybithiophene (PBT) also has been infiltrated into the void space of colloidal crystals. Owing to the low solubility of the monomer in aqueous solutions acetonitrile was used as solvent.[270] Solutions contained 0.1M tetrabutylammonium tetrafluoroborate (TBA BF_6) with bithiophene concentrations that were varied from 5 to 50mM. Figure 3.25a) shows cyclic voltammograms of flat gold electrodes in a solution containing 50mM bithiophene.

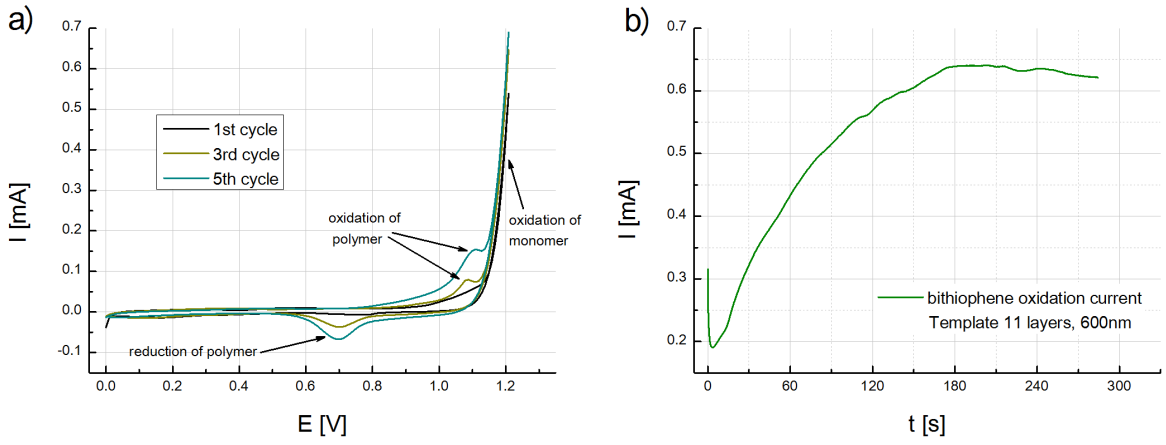

Figure 3.25: a) Electropolymerization of bithiophene by cyclic voltammetry (scan rate: 100mV/s) in acetonitrile containing 50mM bithiophene and 0.1M TBA BF_6. b) Electrochemical infiltration of a colloidal crystal (11layers , 600nm sphere diameter) at an applied potential of 1.23V vs. Ag/AgCl. In this case the concentration of the monomer was 5mM.

Similarly as shown for the PPy deposition in Figure 3.20b), well defined redox peaks of the deposited polymer are visible in cycles successive to the first. Compared with pyrrole potentials higher than E > 1V are required to oxidize bithiophene. In Figure 3.25b) a chronoamperometric curve for PBT deposition in a colloidal template is shown. Here, no oscillations of the current

response were observed and the shape of the curve resembles that for the deposition of PPy on flat gold (see Figure 3.20b).

Directly after electropolymerization of PBT into the colloidal template the cross-section of the sample has been characterized by SEM, which is shown in Figure 3.26a). The same type of volume-templated material as observed for PPy or metal electrodeposits is expected, however PBT reveals a different growth mechanism in colloidal templates.

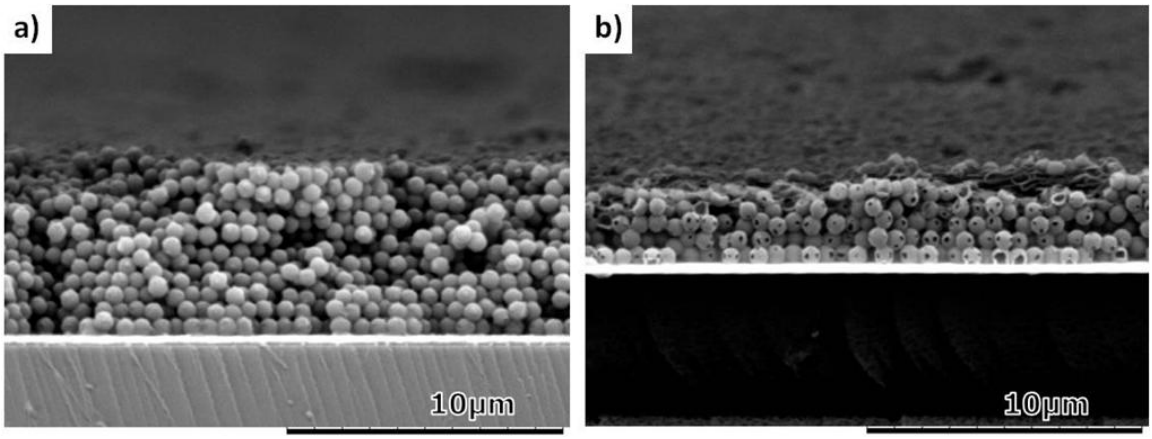

Figure 3.26: SEM cross-section images of composite and macroporous polybithiophene films. a) Polybithiophene was deposited in the colloidal template by encapsulating the spheres with a thin polymer film. b) Removal of the inorganic template resulted in a macroporous "hollow sphere" polybithiophene electrode.

Instead of filling the whole available volume in the template, only a thin polymer film is deposited around the spheres. This guidance effect, probably due to electrostatic interactions between the radicals formed during electropolymerization and the surface groups of the colloidal spheres, was mentioned before in chapter 3.1.3 resulting in surface-templated materials. The macroporous PBT electrode can be seen in Figure 3.26b) showing a 3-dim network of interconnected hollow spheres on the surface of the gold electrode. Interconnection points between spheres of the original silica template now correspond to black air cavities in the hollow PBT spheres. A collapse of the sphere layers at the top surface of the sample is observed due to a lack of mechanical stability of the hollow polymer spheres. In the illustrated sample the polymer film however has been dried by a rather strong nitrogen flow, more gentle drying conditions resulted in less damage at the macroporous surface layers. A similar surface-templated structure has been observed by Bartlett et al. for macroporous PBT films.[212]

3.3.3 **Electrochemical characterization of macroporous conducting polymers**

The macroporous polypyrrole films produced in chapter 3.3.1 have been electrochemically characterized using cyclic voltammetry. In Figure 3.27a) the molecular structure of polypyrrole is shown in its reduced and oxidized form. The switching between both redox states is associated with a movement of electrons and counterions into or out of the polymer structure . When the polymer is reduced, electrons fill the available "holes" in the conjugated structure of the polymer and the counterions move out of the material. Oxidation of the polymer leads to the inverse scenario. The amount of counterions in the polymer will depend on its oxidation state leading either to a contracted (reduced) or expanded (oxidized) state of the polymer. The reduction (or oxidation) of the polymer proceeds from the point of the electrical contact, as illustrated in Figure 3.27b).[267] It is supposed that the reduction front percolates through the polymer material.

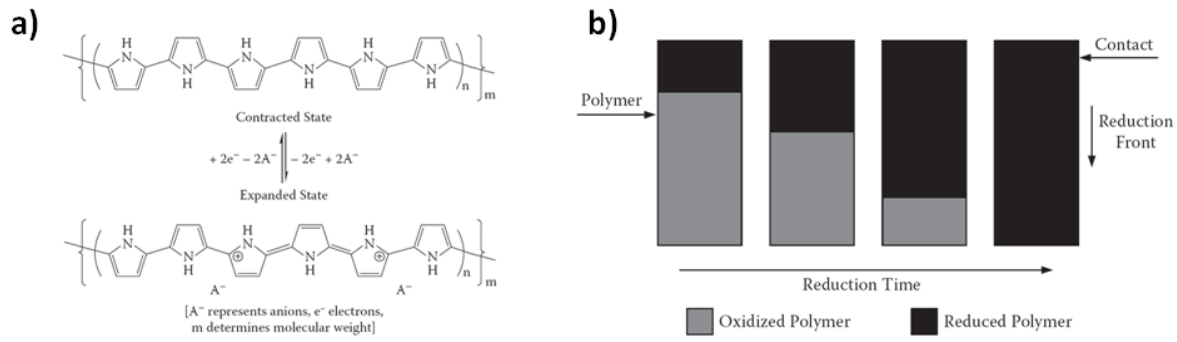

Figure 3.27: a) Switching of polypyrrole between the reduced (contracted) and oxidized (expanded) state. b) Schematic presentation of the reduction of a conducting polymer.[267]

The redox process in conducting polymers significantly differs from that occurring in noble metals which is confined to a thin layer. In CPs, the whole polymer film will get oxidized (reduced) when sufficiently positive (negative) potentials are applied for a certain period of time. Generally no single redox peak but broad distributions of overlapping peaks are observed in the CVs of CPs. This is caused by the different molecular weights of the oligomeric/polymeric species in the CP all possessing oxidation/reduction peaks at different potentials.[267] Figure 3.28 compares the cyclic voltammograms of smooth (*left*) and macroporous (*right*) PPy films. Curves of the same color here stand for samples with the same amount of deposited PPy and hence can be directly compared with each other. In both plots, for macroporous as well as for smooth samples, increasing currents are observed as the amount of deposited polymer increases. A greater film thickness leads to a shift of the oxidation peak towards more positive potentials in smooth PPy samples. A uniform increase of the redox currents with no clearly visible peaks is observed as the thickness of the

macroporous PPy films is increased. The observed shift of the oxidation peaks indicates that the exchange of ions with the solution probably is the rate limiting step in flat PPy films of a certain thickness. Counterions need to diffuse through the polymer film during the redox processes in smooth PPy films. In macroporous films however the solution can enter the pore volume so that the diffusion path lengths of the counterions is significantly reduced.

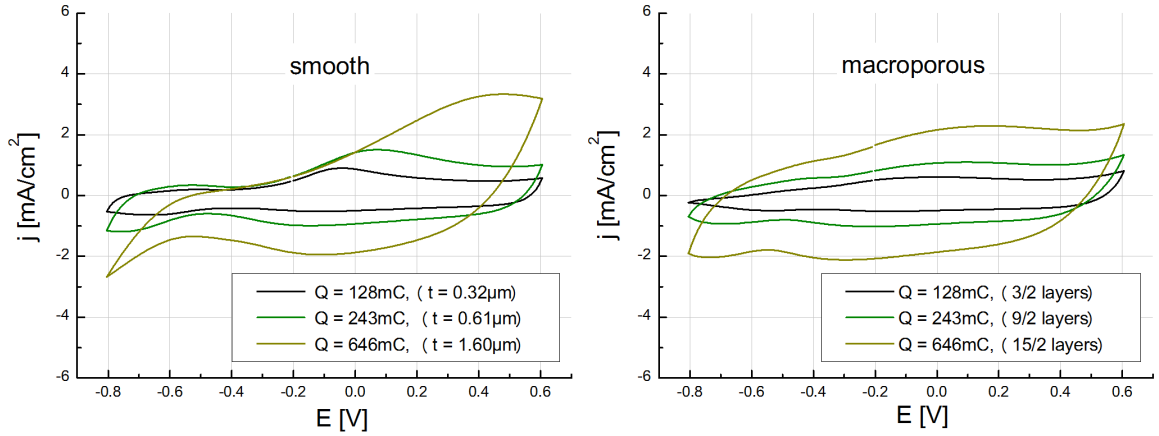

Figure 3.28: Comparison of smooth (*left*) and macroporous (*right*) PPy samples by cyclic voltammetry. The scan rate was 50mV/s in 50mM KCl aqueous solution. Q represents the charge injected during electropolymerization of PPy. In corresponding smooth and macroporous samples the amount of deposited polymer was equal (t: film thickness, macropore size 430nm).

Conducting polymers might be used for many applications that rely on the reversible switching of the polymer between its reduced and oxidized state.[200, 254, 271] A fast and reversible redox process is crucial to enable good perfomance in CP based devices. In order to compare the kinetics of the ion exchange for flat and macroporous PPy films, CVs were recorded at different scan rates which are shown in Figure 3.29.

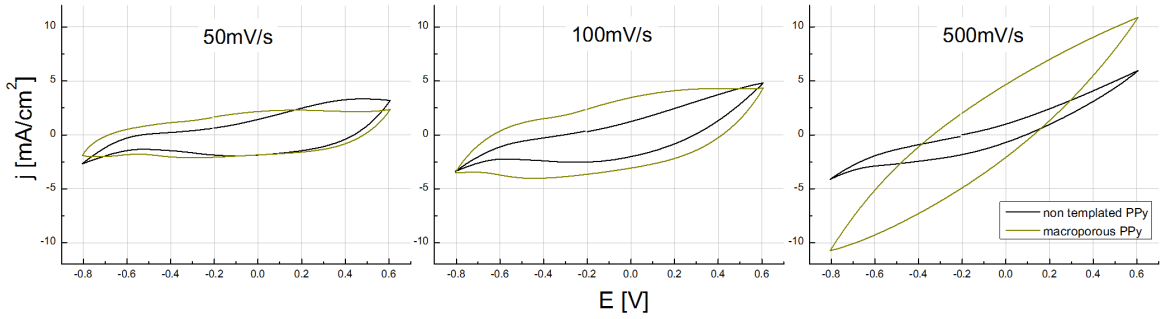

Figure 3.29: Cyclic voltammetry in 50mM KCl at different scan rates (50, 100, and 500mV/s from *left* to *right*). A smooth and macroporous PPy film with the same amount of deposited polymer (injected charge : 646mC) is compared.

In each plot a smooth and a macroporous PPy film are compared containing the same amount of deposited polymer. At a scan rate of 50mV/s the redox currents for the templated and the non-

templated film are in a similar range. At 100mV/s considerably higher redox currents were observed for macroporous than for flat PPy. This trend was confirmed and even more pronounced at higher scan rates of 500mV/s.

The results shown in Figure 3.28 and Figure 3.29 have been obtained by cycling the polymer in a solution which contained the same counterion used during the synthesis of the PPy films. Cl^- is a rather small ion easily diffusing through the polymer structure and facilitating the ion exchange with the solution. Therefore we performed the same scan-rate-dependent experiments in equally concentrated solutions which contained a bigger anionic species, here PF_6^- was used.

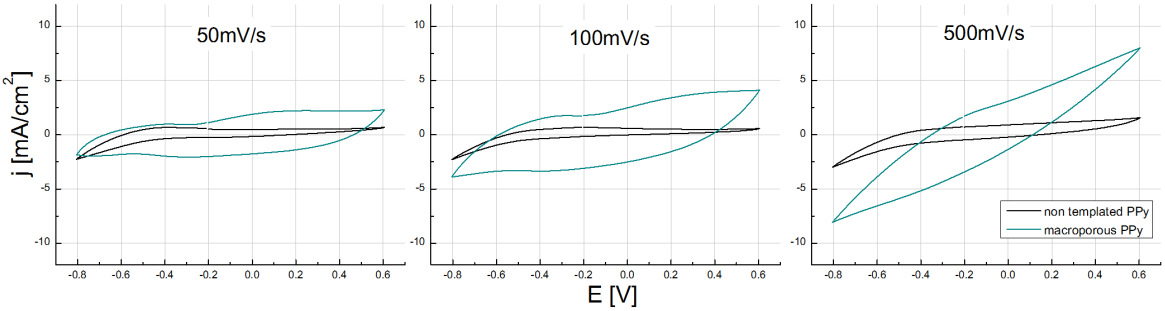

Figure 3.30: Similar scan rate dependent plots to the ones shown in Figure 3.29 are presented. The same samples but a different electrolyte solution (50mM KPF_6 aqueous solution) was used here.

As seen in Figure 3.30, a marked difference in the CVs between the flat and the macroporous polymer film is observed in this case at all tested scan rates. The macroporous polymer seems to exchange PF_6^- anions as readily as Cl^- anions, as the current signals are barely reduced compared to Figure 3.29. In contrast only small oxidation and reduction currents are observed at the different scan rates for the flat PPy samples indicating that PF_6^- anions can hardly be exchanged with the polymer owing to restricted diffusion of these species in the film. Improved performance in electrochomic NiO were also attributed to shortened ion pathways in the macroporous structure.[240]

3.4 Applications of macroporous electrodes

Macroporous materials obtained from organized colloidal templates can be used in various different applications. In chapter 2.4 it has been discussed that photonic crystals with a complete photonic bandgap are possible when colloidal templates are infiltrated with high refractive index materials. Several other applications arise from the structural order present in photonic crystals. As mentioned in chapter 2.3, Bragg diffraction leads to the characteristic coloration in opals and their inverse replicas. The optical response of photonic crystals to electromagnetic radiation

herein depends on structural and also on material parameters. A change of parameters like symmetry, lattice constant or order in photonic crystals will effectively alter the interaction of light with the material. In the same way a refractive index change of the constituent materials in a PC affects its optical properties. By incorporating stimulus-responsive materials into photonic crystals at least one of these parameters can be modified due to chemical or physical stimuli so that the diffraction wavelength in the PC changes. In a recent review on responsive PCs a broad overview is given on the mechanisms and applications in this field that include besides optical sensors also display units or structural color devices.[272] In Figure 3.31 some examples for optical sensors made from hydrogel inverse opals are shown.

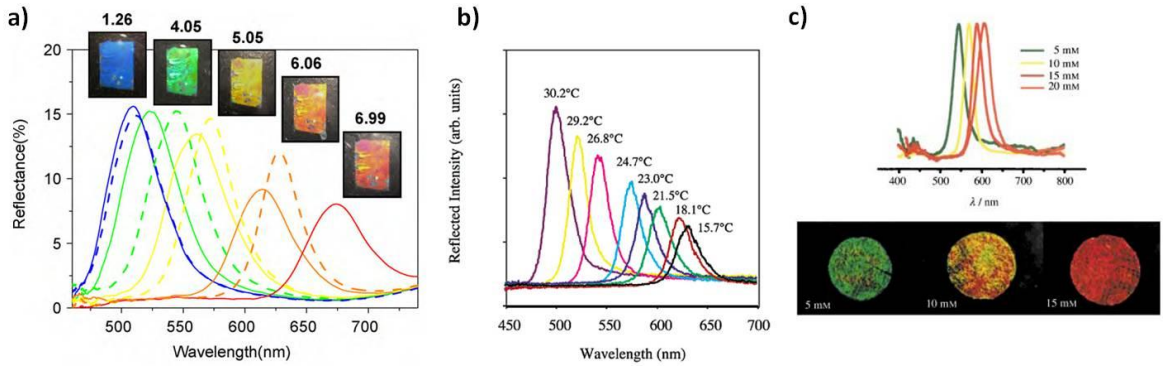

Figure 3.31: Optical sensors based on hydrogel inverse opals. Dependence of the reflection spectra of the hydrogel inverse opal on a) the pH, [273] b) the temperature, [274] and c) the glucose concentration.[275]

A shift of the reflection peak in PCs may be used to measure the pH (a), the temperature (b) or the glucose concentration (c). The change of the peak wavelength in Figure 3.31b) is due to a temperature-dependent swelling or shrinkage of the hydrogel causing the lattice constant in the PC to change.[274, 276] Recently it has been shown that the integration of a defect in the inverse opal can lead to increased sensitivities in pH sensing.[277] Alternatively, phase transitions happening in some inorganic materials lead to a refractive index change in a certain temperature range. An example is barium titanate with a phase transition near the Curie temperature (T_c ~ 120°C). PCs composed of this material equally can serve as a temperature sensor.[278] Refractive index change is also observed when a liquid or gaseous component fills the void space in PCs. This effect allows PCs to be employed for the optical detection of various solvents or vapors including a discrimination between different vapor pressures.[263, 279-281] Compared to colloidal or PC composite structures inverse opals provide more volume for the infiltration with a liquid or gaseous analyte, which results in higher shifts of the reflection peaks.[272] The principle of ion or pH sensitive PCs is based upon a change of the lattice constant in PCs occurring when target ions bind to recognition

units that are immobilized in a hydrogel.[273, 282-284] The selective recognition of metal ions by crown ethers is an example for ion sensitive PC sensors.[282] The response time of the pH sensor illustrated in Figure 3.31a) was reported to be strongly decreased when macroporous instead of composite hydrogel PCs were used.[273] The same strategy can be employed for the optical detection of biomolecules with responsive PCs.[261, 262, 275, 282, 284-286] The example in Figure 3.31c) shows that different levels of glucose concentrations can easily be distinguished by the naked eye using macroporous hydrogel PCs. [275]

Also external forces acting on the PC can change the lattice constant and provoke a mechanochromic behavior. Hence pressure sensors can be realized using porous or composite elastomeric PCs.[287, 288] Examples showing an optical pressure sensor based on elastomeric inverse opals is illustrated in Figure 3.32b) and c). The pressure of a finger pressed onto the porous film locally deforms the crystal lattice associated with a color change in the PC. The resolution proved to be sufficiently high to use these PC devices as fingerprint sensors.[289, 290] In macroporous films the pressure required to trigger a color change was sufficiently reduced compared to composite films. Besides sensing also the emission wavelength in organic lasers can be tuned by a mechanochromic PCs. In Figure 3.32a) uniaxial compression of the PC (PBG) composite film modifies the wavelength of the laser pulse as it propagates through the mechanochromic medium.[291] Even though in this report a PC composite material was used, similar results may be obtained with porous PC films. The performance of actuators equally could be increased by introducing a controlled macroporosity into devices based on PPy .[265] It was shown that actuation in these materials allowed to trap and release small particles in/from the pores in a controlled way.

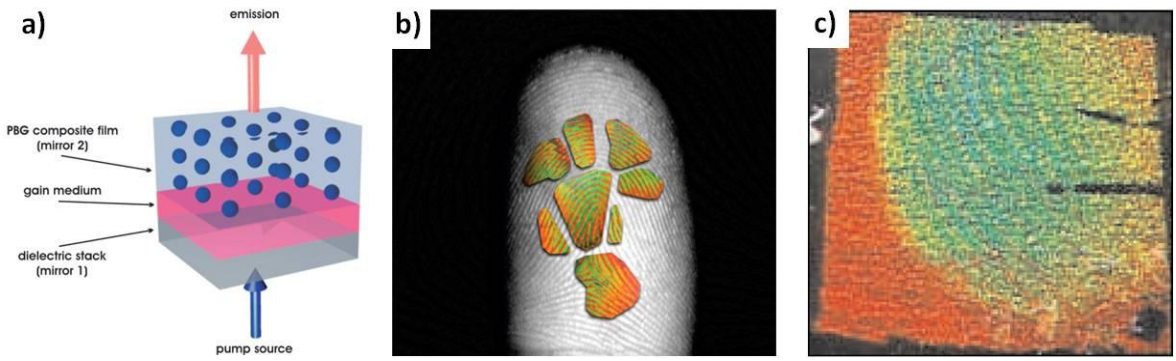

Figure 3.32: Applications of mechanochromic photonic crystals. a) Configuration of a tunable thin-film organic laser: a broadband dielectric stack reflector (mirror 1) is coated with a thin layer of rhodamine B doped poly(methyl methacrylate) (gain medium) and then laminated with a photonic bandgap (PBG) composite film (mirror 2).[291] b) A full-color fingerprint visualized using an elastic photonic crystal (EPC), overlayed onto a grayscale image of an index finger. c) Still image taken during the compression of an EPC film by an index finger.[289, 290]

Using electroactive materials in photonic crystals enables to produce a color change by altering applied potentials. As illustrated in Figure 3.33a) the electroactive material can be reduced or oxidized depending on the applied potential, which is associated with a change in volume and lattice constant of the PC film consequently leading to a color change. The electroactive media may be a ferroelectric material[292] or a conducting polymer.[266, 293] In this regard electrically switchable full color displays based on photonic crystals have been fabricated.[200, 293] In their first report Ozin et al. employed a polyferrocenylsilane/silica composite PC to reversibly change the color of the display.[293] The use of a macroporous structure resulted in faster switching times combined with lower threshold voltages needed to drive the device.[200] As seen in Figure 3.33b) clear and bright colors are obtained as different potentials are applied to the electroactive inverse opal. The colors are adjustable over the whole range of the visible spectrum in such a device as shown in Figure 3.33c). Response times in the range of 10 seconds for a complete color change are still quite high with respect to a commercial application of such PC devices. Instead of electric also magnetic fields were used to tune the color in photonic crystals composed of superparamagnetic spheres.[294, 295]

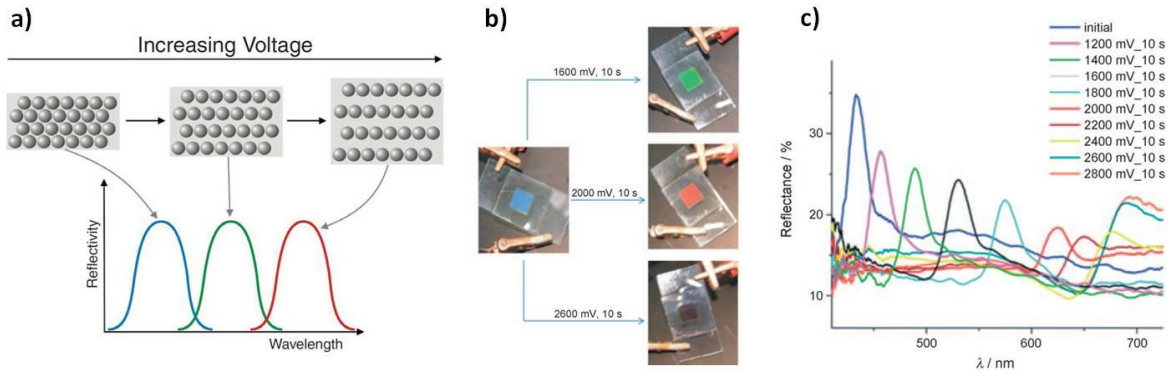

Figure 3.33: Fabrication of electrically controlled display units based on inverse opals. a) Illustration of the mechanism that leads to a color change in redox-active inverse opals. b) Color tuning in the display upon application of different potentials. c) Reflection spectra for different applied potentials. [200, 290]

A different application for PC composite films is photonic paper.[296-298] In Figure 3.34a) the principle of producing a color contrast between unmodified areas and those swelled by local infiltration of a liquid in PC films is shown. By using hygroscopic salts for the infiltration a durable writing is achieved (see Figure 3.34d), which can be erased simply by washing the film in water. Even though photonic paper devices produced so far consisted of compact composite PC structures they are mentioned in this section due to their proximity to the previously discussed work.

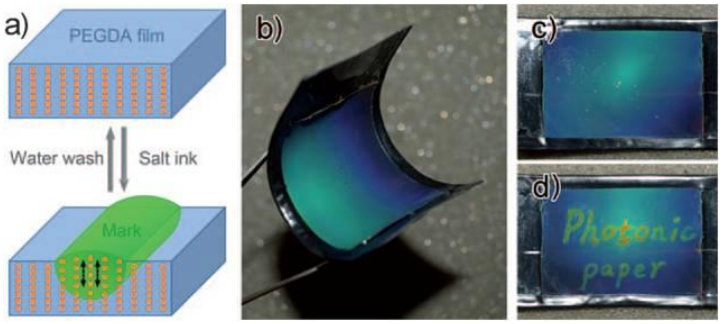

Figure 3.34: Images showing rewritable photonic paper that is based on a poly(ethylene glycol) diacrylate (PEGDA) film containing colloidal spheres assembled into chains a) Schematic illustration of the mechanism of writing and erasing by infiltration or removal of a hygroscopic salt. Photographs of b) the flexible photonic paper (3×4cm) c) without and d) with letters printed. [272, 298]

Coupling photonic crystals to dye-sensitized solar cells (DSCs) based on titanium dioxide has been reported to enhance the light-harvesting performance in the red spectral range.[299] Different mechanisms can be responsible for the increase of photocurrent in DSCs coupled with a PC film. Higher absorption rates can be due to multidirectional scattering at defects in the PC at short wavelengths[300] together with a back reflection of light in the stop band region of the PC.[301] The absorption also can be enhanced by increased matter-radiation interaction times due to resonant modes.[302] The profile that is required for a nanostructured material to effectively improve photovoltaic devices due to plasmon enhanced light absorption has been reviewed by Atwater and Polman.[303] Surface plasmon polaritons (SPPs) are quasiparticles resulting from the interaction of incident light with resonant electronic charge oscillations on a metallic surface.[304] In nanostructured materials, SPPs can be locally trapped on the surface producing significantly enhanced optical fields at precise locations. Atwater and Polman mentioned that light scattering and trapping is very sensitive to the shape of plasmonic nanoparticles. The same is true for the nanovoid structures in metallic films produced by colloidal templating.

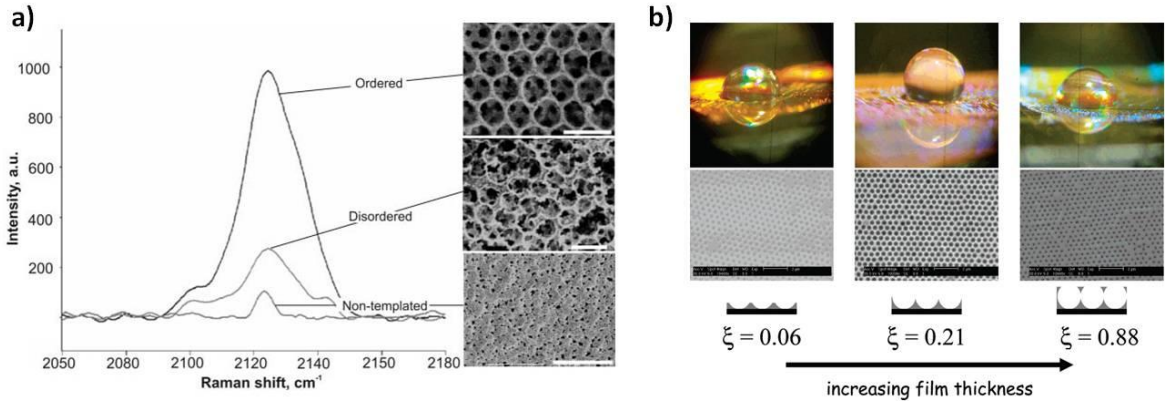

Figure 3.35: a) Effect of the substrate structure on the SERS signal intensity. Sodium cyanide spectra for non-templated, disordered and ordered latex-templated Au nanoparticles (10-20nm). Scale bars in SEM images: top and middle 1µm, bottom 10µm.[305] b) Optical images of 5µl drops of water on macroporous gold films of different thickness with SEM images of the corresponding surfaces below (scale bar is 2µm).[306]

As shown in Figure 3.35a) metallic inverse opals can be used to increase the signal intensity in surface-enhanced Raman spectroscopy (SERS) by several orders of magnitude. A much lower increase of signal intensity was found for disordered compared to ordered inverse opal films templated with Au nanoparticles.[305, 307] A similar approach using electrodeposited metallic nanostructures has allowed to discriminate mutations and to analyze short repeating units in DNA sequences by SERS.[308, 309] It has also been shown that complete omnidirectional absorption of light can be observed in templated metallic nanovoid films, when the thickness slightly exceeds one void layer.[310] Figure 3.35b) illustrates the influence of the surface structure of templated gold films on their hydrophobic properties. The contact angle between a water droplet and nanostructured gold film was found to increase when its thickness approaches a half-sphere layer, whereas decreasing angles were observed for the film thickness reaching a full pore layer. Due to the uniform pore size highly ordered 3-dim macroporous materials also have been used as filters.[311, 312]

The higher active surface areas provided by macroporous in contrast to flat electrodes can also be employed to increase the sensitivities and/or to lower the detection limits of conventional electrochemical sensors. As capacitive currents increase parallel to the faradaic currents in highly porous electrodes, improved performance is expected either when analytes are adsorbed on the electrode surface[10] or when using differential pulse techniques.

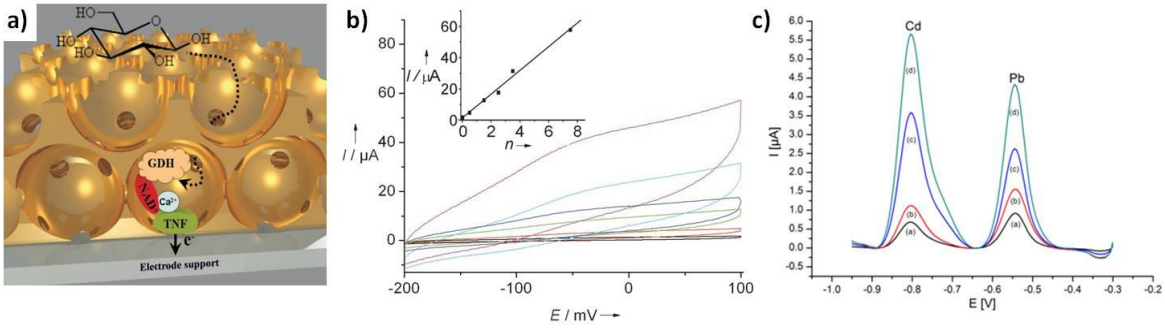

Figure 3.36: a) Representation of a gold electrode with 3/2 pore layers modified with a mediator monolayer (4-carboxy-2,5,7-trinitro-9-fluorenylidene) malononitrile (TNF), Ca^{2+}, NAD^{+}, GDH, and its reaction in a solution containing glucose. b) CVs with macroporous electrodes as shown in a) in the presence of glucose dehydrogenase (3µM) and glucose(10mM). The signal increases as the number of pore layers is increased (inset: oxidation current at 100mV). [217] c) Comparison of the stripping peaks obtained with a nonporous (curve a) and porous bismuth films of increasing thickness (b – d) for Cd and Pb detection.[227]

Figure 3.36a) shows an example of a macroporous glucose biosensor where all necessary species including redox mediator (TNF) and cofactor (Ca^{2+}/NAD^{+}) were immobilized on the gold surface.[217] Alternatively, only the redox mediator can be immobilized on the surface whereas other reagents are added in solution.[216, 313] The interconnecting windows between adjacent pores here were big

enough to allow the glucose to access the whole inner pore volume. The enzymatic oxidation current of glucose increases linearly with the thickness of the macroporous film, as illustrated in Figure 3.36b). A sensitivity gain by a factor 30 together with a detection limit decrease by a factor 3 were reported in those systems. The stability of the immobilized species on the electrode surface could further be improved by encapsulation in electrophoretic paint.[242, 314] Several other biosensors based on macroporous electrodes showed improved characteristics for the detection of glucose, adenosine-5'-triphosphate (ATP) and c-reactive protein (CRP).[241, 315-319] Besides biomolecules, also other species such as heavy metal ions could be detected showing enhanced sensitivity at macroprorous bismuth and antimony electrodes.[227, 228] Figure 3.36c) shows the signal increase for the different stripping curves of cadmium and lead for increasing macroporous film thickness.

Due to the high surface areas, combined with good diffusion kinetics, macroporous electrodes are interesting for energy storage or conversion applications including batteries, supercapacitors and fuel cells.[5] Carbon,[320] manganese and nickel oxide[321, 322] or hybrid materials composed of carbon loaded with a conducting polymer[323] have been used to fabricate well-ordered macroporous capacitor electrodes. A good pseudacapacitive performance was combined with increased reaction rates in these systems. The latter was attributed to the open pore structures in the inverse opal allowing a fast and efficient charge transfer even at elevated scan rates.[322] Using macroporous instead of bulk electrodes as the anodic or the cathodic part in a battery allows to significantly enhance the charge transfer kinetics with the electrolyte.[226, 324-326]

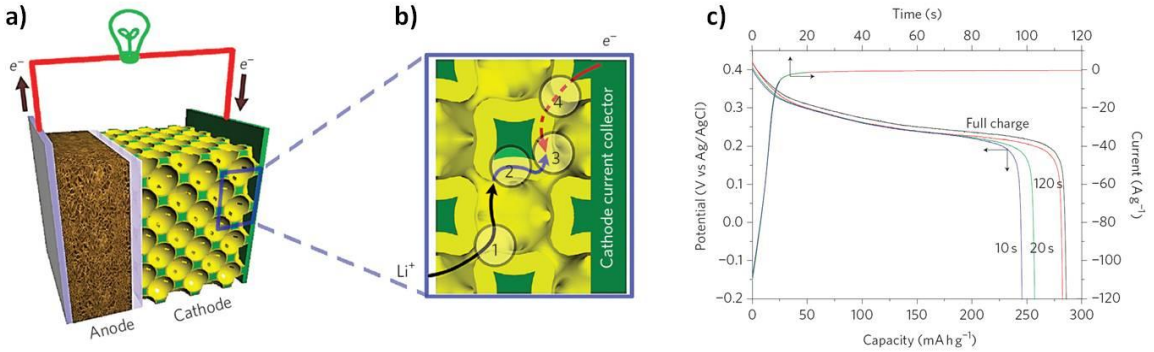

Figure 3.37: a) Scheme of a battery containing a bicontinuous cathode fabricated by colloidal crystal templating . The electrolytically active phase is yellow and the porous metal current collector is green b) Illustration of the four primary resistances in a battery electrode c) Ultrafast discharge and charge of the NiOOH electrode. Constant potential charge curves (0.45 V vs. Ag/AgCl) and 6C discharge curves after charging at constant potential for the indicated time. The curve labelled 'full charge' was charged galvanostatically at 1C. [226]

Figure 3.37a) schematically illustrates a battery where the cathodic compartment is based on an inverse opal structure. The fabrication of the bicontinuous cathode involved pulsed

electrochemical deposition of electroactive materials (NiOOH for nickel-metall hydride and MnO_2 for lithium-ion batteries) into the inverse nickel opal. The pore volume and the interconnecting windows in the opal however first had to be enlarged, to enable high loadings with the active material by simultaneously keeping the pore windows in the structure opened. Electropolishing of nickel here enabled to increase the overall porosity in the opal to ~94%. [225, 226] As illustrated in Figure 3.37b), the final structure combines fast ionic transport in the electrolyte and the electrode material with high electronic conductivity owing to the metallic nickel phase in the composite material. As a result the battery could be charged or discharged in a fraction of the time that would have been required for a cell composed of bulk electrodes. Figure 3.37 shows that the electrode is already 85% charged after 10s, 90% after 20s and 99% after 120s.

4 Macroporous materials with a gradient in pore diameter

In chapter 2.2 we introduced different methods allowing to assemble colloidal spheres into three dimensional colloidal crystals, whereas chapter 3 focused on the infiltration of colloidal templates with various materials to produce macroporous materials. In this chapter a strategy for the elaboration of macroporous materials with a complex pore gradient architecture will be presented. Besides the fabrication of homogeneous colloidal crystals based on one single bead size, different assembly techniques allowed building up various superstructures combining spheres of different sizes[327] or chemical composition[328] in one template. Additionally, point,[136, 138] line[135] or planar[139, 140, 329] defects were successfully integrated in colloidal crystals in order to explore their influence on the photonic properties of the material. Yan et al. gave a broad overview over existing strategies to introduce different artificial defects in 3-dim colloidal crystals.[137] A drawback of most assembly techniques, however, consists in the poor control over the number of particle layers deposited during the assembly process, hence leading to restrictions for example when gradients in colloidal crystals with different sphere sizes in successive layers have to be produced. The few attempts made to fabricate graded colloidal crystal structures consisted in top-down modifications of previously assembled polystyrene spheres by heating[330] or by plasma etching[331] associated with a considerable lack of control over the resulting bead size and structure of the gradient. This limitation can be overcome by using a layer-by-layer assembling process of colloidal particles. As shown in chapter 2.2.3, LB allows to elaborate colloidal crystal assemblies with an extremely well-defined geometry. Additionally Langmuir films can be prepared from silica particles with a range of different diameters. In the past, architectures using two different sphere sizes have been realized using the LB technique.[141, 142, 332-336]

Here we have taken advantage of all the benefits of the LB technique to build up colloidal superstructures with an unprecedented degree of complexity using up to six different particle sizes, the sequential deposition of monolayers allowing to exactly generate a predefined architecture. In a second step these templates have been infiltrated either with gold or polypyrrole by chronoamperometric electrodeposition, providing a perfect control over the filling level of the colloidal template. Finally, the inorganic template was removed using wet etching techniques revealing a macroporous electrode with the exact inverse structure of the original template. Figure 4.1 illustrates schematically the different steps leading to macroporous elecrodes with a pore gradient structure.

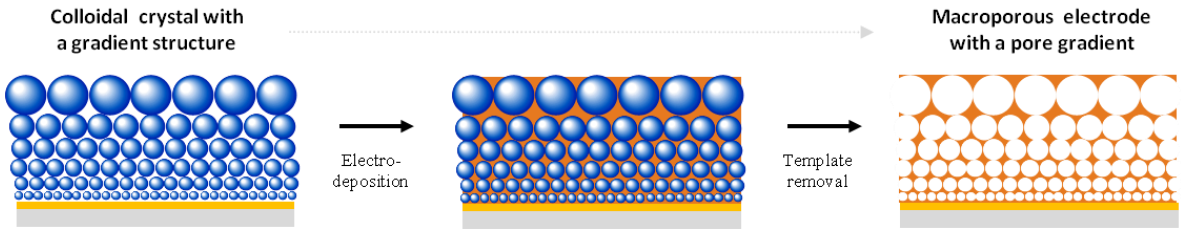

Figure 4.1 Scheme illustrating the different steps involved in the fabrication of well-defined macroporoues electrodes with a pore gradient. The key steps here are the assembly of the colloidal template using LB and the controlled infiltration by electrochemical deposition.

In the following section the different colloidal templates fabricated by LB are introduced and characterized by SEM imaging serving in a second step as templates for the electrochemical infiltration.

4.1 Template fabrication with increasing and decreasing bead diameters with LB

Among others, one of the great advantages of the LB technique is the possibility to build up colloidal crystals with a control at the single bead layer level. As described in chapter 2.2.3, well-compressed monolayers of silica particles are transferred from the air-water interface onto solid substrates and this process can be repeated until a desired number of layers, up to several tens of layers, has been deposited on the sample. Following this strategy colloidal crystal templates with various morphologies were synthesized using silica particles of different diameters. More precisely, three main families of templates with an increasing complexity, that may lead to various types of applications, were generated which are schematically shown in Figure 4.2.

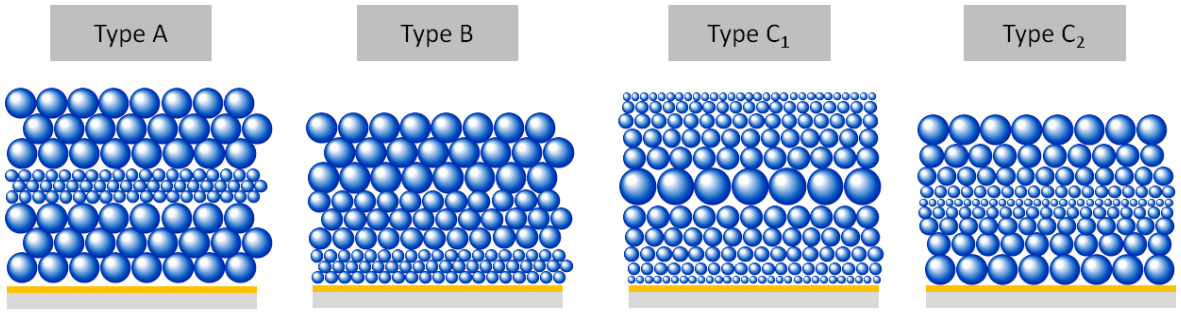

Figure 4.2 Illustration of the different template architectures produced in this work. In "Type A" templates with two sizes of particles are used to assemble a colloidal crystal with a well-defined planar defect. In "Type B" templates with three sizes of particles allowed to build up "single gradient" structures. "Type C_1" and "Type C_2" templates consist of up to six different particle sizes with "ascending-descending" and "descending-ascending" architecture, respectively. Sphere layers in these "double-gradient" structures were symmetrically organized with respect to a central layer of large or small particles.

In "Type A" templates two sizes of particles were used to build up a colloidal crystal with a well-defined planar defect consisting of a stack of smaller in between two stacks of bigger particles. For the generation of "Type B" templates three different particle sizes were assembled into "single gradient" structures. Stacks of bigger particles were here deposited onto those of smaller ones. The most complex architecture is shown in "Type C" templates. Monolayers of up to six different sphere diameters have been assembled into "double-gradient" colloidal crystals. The sphere layers have been symmetrically arranged with respect to the central layer consisting of the larger or smaller particles. In "Type C_1" templates the sphere layer succession was "ascending-descending" whereas a "descending-ascending" architecture was realized in "Type C_2" samples. All colloidal templates have been assembled on gold coated glass slides and were uniform over an area of more than $2cm^2$, similar to those shown in Figure 3.6b). Generally, Langmuir-Blodgett films could perfectly be deposited onto larger surfaces without any restriction, as long as the required equipment – a Langmuir trough with a large working area and a sufficient immersion depth – is available.

After assembling the different types of colloidal templates by LB, some samples were broken in order to characterize the sphere layer stacking in the corresponding cross-section SEM images. Figure 4.3a) shows a "Type A" colloidal template containing a 5-layer stack of smaller particles in between two 5-layer stacks of bigger particles. Figure 4.3b) shows a "Type B" template composed of three successive stacks, each containing 10 particle layers. The thickness and the composition of both templates was very regular. Especially in templates based on successive stacks of layers with increasing diameters of silica particles (e.g. Figure 4.3b), the eventual irregularities of the first stackings have little influence on the arrangement of the upper ones.

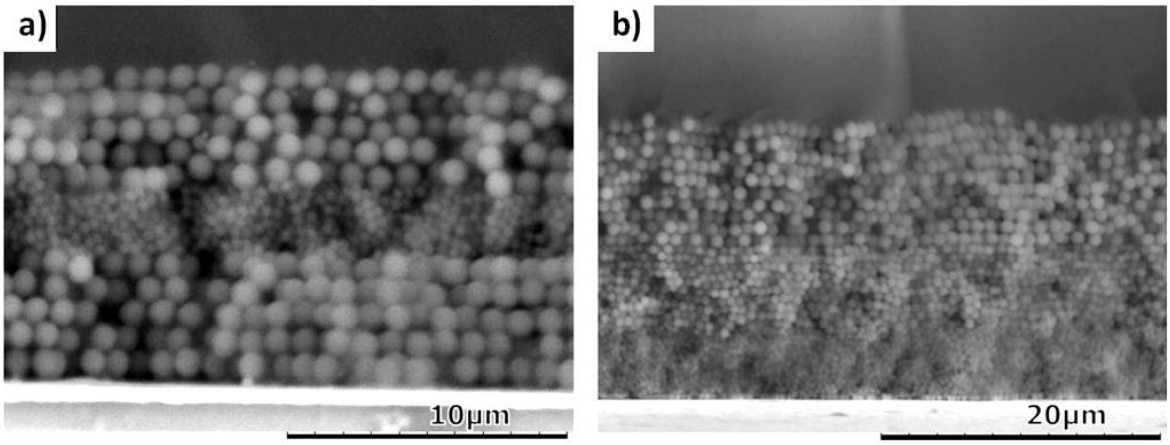

Figure 4.3: SEM side views of silica colloidal templates produced by LB showing a) "Type A" and b) "Type B" structure. In a) two 5-layer stacks of 1000nm-particles are separated by a 5-layer stack of 430nm-particles. In b) a sample consisting of three 10-layers stacks of 430, 740 and 1000nm-particles is shown.

As mentioned, it is possible to take advantage of the specific "layer-by-layer" iterative process, characteristic for the LB strategy, to get templates with an even higher degree of complexity. Indeed, sequential stacking of single layers of particles with different diameters can lead to structures with a "double-gradient" ("Type C" templates). In Figure 4.4a) and b) a "Type C_1" template composed of 11 layers comprising particles of six different diameters ranging from 240 to 1200nm is shown. In this case, the particle diameter was gradually increased for the first six layers and decreased for the following five ones, leading to an “ascending-descending” architecture. By taking a close look at the template structure (see Figure 4.4a), one can notice that the first six layers are homogeneously organized throughout the colloidal crystal, without any significant variation in thickness. The remaining five layers however show a slightly wavy character, which is attributed to the fact that layers of smaller particle size are deposited onto bigger ones. It is found that this effect is particularly pronounced for big variations of the particle size from one layer to the next one (e.g. the step of 1200 to 600nm spheres, as seen in Figure 4.4a).

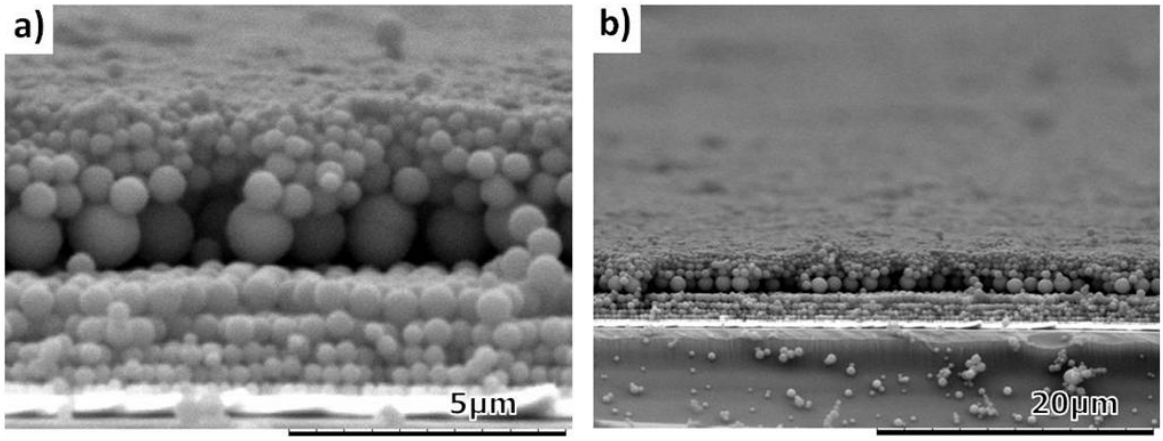

Figure 4.4: SEM side views of a double-gradient colloidal template ("Type C_1") produced by LB. Spheres of six different diameters are symmetrically arranged with respect to the middle layer in the ascending-descending architecture (sphere diameters: 240, 325, 395, 470, 600, 1200, 600, 470, 395, 325 and 240nm).

By selecting particles with diameters varying only slightly from one layer to the next one it is possible to minimize the influence of this effect. In Figure 4.5 a) and b), a reverse type of template ("Type C_2", descending-ascending) is illustrated: the particle diameter first decreases for five layers from 1000nm to 240nm and subsequently becomes larger for the last four layers. A top view of these samples is given in Figure 4.5 c) and d). The homogeneity of the top surface is noticeable and might be put down to the more regular variation of the particle diameters in the descending or ascending parts (diameter ratios between consecutive layers were always close to 1.25). As Figure 4.5c) shows areas with a perfectly close packed sphere arrangement exist in the

template which is remarkable given the complexity of the template architecture. At lower magnifications some defects including missing spheres or grain bounderies are visible in Figure 4.5d) in the top layer of the colloidal crystal template.

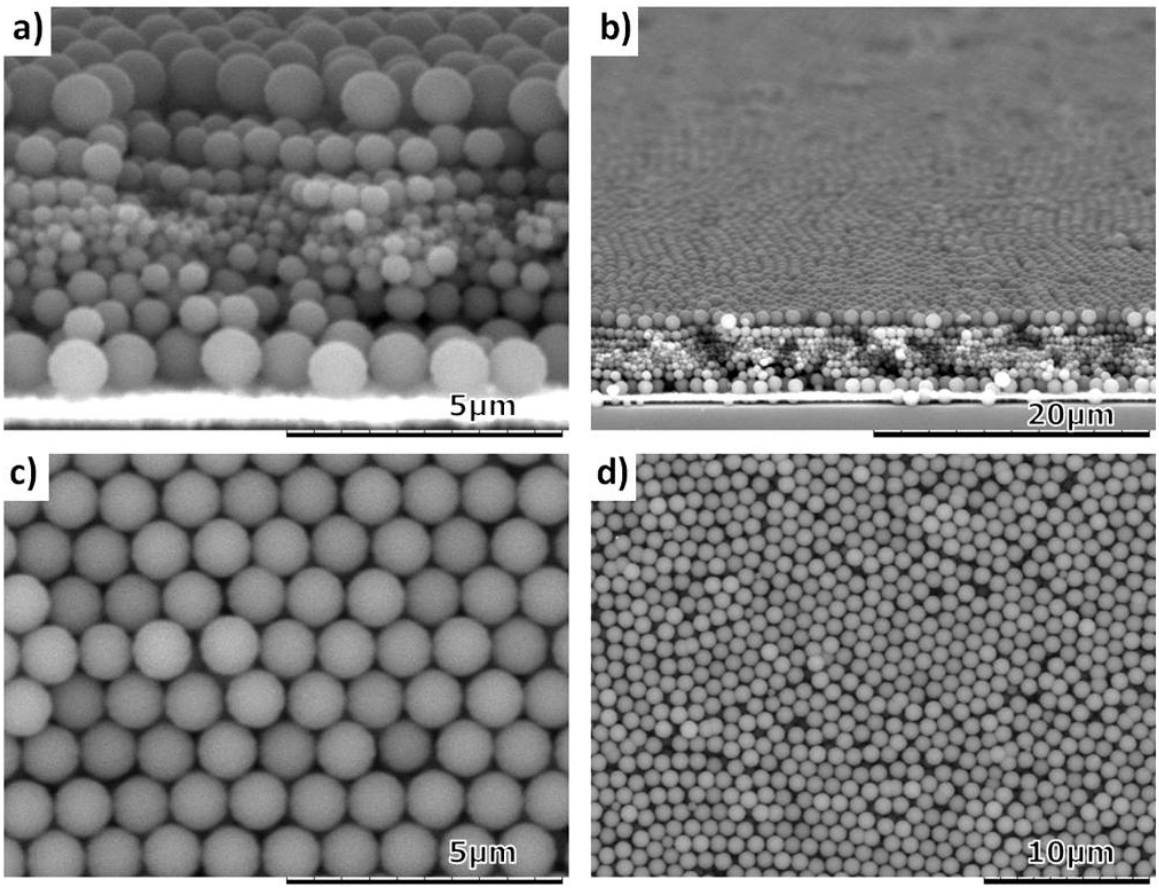

Figure 4.5: SEM side (a +b) and top (c +d) views of a double gradient colloidal template ("Type C_2") produced by LB at different magnifications. Spheres of five different diameters are symmetrically arranged with respect to the middle layer in the descending-ascending architecture (sphere diameters: 1000, 740, 470, 325, 240, 325, 470, 740 and 1000nm).

Since they are deposited on a gold substrate, reflectance spectroscopy is a very convenient and non-destructive technique to optically characterize the structure of our templates similarly as shown previously in chapter 2.3. Measurements have therefore been carried out using a microspectrophotometer working at normal incidence in the UV-visible-IR range between 250 and 1650 nm. Similarly to previous observations, regular oscillations, known as Fabry-Pérot fringes and testifying of the thickness homogeneity, can be observed in a certain range of wavelengths (here, between 1200 and 1600 nm), as shown in Figure 4.6 for three “Type B” samples consisting of three consecutive stacks of N layers of 430, 740 and 1000-nm silica particles (with N=3, 5 or 10). While the overall reflectance signal becomes more and more attenuated when the sample gets thicker, the number of fringes, resulting from interference phenomena at the air-template and template-substrate interfaces, increases as a result of a larger optical pathway. The wavelength

positions of consecutive reflectance maxima allow to estimate the thickness Θ of a sample, [95] following equation 2.7.

$$m \cdot \lambda_1 \cdot \lambda_{1+m} = 2 \cdot n_e \cdot (\lambda_{1+m} - \lambda_1) \cdot \Theta \quad (2.7)$$

λ_1 here is the wavelength position of the first visible fringe taken into account and n_e the mean refractive index for a compact arrangement of silica spheres in the air, assumed to be close to 1.33. For each sample, Θ is therefore equal to the slope of the linear fits plotted in the inset of Figure 4.6 and the calculated values are 5.3, 9.4 and 19.4 µm for the three "Type B" examples with three consecutive stacks of N layers (N=3, 5 and 10, respectively). This result is in good agreement with the thicknesses inferred either from the SEM observations or from geometrical calculations assuming a fcc packing of the spheres in each stack.

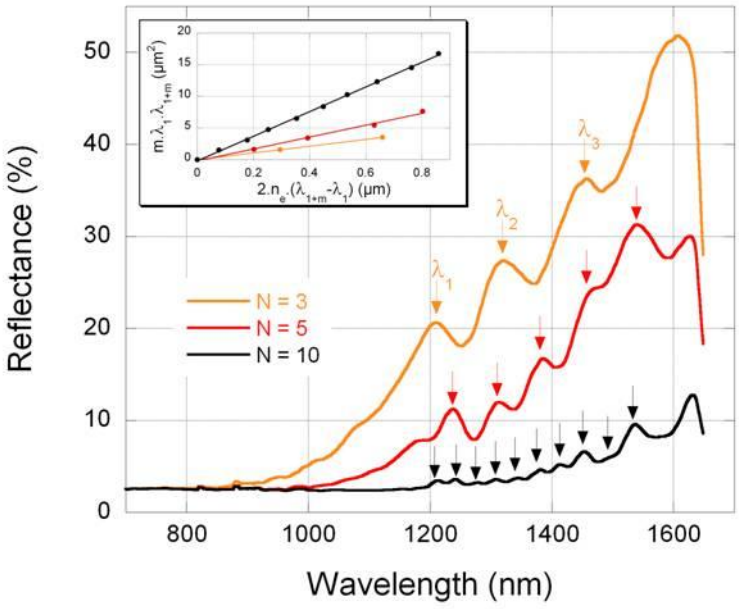

Figure 4.6 UV-Vis-NIR reflectance spectra of three "Type B" templates consisting of three consecutive stacks of N layers of silica particles with an increasing diameter (430nm for the first stack, 740nm for the second and 1000nm for the third). Arrows indicate the positions of the Fabry-Pérot fringes taken into account for calculating the thickness of each sample, given by the slope of the linear fits shown in the inset.

As shown in this section, extremely well defined colloidal crystals of different, very complex architectures have been assembled by LB. In the following they will serve as templates for the controlled infiltration with gold and polypyrrole using electrochemical deposition.

4.2 Electrodeposition of metals and conducting polymers

The templates fabricated in section 4.1 served as working electrodes for the electrodeposition of gold and polypyrrole. The electrodeposition was performed in potentiostatic mode which already had proven efficient to control the filling level of the infiltration of homogenous colloidal templates thanks to the oscillating currents caused by periodic variations of the electroactive area in the template (see Chapter 3.2.1). The experimental conditions including the electrolyte solutions, the experimental setup and the applied potential were identical to those previously employed in chapters 3.2.1 and 3.3.1. In all the figures presented below, for the sake of clarity, the intensity of the faradaic current signal that was recorded during the electrodeposition process was divided by the geometrical surface area of the electrode.

A typical example of such a chronoamperometric curve, recorded for the infiltration of the "Type A" colloidal template shown in Figure 4.3a), is presented in Figure 4.7a). Similarly as for the potentiostatic deposition of gold into homogeneous colloidal templates, we were able to observe current oscillations during the infiltration of templates with a more complex architecture.

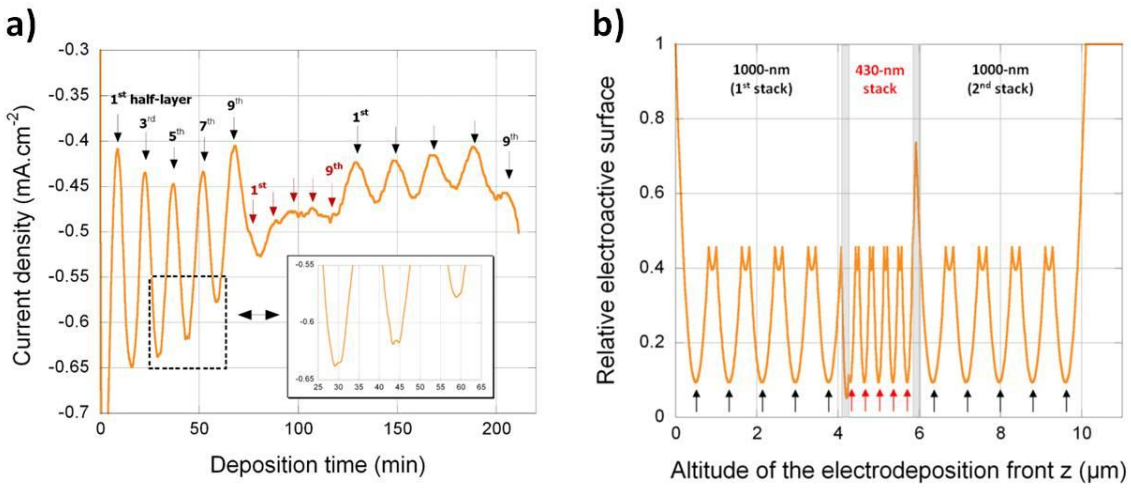

Figure 4.7: Chronoamperometric curves corresponding to the electrodeposition of gold (E = -0,66V) in a "Type A" template presenting an artifical planar defect with two 5-layers stacks of 1000nm-particles separated by a 5-layers stack of 430nmparticles. b) Theoretical calculation of the electroactive area as a function of the position of the progressing electrodeposition front.

The chronoamperometric curve in Figure 4.7a) shows that the shape of the oscillations depends on the sphere layer architecture in the template. The first and the last five oscillations of the curve exhibit relatively high amplitudes corresponding to the filling of the two 1000nm-sphere stacks in the template. The infiltration of the intermediate 430nm-sphere stack resulted in oscillations of higher frequency and much smaller amplitude. As explained in chapter 3.2.1 these

current oscillations allow to follow the growth of the metallic deposit in these homogeneous and crack-free colloidal templates. The absolute minima of the current density correspond to minima of the electroactive area and hence to half-layer filling levels in the template indicated by the arrows in the plot.

Another remarkable feature is particularly visible when the electrodeposition occurs in templates containing large particles. As expected – but never observed experimentally – by others authors,[221, 224] the interpenetration of two consecutive layers of particles in a fcc arrangement should generate a local extremum for the current density when the electrodeposition front reaches the middle of the junction between two consecutive layers. As shown in the inset of Figure 4.7a), the first minimum in current density indeed presents a small local maximum, thus corresponding to a local minimum of the electroactive surface area. This observation is in perfect agreement with the theoretical variation of available surface area, calculated as a function of the altitude z of the growth front in the same Type B template (5 layers of 1000nm, 5 layers of 430nm, 5 layers of 1000nm). Assuming the velocity of the electrodeposition process is constant, this z-dependency, plotted in Figure 4.7b), could be considered as a function of time. Two symmetrical cusps are observed around the extrema for each even number of half-layers, illustrating the anti-monotone surface area variation for the overlap zone of two consecutive layers.

Three other characteristics emerge from this theoretical calculation based on pure geometric considerations. First, the absolute minimal area should equal 10% of the whole surface for each half-layer thickness, in agreement with the value of 0.9 for the surface compacity – or packing factor – expected for a hexagonal pavement of disks (see chapter 2.2.3). It is worth noting that this minimum value is independent on the diameter of the particles. Second, the variation of the surface in the overlap between two consecutive stacks, around values of z close to 4.2 and 5.9 µm also exhibits local extrema that are not visible experimentally. Finally, when the metallic deposit reaches the top surface of the template, the electrochemically active area increases again until its maximum value, i.e. the geometrical surface of the bare substrate. This last feature was however not observed in our experiments, since we systematically stopped the electrochemical reaction just before the gold deposit reaches the top surface. To be more precise, the electrodeposition was performed until observation of the last maximum, corresponding to the 9^{th} half-layer in Figure 4.7.

Figure 4.8 a) and b) show cross section SEM images of macroporous gold electrodes obtained from the infiltration of Type A templates containing (a) three and (b) five sphere layers per stack. As intended, the infiltration of the templates has been stopped in the top layer of the template. In our experimental results we found that oscillations had much smaller amplitudes for the

infiltration of the stack composed of 470nm-spheres as theoretically would have been expected (see Figure 4.7a and b). This difference is due to the fact that layers of smaller particle size have been deposited onto bigger ones which creates a certain amount of disorder in this region of the template not being included in the theoretical model. Pore layers in the "defect stack" of the sample hence are found to exhibit a slightly wavy character (visible in Figure 4.8b), this lack of sphere layer alignment in the template being sufficient to suppress the emergence of well pronounced oscillating currents with a high amplitude.

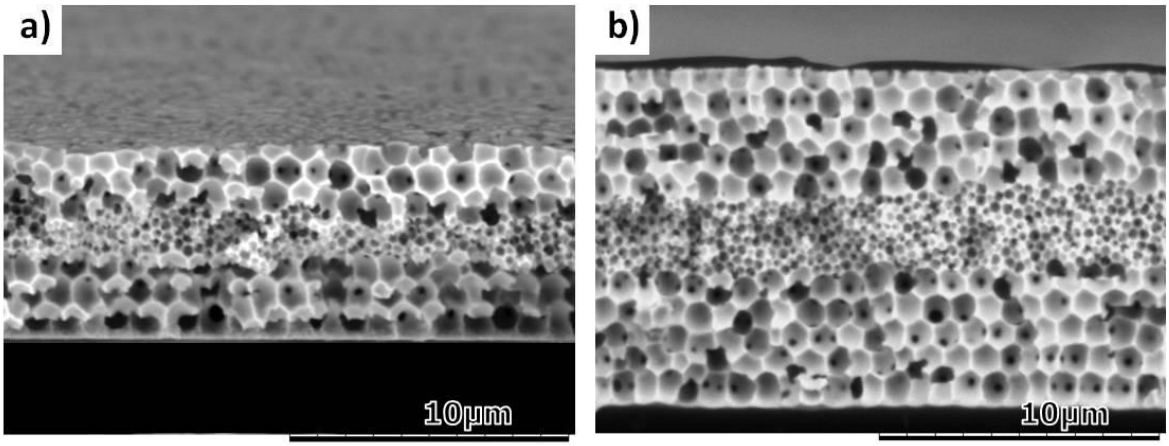

Figure 4.8: SEM side views of macroporous gold electrodes obtained by infiltration of "Type A" templates and subsequent template removal. Templates were composed of three stacks of a) N = 3 and b) N = 5 sphere layers.

In Figure 4.9 chronoamperometric curves for the infiltration of gold into "Type B" templates which consisted of three stacks of particles with an increasing diameter are presented. Certain half-layer filling levels at absolute current minima have been indicated by arrows in the plot, each color corresponding to a different sphere size in the different stacks of the "single-gradient" template. In both plots a decrease of the oscillation frequency is observed when stacks of bigger particles are infiltrated with gold. The electrodeposition was stopped after the 5^{th} and the 19^{th} half-layers of their respective third stack, consisting of three (*top figure*) or ten (*bottom figure*) layers of 1000nm silica particles.

The characterization of "Type B" templates by SEM images after the infiltration with gold and the removal of the template are shown in Figure 4.10 a) and b), respectively. The SEM image of the silica-gold composite illustrates well the level of precision provided by potentiostatic electrodeposition during the filling of the colloidal templates. As seen in Figure 4.10a) the deposition of gold into the void space of the template has precisely been stopped before the metal front began to grow out of the top layer of the template. This allowed to remove the silica template by dissolution, requiring diffusion of a dilute solution of hydrofluoric acid from the top surface to the bottom of the electrode.

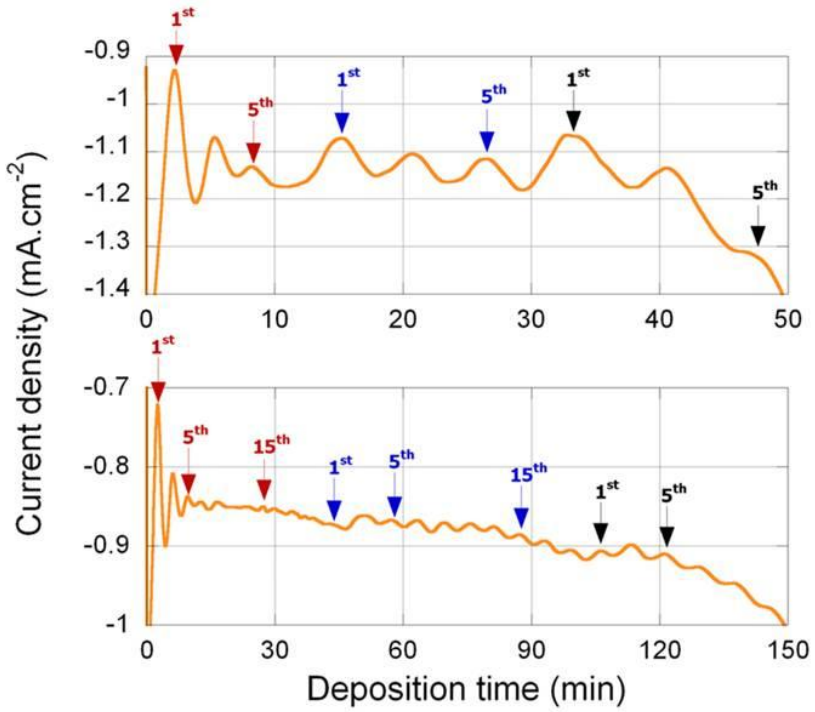

Figure 4.9: Chronoamperometric curves corresponding to the electrodeposition of gold in a "Type B" "single-gradient" template consisting of three consecutive stacks of N = 3 (*top figure*) or N = 10 (*bottom figure*) layers of 430, 740 and 1000nm-particles. Arrows indicate the maxima corresponding to significant the half-layer positions in each stack.

In Figure 4.10b) a macroporous "single-gradient" gold electrode with N = 10 pore layers per stack is shown, corresponding to the amperometric deposition curve presented in Figure 4.9 (*bottom figure*). The final macroporous material presents interconnected pores and a top surface with a remarkable flatness, illustrating the homogeneity of the electrodeposition process due to both, the adequate plating solution and the template quality. This is particularly well illustrated by the registered current transients in Figure 4.9 where almost every maximum of the current was resolved (up to 30 for the "Type B" sample shown in Figure 4.10b), whereas the best results described in the literature quote the detection of a mere 10 maxima of the current density for the infiltration of colloidal crystals composed of a single sphere size.[209]

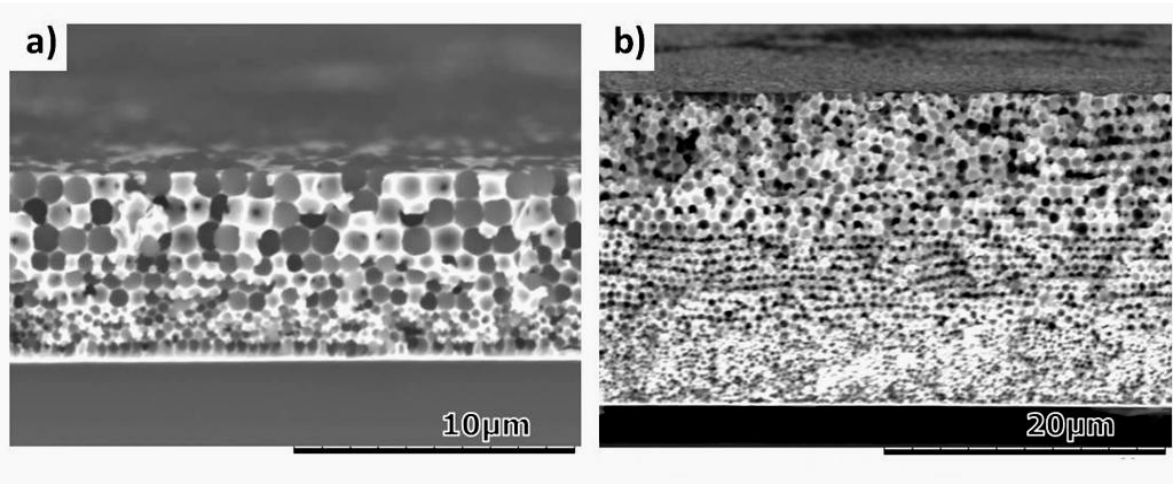

Figure 4.10: SEM side views of maroporous gold electrodes originating from gold deposition into "Type B" templates. a) After infiltration with gold for N=3 and b) after the template removal for N=10.

Additional experiments were also carried out under similar conditions using the "Type C" templates shown in the Figure 4.4 and Figure 4.5. Again, the variation of the current density versus time has to be correlated to the architecture template, the amplitude of the oscillations decreasing slowly during the electrodeposition process, either due to a laterally inhomogeneous growth front of the gold deposit or a slight imperfection in the ordering of the colloidal particles in the template.

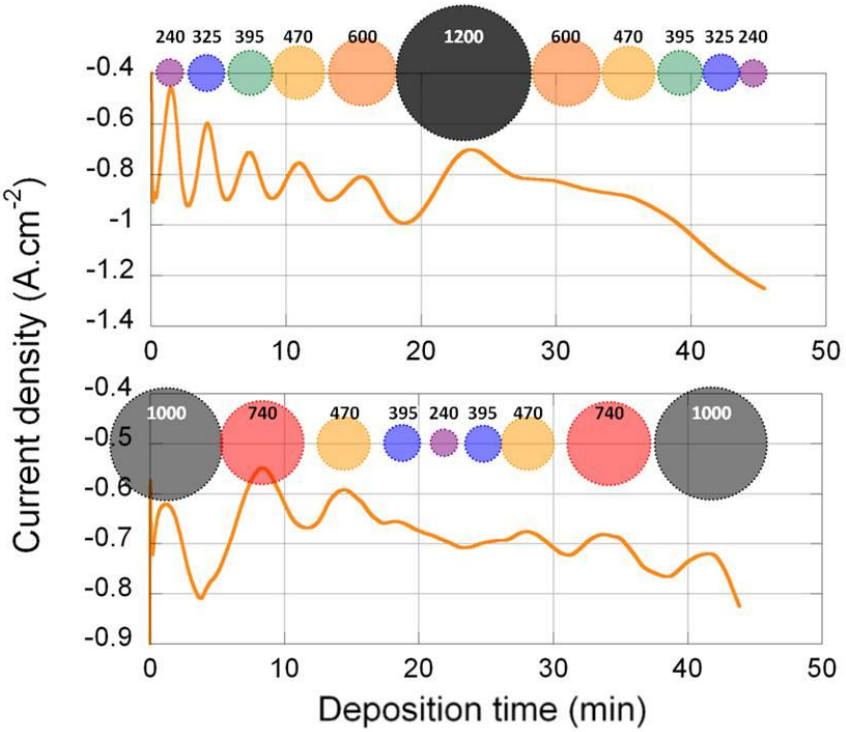

Figure 4.11: Chronoamperometric curves corresponding to the electrodeposition of gold in double-gradient templates with ascending-descending ("Type C_1", *top figure*) and descending-ascending ("Type C_2", *bottom figure*) structures (Numbers on spheres indicate the diameter of the particles used in the template).

A good example for the last-mentioned point is presented in Figure 4.11 (*top figure*) with the "ascending-descending" sequence. For the sake of clarity, the structure of the template was reminded at the top of the figure, using spheres that were positioned symmetrically around each extremum (corresponding to each half-layer) and whose size was exactly proportional to the actual size of the silica particles used experimentally.

Indeed, the corresponding chronoamperometric curve is particularly remarkable since the first six current oscillations, related to each of the six monolayers of the "ascending" stack, are clearly visible and their period matches almost perfectly with the size of the particles. However, electrodeposition in the "descending" stack generates less pronounced oscillations. This result is in good agreement with the SEM images of the resulting inverse material, shown in Figure 4.12 a) and b), where a highly ordered porous structure is observed in the lower part of the sample (until the middle layer), whereas the degree of disorder is higher in the upper five layers, this being directly attributable to the stacking irregularities observed in the template (see Figure 4.4).

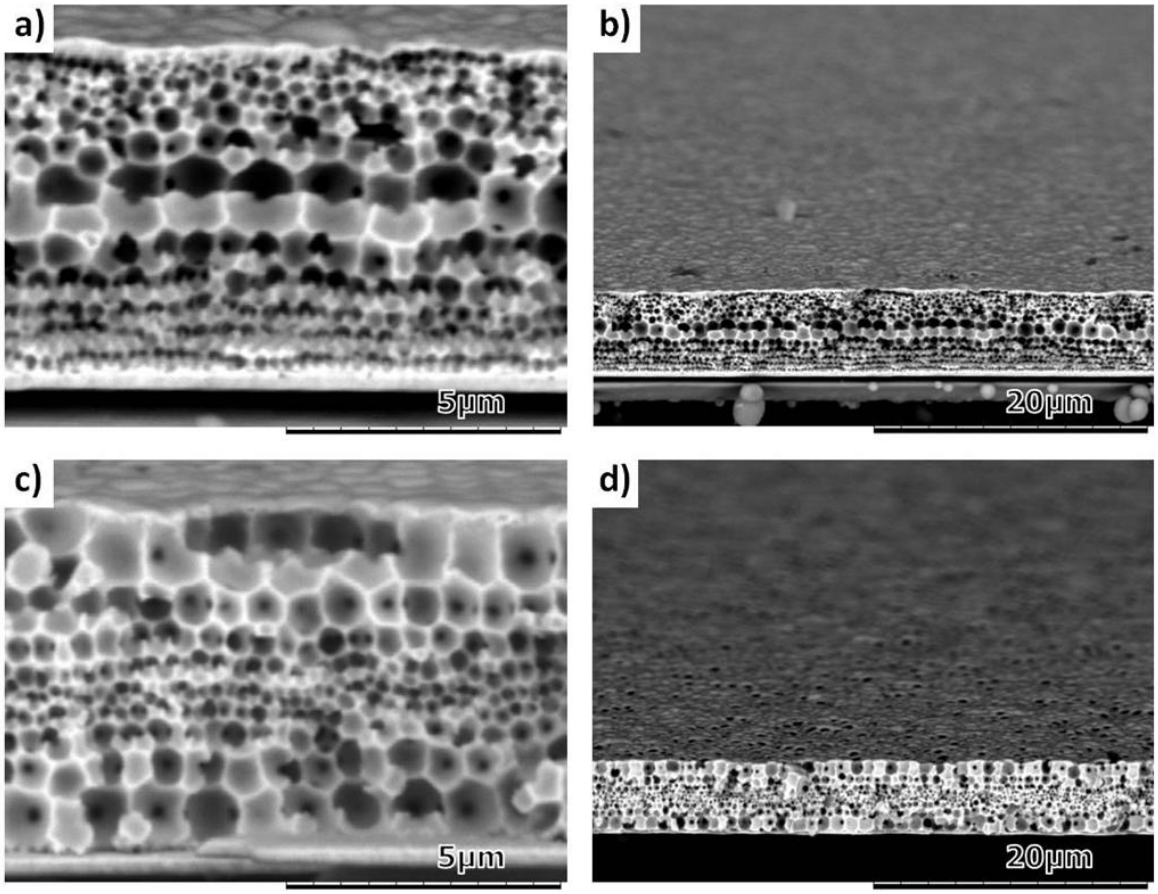

Figure 4.12: SEM side view-images of macroporous double-gradient gold electrodes with ascending-descending (a +b) and descending-ascending (c+d) pore size structures at different magnifications.

On the opposite, electrodeposition in the "descending-ascending" structure, where the variation in the particle size was more progressive between consecutive layers, leads to a much more symmetrical chronoamperometric profile, the maxima of the current density being still visible in the second "ascending" stack. The SEM images of the corresponding macroporous gold structure is shown in the Figure 4.12 c) and d). A very regular pore architecture is found in the double-gradient structure, with a remarkable flatness of the top pore layer. As can be seen, the whole template was infiltrated with gold, using electrochemical deposition without growing over the top surface layer using the control provided by the recorded current oscillations.

As mentioned in chapter 3.1.3, a wide range of materials including different metals, conducting polymers, oxides and certain semiconductors can be infiltrated into the void space of colloidal crystals using electrochemical deposition. To illustrate that the results we showed so far are mainly depending on the quality of the template, electrodeposition of a conducting polymer film was performed into the "Type C" templates. Polypyrrole was deposited in potentiostatic mode as described in chapter 3.3.1.

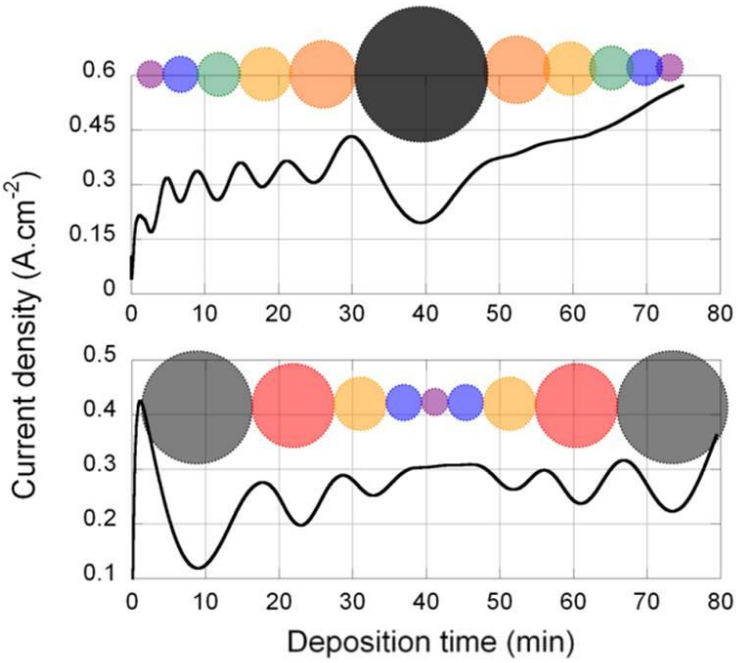

Figure 4.13: Chronoamperometric curves corresponding to the electrodeposition of polypyrrole (E = +0,6V) in double-gradient templates with ascending-descending ("Type C_1", *top figure*) and descending-ascending ("Type C_2", *bottom figure*) structures.

Figure 4.13 presents the chronoamperometric curves obtained during the electrodeposition within "Type C" templates, identical to those shown in the Figure 4.4 and Figure 4.5. Since the formation of polypyrrole results from an oxidation process of pyrrole, the faradaic current has a

positive sign and as a consequence, each current density minimum now corresponds to a minimum of the electroactive surface.

Similarly to the results obtained with the gold plating solution, we again observe regular oscillations of the current density, here around a mean value of 0.3 mA/cm^2. In the "ascending" stack of the ascending-descending structure, the interdistance between consecutive maxima is again in perfect agreement with the size variation of the particles from consecutive layers. As expected, oscillations are however less visible in the "descending stack". The order in the last five pore layers in Figure 4.14a) is considerably lower than in the first six layers explaining the lack of oscillations during the infiltration of the second part of the template. The flatness of the top surface is also less regular in PPy films compared to its gold homologue, as it can be seen in Figure 4.14 a) and b). On the other hand, electrodeposition in the "descending-ascending" structure leads to an almost perfectly symmetrical chronoamperometric curve, indicating both (i) the good symmetry of the template architecture and (ii) a constant rate of reaction – or film growth velocity – suggesting that the electrochemical oxidation of pyrrole proceeds homogeneously.

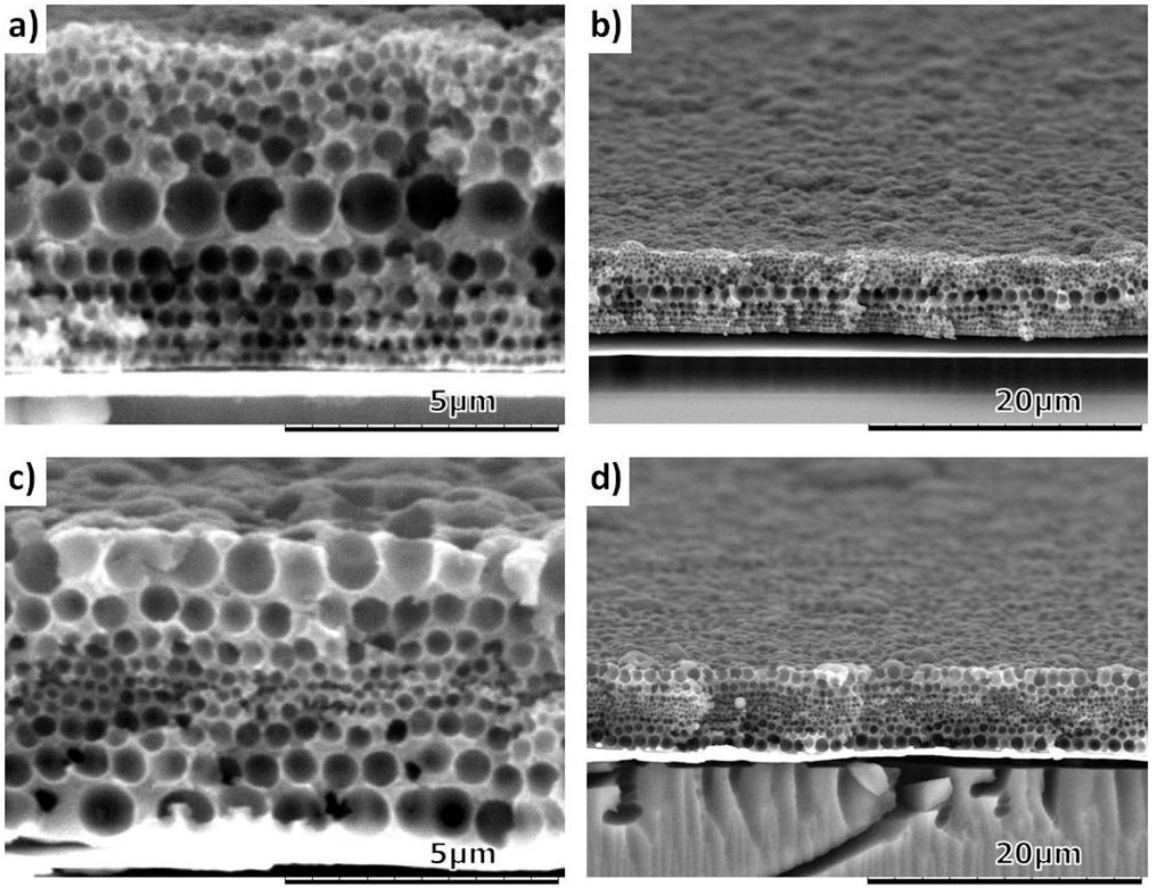

Figure 4.14: SEM side view-images of macroporous double-gradient polypyrrole electrodes with ascending-descending (a +b) and descending-ascending (c + d) pore size structures in different magnifications.

Again, the SEM side view pictures in Figure 4.14c) and d) after dissolution of the silica particles in dilute HF confirm this statement.

Figure 4.15 illustrates SEM cross-section images showing a macroporous PPy electrode with a pore size gradient in high resolution. It has been obtained from a template consisting of the "ascending" part of the "Type C_1" structure with one additional layer of 1200nm-spheres deposited on top. Filling this template up to the last half-sphere layer with PPy and removing the template led to the macroporous gradient structure shown in Figure 4.15 a) and b). The well-ordered and uniform character of the structure found in "ascending" stacks of pore layers is particularly visible in these images.

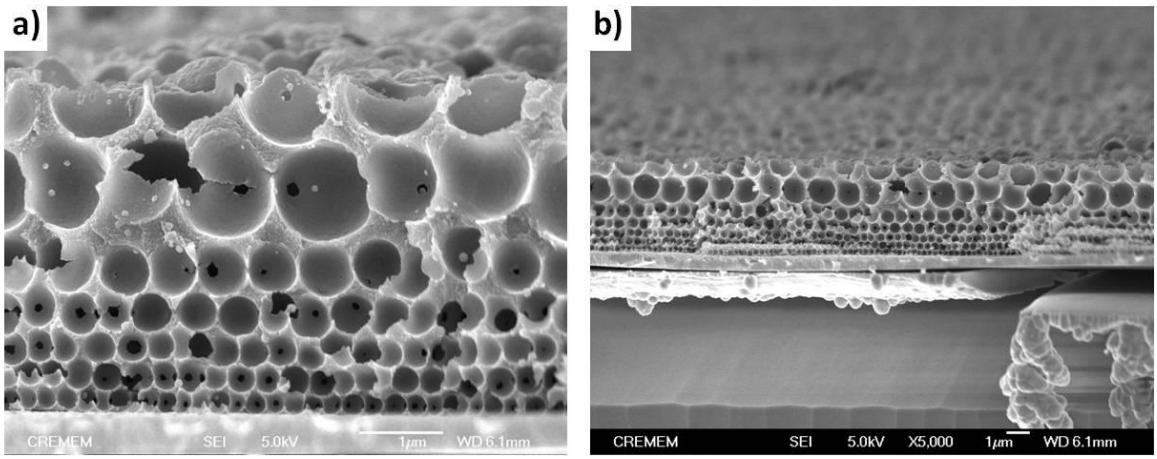

Figure 4.15: Macroporous PPy electrodes with a pore size gradient. Pore sizes are increasing from 240 to 1200nm. The top half-layer pore exhibits the same diameter as the underlying pore layer (d = 1200nm). Images with a a) high and b) lower magnification.

In this section we successfully produced macroporous electrodes with complex pore architectures including defect, single- and double-gradient structures with a remarkably well-defined structural integrity. Current oscillations observed during the potentiostatic electrodeposition provided excellent control over the filling of the void space in the templates and hence the final thickness of the nanostructured electrode films. In the next chapter we will show how multilayers of different materials can be electrodeposited into colloidal monolayer templates. This leads to materials characterized by a 3-dim, periodic nanostructure in the subwavelength range, being interesting for different kind of applications, especially in the context of metamaterials.

5 Multilayer deposition of different materials in colloidal crystals

In chapter 2.5 we introduced a group of materials gaining their exceptional optical properties (e.g. negative refractive index nonexistent in natural materials) from the structuration rather than from the single components in the material. We discussed principle metamaterial designs, including split ring resonators, double-fishnet structures and structures based on metallic wires or holes in metallic films and some of the applications that can be realized with these nanostructured materials. Metamaterials all have in common that the scale, at which inhomogenities are introduced in these materials, is much smaller than the wavelength of light at which the material is meant to operate. Usually top-down approaches are used for the fabrication of metamaterials, requiring expensive equipment and limiting the size of the smallest attainable structures (e.g. resolution limited lithographic processes).[153, 160, 162] Bottom-up approaches based on self-assembly strategies hence represent a promising alternative towards a cost-effective realization of large-scale metamaterials. In the past templated electrodeposition already proved to be a feasible strategy to produce negative index materials.[157]

In colloidal crystals different multilayer structures have been deposited so far to modulate the optical properties. High refractive semiconductor (Si/Ge)[337] or inorganic ZnS/TiO_2[338, 339] multilayer structures were deposited around the spheres in colloidal templates or into the pore volume (after removal of the template) using CVD and ALD, respectively, in order to modify the photonic bandgap or the photoluminescence in the material. Furthermore semiconductor quantum dots dispersed in titania inverse opals allowed to control the dynamics of spontaneous emission from these materials.[340] However, the number of multilayers deposited in colloidal crystals and hence the modification of the colloidal structure is limited when CVD techniques are employed. In contrast, electrodeposition enables to fill a colloidal monolayer from the bottom to the top of the template with layers of different materials in a desired sequence. The thickness of each layer can be adjusted at will by controlling the charge used for the deposition of the respective layers. Principally, structures very similar to the double-fishnet design, hence could be generated by depositing alternating layers of two different materials in a colloidal template. However, using electrochemical deposition only conductive materials can be stacked in a multilayer structure, thus excluding metal-dielectric combinations, which are commonly used in metamaterials (see chapter 2.5).

Our strategy is based on the electrodeposition of a multilayer structure of different materials in colloidal monolayers. We first focused on the deposition of alternating layers of a conducting polymer and a metal into the colloidal template (see chapter 5.1). Owing to the refractive index

contrast between the conducting polymer and metal layers, the optical response of the material was expected to be significantly modified. In the second approach the void space in a colloidal monolayer was filled with alternating layers of gold and nickel (see chapter 5.2). In this case the material further could be modified by selectively dissolving either the colloidal template or the nickel in the multilayer structure. The optical properties of the materials were characterized using reflectance spectroscopy by comparing the experimental to the theoretically calculated spectra (see chapter 5.3).

5.1 Alternating electrodeposition of conducting polymer and metal layers

In this section, the electrodeposition of alternating metal and conducting polymer layers in colloidal templates will be discussed. In Figure 5.1 the different fabrication steps are illustrated. Colloidal monolayers, which are transferred on gold coated glass slides using LB, serve as templates for the electrodeposition. Thin conducting polymer and metal films, e.g. PPy and gold, are alternately deposited in the template. The same experimental setup as shown in Figure 3.7 was employed, carrying out the deposition of the different materials in separate electrolyte solutions by applying an adequate potential. The control of the charge passed in each deposition enables to adjust the thickness of the individual layers. After the deposition, template removal leads to a material, in which the refractive index periodically changes for different angles of an incident light beam (indicated by arrows in the scheme at the bottom in Figure 5.1).

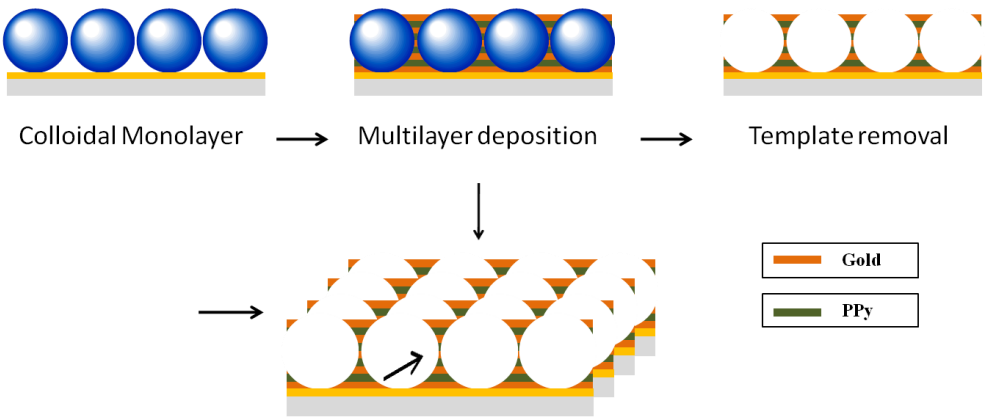

Figure 5.1: Schematic representation of the fabrication of an inverse 2D colloidal crystal with omnidirectional varying refractive index (indicated by the arrows in the bottom figure). The concept is based on electrodeposition of a conducting polymer/metal (e.g. PPy and gold) multilayer structure in the colloidal template followed by the removal of the template.

As the conducting polymer we chose polypyrrole due to the relatively low oxidation potential of the monomer of +600mV vs Ag/AgCl (see chapter 3.3.1). This is important as concurrent metal oxidation reactions may occur when applying high positive potentials during the polymerization. Consequently, the choice of the metal was restricted to gold and eventually platinum, which do not get oxidized at the oxidation potential of pyrrole. We first verified the feasibility of an alternating deposition of PPy and gold on gold coated glass slides without colloidal template. As shown in chapter 3.3.1, thin PPy films could be uniformly deposited on gold electrodes using chronoamperometric deposition. However, a certain minimum thickness is required to ensure a uniform coverage with PPy and to prevent the access of the solution to the underlying gold film during the subsequent gold deposition. Therefore, we reduced PPy films of different thickness, which had been deposited onto gold electrodes before, by applying a constant negative potential in acidic medium. Figure 5.2 shows that complete reduction of PPy films, assumed when the current reaches a constant low negative value, occurs, as expected, faster in thinner PPy films. For 50nm-PPy films, however, the currents are much higher, indicating that besides the PPy reduction also hydrogen evolution at the underlying gold electrode contributes to the recorded current signal. Consequently, we used PPy films thicker than this threshold value of 50nm, typically about 100nm thick, for a subsequent deposition of gold onto the polymer.

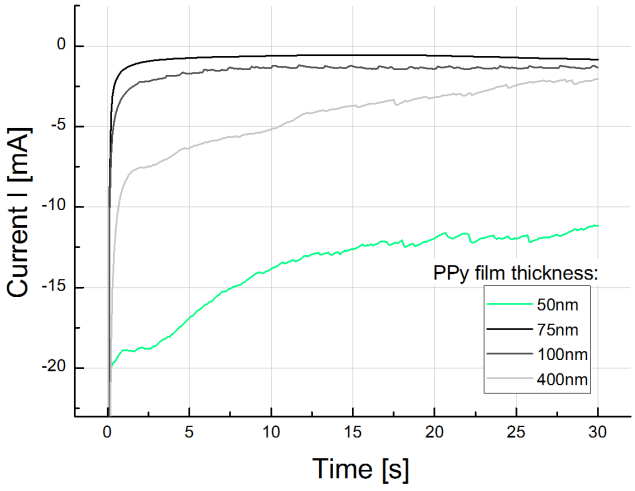

Figure 5.2: Plot of the PPy reduction current as a function of time for PPy films of different thickness on gold coated glass slides. A constant potential of -700mV was applied at the gold/PPy electrode during 30s in aqueous solution containing 0.5M HCl and 0.15M KCl.

Metal deposition on conducting polymers is a quite complex process owing to the high number of parameters influencing the morphology of the metal film deposit. One of them is the polymer film thickness which was kept constant during our experiments. Another being the conductivity, changing as the polymer is converted from its reduced to the oxidized state. The maximum

intrinsic conductivity in conducting polymer depends on the synthesis conditions, e.g. the incorporated counterion, the applied potential and the employed solvent.[267] When depositing gold on PPy films of constant thickness, we found that the morphology of the gold deposit was strongly dependent on the oxidation state of the polymer. Figure 5.3a) and c) show SEM images of gold deposits on oxidized PPy films, whereas in the samples shown in Figure 5.3b) and d) the PPy films were in the reduced state. For both cases the gold film did not cover the whole electrode area. The deposition of gold on oxidized PPy films occurred locally at certain spots of the film, whereas on reduced polymer films a more homogeneous distribution of gold nucleation sites was found. Using the commercial plating solution a potential of -700mV had to be applied to deposit gold on the polymer films (see Figure 5.3a and b). The initially oxidized polymer film for the sample in Figure 5.3a) hence is likely to be reduced during the gold deposition. In contrast using an aqueous gold salt solution ($HAuCl_4$) allowed to deposit gold on the polymer films at more positive potentials, the polymer film thus being in its oxidized state during the gold deposition (see Figure 5.3c).

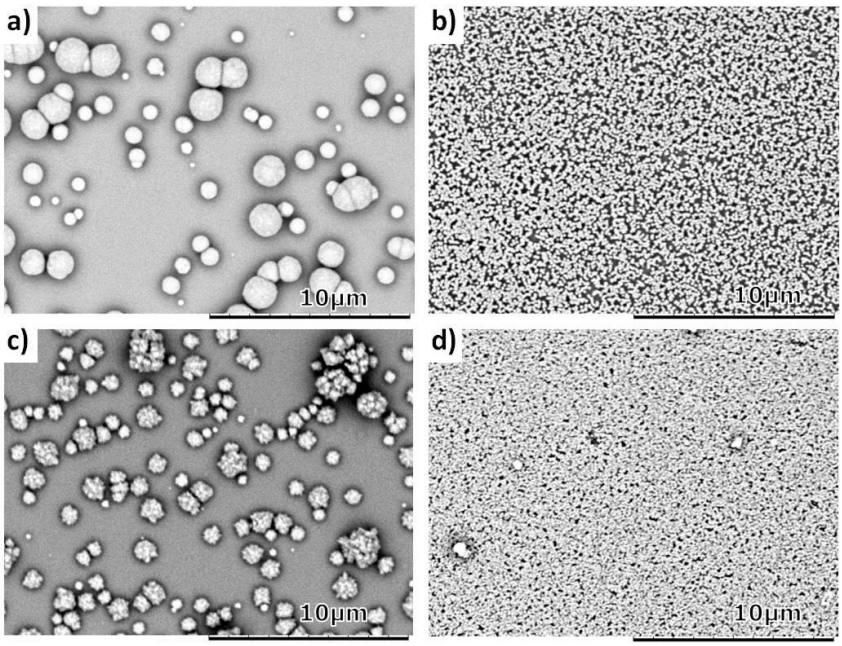

Figure 5.3: SEM top views of samples illustrating the influence of the oxidation state of PPy films (thickness: 100nm) on the morphology of the subsequent gold deposit. In a) and b) gold was deposited from the commercial gold plating solution ECF 60 at -700mV vs. Ag/AgCl, whereas in c) and d) a potential of +300mV was applied to reduce Au^{3+}-ions in a 10mM $HAuCl_4$-solution. In a) and c) the PPy film was in the oxidized, in b) and d) in the reduced state prior to the gold deposition. The same amount of gold (corresponding to a ~100nm-gold film in an even configuration) has been deposited on all samples by controlling the charge during the deposition.

Similar works dealing with the deposition of metals on conducting polymers pointed out the importance of the porous structure in the polymers on the resulting metal deposit.[341] It is likely that the metal ions reach the underlying metal electrode by diffusion where they are reduced.

Hence, a competition exists between the reduction of metal ions at the underlying electrode and the inner/outer surface of the polymer.[341] In reduced conducting polymer films, metal deposition is likely to start at the underlying metal electrode with a network of fine metallic wires growing through the microdefects in the polymer film. Reduction of metal ions on oxidized conducting polymers should preferentially occur at the surface of the polymer. However, as thin conducting polymer layers are often highly defective and ill reproducible in their microstructure, it is rather difficult to study the nucleation and growth processes of metals on these films.[341]

In order to achieve a smooth and uniform metal growth on the PPy films, we also tested galvanostatic and pulsed deposition methods, by varying the applied current density and the pulse duration under different potentials and current densities, respectively. A significant improvement of the metal film homogeneity, similar as for platinum deposition on PPy, however could not be attained. The rather rare examples where gold has been uniformly deposited on polypyrrole was obtained in anodized alumina templates to produce Au-PPy-Au nanowires.[342-344] The confined volume which is available for the growth of material in the template here may lead to a quicker coalescence of individual nucleation spots compared with a deposition on planar PPy films. Thus, we electrodeposited a multilayer structure of gold and PPy into the void space of a colloidal template.

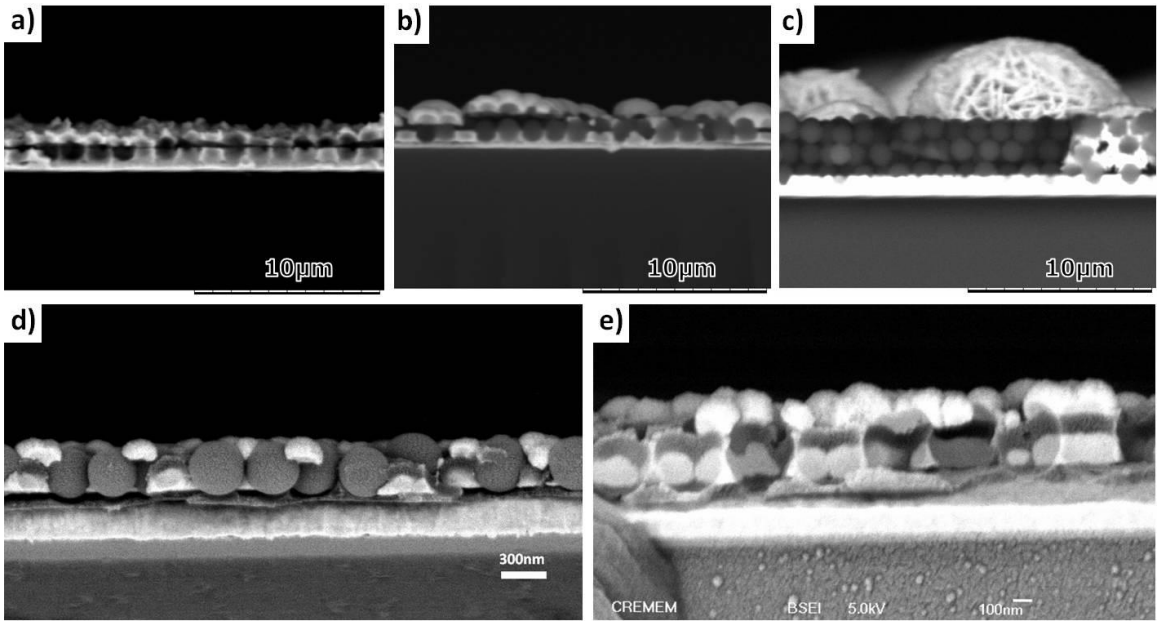

Figure 5.4: SEM cross section views of colloidal (monolayer-) templates after alternating deposition of gold and PPy. In a) - c) a thin PPy layer (about 80-100nm) has been deposited on top of the gold film (deposited from ECF 60 plating bath) which filled half of the 600nm-sphere template. The subsequent gold deposit was carried out from a) 10mM $HAUCl_4$ at +0,3V b) first from 10mM $HAUCl_4$ at +0.3V and then from ECF 60 at -0,7V and c) Oromerse gold plating bath at -0,5V. In d) four alternating layers of PPy and gold were deposited in a 395nm-monolayer template. Gold was deposited at -0,7V in ECF 60 plating solution on the previously reduced PPy films. The same sample is shown in e) after the removal of the silica template.

In Figure 5.4a) to c) SEM cross section views of colloidal templates filled with a primary gold (slightly less than a half-layer filling level), subsequent PPy (~80-100nm thick) and a top gold layer are shown. Different electrolyte solutions and applied potentials were used to deposit the top gold layer on the oxidized PPy films. Using commercial gold plating solutions (see Figure 5.4b and c) resulted in non-coherent metal films of inhomogeneous thickness. More coherent film growth was observed when aqueous gold salt solutions were used (see Figure 5.4a). However, the surface roughness of the deposits was considerably higher in this case. Four alternating layers, each bout 100nm thick, of PPy and gold were deposited into the colloidal monolayer shown in Figure 5.4d). In Figure 5.4e) the same sample is shown after removal of the silica template in hydrofluoric acid. The individual gold and polymer layers are clearly separated and can be well distinguished in SEM images due to the difference in electrical conductivity. Although we showed that it is possible to produce such thin multilayer structures of gold and PPy in colloidal templates, the film quality was not sufficient to allow an extensive study of their optical properties.

Therefore we focused on the deposition of alternating metal layers in colloidal templates which was meant to lead to the growth of more homogeneous film layers combined with a better control and reproducibility of the structure.

5.2 Electrodeposition of metal multilayers

In the past, electrodeposition already proved to be a well-suited technique to generate metal multilayer films.[345-349] In order to electrodeposit multilayered films, either single-[346, 348, 349] or double-bath[345, 347] methods can be employed. In the single-bath method the electrolyte contains the salt of all metals that are deposited. The most noble metal is deposited at the least negative potential whereas the less noble metal is co-deposited with the more noble one.[348] The composition of the mixed metal phase can be altered by changing the ratio of the metal salts in the electrolyte or the conditions during the electrodeposition. The benefit of this technique is related to its simple setup. In the double-bath method the electrodeposition of each metal is carried out in separate electrolyte solutions (see previous chapter). This offers the advantage that homogeneous films of pure metals with a sharp interface between the individual layers can be obtained.[347] Using either of these methods allowed to produce a range of different multilayered metal films including Co/Pt,[345] CoPt/Cu,[347] Fe/Pt,[349] CoCu/Cu[348] and Ag/Sb[346]. The thickness of the individual layers can be controlled by the charge applied in the different deposition steps. Layers of only a few nanometer thickness could be successfully deposited forming multilayer structures.[345]

In our experiments two separate plating solutions were employed to deposit Au/Ni multilayers in a colloidal template. We used potentiostatic electrodeposition with the same applied potentials and plating solutions as previously described in chapters 3.2.1 and 3.2.2. The experimental setup for the electrodeposition of gold and nickel multilayers was similar to that shown in Figure 3.7, the deposition alternately occurring in one of the two plating solutions. Among different possible metal combinations we chose gold and nickel, as none of the two metals was oxidized at the different deposition potentials (-0.66V and -0.93V for gold and nickel, respectively) and the electrodeposited films proved to be smooth and homogeneous (see chapters 3.2.1 and 3.2.2). Furthermore nickel is chemically less stable than gold, which allows selective dissolution of the nickel phase in aqueous sulfuric or nitric acid solutions. The schematic representation of the fabrication steps is shown in Figure 5.5. The process is similar to the one shown earlier in Figure 5.1. After the multilayer deposition, however, either the colloidal template or the nickel phase could selectively be dissolved leading to materials of different composition and hence different optical properties.

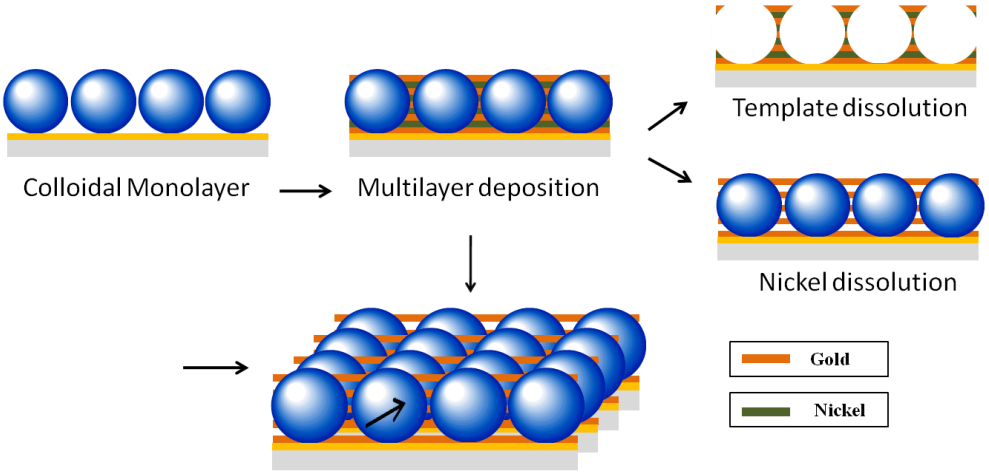

Figure 5.5: Schematic representation of the deposition of gold and nickel multilayers in a colloidal monolayer template. After the deposition either the template or the nickel phase can be dissolved leading to materials with different optical properties. In the bottom figure the material is illustrated after the dissolution of nickel showing a 3-dim varying refractive index.

By depositing only a single or two alternations in a colloidal template we first verified the feasibility of generating multilayer structures of gold and nickel using electrodeposition. Figure 5.6 shows the chronoamperometric curves for the successive deposition of a (Au/Ni/Au) structure in a colloidal template. As described in chapter 3.2.1, current oscillations were observed during the amperometric deposition in colloidal templates due to a periodic variation of the electroactive area. The same phenomenon is in principle observed in Figure 5.6, with one oscillation being divided into distinct parts. When gold grows into the void space of the first half-layer in the

template, the available electroactive area is reduced and the absolute current value consequently decreases (for t > 100s). In the subsequent nickel deposition, we observed first decreasing (t > 50s) and then increasing (t > 200s) values of the absolute current passing through a local maximum in the plot. The nickel growth front hence passed the centre line of the first sphere layer in the template. In the last gold deposition the absolute current continued to increase. Adding up these three deposition curves equals a full oscillation indicating that one sphere monolayer in the template has been filled with the (Au-Ni-Au) deposit.

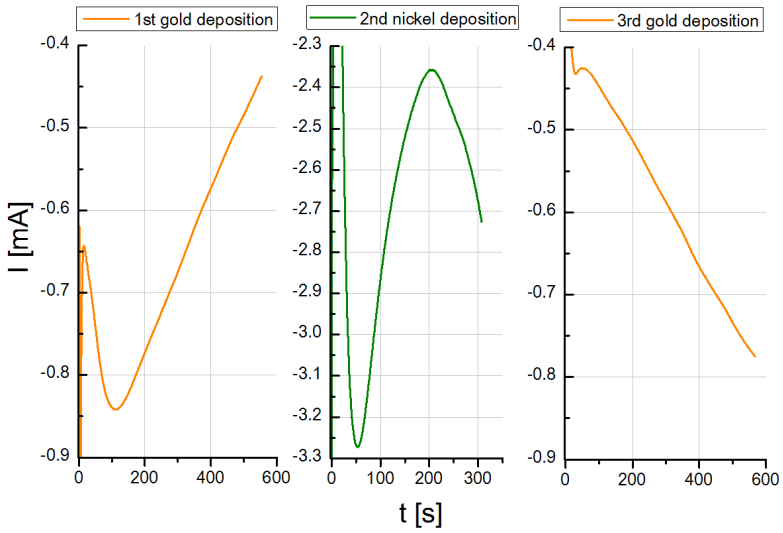

Figure 5.6: Chronoamperometic curves of 1) gold (*left*), 2) nickel (*middle*) and 3) gold (*right*) deposition in a colloidal monolayer template (sphere size 1200nm). The potential applied during the gold and the nickel deposition was fixed at -0.66V and -0,93V, respectively.

To verify this, we broke the sample after the deposition of the multilayer structure and examined its cross section in the SEM. As can be seen in Figure 5.7c), three successive layers of gold, nickel and gold exactly filled the void space of one sphere layer. Due to the higher conductivity of gold compared to nickel, the former is brighter in the SEM images and can be clearly distinguished from the nickel layers. The interface between successive layers is found to be remarkably smooth and uniform over the entire sample area. Figure 5.7a) shows a sample with the first half-layer of the template filled with nickel and the second one with gold. Similar current oscillations allowed to control the filling level in each deposited metal layer. Owing to its lower chemical stability compared to gold, nickel can be selectively dissolved in aqueous nitric or sulfuric acid solutions. Figure 5.7b) and d) show a cross section view of the same samples as illustrated in Figure 5.7a) and c), respectively, however after the nickel dissolution. In Figure 5.7b) the remaining gold layer in the silica template is stable and does not collapse even after the complete dissolution of the

underlying nickel layer. In Figure 5.7d) the distance between the remaining gold layers is found slightly increased in certain areas.

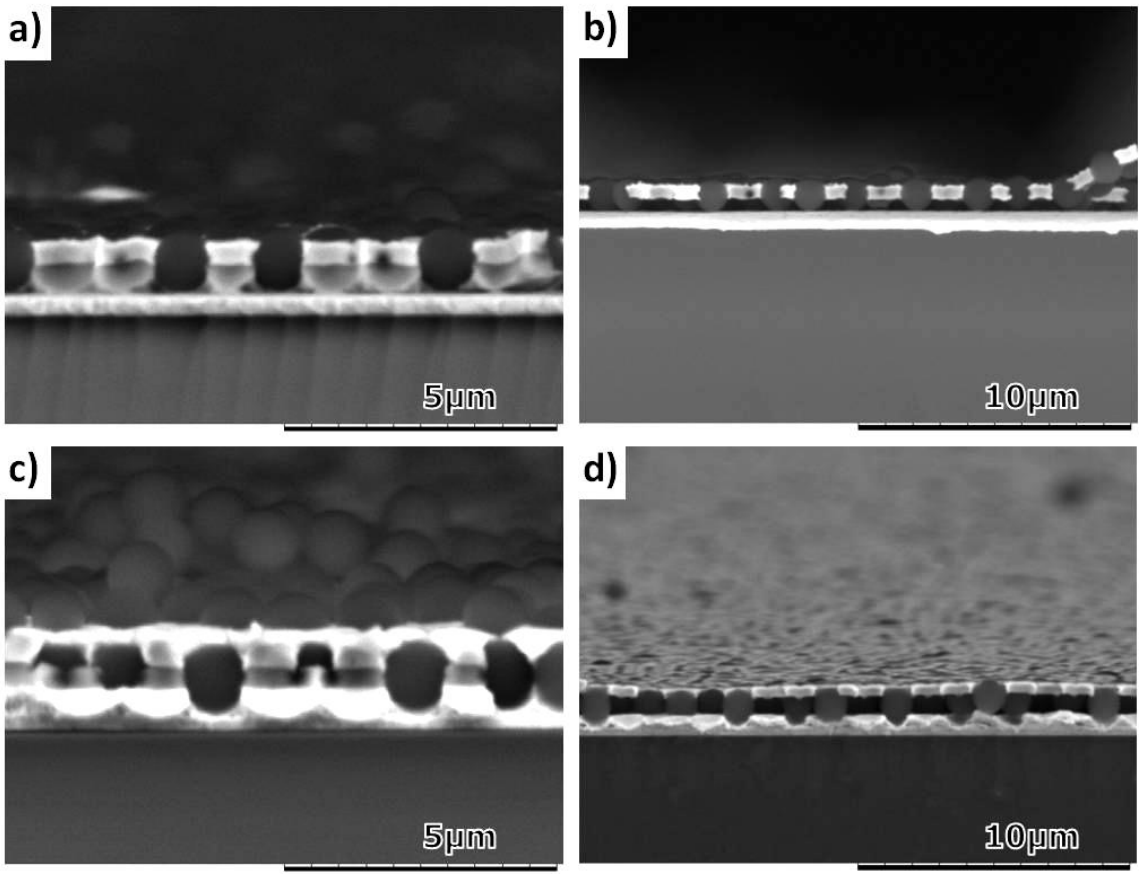

Figure 5.7 Cross section SEM views of samples obtained by gold and nickel electrodeposition into a colloidal templates (sphere size: 1200nm). a) Nickel-gold deposit in the template. b) Sample shown in a) after dissolution of the nickel layer in nitric acid (13%). c) Gold-nickel-gold deposit (sample corresponding to the chronoamperometric curves shown in Figure 5.6). d) as c) but after the nickel dissolution.

Next, we deposited a multilayer structure with a higher number of alternations in a colloidal monolayer by reducing the thickness of each layer. This could be attained by reducing the electrodeposition time for a single layer. Figure 5.8 schematically shows the cross section of a colloidal monolayer template filled with 14 alternating layers of nickel and gold allowing to illustrate the sample which has been produced. The different layers were deposited by stopping the electrodeposition manually after a certain, not constant time. The chronoamperometric curves for some of the deposited layers are plotted in Figure 5.9a) and Figure 5.9b) for the nickel and gold depositions, respectively. In both cases the curves were observed to shift in successive layer depositions towards lower absolute reduction currents until reaching the 10th layer in the template. From the 10th to the 14th layer, the reduction currents increased again towards higher absolute values.

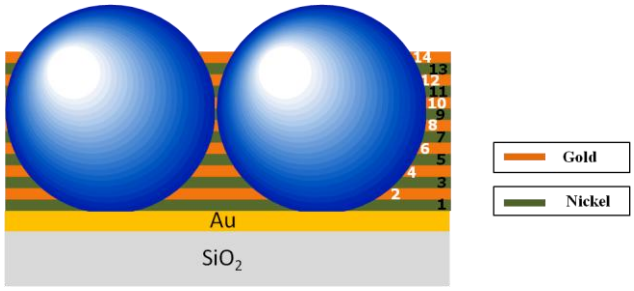

Figure 5.8: Scheme of a multilayer structure containing a total of 14 alternations of nickel and gold layers deposited in a colloidal template monolayer.

As seen in the 2D illustration of the sample in Figure 5.8, the electroactive area between neighboring spheres is constantly reduced until a half-layer filling level is reached, in the present case this point was reached during the deposition of the 10th layer in the template. In subsequently deposited layers, the electroactive area, and hence the reduction current increases again.

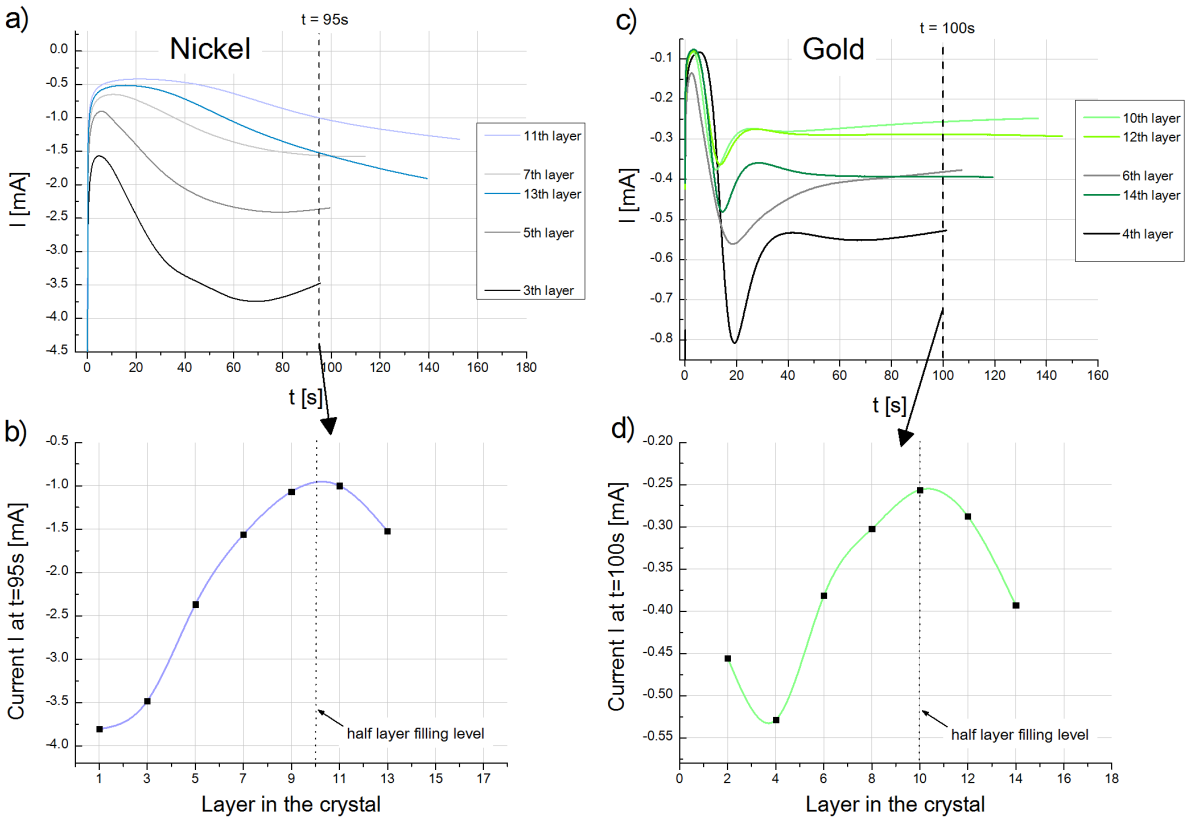

Figure 5.9 a) and b): Selected chronoamperometric curves of the 14 alternating layers of a) nickel and c) gold, deposited in a colloidal monolayer template (sphere size: 1200nm). The absolute current values are found to decrease up to the 10th layer in the crystal (half-layer filling level!) and increase afterwards for the remaining layers. b) and d) show a plot of the current at fixed deposition times ((b) t = 95s for nickel and (d) t = 100s for the gold deposition curves) as a function of the number of the deposited layer in the crystal.

This finding is also well illustrated by plotting the reduction currents (at a fixed time, t= 95 and 100s for nickel and gold deposits, respectively) as a function of the number of the layer deposited in the colloidal template, shown in Figure 5.9b) and d) for nickel and gold, respectively. In both figures the same trend is visible confirming the previously described findings. In fact, in each of the figures we obtain a part of an oscillation providing information about the filling level in the template.

SEM cross section views of the corresponding sample with 14 alternating nickel and gold layers deposited in a 1200nm-sphere template are shown in Figure 5.10a) - d) either directly after the electrodeposition (a), after the dissolution of the silica template (b and c) or after the dissolution of the nickel layers (d). Both, the thickness of the whole deposit and of the individual layers are very uniform throughout the entire sample.

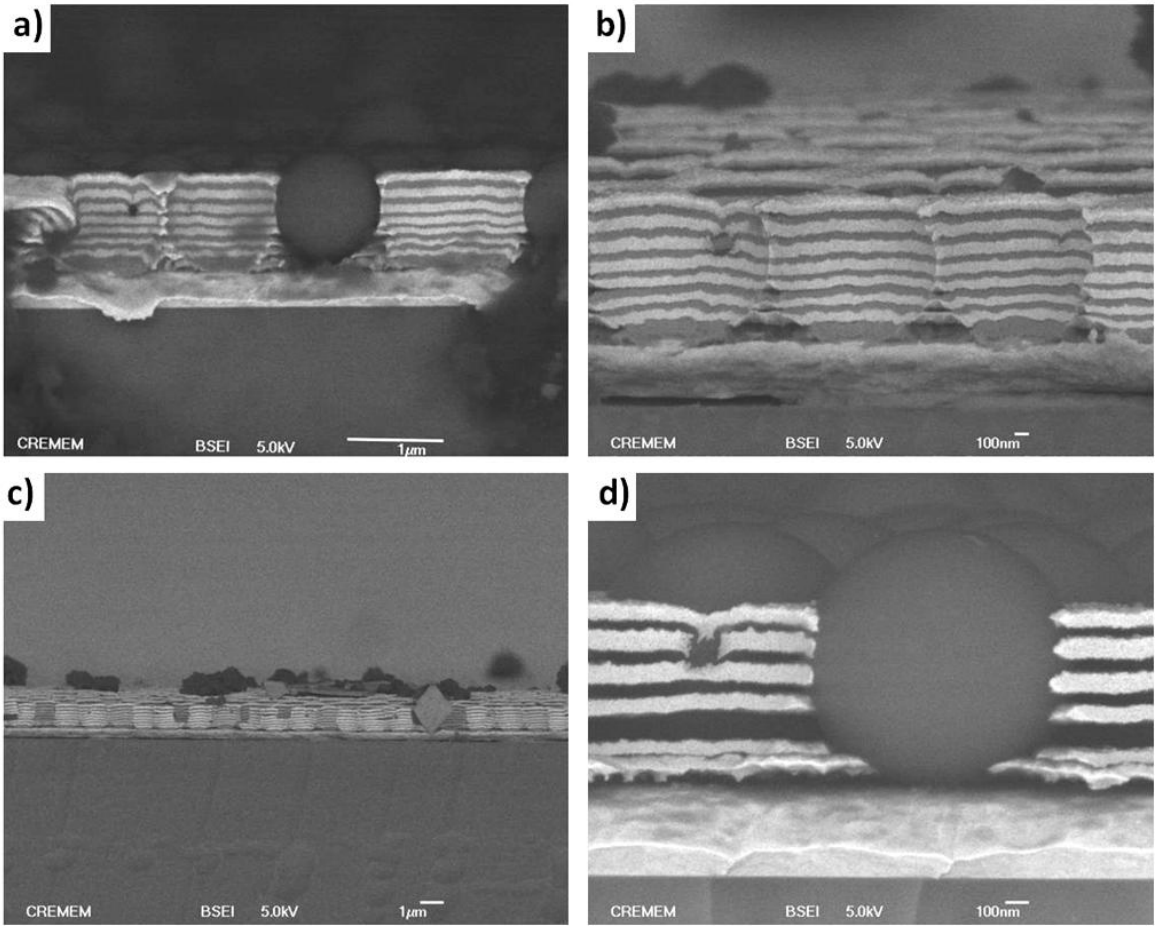

Figure 5.10: SEM cross section views of a) 14 alternating nickel-gold film layers deposited up to a height of about 1µm in a colloidal monolayer (sphere diameter: 1200nm). b) and c): the same sample as shown in a) after the dissolution of the silica template at different magnifications. d) the same sample as in a) after the dissolution of nickel in nitric acid solution (13%).

Owing to the varying deposition times, the thickness of the individual layers slightly varies (e.g. compare the 4th and 10th gold layer). In Figure 5.10b) the curvature in the multilayer metal film

produced by the colloidal template is visible. At spots, where the spheres in the original template were in contact, no metal deposition occurred thus leaving air voids in the film after the template dissolution. These voids are located exactly in the half-layer plane of the template. The void in Figure 5.10b) is centered in the 10th deposited layer, hence supporting the prediction made on the basis of the results shown in Figure 5.9a) - d). As metal growth was inhibited at these spots, the metal layers on top are found slightly bent down, providing evidence for the growth front proceeding in a not completely homogenous way during the infiltration of the colloidal template. When dissolving the nickel in the multilayer structure (see Figure 5.10d), thin gold layers tend to stick together (2nd and 4th gold layer), whereas thicker ones (8th to 14th gold layer) stay well separated preserving their original configuration.

An impression of the 3-dimensional structure of certain samples is given in Figure 5.11. In Figure 5.11a) a multilayer structure composed of 6 alternating Au-Ni layers is shown. Parts of the multilayer film were detached from the surface of the sample allowing to characterize its structure from below. In some spots the multilayer structure is hidden by remaining spheres, whereas it is clearly visible in other parts where the spheres had vanished. In this case the spheres were not in a close packed arrangement prior to the infiltration.

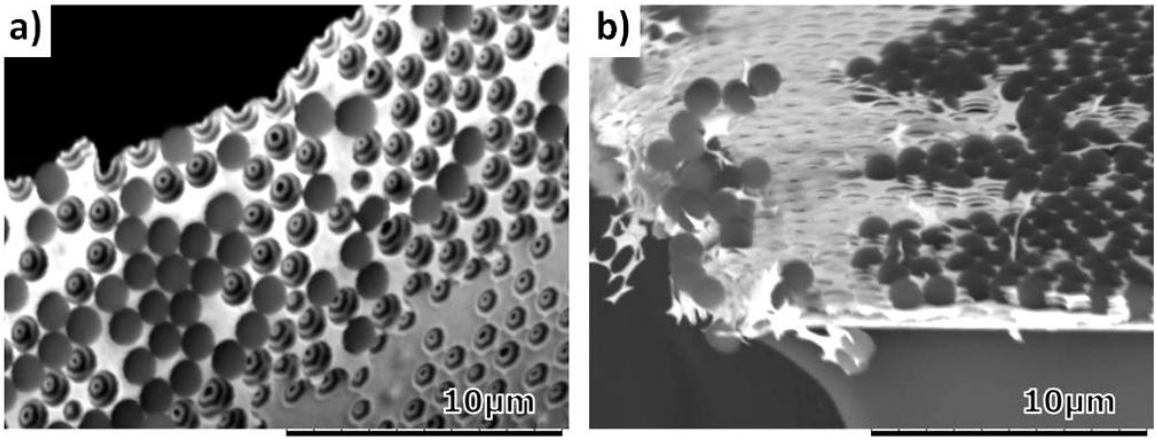

Figure 5.11 a) SEM view from below of a part of a Au/Ni multilayer film with 6 alternating layers. In certain areas the sphere template remained in the film, in others it had vanished. b) The same sample as shown in Figure 5.10d) at the edge of the sample.

Figure 5.11b) provides a view of the border of the sample previously shown in Figure 5.10d). By taking a close look, one can see the different gold layers which are stacked onto one another separated by air. Evidently, without spheres the gold films lack the mechanical stability as seen in the left part of the image. But seemingly, the gold layers are well organized and separated from each other at the interface where the sphere template is still existent.

In order to evaluate the possibility to deposit an even higher number of alternating metal layers in a monolayer sphere template, we further reduced the thickness of the individual gold and nickel layers by reducing the electrodeposition time for each layer. Additionally, we chose a nearly constant deposition time in order to grow gold (t = 54 ± 1s) and nickel layers (t = 60 ± 1s, exception: 1st layer) in the template. In this way 42 alternating layers of nickel and gold were deposited into the void space of a 1200nm-sphere template.

Similarly as shown in Figure 5.9a) and c), chronoamperometric curves for the deposition of selected nickel and gold layers in the template are presented in Figure 5.12a) and c), respectively. The same trend as before is observed showing first a decrease of the absolute reduction currents until the growth front reaches a half-layer filling level in the template (from the 3rd to the 25th and the 2nd to the 24th deposited layer for nickel and gold, respectively), while the deposition of subsequent layers leads to increasing absolute values of the current.

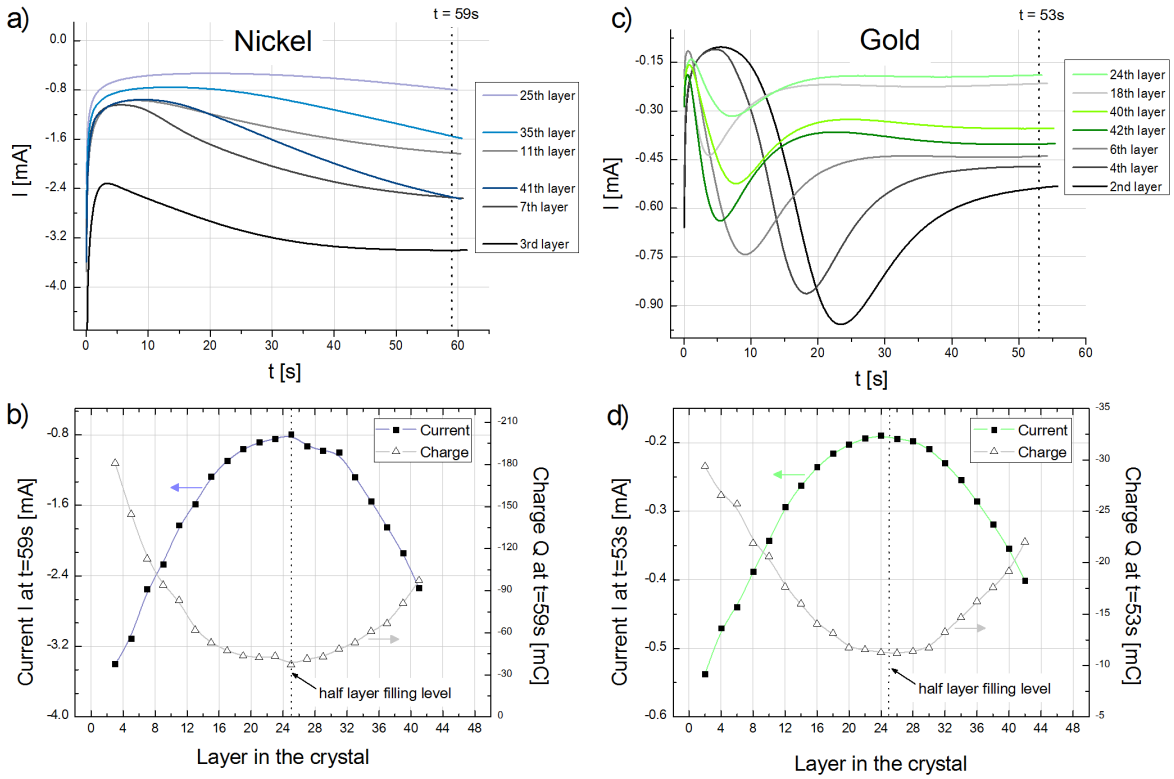

Figure 5.12 a) and b): Selected chronoamperometric curves of the 42 alternating layers of a) nickel and c) gold deposited in a colloidal monolayer template (sphere size: 1200nm). The absolute current values are found to decrease up to the 25th layer in the crystal (half-layer filling level!) and increase afterwards for the remaining layers. b) and d) show a plot of the current and the charge passed at fixed deposition times ((b) t = 59s for nickel and (d) t = 53s for the gold deposition curves) as a function of the different deposited layers in the crystal.

By plotting again the reduction current at a fixed time (t = 53s for gold and t = 59s for nickel layers) as a function of the deposited layer, this trend is confirmed and a well defined "current

oscillation" is obtained for both, nickel and gold layer deposits. The charge consumed during the deposition of the different metal layers is also represented in both figures and shows the same trend. In the present case the half-layer filling of the template is reached for the 25th deposited layer, being located at the minimum of both, the absolute current and the applied charge. These results suggest that the deposition occurs uniformly in the template over the entire sample area.
SEM cross section images of the sample containing 42 alternating layers are illustrated in Figure 5.13a) - d). Figure 5.13a) - c) show the sample after the electrodeposition at different resolutions while in Figure 5.13d) the nickel in the multilayer structure has been dissolved.

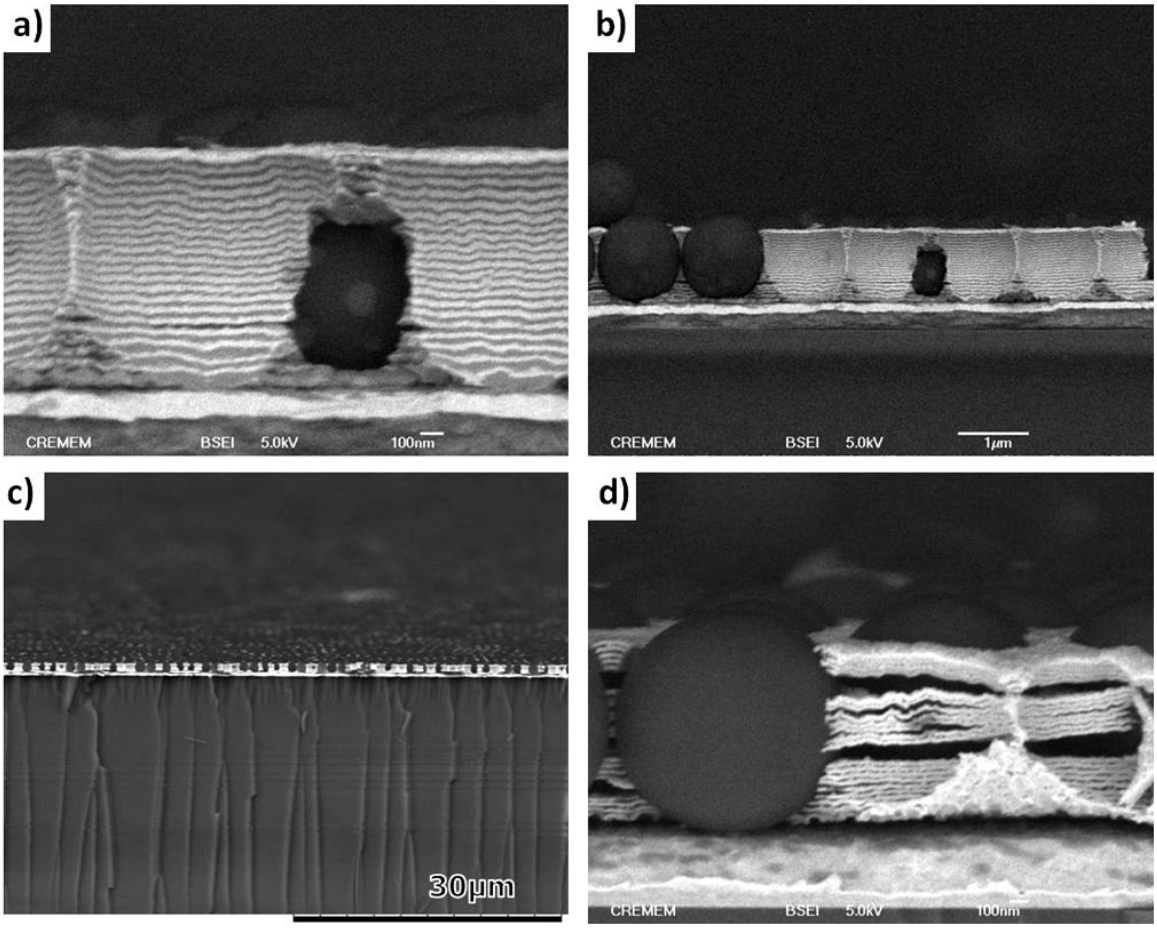

Figure 5.13 a) - c): SEM cross section views of 42 alternating nickel-gold layers deposited up to a height of about 1050nm in a colloidal monolayer (sphere diameter: 1200nm) at different magnifications. d) The same sample as in (a - c) after the dissolution of nickel in nitric acid solution (13%).

The template was infiltrated with the multilayer film up to a height of about 1050nm leading to a thickness of 25nm for the individual layers supposing that all layers have the same thickness. The SEM images suggest that the gold layers are slightly thicker compared to the nickel layers. A remarkable flatness and uniformity is found for both, the individual layers and the entire multilayer film at the different scales. Owing to the constant deposition time, layers of the same

metal all have the same thickness (except for the first nickel layer where the electrodeposition time was longer). The reduced thickness of the individual layers is found to result in a considerable loss of stability in the structure when the nickel intermediate layers are dissolved in acidic solution. In Figure 5.13d) individual layers are found to stick together building distinct gold multilayer blocks in the sample. Although only the cross section of the films could be examined by SEM, it is likely that the configuration of individual gold layers was also changed in other areas of the sample when nickel was dissolved in the multilayer structure.

Despite the promising results shown so far, certain points still may be optimized in order to improve the structural quality of the final material. First of all, a perfectly organized monolayer of spheres is crucial to reduce the losses due to structural inhomogeneity in the material during optical measurements. As shown in Figure 5.11a) the sphere monolayer produced by LB was not in a close-packed arrangement in certain samples. On the other hand, the electrodeposition into close-packed templates leads to pores which are interconnected by air voids, thus preventing the complete separation of solid and air phases in the inverse structure. However, in metamaterial design (e.g. the double-fishnet structure) the solid phase is completely separated from the air phase. Hence, organized non-close packed sphere assemblies might be an alternative template for the electrodeposition of multilayers.[350] Lower packing densities in 2D colloidal films can be obtained by liquid- [178] or plasma-etching techniques[351] or methods based on controlled pyrolysis.[352] Using prestructured substrates in the LB technique also enabled to fabricate non-close packed sphere monolayers by adjusting the compression of the Langmuir-films.[353] Finally, the selective dissolution of nickel was carried out in acidic solution. It may also be possible to remove the nickel by exposing the sample to a gaseous, acidic atmosphere, probably resulting in smaller structural changes during the removal of intermediate nickel layers.
In the following section an optical characterization of certain of the fabricated samples is performed using reflectance spectroscopy.

5.3 Optical characterization of metal multilayer samples

Reflectance spectroscopy was employed to record optical spectra of the samples shown in Figure 5.10 a) - d) based on 14 alternating gold and nickel layers deposited in one sphere monolayer. Experiments were carried out using a 20/20 PV^{TM} UV-visible-NIR microspectrophotometer from CRAIC Technologies operating at normal incidence in the 250-1700nm range. The experimental spectra recorded in the 250-1700nm range were then compared to simulated ones, calculated in

the 400-8000 nm range, according to a finite-difference time-domain (FDTD) method. We assumed a fcc arrangement of monodisperse spheres that has been filled with alternating gold and nickel layers, each having a thickness of 75nm (see further details in chapter 9.1.3.1). The results of the experimental and the calculated spectra are compared in Figure 5.14 for three different samples containing either all components (a), all except the silica template (b) or all but the nickel layers (c). The intensity of the calculated spectra has been reduced by a factor two in order to enable a better comparison with the experimental results.

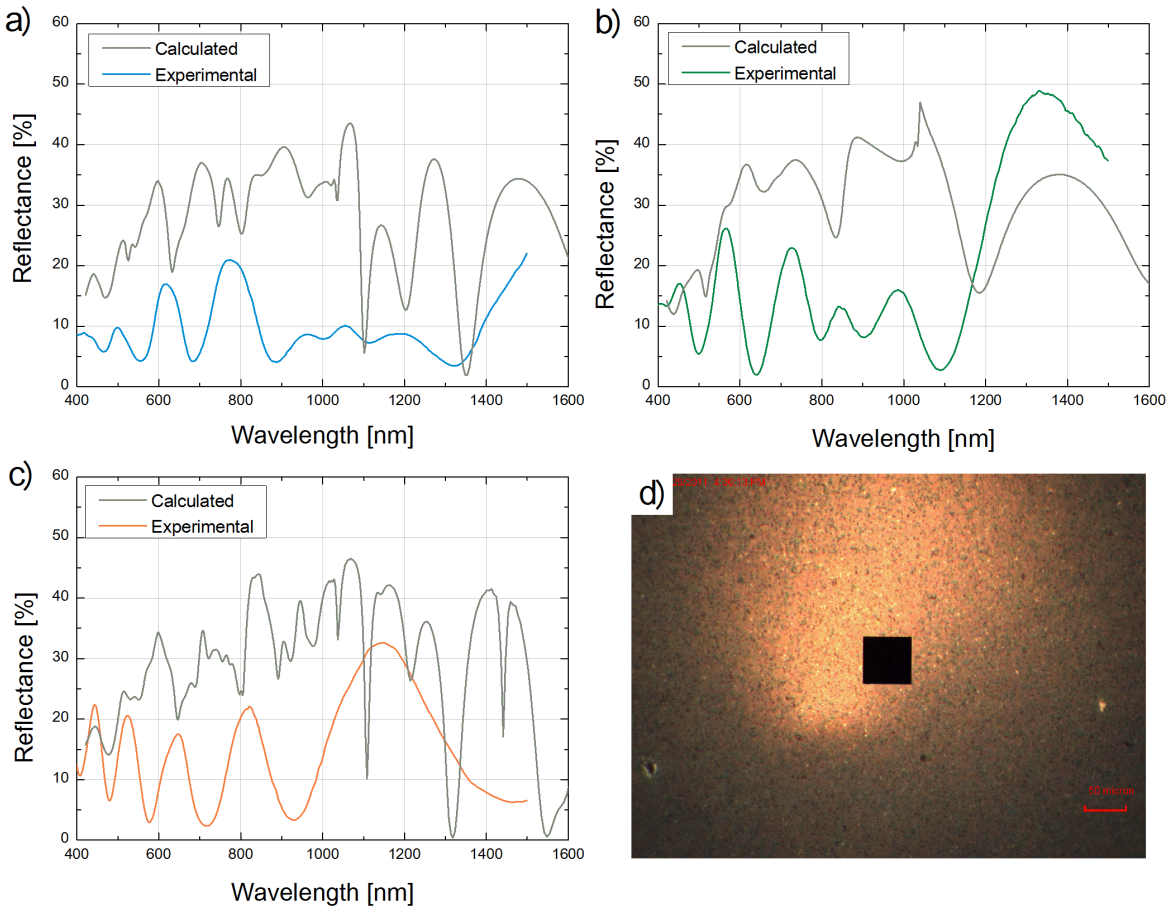

Figure 5.14: Experimental compared to calculated reflectance spectra for samples based on 14 alternating (Au/Ni) layers (theoretical thickness: 75nm) deposited in a 1200nm-silica sphere monolayer. Spectra for a) the sample after the electrodeposition composed of silica spheres and metal multilayer structure (see Figure 5.10a). b) the sample without the colloidal template (Au/Ni-multilayers with air voids, see Figure 5.10b and c). c) the sample without the intermediate nickel layers (Au/Air-multilayers with silica spheres, see Figure 5.10d). d) Optical view of the sample employed for the recording of the spectrum shown in c) without nickel. The black square indicates the measurement zone. Five spectra were recorded at different spots in the samples (a - c) by representing their mean value in the plots.

For the interpretation of the results it has to be considered that the spectra were calculated for an ideal sample with fcc sphere packing and a constant layer thickness of 75nm for each multilayer film differing from the real configuration in the fabricated samples. Nevertheless, a quite good agreement between measured and calculated spectra is obtained.

In Figure 5.14a) a fairly good correlation between both spectra is visible for wavelengths below 1100nm. Double peaks in the calculated spectrum may be expressed by a broad single peak in the experimental curve (e.g. at ~700 and 770nm - *calculated* and ~780nm -*experimental*). The peaks lying between 1100 and 1350nm are not observed in the experimental spectrum. The best match between the experimental and the calculated spectra was obtained for samples where the silica template has been replaced by air. In Figure 5.14b) all peaks in the calculated are also resolved in the experimental spectrum, shifted towards smaller wavelengths. In this case the recorded intensity of the reflectance also was higher compared to the sample containing silica spheres which is attributed to a reduced absorption of light in the material. The last example compares experimental and calculated spectra for the sample where the intermediate nickel layers have been dissolved in the multilayer structure. Probably owing to the structural changes occurring in the remaining gold layers during the nickel dissolution the least agreement between both, calculated and measured spectra is observed for this case. By changing different parameters (sphere size, number and thickness of individual layers, filling level of the template...) in the fabrication of these multilayer samples, the influence of each parameter on the evolution of the optical spectra can be assessed. This should allow to tailor materials with optical properties depending on the nanostructuration of its components.

6 Catalytically active macroporous microelectrodes with cylindrical geometry

Improving the performances of electrochemical devices for applications ranging from analysis to catalysis and energy conversion has become one of the most important issues of research during the last years.[6, 354] In this field, controlling the architecture of an electrode in order to achieve a higher accessibility or a better mass transport, as well as obtaining larger active areas, are development strategies of high interest for example for analytical [10] or optoelectronic applications.[355] As described in chapter 3.4, macroporous electrodes showed superior performance compared to their non porous homologues for different applications in fields including analysis, catalysis and energy storage or conversion. In electroanalysis, they outperformed smooth electrodes offering improved sensitivity towards the detection of different biomolecules[217, 241, 315-319] or heavy metal ions.[227, 228] Higher catalytic activities for hydrogen peroxide reduction,[217] NADH,[216] methanol or ethanol oxidation[356] equally were reported when macroporous instead of flat electrodes were used.

However, the application of these devices is limited due to their macroscopic size and planar geometry. Therefore, a huge application potential still remains for this type of materials, assuming they can be prepared with a smaller overall size. Miniaturized systems might indeed be really useful for some applications like in vivo measurements, biofuel cells,[357] and more generally, all devices where confined media with a limited accessibility are involved.[358] In this field, cylindrical structures may be very convenient to use and they already proved to be of high interest for analytical purposes,[359] despite the difficulty of the theoretical aspects since equations for diffusion cannot be solved analytically for a cylindrical geometry, unlike for planar or spherical ones.[360] Gold, platinum or carbon fiber microelectrodes have for instance been used successfully for detection of mercury and copper ions by anodic stripping voltammetry. [361-364]

In porous cylindrical microwires, which can be produced by colloidal crystal templating, small overall dimensions are combined with high active electrode areas. However, very surprisingly, there are very few reports in the literature dealing with the elaboration of colloidal templates with a nonplanar geometry. In these works, templates were obtained either by sedimentation of latex or silica dispersions in glass capillaries and poly(methyl methacrylate) (PMMA) or Kapton tubes,[365-367] dip-coating onto glass fibers,[368] or electrophoretic deposition onto carbon fibers[369] and were then infiltrated to obtain porous polymeric[365-368] or metal replicas.[369] We used a different strategy allowing to control both, the thickness of the colloidal template and the infiltration of the latter using electrodeposition with a very high accuracy. A scheme illustrating

the different steps involved in the fabrication of macroporous gold cylinders is shown in Figure 6.1.

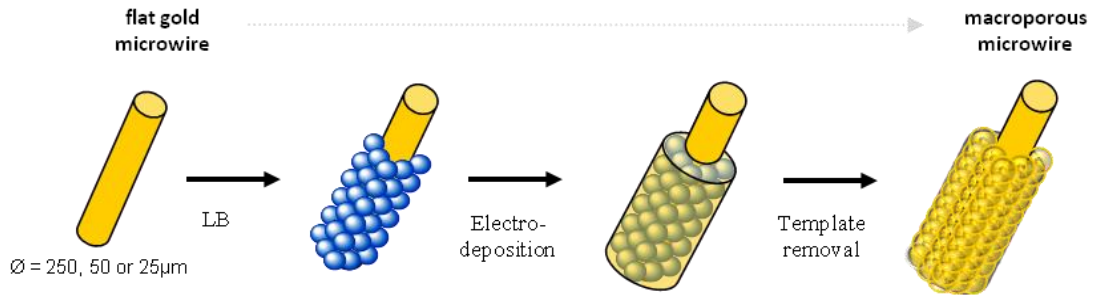

Figure 6.1 Schematic representation of the fabrication steps involved in the generation of macroporous gold microelecetrodes with cylindrical geometry.

Gold microwires of three different diameters ranging from 25 to 250µm served as substrates for the deposition of silica colloidal crystals. The desired number of sphere monolayers could be transferred onto the wires by using the LB technique (see chapter 6.1). Similar as for electrodes with a planar geometry, the filling ratio of the colloidal template with gold or polypyrrole could be precisely controlled during the potentiostatic electrodeposition due to the oscillating current response. After the removal of the inorganic template the macroporous wires were characterized by SEM imaging (see chapter 6.2). Additionally, the active surface area of the macroporous gold wires was determined electrochemically (see chapter 6.3) and their usefulness towards the catalytic reduction of oxygen was examined (see chapter 6.4). Finally, a strategy is presented how miniaturized electrochemical cells could be fabricated in a single device using colloidal crystal templating (see chapter 6.5).

6.1 Fabrication of colloidal crystal templates on gold wires

Synthetic 2D or 3D colloidal crystals of silica particles obtained through the LB technique have mainly been considered, if not exclusively, on planar glass substrates. This is due to the interest in the optical properties of the opal films being readily studied in UV-vis spectroscopic measurements on transparent glass substrates. The transfer of silica Langmuir films on clean hydrophilic glass slides occurs readily and further treatment of the substrates is not required. Similarly, as we have shown in chapter 4.1, reflectance spectroscopy can be used to characterize colloidal crystals assembled on glass slides covered with a thin gold layer. As mentioned in chapter 2.2.3, a transfer of silica Langmuir films occurs on sufficiently hydrophilic substrates building up a meniscus at the water-substrate interface during the upstroke. The successful

transfer of Langmuir films consequently is not restricted to a planar substrate geometry. In this work, for the first time cylindrical LB films with silica particles in the micrometer size range were synthesized. To achieve this, commercial gold wires were first cut in small pieces with a length between 25 and 30 mm and, after a fast cleaning treatment, were used as substrates for the LB deposition. A home-made Langmuir trough (see Figure 6.2b) with two mobile barriers and a maximum interface area of 1000cm^2 was successfully used to form Langmuir films of silica particles with various diameters (see details in the experimental section 9.1.4.1). As shown in Figure 6.2a), the gold wires were fixed to a glass substrate which then was attached to the dipping mechanism (see Figure 6.2b). Fast immersion followed by slow withdrawing cycles allowed to transfer silica sphere monolayers onto the cylindrical gold wires up to a desired number N of deposited layers.

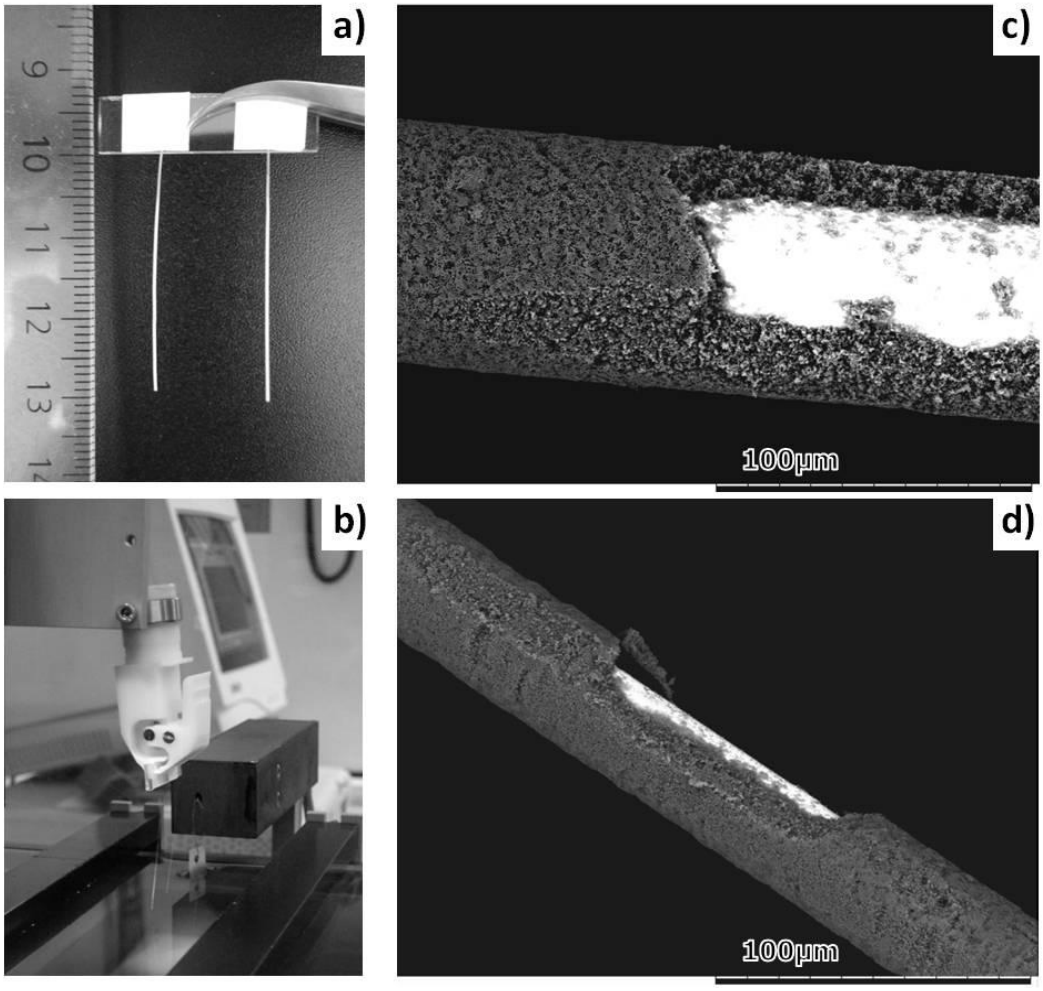

Figure 6.2: Photographs of a) cylindrical gold wires (diameter 250µm) after the deposition of 50 layers of 420nm silica particles. b) the home-made Langmuir trough with two mobile barriers, a pre-cut paper as Wilhelmy plate for surface pressure measurement, and a dipping system. On this picture, the dipper holds two pieces (3cm-long) of a 50µm gold wire as substrates. c) and d): SEM images of LB films deposited onto gold wires of different diameters with (c) 25 layers of 690nm-silica particles onto a 50µm-wire. (d) 25 layers of 420nm-silica particles onto a 25µm-wire.

As illustrated in Figure 6.2c) and d), SEM side view pictures of the so-formed LB films show that the colloidal stacking is regular over very large distances, whatever the diameter of the wire. In order to better illustrate its thickness, a small portion of the template has been removed in these pictures. The cylindrical gold substrate is clearly visible (it appears in white due to its high conductivity) and the thickness of the homogeneous LB film can be measured quite precisely. Due to the small dimensions and the cylindrical geometry of the samples reflectance spectroscopy here was not an adequate technique to measure the thickness of the colloidal template. The experimental value for the thickness of the template retrieved from SEM observations can then be compared with the theoretical one given by the equation 2.8, assuming a compact stacking of the monolayers:

$$e = \left[1 + (N-1) \cdot \sqrt{\frac{2}{3}}\right] \cdot d \quad (2.8)$$

with d being the diameter of the silica particles, N the number of bead layers and e the total thickness of the template.[95] For the template pictured in Figure 6.2c), values of d = 0.69µm and N = 25 result in a theoretical thickness of e = 14.2µm. This is in excellent agreement with the thickness estimated from the SEM pictures whose mean value was found to be close to 14.1 µm. In other words, cylindrical colloidal assemblies with a regular thickness and a well-controlled architecture can be obtained by the LB technique with all the interesting features already mentioned before for planar geometries in this work.

6.2 Electrodeposition of metals and conducting polymers

The gold wires coated with silica colloidal crystal films were then used in a second step as working electrodes in a conventional three-electrode electrochemical cell, illustrated in Figure 6.3. Contrary to the setup employed for the electrodeposition onto planar samples (see Figure 3.7) a cylindrical platinum mesh served as counter electrode in order to ensure that the whole cell has the working electrode as a symmetry axis. This enabled a homogeneous deposition with a uniform growth speed throughout the wire. In contrast, using planer CEs was found to lead to a preferential deposition on the side of the wire facing the CE. After a few seconds, to allow diffusion of the commercial gold plating solution into the silica deposit, the potentiostatic reduction of the gold sulphite ions, $AuSO_3^{2-}$, contained in the electrolytic bath was carried out at a potential of -660mV vs. Ag/AgCl. The intensity of the faradaic current was then measured as a function of time.

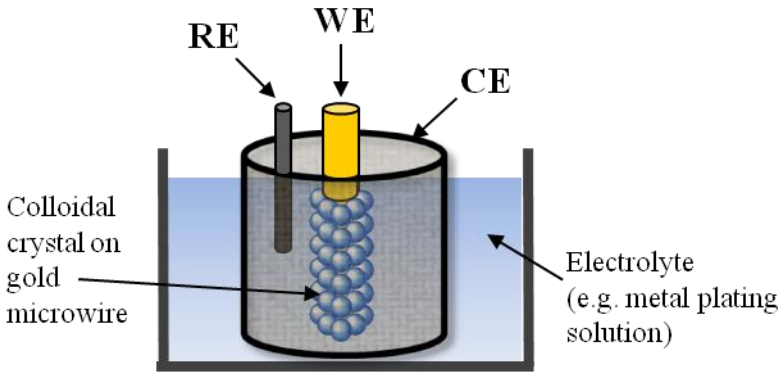

Figure 6.3: Experimental setup employed for the electrodeposition in colloidal templates on microwire electrodes. A cylindrical platinum mesh (CE) was placed symmetrically around the gold wire (WE) in order to ensure homogeneous film growth on the wire.

Similarly as shown for samples with planer geometries we were able to observe oscillating currents in the chronoamperometric curves during the infiltration of colloidal templates on gold wire electrodes. This can be attributed to a periodic variation of the active surface area of the growing gold deposit during the infiltration of the template voids. In Figure 6.4 the chronoamperometric curves for the deposition into templates composed of different sphere diameters on 50µm gold wires is shown.

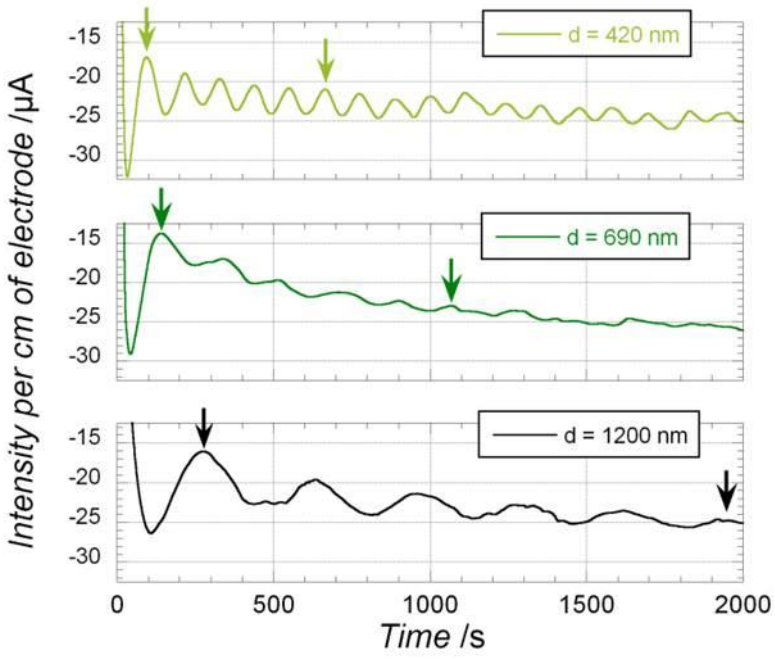

Figure 6.4: Chronoamperometric curves (E = -0,66V vs. Ag/AgCl) corresponding to the electrodeposition of gold within multilayered templates of silica particles with different diameters. Arrows indicate the positions of the first and sixth local maxima corresponding to the 1st and 11th half-layer. Diameter of the supporting gold wires: 50µm.

For the sake of comparison, intensity was normalized to an intensity per electrode length by dividing the experimental i(t) signal by the estimated depth of immersion of the wire in the gold plating bath (with an accuracy of ±1 mm). The current was found to oscillate more or less regularly around a mean value close to 23µA during the infiltration of the different templates. Such a result already suggests, without any other information, that the top surface of the growing structure is smooth and homogeneous and that the packing of the colloidal template is regular.
Therefore, each local maximum on this graph should correspond to a minimum of the surface area of the growing film, i.e. when the thickness of the gold deposit equals an uneven number of half-layers of particles. In a planar geometry, this would match the equatorial planes of each deposited layer of particles. Assuming a compact stacking and the corresponding geometric considerations, the distance a between two consecutives planes is given by equation 6.1:

$$a = \sqrt{\frac{2}{3}} \cdot d \quad (6.1)$$

where d is the diameter of the colloidal particles.

As seen on the plot, the deposition time Δt between the first equatorial plane (first half-layer of particles) and the sixth one (eleventh half-layer) is strongly depending on the size of the silica particles. Similar to the results shown in Figure 3.11a) a decrease in the oscillation frequency was found in templates with bigger spheres. From the peak positions, we can easily estimate for each particle size a mean growth speed <v> of the gold film in the colloidal crystal structure described by equation 6.2:

$$< v >= \frac{5.a}{\Delta t} = \frac{5.a}{t_{11/2} - t_{1/2}} \quad (6.2)$$

As summarized inTable 6.1, it seems that the particle size does not affect the growth speed of gold in the templating structure, which is rather constant and close to 3nm.s^{-1} in our experimental conditions. This result also suggests that the particle size has no incidence on the diffusion of gold sulphite ions and therefore does not affect the deposit growth mechanism. A parameter exhibiting strong influence on the growth speed of the metal deposit is the concentration of metal ions in the plating bath. Due to depletion of metal ions in the electrolyte, slower growth rates can be observed in the course of the electrodeposition experiments. However the total amount of deposited gold here was rather small with respect to the employed electrolyte volume, so that this effect was of minor importance for the deposition onto cylindrical microwires.

	d = 420 nm	d = 690 nm	d = 1200 nm
a (nm)	342.9	563.4	979.8
$t_{1/2}$ (s)	94.4	141.6	274.7
$t_{11/2}$ (s)	665.6	1068.0	1953.0
<v> ($nm.s^{-1}$)	3.00	3.04	2.92

Table 6.1: Calculation of the growth speed <v> of the gold deposit in colloidal templates composed of spheres with different diameters d.

We have also verified that it was possible to observe this periodic evolution of the faradaic current during longer periods of time, i.e. until the gold deposit reaches a large thickness. As it becomes clear from Figure 6.5, oscillations are visible up to at least 41 half-layers – thus corresponding to over 20 layers of particles – whatever the diameter of the gold wire. It is worth noticing that during the first minutes of the deposition, the current oscillates around a mean value of -22(±1)µA for the 50µm wire and -95(±5)µA for the 250µm wire. This result confirms that the electroactive surface is directly proportional to the geometrical surface of the bare substrate.

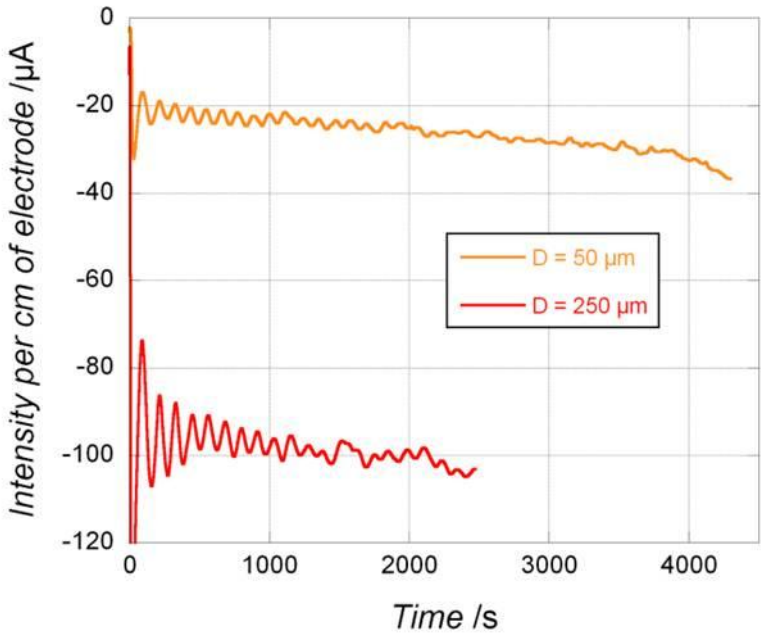

Figure 6.5: Chronoamperometric curves (E = -0,66V vs. Ag/AgCl) corresponding to the electrodeposition of gold within colloidal assemblies of 50 and 25 layers of 420nm-silica particles deposited onto gold wires of 50 and 250 µm, respectively.

Gold wires have been characterized directly after the electrodeposition process by cutting the cylindrical wires allowing to examine the cross section of the gold deposit in the colloidal

template by SEM imaging. In Figure 6.6a), the edge of a 250µm-gold wire used as an electrode with 25 layers of 690nm-silica particles as template is observed at low magnification. In this particular case, electrochemical deposition was carried out until the gold deposit became slightly thicker than the template. The surface of the electrode seems homogeneous at this scale without any porosity, but peeling off the porous layer and observing it at higher magnification reveals that there were exactly 25 layers of silica particles deposited onto the gold wire during the Langmuir-Blodgett deposition which are completely filled with gold (see Figure 6.6b). On the right side of this image, the bottom surface of the gold-silica layer (which was in direct contact with the wire) looks very smooth whereas on the left side, it appears that the thickness of the metallic deposit is, as expected, just a few hundreds of nanometers thicker than the original LB film.

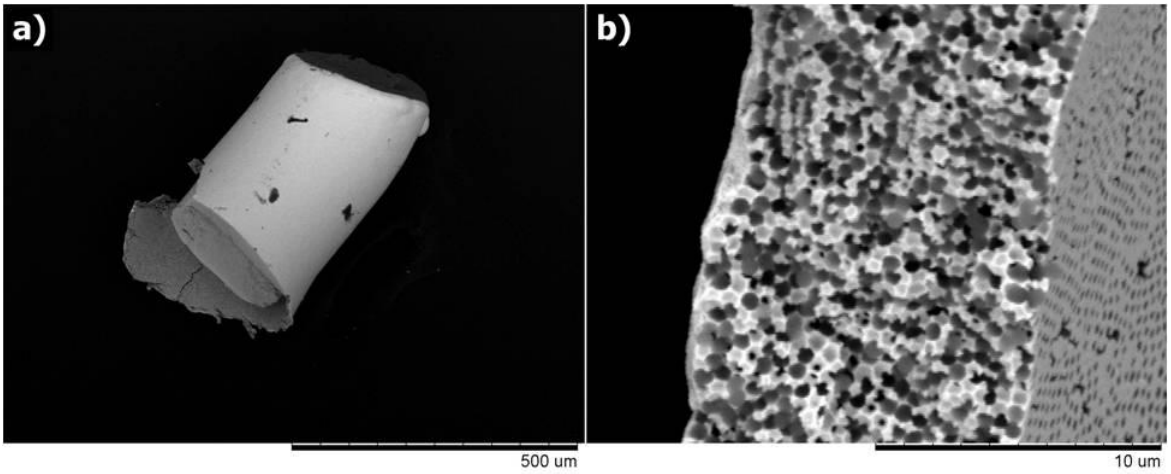

Figure 6.6 SEM pictures of a gold-filled colloidal crystal deposited onto a 250µm gold wire: a) Top view of the edge of the electrode; b) Side view of the gold-silica composite layer with 25 monolayers of 690nm-silica particles as template.

When the growth of the gold deposit was stopped before reaching the top surface of the template, removal of the silica particles was possible by infiltration of a dilute hydrofluoric acid solution. Under these conditions, SEM side views provide important information about the architecture of the electrodes. First, the homogeneity of the samples is particularly obvious over large distances, not only over half a millimeter as pictured in Figure 6.7a), but all along the wire electrode. This homogeneity suggests that there were no preferential pathways for the growth of the gold deposit in the silica template, which was containing few vacancies and was, most importantly, crack-free. At higher magnifications, as shown in the Figure 6.7 b) and c), the thickness of the electrodeposited layer can be measured easily and the original wire used as support is also clearly visible. For instance in Figure 6.7c), the thickness of the gold deposit is close to 19.1 µm. Taking d = 690nm, it can be calculated from equation 2.8 that the gold deposit reached the 34^{th} layer of particles within the 50-layers LB template.

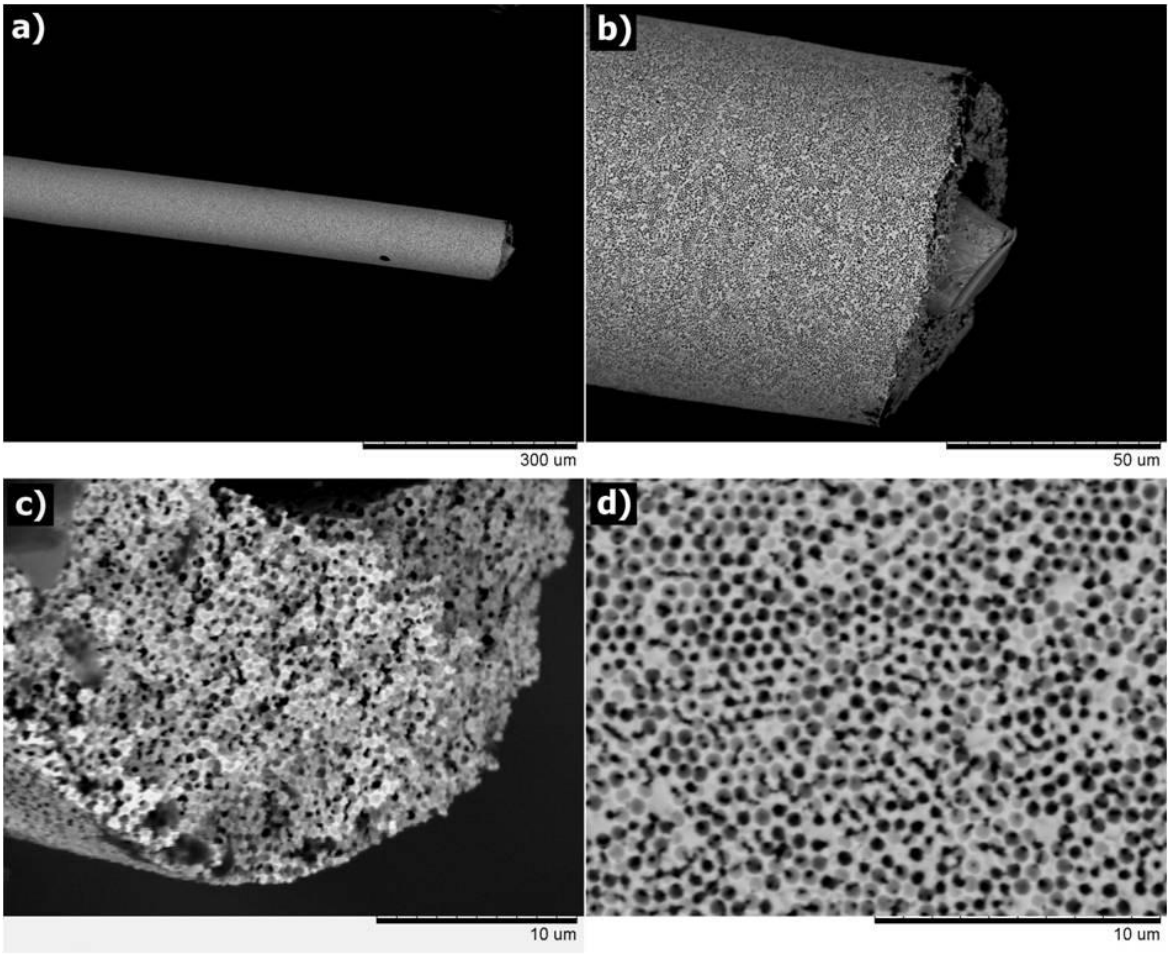

Figure 6.7 SEM pictures of a porous gold electrode based on a 50µm gold wire. The silica template consisted of 50 layers of 690nm-silica particles. a) and b): View of the macroporous wire at different magnifications. c) Cross section image of the macroporous film deposit. d) Surface of the macroporous gold wire.

Additional views such as pictured in Figure 6.7d) also provide good information about the morphology of the electrode surface where macroscopic pores organized in a reasonably compact arrangement –sometimes hexagonal – illustrate the quality of the original silica template. It is also obvious that pores of two consecutive layers are well-connected with each other.

Finally, taking advantage of the periodic current oscillations during the gold deposition, we have tested the possibility of controlling precisely the thickness of the porous structure. To do so, the electrochemical reaction was stopped as soon as the faradaic current reached values of the corresponding local maxima of the characteristic chronoamperometric curves. As illustrated by the SEM images of Figure 6.8, showing side views of the porous gold layer, this feature has also been verified successfully.

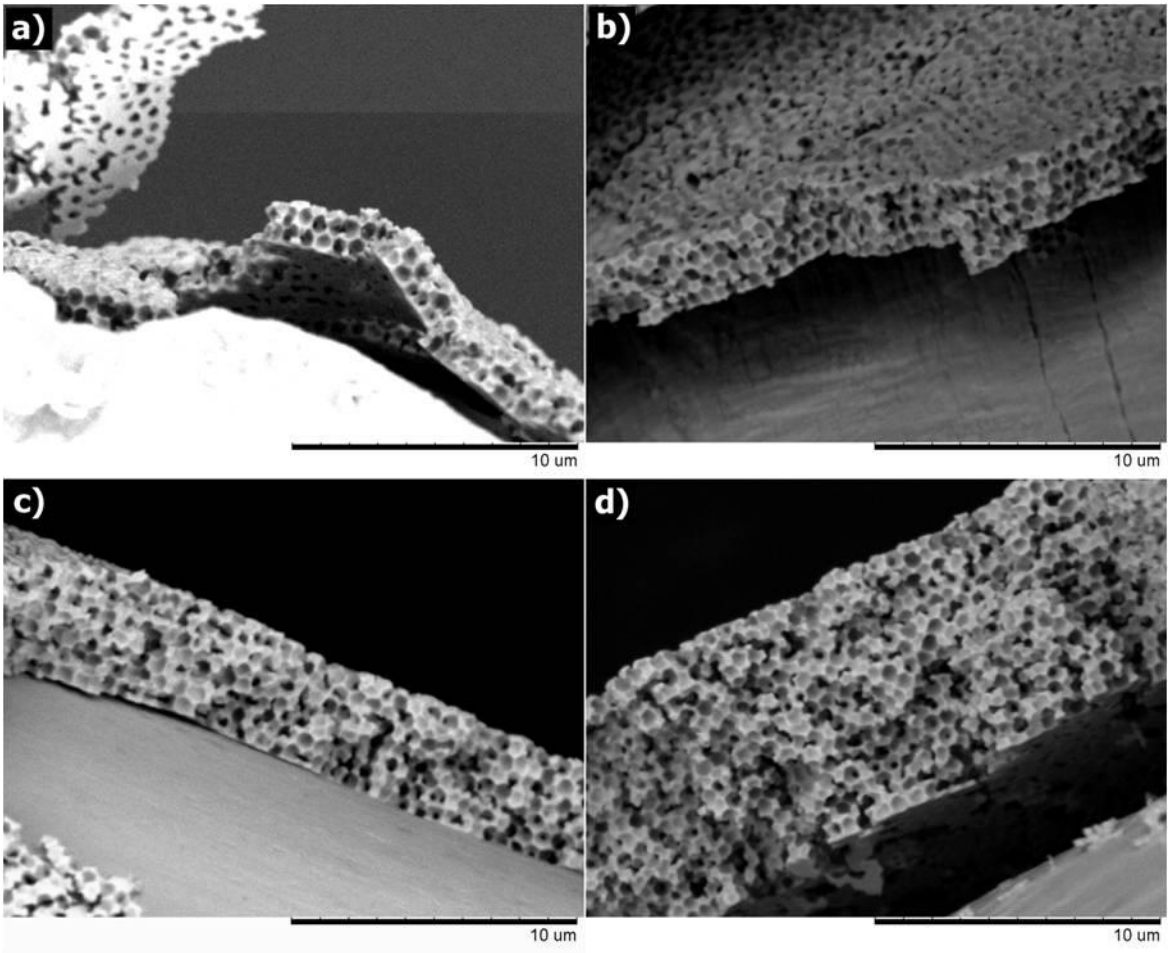

Figure 6.8 SEM pictures of porous gold deposits of various thicknesses on microwires after dissolution of the 690nm silica particle templates. Images show macroprorous gold films with a) 5, b) 9, c) 15 and d) 29 half-layers.

As pointed out earlier, besides gold, also a range of other materials can be electrodeposited, hence we infiltrated the void space of the colloidal template on the microwire electrodes also with polypyrrole.

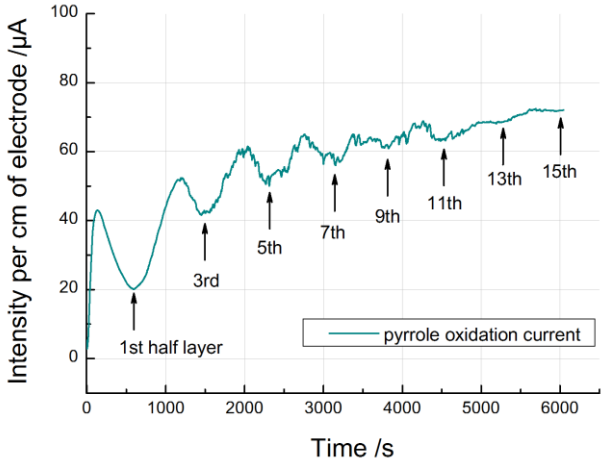

Figure 6.9: Chronoamperometric curve (E= 0,6V) for the polypyrrole deposition into a colloidal template composed of 10 layers of 1200nm-particles assembled on a 250µm-gold wire.

To do so, the same experimental setup as for the gold deposition was used, the electrolyte solution and the potential applied during electropolymerization of pyrrole were adopted from chapter 3.3.1. Figure 6.9 shows a chronoamperometric curve for the deposition of PPy on a 250µm gold wire coated with 10 layers of 1200nm silica spheres. Although the current oscillations observed during the infiltration of the template with PPy were less regular than shown earlier for the potentiostatic gold deposition, they still enabled to follow the progression of the PPy growth front in the template and so to control the final thickness of the deposit.

The characterization of the gold wires coated with macroporous PPy by SEM is shown in Figure 6.10. Cross-section views of a 50µm-gold fiber are provided in Figure 6.10 a) and b). Despite cutting the fiber using a scalpel the PPy film adhered well to the substrate showing a uniform thickness all around the gold fiber. Figure 6.10 c) and d) show a surface view of the PPy coated microwires at different magnifications. By taking a close look one can see that the voids in PPy are interconnected similarly to what was found in the macroporous gold film deposits.

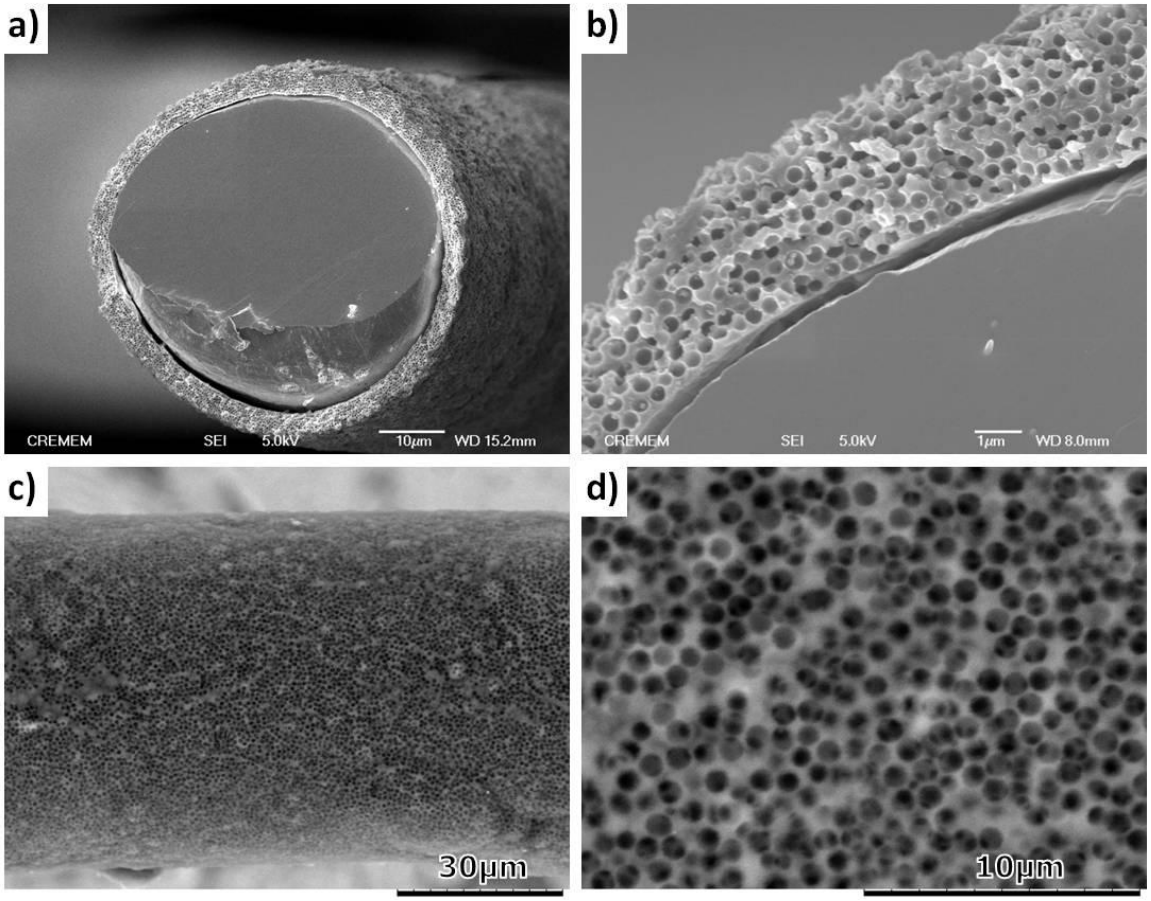

Figure 6.10 SEM characterization of macroporous PPy films on gold microwires (diameter: 50µm). a) and b): Cross section images of the gold wire with the maroporous PPy film (pore size 420nm) at different magnifications. c) View of the macroporous PPy film (pore size 1000nm) deposited on the cylindrical gold wire. d) As c) but with higher magnification.

As evidenced by the SEM pictures, we managed to synthesize macroporous gold and PPy microwires with a highly interconnected pore network. The latter is of special interest considering possible applications of these macroporous wires as miniaturized electrode materials in sensors and catalytic or energy-related devices. Thus in the following the active surface area of the gold microwires hence has been determined using electrochemical methods.

6.3 Electrochemical characterization of macroporous gold cylinders

Similarly to their planar homologues (see chapter 3.2.3), macroporous gold wires are likely to possess a much larger active surface area compared to the bare wire substrate. To confirm this statement, stripping of gold oxide using cyclic voltammetry has been carried out in an acidic medium using the porous structure as working electrode. Figure 6.11a) presents the cyclic voltammograms obtained with materials based on a 250µm-wire with porous layers of an identical pore size of 690nm but different thicknesses. These stripping curves are typical for a pure gold electrode with a gold oxidation between 1 and 1.5V (vs. Ag/AgCl) and a reduction peak, centered on around 0.8V, related to the gold oxide reduction. As shown in chapter 3.2.3, the area of this peak is directly proportional to the active surface of the macroporous gold electrodes. From a qualitative point of view, Figure 6.11a) already shows that the intensity of the oxidation and reduction processes increases with the porous layer thickness.

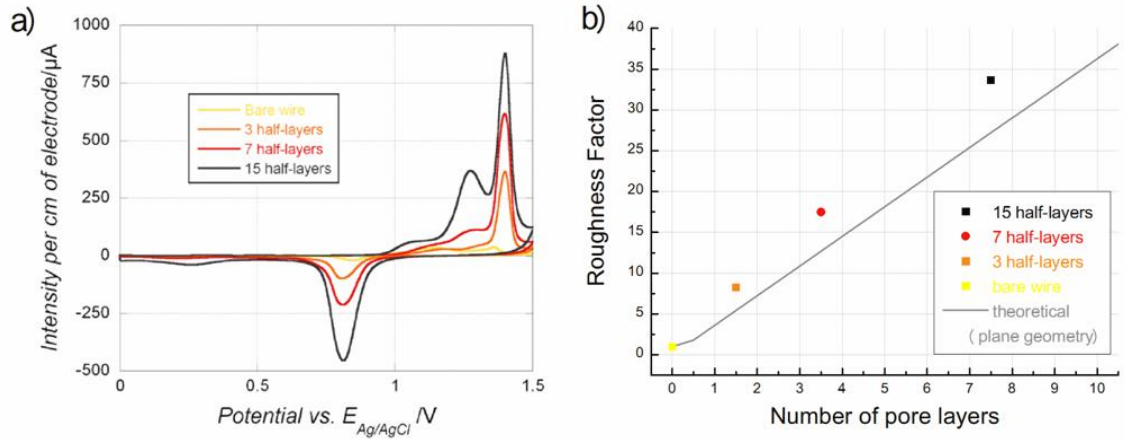

Figure 6.11: a) CV stripping curves obtained from macroporous gold structures of different thickness (pore size 690nm) on 250µm gold wires. A 0.05M H_2SO_4 aqueous solution together with a scan rate of 100 $mV.s^{-1}$ was employed. b) Evolution of the roughness factor as a function of the porous layer thickness for macroporous gold microwires.

As shown in chapter 3.2.3, we can calculate the electroactive surface area of macroporous gold samples from the charge associated to the gold oxide reduction peak in the CV, allowing us further to quantify the increase of the surface area by calculating the roughness factor for gold

microwires with different numbers of porous layers (see Figure 6.11b). Similar as for samples with plane geometry we observed a linear increase of the roughness factor with increasing number of pore layers on the gold wires. However, for a cylindrical substrate geometry, the experimental values are higher than theoretically expected for samples with a planar geometry. Due to the increase of the diameter of the wires with increasing number of porous layers, a greater number of pores (spheres) is present in successive layers, explaining the deviation of the experimental from the theoretical values.

6.4 Catalytic Applications of macroporous gold cylinders

In recent literature work, the ability of nanoporous and/or enzyme-modified gold electrodes to catalyse the reaction of species like oxygen[370] or glucose[217] has attracted much interest for their potential application in biofuel cells.[371, 372] We have therefore carried out experiments in order to estimate the potential usefulness of these macroporous structures as miniaturized electrochemical devices. Because the reduction of oxygen is of great importance as it usually determines the operating voltage and thereby the efficiency for example of fuel cells, it was chosen as a key test to estimate their utility. Figure 6.12a) presents the cyclic voltammograms recorded in an oxygen-saturated 0.05M sulfuric acid solution. In the chosen potential window, the only electrochemically active species is oxygen which is reduced to H_2O_2, which is further reduced to H_2O below -0.4V.

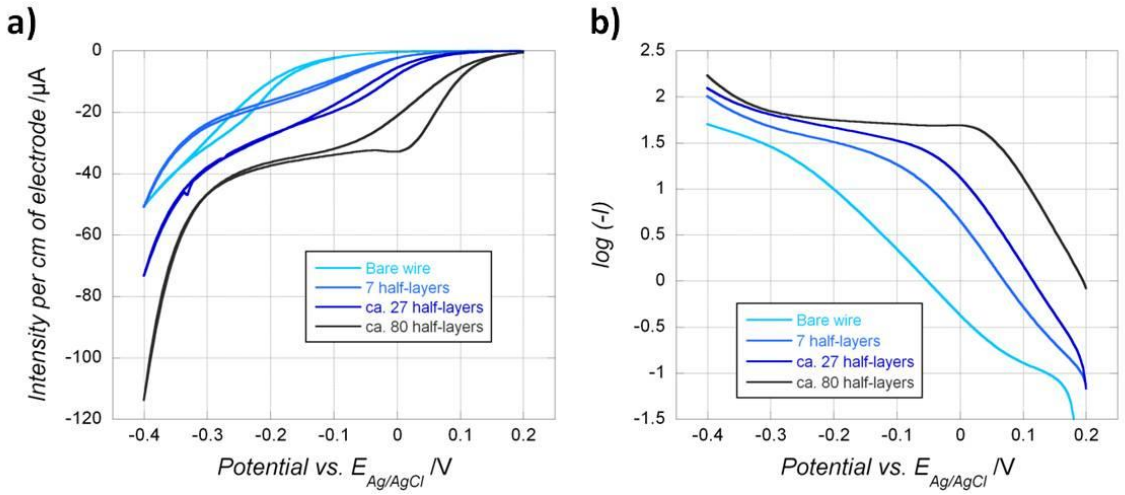

Figure 6.12: CVs obtained with macroporous gold structures of different thickness (pore size 1200nm) on 50µm gold wires. The electrodes are exposed to 0.05M H_2SO_4 aqueous solution saturated with oxygen (scan rate: 5 $mV.s^{-1}$) in order to check their electrocatalytic activity. b) Tafel plots obtained with the same electrodes.

When the porous gold layer gets thicker, the intensity of the O_2 reduction current becomes significantly higher, similarly to what has been previously observed for the reduction of hydrogen peroxide on macroporous planar electrodes.[217] However, an even more interesting feature is the evolution of the threshold for the O_2 reduction, defined as the potential at which the electroreduction of oxygen starts. The thicker the porous layer, the more positive is this characteristic potential value. Although we do not have so far a detailed explanation of the underlying mechanism of this observation we can conclude that the overpotential for oxygen reduction is significantly decreased by around 300mV when using thick porous electrodes instead of non-porous ones. From the Tafel representation in Figure 6.12b) we can furthermore deduce that the kinetics of the reaction, usually expressed by log i_0, is also drastically improved. The identical slopes of the three tested electrodes in the positive potential range indicate that the reaction mechanism (number of exchanged electrons, transfer coefficient) is not affected by the porosity. However the exchange current i_0 varies by more than one order of magnitude, which is in good agreement with the surface increase obtained from the gold oxide stripping curves. These two aspects, improved overpotentials and increased kinetics, are very encouraging with respect to exploring this type of electrodes as promising candidates for the oxygen reduction in fuel or biofuel cells. In the next section we will show how miniaturized electrochemical cells with independently addressable macroporous electrodes can be designed using colloidal crystal templating.

6.5 Two electrodes in one device

In miniaturized electrochemical systems the overall dimensions of a device depend on the size of the single components. For example, in batteries, a steel case generally is used to prevent corrosive or toxic components from leaking, dominating the size and limiting efficient miniaturisation of the device.[358] Another example are implantable biofuel cells, which may deliver the electrical power for small medical devices (e.g. glucose sensors) permanently remaining in the body. The subcutaneous interstitial fluid here serves as the electrolyte and thus no case is required. But in order to drive the electrochemical reaction still two independent electrodes, serving as the anode and the cathode, need to be available. The integration of two independently addressable electrodes in a single device would offer great potential for a further miniaturization of electrochemical cells, especially in fuel cells or batteries.[373] As schematically illustrated in Figure 6.13, colloidal crystal templating may be used to fabricate miniaturized electrochemical cells which are composed of two macroporous electrodes with a high active surface area. As already

introduced in chapter 5.2, our strategy is based on the alternating deposition of two different metals (gold and nickel) in a colloidal template.

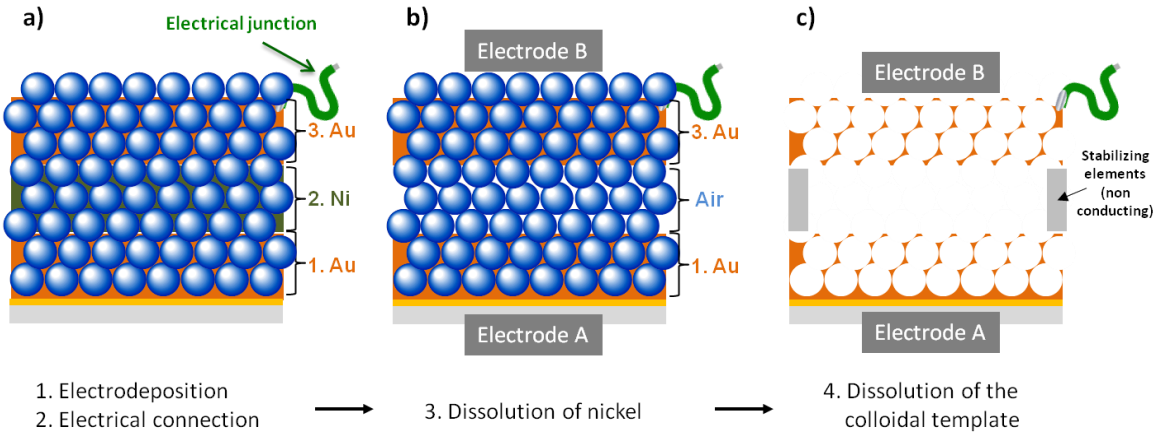

Figure 6.13 Scheme showing the different steps involved in the fabrication of an electrochemical cell composed of two independent macroporous electrodes A and B. The device is produced by a) alternating electrochemical deposition of gold and nickel in a colloidal template, b) followed by dissolution of the intermediate nickel layer c) and dissolution of the colloidal template after adding elements stabilizing the structure.

Using electrochemical deposition the void space of a colloidal template can be filled with a nickel layer "sandwiched" between two gold films (see Figure 6.13a). Prior to the selective dissolution of the nickel layer in acidic medium (nitric or sulfuric acid), an electric contact is established with the gold film situated at the top of the multilayer structure, allowing it to be electrically addressed. In Figure 6.13b) the intermediate nickel layer has been completely dissolved, resulting in two gold films embedded in a colloidal crystal which are separated only by colloidal spheres (and air). Here both gold films (Electrode A and B) already can be independently addressed and the required mechanical stability is provided by the colloidal template. With respect to a possible application of the cell (e.g. immobilization of different enzymes in the electrodes A and B for the use as a biofuel cell), macroporous instead of silica-gold composite electrodes would be preferable. This can be realized by dissolving the inorganic template in dilute hydrofluoric acid (see Figure 6.13c). Integrating isolating elements between the macroporous electrodes (e.g. infiltration of varnish at certain points of the sample) should prevent a collapse of the structure. Applying this concept to gold microwires hence would allow to build electrochemical cells which combine small overall dimensions and high electrode surface areas owing to their macroporous structure.

We first focused on a flat electrode design in order to validate the concept. Figure 6.14 shows three chronoamperometric curves obtained for the consecutive depositions of a gold, a nickel and the top gold layer into a colloidal template. The latter was composed of 20 sphere layers (diameter 600nm) which have been transferred on a planar gold coated glass slide by LB. As

shown in the different curves, we were able to observe current oscillations not only for the first gold deposition, but also during the second and third depositions of nickel and gold in the colloidal template, respectively. Such a result already indicates that for both, the gold and the nickel deposition, the respective growth front proceeds uniformly in a well organized colloidal template structure. It also enabled to perfectly control the thickness of each metal stack, allowing to choose independently the dimension of the bottom- and the top-layer electrode as well as their respective distance in the final cell. In the example shown in Figure 6.14, about five layers were infiltrated in the template for each metal stack corresponding to ~3µm thick films (the first gold film being slightly thicker). As for the potentiostatic deposition of a single material in the colloidal template, the amplitude of the oscillations decreases in the course of the infiltration (note the different current scales in the different plots).

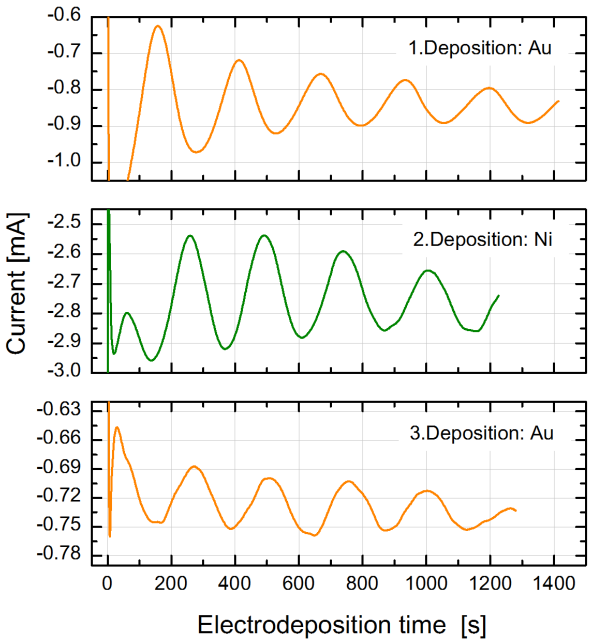

Figure 6.14: Chronoamperometric curves obtained for three alternating electrodeposition steps of 1) gold (*top,* E=-0.66V) nickel (*middle,* E=-0.93V) and 3) again gold (*bottom,* E=-0.66V) in the same colloidal template composed of 20 layers of 600nm-silica spheres. (A cross section of the template after the electrodeposition steps is shown in Figure 6.15a).

After electrodeposition, the sample was broken and its cross-section has been characterized using SEM. Figure 6.15a) demonstrates that the expected number of layers in the template has been filled with gold and nickel films. Similarly as seen in chapter 5.2, nickel is less conductive than gold allowing to discriminate both metals in the SEM images. As shown in Figure 6.14b), where the colloidal template has been removed by etching, the different metal stacks are extremely well defined and their thickness was uniform over the whole sample area covering almost 1cm^2. A

remarkably flat surface is found for macroporous metal layers at the interface between the individual stacks.

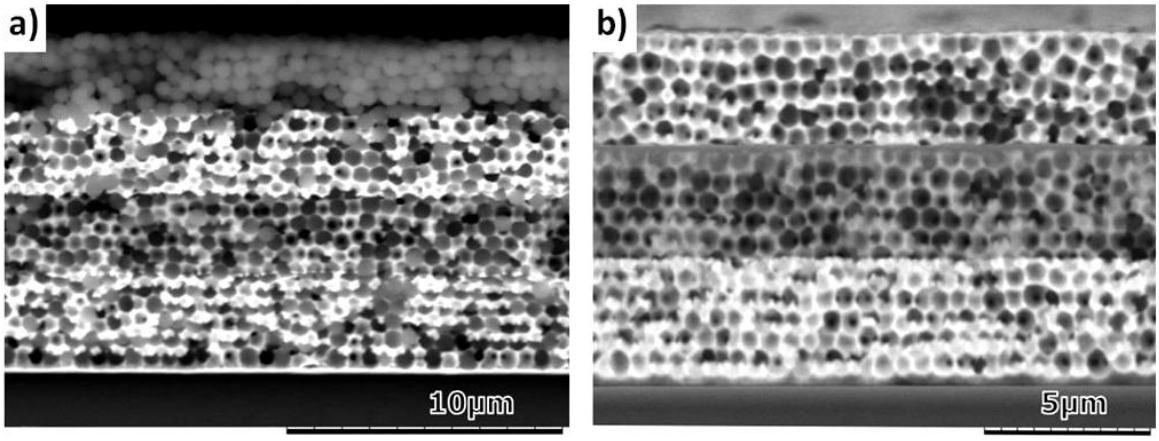

Figure 6.15: Cross-section SEM images of a) the colloidal template (20 layers, sphere size 600nm) filled with alternating deposits of gold, nickel and again gold. b) the same electrode as shown in a) after the removal of the silica template resulting in a macroporous hybrid material.

In the next step the intermediate nickel layer was dissolved in acidic solution. Therefore the sample shown in Figure 6.15b) was exposed to sulfuric acid solution (24%) and the progressive dissolution of the nickel layer was documented by SEM images that were taken after different immersion times in the acidic solution (see Figure 6.16). By comparing Figure 6.16a) and b), the nickel layer is found partly dissolved after 30 minutes in the solution. After seven hours (not shown here) nickel still was present but its porous structure had completely vanished. After a period of 19 hours in the etching solution, the nickel layer had been entirely dissolved so that a structure composed of two macroporous gold films separated by an air gap is obtained. In order to stabilize the structure, a thin line at the sides of the sample (all except the cross section) had been infiltrated with varnish before nickel dissolution. Despite this, the structure had collapsed in certain areas, which caused a short-circuit between both gold films, preventing it from being used as an electrochemical cell.

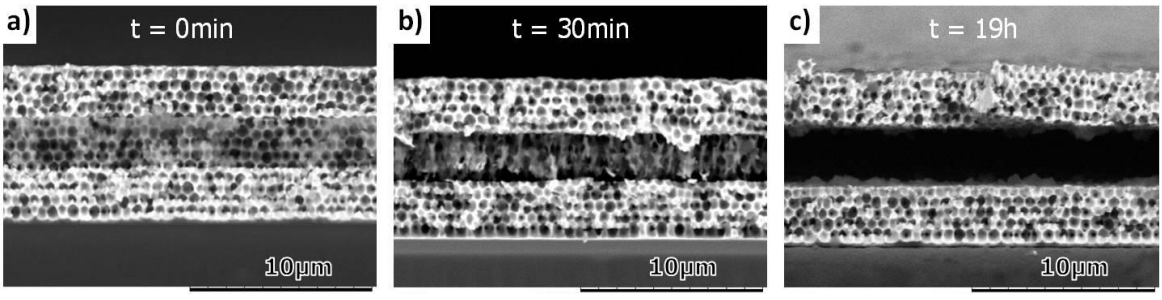

Figure 6.16: Time dependent dissolution of the intermediate nickel layer of the macroporous Au-Ni-Au electrode visualized by cross-section SEM images taken after different immersion periods in sulfuric acid solution (24%). a) before immersion. b) after 30 min in the etching solution. c) After 19 hours the nickel has been completely dissolved.

To circumvent this problem the colloidal template was left in the sample during the nickel dissolution allowing to further stabilize the structure (see Figure 6.13b). Figure 6.17a) shows the cross section of a sample with a (Au-Ni-Au) multilayer structure deposited in a colloidal template. In this case, we took advantage of the current oscillations to produce macroporous gold films with different thickness (3/2 for the bottom and 5 layers for the top gold film), which serve as top and bottom electrode in the final device. An electrical contact was established to the top gold film before dissolving the nickel layer by exposing the sample to acidic solution. As shown in Figure 6.17b) - d) the nickel had been completely dissolved and it was found that the two gold film electrodes were well separated over the whole length of the sample cross section (see Figure 6.17d). In some areas the colloidal template was still existent (Figure 6.17b) whereas in others, it had been eliminated by the solution (Figure 6.17c and d).

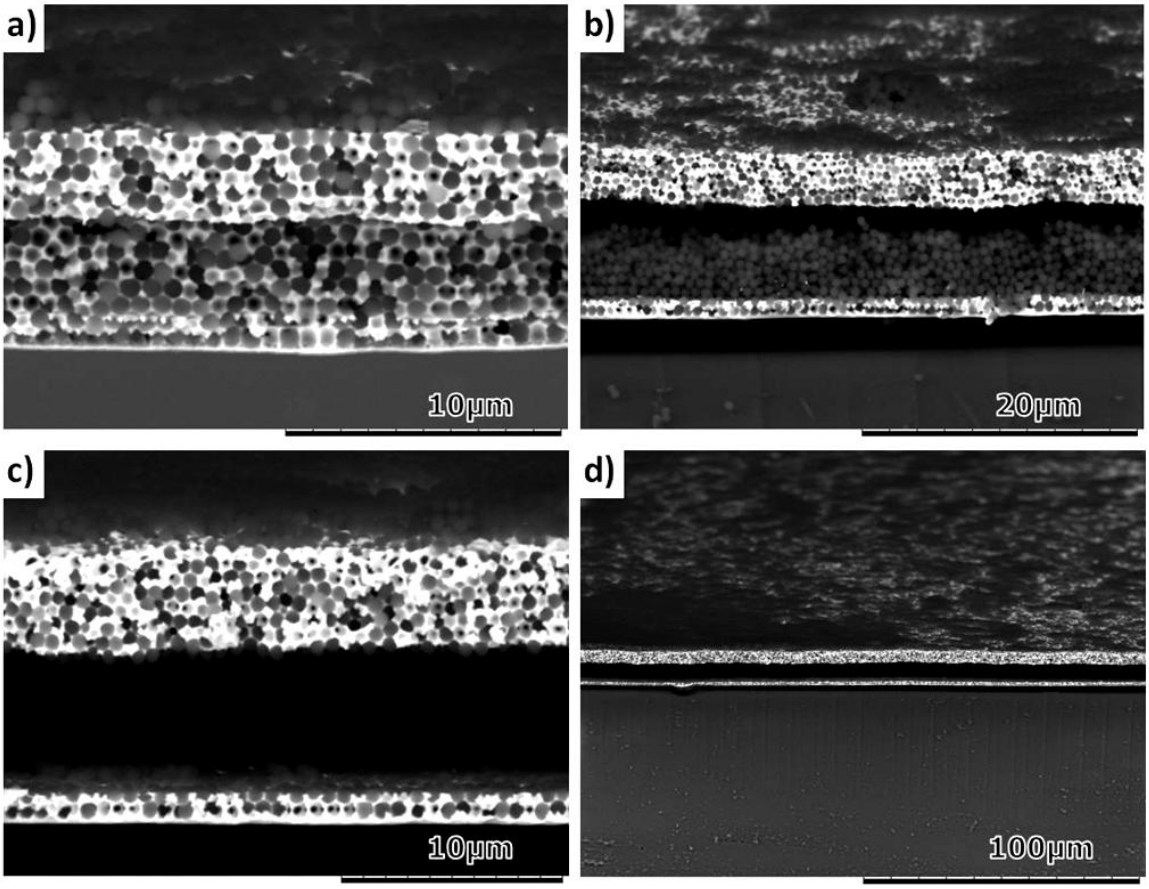

Figure 6.17: SEM cross-section views of a) a colloidal template (25 layers, sphere size 740nm) after infiltration with 1) gold (3/2 layers), 2) nickel (6 layers) and 3) gold (5 layers). b)-d) the same electrode as shown in a) after dissolution of the nickel intermediate layer in nitric acid solution (13%).

In order to confirm the lack of any short-circuit between the two macroporous film electrodes their active surface area had been determined using the CV stripping signal of gold. In the case of a short-circuited sample, the surface area detected by the CVs should be the same for the bottom

(electrode A) and the top electrode (electrode B). As shown in Figure 6.18, electrode B showed higher oxidation and reduction peaks than electrode A, indicating that the active surface area of the top electrode is significantly higher than that of the bottom electrode and that no electrical connection exists between both electrodes. In a control experiment we connected both electrodes A and B to the working electrode and measured the CV signal. In this case we observed the highest peak intensities. By calculating the active surface area from the charge associated to the gold oxide reduction peak (see chapters 3.2.3 and 6.3) we found values of 2.0 , 6.2 and 8.82 cm^2 for electrode A, electrode B and both electrodes connected together, respectively. Addition of the surface areas calculated for electrode A and B equals approximately the value measured for both electrodes. Keeping in mind that the inaccuracy of the surface determination by the reduction of an oxide monolayer is in the range of ± 10%,[245] the determined values demonstrate that both electrodes A and B are not interconnected and thus are independently addressable. Additionally, the experimentally determined roughness factors of 6.0 and 18.8 for electrode A and B correspond well to the theoretically expected values of 5.4 and 18.1 for electrodes with 3/2 and 5 porous layers, respectively.

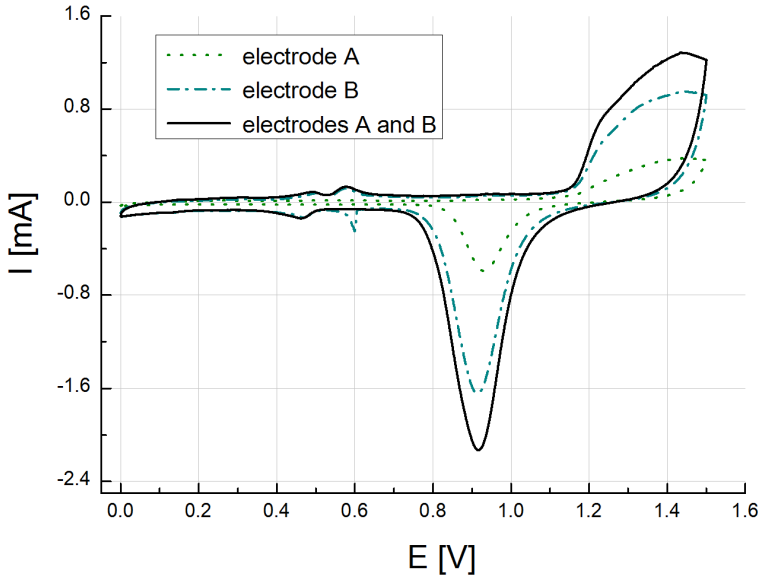

Figure 6.18: CV stripping curves of macroporous gold electrodes (see Figure 6.17 b - d) deposited on a single support and separated by silica particles and/or air. Electrode A corresponds to the lower electrode (3/2 layer macroporous gold film) and electrode B to the upper one (5 layers macroporous gold). The geometrical surface area of the sample was 0.33cm^2.

In order to show that our concept is also applicable to samples with cylindrical geometry we electrodeposited a similar multilayer structure of gold/nickel/gold into the colloidal templates on gold microwires. Figure 6.19 a) and b) show a 250µm gold wire after the electrodeposition of the

alternating metal layers and subsequent dissolution of the colloidal template. Each macroporous metal stack extended to about 4 pore layers and the thickness of the individual stacks was found homogeneous over the whole cross section of the sample. A gold/nickel/gold film deposited on another 250µm wire is shown in Figure 6.19 c) and d) obtained from a colloidal template composed of 20 layers of 1200nm spheres. In both figures, either before or after dissolution of the colloidal template, the gold and nickel films can be clearly discriminated and show a homogeneous thickness. By dissolving the intermediate nickel layer it should be possible to address independently either the top or the bottom gold electrode in these macroprous microwire electrodes. A challenge still consists in stabilizing the two macroporous gold electrodes in such a way that the distance between both electrodes stays constant during the removal of the colloidal template in order to prevent a short-circuit between the electrodes.

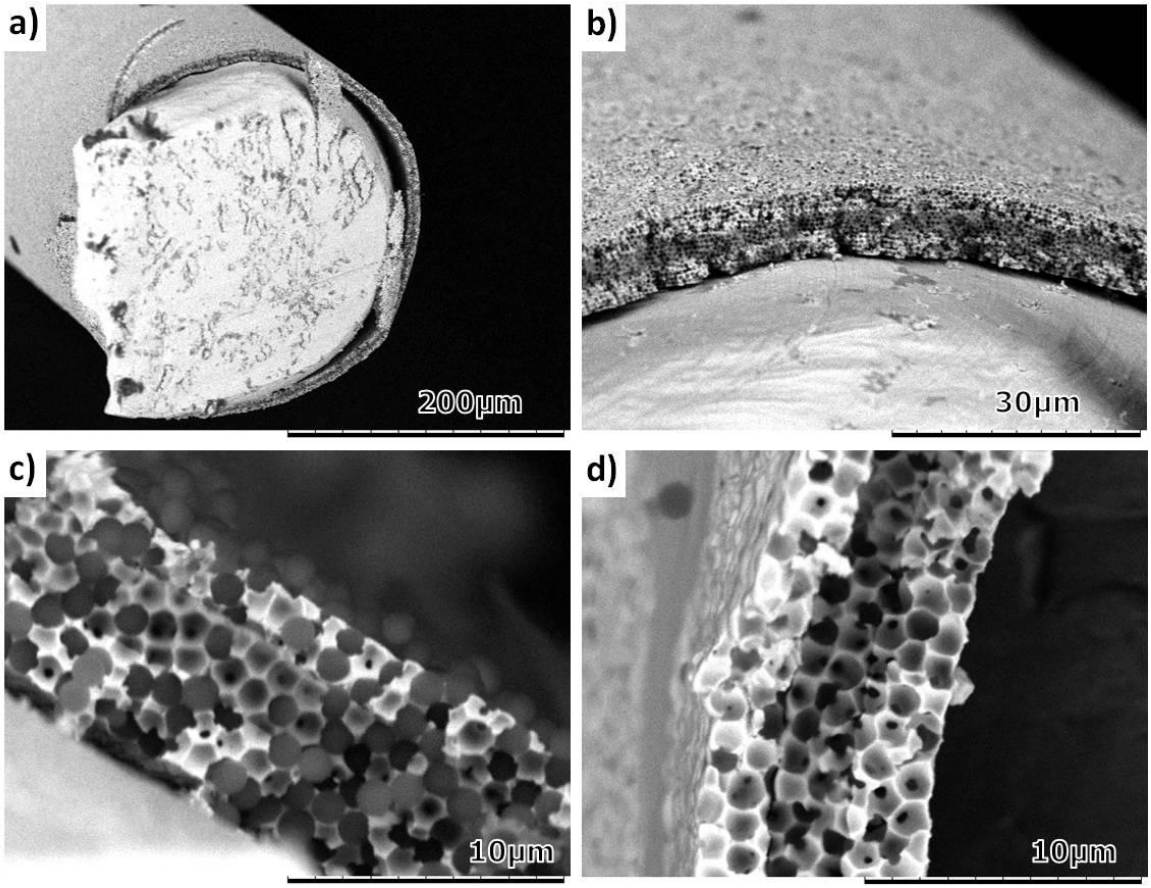

Figure 6.19: a) and b): Cross-section images of a 250µm-gold wire with a macroporous gold, nickel, gold film deposit (pore size 690nm). c) Alternating Au-Ni-Au deposition in a colloidal template (20 sphere layers, sphere size 1200nm) on a 250µm-gold wire. d) The same sample as in c) but after removal of the silica template.

Finally, by changing the sequence of the electrodeposited metal films it is also possible to produce freestanding inverse opal films of different metals. Here we first deposited a layer of nickel followed by gold into the void space of a colloidal template. The previously mentioned current

oscillations allowed us to control the thickness of both films in the template during potentiostatic deposition. An example of such a structure shows Figure 6.20d). Roughly ten layers here have been filled in the template with nickel followed by a five-layer gold film. As previously shown, the nickel layer can be dissolved so that the top layer gold film will get detached from the sample. Depending whether the colloidal template is removed or not before the nickel dissolution, inverse gold opals or silica opals filled with gold (see Figure 6.20c and e) can be obtained as freestanding films, respectively. Before immersion in acidic solution the sample shown in Figure 6.20d) has been fixed at the sides of the substrate by using varnish. In this way the film stays attached to the substrate even when the nickel layer has been completely dissolved. The sample then was exposed to acetone to dissolve the varnish and release the composite structure from the gold substrate (see Figure 6.20a). The freestanding film could now be transferred onto a desired substrate (see Figure 6.20b and c). In Figure 6.20e) a SEM image of the freestanding macroporous gold film is shown after its transfer onto a glass substrate.

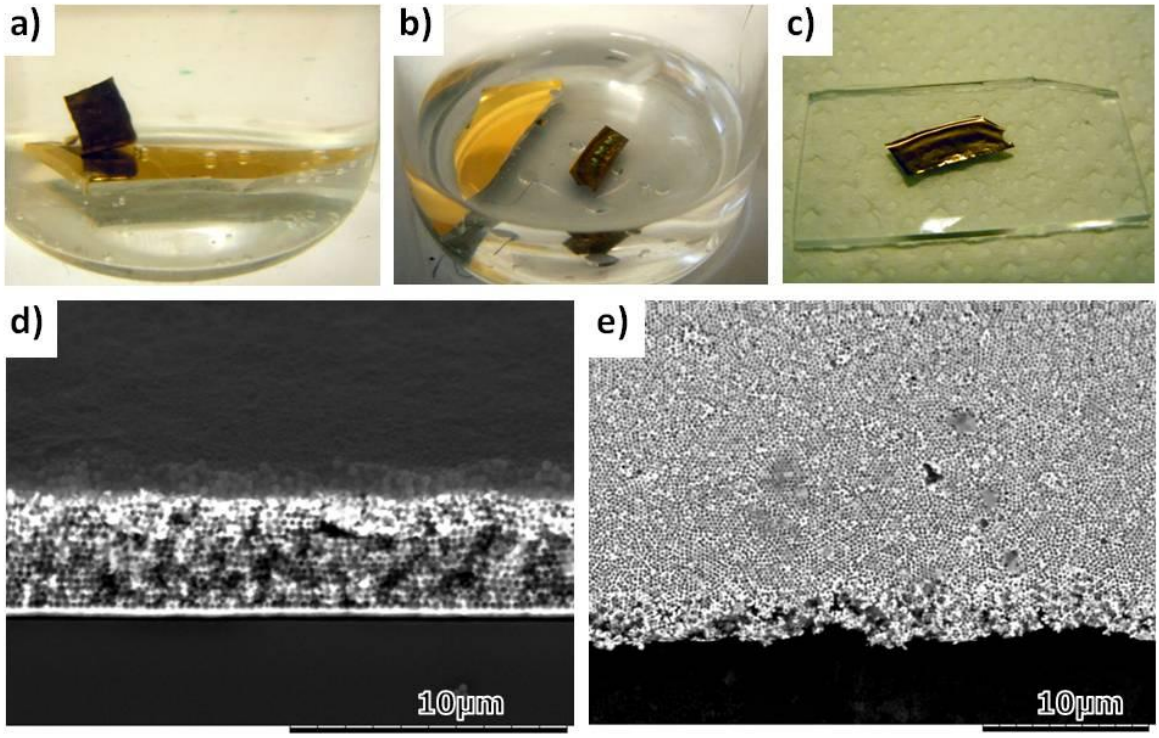

Figure 6.20: Producing freestanding macroporous gold films. a) - c): After nickel dissolution the macroporous gold film gets detached from the substrate by dissolving the varnish at the edges of the sample in acetone and can be transferred to other substrates (here glass slide) d) SEM cross section view of a colloidal template (17layers, 330nm) after infiltration of nickel and gold into the structure. e) SEM image of the freestanding macroporous gold film obtained by dissolving the nickel layer in the sample shown in d).

7 Mesoporous microelectrodes on multielectrode arrays (MEAs) for low noise neuronal recording

7.1 Introduction to multi electrode arrays (MEAs)

7.1.1 Applications and trends in MEAs

Almost 40 years ago the first microelectrode array (MEA) was designed to record electrical signals from cultured cells.[374, 375] Since this time a lot of progress has been achieved in the domain, especially during the last 15 years due to the commercial availability of MEA systems and affordable computing power.[376, 377] A variety of different MEA layouts were fabricated using lithographic techniques, reflecting a wide spectrum of in vitro or in vivo applications.[378-380] MEAs are used for various purposes including pharmacological studies in dissociated neuronal networks, different stimulation implants (cochlear, retina, cortical, spinal) and fundamental research aiming at better understanding the functioning of neuronal networks. Compared to neurobiological measurements performed with single electrodes (e.g. tungsten or glass capillary electrodes) MEAs offer the advantage that information from electrogenic cells can simultaneously be analyzed in different regions of the same tissue over long periods of time.[381] The acquired data can be used to map the spatio-temporal dynamics of the activity in neuronal networks in order to study interactions between the different cell populations. [382] Further evolution of MEA measurement technology requires maximization of available information density. A recent trend in MEA research consists in working with microelectrodes of reduced size. In this way recording and stimulation can be confined to small populations up to single neurons preventing the interference with neighboring cells. Hence the number of electrode sites on one array can be increased leading to high density microelectrode or microtransistor arrays with very high spatial resolution. [383-386] However decreasing the geometric area of the microelectrodes results in an increase of electrode impedance and consequently higher electronic noise during recording of neuronal signals. Equally the charge that can be safely injected through an electrode in order to stimulate the surrounding tissue is reduced. [387] Those factors present serious drawbacks for using microelectrodes of small surface area on MEAs and current work should now focus on strategies to overcome these limitations. Generally this can be achieved by increasing the effective surface area of an electrode while maintaining its small overall geometry. This presents a widely used approach to improve the

performance of electrodes in application fields including analytical chemistry or energy conversion systems. Different techniques exist that allow increasing the active surface area of electrodes by creating porous, nanostructured surface morphologies. Among these approaches some have been applied to MEAs in order to enhance their performance at the interface with the solution containing cultured cells. The objective of this contribution consists in presenting different nanofabrication techniques that have been successfully adapted to MEAs and to point out their utility for improved neuronal recording and stimulation processes.

7.1.2 Interfacial behaviour of microelectrodes in neural recording or stimulation

In order to understand which parameters are of a special interest in neurobiological recording and stimulation with MEAs, a brief description of both processes is given here with a special emphasis on the processes occuring at the interface between the electrode and the solution. When an electrogenic tissue is immersed in physiological solution in close proximity to the electrodes of MEAs, extracellular signals that may originate from different cells can simultaneously be recorded at the electrode. Electrical activity of the cells causes a current to flow around its signal source in the extracellular medium. This current corresponds to a voltage gradient present in the extracellular fluid which is a function of the number, spatial distribution and orientation of active cells. The voltage finally is recorded at the microelectrode site as a function of time with respect to a reference electrode that is immersed into the physiological solution. The electric signal is then further amplified and filtered before signal post-processing steps can be performed with specially adapted software. Although several parameters in this acquisition chain may be important, a crucial factor directly affecting the quality of recorded signals is the interface between the electrode and the extracellular fluid. A small area in contact with the solution results in high electrode interfacial impedance and consequently a high thermal noise which can be expressed by equation 7.1.[388-390]

$$N_{th} = \sqrt{4K_B T \int Re(Z)\, df} \quad (7.1)$$

Here, N_{th} corresponds to the rms value of the thermal noise [V], K_B is the Boltzmann constant, T is the temperature [K], Re(Z) is the real part of the microelectrode interfacial impedance [Ω] and f is the frequency [Hz]. Low sensitivity in the recording process due to high noise therefore especially presents a problem for small microelectrodes on MEAs. A significant decrease in impedance has

to be obtained in order to reach signal-to-noise ratios (SNRs) that allow detection of neuronal signals. The stimulation process of electrogenic tissues relies on an inversion of the above mentioned events. Now current pulses that are applied to the electrode induce a change of the distribution of ionic species in solution so that a potential gradient is established throughout the electrolyte, which may eventually activate cells. An injection of current into an electrode generally may result in different forms of charge transfer, a capacitive and eventually also a faradaic charge transfer. As long as the current amplitude and hence the potential at the electrode does not exceed a certain value only redistribution of charge carriers happens, resulting in charging of the double layer at the interface between electrode and electrolyte. Inversing the polarity of the applied current leads also to a reversal of the charge distribution at the interface. This capacitive charge transfer is reversible and no electron transfer occurs between the electrode and the solution, which is a characteristic found in electrical capacitors. In contrast, a faradaic charge transfer involves electron transfer from the electrode to the electrolyte and vice versa due to reduction or oxidation reactions occuring at the electrode surface. Faradaic reactions can occur when the current values injected into an electrode are sufficiently high to generate an overpotential that is needed for certain redox reactions to take place. Principal faradaic reactions at metal surfaces in aqueous solutions include the reversible formation and reduction of oxide layers, but also oxidation or reduction of water as well as corrosion reactions. [391] Therefore currents injected into a microelectrode should not exceed a certain limit in order to avoid irreversible faradaic reactions at the electrode surface. Besides damaging of the electrode by corrosion, these reactions may be responsible for cell death due to accumulation of reaction products in solution, creating a toxic environment for cells. The maximum charge that can be injected "safely" through a microelectrode depends on several factors including the material used for the electrode, the electrolyte, stimulation parameters as well as the size and shape of the electrode. [392] Obviously microelectrodes of small overall dimensions may safely inject less charge than macroelectrodes. Thus sufficient charge injection into the electrode often presents the limiting factor for efficient stimulation of the surrounding tissue with MEAs. Increasing the effective surface area of microelectrodes therefore not only leads to a decrease of impedance and thermal noise of the electrode, but also allows to inject higher charges, necessary for an efficient and reliable stimulation process of electrogenic tissue. Besides the tissue damage that is caused by electrochemical reactions at the electrode also a second mechanism referred to as the mass action theory has been described. Here, the tissue is overstimulated due to many neurons firing simultaneously or over prolonged times which causes the local environment, e.g. ionic, oxygen or glucose concentrations to change. [392] The domain of safe stimulation will depend on the injected

charge density and the charge injected per phase for different types of tissue. [393, 394] In deep brain stimulations the limit for safe stimulation conditions was found to be 30µC/cm^2 for an injected charge of 2µC per phase. [395]

7.1.3 **Electrode materials in MEAs**

A short overview on electrode materials suitable for the use in MEAs is given in this chapter. Well documented reviews on stimulation of electrogenic tissue and the electrode materials employed for this purpose are available in the literature. [387, 392, 396] Principally some basic criteria have to be met for an electrode material in MEAs. First of all the proximity of living tissue to the electrode material absolutely demands biocompatibility to avoid a necrotic cell response as observed for example for cells that were cultured on silver. Ideally, a cell attachment to the material allows a stable junction to be formed between electrode and tissue, a factor which is of importance especially in long term in vitro and in vivo measurements. Electrode materials further should offer sufficient mechanical strength combined with stable electrical properties guaranteeing reliable long term performance of the MEA. High charge injection capacity per surface area is a key parameter for electrode materials used for efficient stimulation of electrogenic tissue. A way of achieving safe stimulation conditions presents the use of capacitor electrodes. [397, 398] Here the underlying metal electrode is separated from the electrolyte by a dielectric material (TiN, Ta_2O_5) allowing charge to be injected into the tissue strictly by capacitive action. [392, 399-403] This prevents potentially destructive faradaic reactions at the electrode surface. The maximum charge however that can be injected into a smooth electrode just by capacitive coupling is about 20-30µC/cm^2. [401] Considering a typical stimulation protocol of 50µA for 200µs pulses per phase, [404] a capacitor electrode reaches this maximal injectable charge density for a diameter exceeding 220µm, which is much too big to enable stimulation in a very confined area. To be able to inject higher currents, materials showing reversible faradaic reactions occurring within the potential window of water decomposition are required. Among metallic conductors the noble metals gold, platinum and iridium usually are employed as electrode materials in MEAs due to their high electrical conductivity and corrosion resistance. Gold is often selected due to the relative ease in fabrication and hence serves in many studies as a reference material. However gold microelectrodes adsorb many substances on their surface making them very unstable over time. [400] Platinum offers more stable noise and additional storage of charge due to a reversible ad- and desorption of hydrogen atoms at and from the electrode surface. This pseudocapacity together with double layer charging and a reversible oxide formation and reduction at the surface allows the injection of charge

densities into platinum electrodes that range from 50 to 350µC/cm^2 depending on the stimulation protocol. [392, 396, 405] A material that can store extremely high amounts of charge is iridium oxide. In IrO_x reversible valency changes between different oxidation states are the reason for this high charge storage capacity. The redox centers in the electroactive material are represented by iridium ions with the main redox process involving a reversible switching between the Ir^{3+} and Ir^{4+} oxidation states. [406] Charge injection limits were reported in a range of 1 to 3.5mC/cm^2 for iridium oxide, which is about one order of magnitude higher than the values observed for platinum. [407] Figure 7.1 points out the amount of charge that can be stored in the different materials including TiN, platinum and iridium oxide.

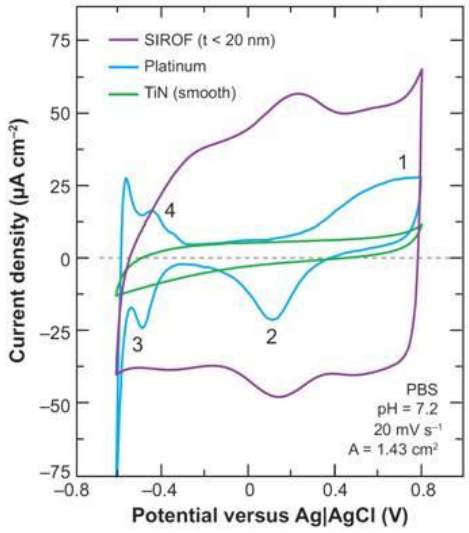

Figure 7.1: Cyclic voltammograms of platinum, TiN and iridium oxide, produced by sputtering (SIROF), at a sweep rate of 20mV/s. Points 1 and 2 indicate platinum oxidation and reduction of platinum oxide, 3 and 4 hydrogen adsorption and desorption on Pt, respectively. Cathodic charge storage capacities (CSCs) are 0.25mC/cm^2 for TiN, 0.55mC/cm^2 for Pt and 2.8 mC/cm^2 for SIROFs. [387]

Emerging materials in the field of neuronal recording and stimulation are conducting polymers. Among them especially polypyrrole (PPy) and poly(3,4-ethylenedioxythiophene) (PEDOT) were used in MEAs. Compared to metals they present a relatively soft material when coated onto the electrode surface offering a biocompatible platform which promotes the cell attachment onto the electrode. [259] During synthesis of conducting polymers using electropolymerization, anionic counterions are incorporated into the material establishing charge neutrality in the polymer. Charge injection into conducting polymers may change their oxidation state accompanied by counterions leaving or entering the material. This can represent a limiting step for a fast and efficient charge injection into conducting polymers. [408] Nevertheless charges of 3.6 mC/cm^2 were injected through PEDOT microelectrodes and the stimulation efficiency was proven to be superior

compared to ITO electrodes for a period of 2 months. [409] Electrodeposited films of conducting polymers also were reported to reduce electrode impedance. [410-413] An improvement of the long term chemical and mechanical stability of conducting polymers, which was found superior in the case of PEDOT compared to PPy [414], presents the main challenge for a broader application in MEAs.

7.1.4 **Porous and nanostructured MEAs**

There are several reasons for using microelectrodes with a nanostructured surface film in MEAs. [415] The engineering of materials at the nanoscale can offer new solutions for challenges such as controlled drug release. [416, 417] Topographical patterning of nanostructured materials on electrode surfaces enables guiding cells and controlling their attachment and growth on the electrode. [418] The principal motivation however that is addressed in this work for using nanofabrication methods consists in improving the performance of MEAs with respect to neuronal recording and stimulation. Especially smooth microelectrodes of small geometric dimensions suffer from high electrode impedance, leading to high levels of thermal noise in extracellular recording and limited charge injection for efficient stimulation of tissue. Therefore a lot of different nanofabrication techniques have successfully been applied to MEAs during the last decade aiming to lower the interfacial impedance between the electrode and the electrolyte by an artificial increase of the active electrode area. The type of method to be employed in order to modify the surface of a microelectrode has to be compatible with microelectrode arrays that are typically fabricated in a photolithographic process. Surface structures can readily be generated by using either top down or bottom-up processes, involving the addition of material to the electrode. Early studies dealing with porous silicon produced in an anodic etching process however did not change the electrical properties of the MEAs, so that this route has not been further followed. [419, 420]

7.1.4.1 Platinum black electrodes

In thin film deposition the morphology of a deposit can be varied by changing the process parameters resulting either in smooth, compact or rough and porous films. For example in electrochemical deposition the electrolyte composition and the potential applied to the working electrode are important parameters that affect the growth and hence the structure and appearance of deposited films. Platinum films with a rough surface structure referred to as

platinum black [421] were frequently deposited on electrodes of MEAs helping to lower the electrode impedance by up to two orders of magnitude. [422-425] Although platinum black films strongly increase the active surface area of an electrode due to their amorphous structure, their application in MEAs is not straight forward due to a lack of mechanical stability. An improvement of the durability of these coatings could be achieved by performing platinum electrodeposition with simultaneous ultrasonic treatment. [426] The harsh conditions during electrodeposition were meant to immediately remove loosely bound material by preserving the rough nature of the film deposit. An enhanced stability was confirmed in a study performed with microwire multi-electrode arrays obtained by this ultrasound assisted approach. [427] Using artificially roughened substrates for a subsequent film deposition also represents a way to increase the active surface area of an electrode and can lead to improved stability and adherence of electrodeposited polymer films on the electrode surface. [411, 428]

7.1.4.2 Iridium oxide electrodes

Iridium oxide presents a commonly used electrode material in MEAs due to the high intrinsic charge injection capacities. It can either be formed from metallic iridium using an electrochemical activation process (AIROFs) [429-431], directly be deposited using reactive sputtering of iridium in the presence of an oxidizing plasma (SIROFs) [406, 432-435] or using electrochemical deposition (EIROFs). [436-439] The microstructures obtained with iridium oxide films will depend on the synthesis technique and the process parameters. In AIROFs considerable amounts of water are incorporated into the structure during prolonged potential cycling, which explains the lower density found for AIROFs (2 g/cm^3) in contrast to bulk crystalline iridium oxide (11.68g/cm^3). [406, 440] A highly porous structure with good electrolyte permeability is on one side attractive for reaching high charge storage capacities, but was reported to lead to flaking and delamination of AIROFs from the substrate in long term use. Deposition of iridium oxide by sputtering leads to more compact films (7 g/cm^3) with a better mechanical stability.[406] The influence of various process parameters including the oxygen flow rate [406, 441], the sputtering pressure [434], substrate temperature [432] and pulsed dc sputtering [435] on the composition and microstructure of SIROFs has been recently examined. It was found that the amount of oxygen present during sputtering had a fundamental influence on the microstructure and the electrical properties of SIROFs. Too high oxygen concentrations resulted in lower mechanical stability and decreased charge storage capacities, although the roughness of the films was shown to increase. This finding was attributed to varying material compositions with increasing oxygen content, causing among others a lower

electrical conductivity. Optimization of the process parameters allowed the fabrication of SIROFs reaching charge injection limits that were comparable or even superior to those observed in AIROFs during in vitro measurements. [442, 443] So far only few studies focused on electrodeposited iridium oxide films (EIROFs) for neurobiological applications, even if the stability and charge injection values seem comparable to SIROFs. [439] Electrochemical deposition presents a technique that is easily integrated in microfabrication processes and additionally allows nanostructuration of electrode surfaces which cannot be obtained when PVD techniques are used. Macroporous iridium oxide produced in template assisted electro- [237] or atomic layer deposition was reported to have increased charge storage capacities over non porous iridium oxide. [444] A coating of highly porous iridium oxide films on neural electrodes could present a way to further improve the performance of this material for the application in MEAs.

7.1.4.3 Carbon nanotube modified electrodes

The high surface to volume ratio makes carbon nanotubes (CNTs) interesting candidates in both recording applications with a low noise level and efficient stimulation of cultured tissues. Despite the benefits of being able to create patterned surface structures and to vary the surface chemistry of CNTs, their biocompatibility still presents a controversial issue in current research. [445] One possibility to obtain CNT modified substrates is the evaporation of the solvent from a CNT containing solution that has been spread onto a surface. In this manner CNTs were deposited on glass slides in order to examine the neuronal activity using a patch clamp setup. A higher frequency response together with increased intensities was found in spontaneous postsynaptic currents of neurons placed on CNTs compared to the bare glass slides. [446, 447] However, for MEAs different immobilization techniques have to be employed, guaranteeing a long lasting stable deposit of CNTs on the electrode (see Figure 7.2a). This can be achieved by direct growth of CNT films from a thin catalyst layer (e.g. Ni) coated onto the electrode using a chemical vapor deposition (CVD) method. Depending on the growth conditions either randomly deposited [448-450] or vertically aligned carbon nanotube (VACNTs) [451-454] networks are obtained (see Figure 7.2c).

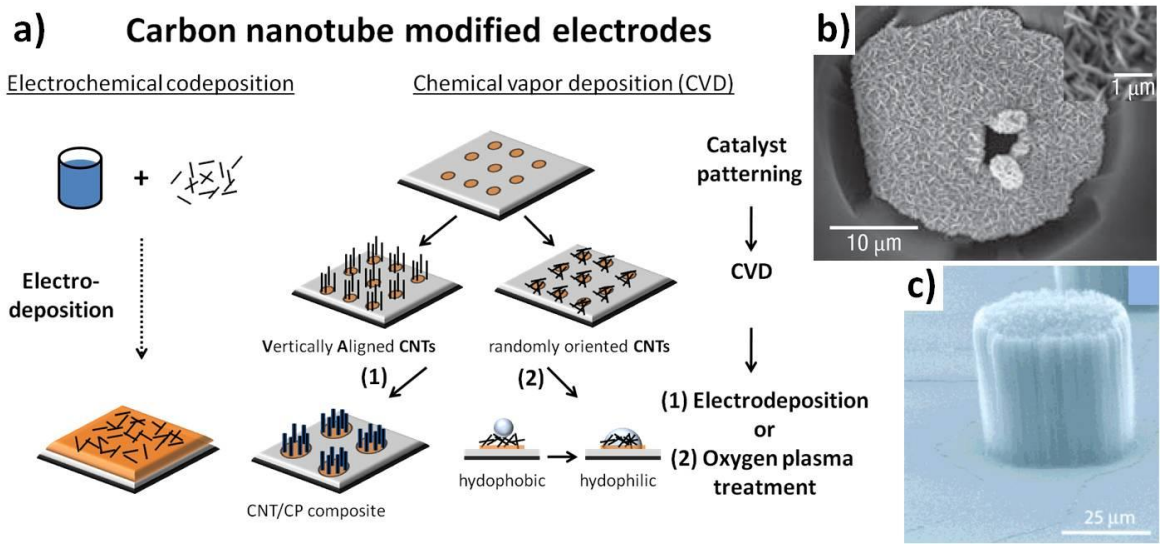

Figure 7.2: a) Illustration of different routes to obtain carbon nanotube modified electrodes and composite materials with CNTs. b) CNT/Au composite structure fabricated due to electrochemical reduction of gold ions in aqueous solution containing CNTs. [455] c) Vertically aligned CNTs grown by CVD on a microelectrode of 50µm diameter. [452]

Microelectrodes modified with CNTs showed higher capacitance and lower impedance values compared to smooth metal electrodes. [450] Stimulation performed on hippocampal sliced cultures on CNT modified MEAs revealed charge injection limits of 1 - 1.6 mC/cm^2 which are superior to platinum and slightly smaller than those for iridium oxide. [452] From the same type of tissue spontaneous neuronal activity was recorded using 10µm long carbon nanofiber (CNF) electrodes with an average diameter of 4µm. [454] Surface wettability generally is an important parameter in porous films because it determines the degree penetration of a liquid into the porous structure. Surface wettability was proven to be considerably increased when carbon nanotube films were exposed to an oxygen plasma. [456] Consequently oxygen reactive ion etching (RIE) was also applied to MEAs covered with CNTs so that the interfacial impedance between the electrode and the solution could be further decreased. [448, 449, 457] Although carbon nanofibers are well separated from one another directly after their synthesis, they tend to stick together building bundles of nanofibers once they have been immersed in a liquid and dried afterwards. [451, 453] Deposition of a conducting polymer onto the nanofibers stabilizes them and helps to maintain their original structure for future use. It also has been shown that composites of CNTs and polypyrrole (PPy) exhibit higher capacitance and lower impedance values than the bare polymer. [458] It seems likely that similar results could be obtained performing electrochemical codeposition of CNTs and conducting polymers out of a single solution. [459] This technique has been applied to modify MEAs offering the convenience of avoiding high temperature ranges between 400°C and 900°C, needed in CVD, that can limit the choice of materials in the MEA fabrication process. [455, 460, 461] By optimization of the electrodeposition parameters, a highly porous composite of single-walled

carbon nanotubes (SWCNT) coated with polypyrrole could be obtained that offers charge injection limits of 7.5mC/cm^2 for anodic pulses. [460] Increased electrical conductivity and lower impedance was found for composites when CNTs first were immobilized at the surface followed by the electropolymerization step. [461, 462] A codeposition of CNTs and gold on MEAs (see Figure 7.2b) and wire electrodes showed good performances for the recording from cultured neurons and in the rat motor cortex. Using this approach it was possible to record local field potentials, multiunit activity and neuronal spikes with one single electrode. [455] Furthermore also a layer-by-layer attachment of CNTs with polyelectrolytes recently led to neural electrodes showing promising results in comparison to PEDOT or iridium oxide. [463] In works focusing on CNT modified electrodes very few data is provided dealing with long term stability of the devices in vivo or in vitro. The lack of in vivo measurements may be attributed to the unclear biocompatibility issue of CNTs. [445] Lu et al. reported lower astrocyte and a higher neuronal density around PPy/SWCNT composite electrodes in contrast to Pt controls after a 6 week implantation period in a rat brain tissue. The stability of the impedance and the recording performance over prolonged times in vitro represent important parameters that should be studied in future works on CNT coated electrodes.

7.1.4.4 Conducting polymer coated electrodes

With coatings of conducting polymers different targets may be addressed in the field of neural electrodes which include the improvement of the recording performance, the promotion of cell growth at the electrode surface and the minimization of the immune responses of the tissue. The rough nature of electrodeposited PPy or PEDOT films which resemble cauliflower structures together with inherently more or less pronounced porosity enabled to decrease the electrode impedance by more than one order of magnitude in contrast to bare metal electrodes. [410, 412] This value can further be decreased by nanostructuring the polymer film. Abidian et al. reported impedance values of 2.5 ± 1.4 kΩ for electrodeposited PEDOT nanotubes (see Figure 7.3e), corresponding to a decrease of two orders of magnitude compared to bare iridium oxide electrodes (468.8 ± 13.3 kΩ). In the same way the charge injection capacity was increased by three orders of magnitude reaching a value of 392 ± 6.2 mC/cm^2. [464] To achieve efficient recording or stimulation of extracellular neuronal activity, the tissue should ideally be in close contact or attached to the electrode surface. In this regard, the neurite outgrowth length of PC12 cells was reported superior on polypyrrole than on a passive substrate. [465] Electrical stimulation further increased the neurite growth length on polypyrrole in the first 24 hours, which was

attributed to the adsorption of serum proteins, specifically fibronectin onto the film. [466] By entrapping various bioactive molecules during the synthesis of conducting polymer films the cell-tissue interaction could be further intensified. Preferential neurite growth was observed on polymer films containing different peptides [413, 467, 468] and nerve growth factor. [469] Another strategy to assure intimate contact between the tissue and the electrode is electropolymerization of conducting polymer film around the cultured living cells. [470, 471] In this way the cells could be enclosed in a PEDOT film at the surface of the electrode. However, the cells lasted viable for only less than one week in this study which was attributed to the polymer film restricting the nutrient transport towards encapsulated cells. A general issue encountered in long-term implants represents fibrous encapsulation of the electrode resulting from the immune response to the foreign body implant. In a recent study PEDOT coated microelectrodes of small geometry (15µm diameter) were meant to reduce the inherent immune response of the tissue and enabled recording of neuronal activity, which was not possible with the control gold electrodes. [472]. Another strategy to limit the immune response could be to encapsulate anti-inflammatory drugs into conducting polymer films in order to release them locally at the electrode level. An example represents the incorporation of Dexamethasone (DEX) into PPy and PEDOT films that could be released in a controlled manner by cycling the polymers between the oxidized and the reduced state, leading to movement of ions (involving DEX) into or out of the polymer. [417, 473] Indeed, in vitro studies on murine glial cells showed that the release of DEX from the PPy electrodes reduces the count of reactive astrocytes proportionally to the amount of the added drug. [473] To date the initial low impedance value that was observed directly after surgery in chronic implants realized with polymer coated microelectrodes could not be maintained over longer periods exceeding a few days. [472, 474, 475] Nevertheless PEDOT nanotube modified microelectrodes (see Fig. 3e) allowed stable chronic recording of neural signals over a period of 7 weeks at an electrode impedance around 500 kΩ for a size of 1250 μm^2. High quality unit activity (signal to noise ratio SNR > 4) was detected on 30% more sites than controls. [475]

7.1.4.5 Hydrogel-coated electrodes

Hydrogels are important materials for biomedical applications due to their ability to incorporate high amounts of water and their soft nature makes them good candidates to be used at the interface of electrode and tissue. [476] It was proposed to use hydrogels as scaffolds for the deposition of conducting polymers resulting in porous polymer films with high electrolyte permeability. [477] Either hydrogels and conducting polymers were copolymerized [478] on MEAs or a

coating of the electrode with a hydrogel served as a scaffold in the subsequent electrodeposition. [479] Very low electrode impedance was reported using this approach, but care had to be taken not to dehydrate the hydrogel which would have led to bad electrical properties. Using hydrogels, a more sophisticated approach to control drug release in combination with a low-impedance electrode interface has been proposed by Abidian et al. [480] The basic fabrication process is shown in Figure 7.3a) and includes electrospinning of drug-incorporated biodegradable nanofibers onto the electrode sites (B), encapsulation of these nanofibers in an alginate hydrogel layer (C) followed by the electrodeposition of PEDOT around the nanofibers to form conducting polymer nanotubes (D).

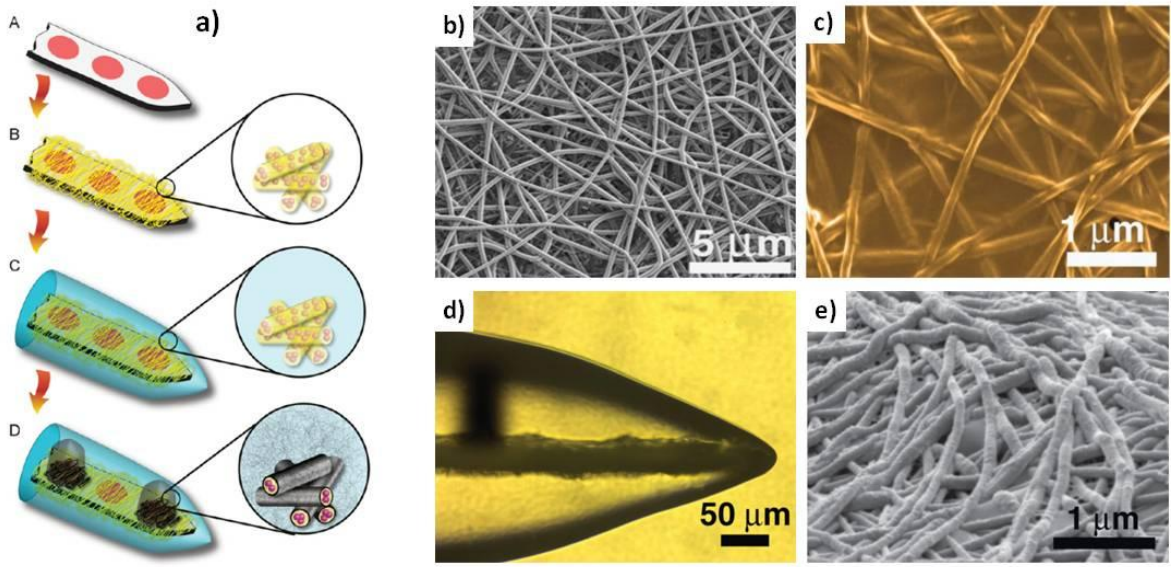

Figure 7.3: Multifunctional nanobiomaterial based on PEDOT nanotubes with DEX encapsulated in a hydrogel a) Basic fabrication steps B: Electrospinning of nanofibers C: Encapsulation in hydrogel D: Electropolymerization of PEDOT perpendicular to the electrode surface generating the PEDOT nanotubes. SEM images of b) the obtained polymer nanofibers containing DEX. c) Nanofibers coated with hydrogel (False colored) d) Cross section of the electrode after electropolymerization of PEDOT into the hydrogel. e) PEDOT nanotubes. [480]

The very low impedance of 2.5 kΩ attained by this hybrid electrode material is due to a combination of two effects that effectively increase the active surface area of the electrode. As shown in Figure 7.3d) PEDOT grows vertically from the electrode site into the hydrogel scaffold leading to "cloudy" PEDOT. Together with the high surface area provided by the PEDOT nanotubes (see Figure 7.3e), this leads to a very low electrode impedance. Due to hydrolytic degradation, the nanofibers release the encapsulated DEX molecules. The drug has to migrate through the layer of hydrogel before reaching the tissue, which makes it be delivered more slowly than without hydrogel encapsulation. In recent studies however it has been shown that composites formed from hydrogels and PEDOT implanted in the auditory cortex of guinea pigs displayed a lower

signal to noise ratio and less detectable signals compared to bare gold electrodes. [481] This loss in recording functionality was ascribed to the increased distance between neurons and electrode sites due to the hydrogel thickness.

7.1.4.6 Templated macroporous electrodes

Microelectrodes on MEAs have also been coated with macroporous overlayers of gold[482] and conducting polymers[483, 484] in order to increase the electrode surface area and enhance the performance of the MEA in recording and stimulation. These macroporous films obtained by electrodeposition in colloidal templates offer good control over the surface enhancement combined with highly interconnected pores resulting from a close packed sphere arrangement. [242] Recent work in our group showed that the thermal noise in MEAs could be reduced for macroporous microelectrodes (see Figure 7.4b) due to a higher contact area with the surrounding solution. The surface enhancement of macroporous compared to the flat gold microelectrodes was evaluated using cyclic voltammetry. Figure 7.4a) shows the charge associated to the gold oxide reduction for the different microelectrodes on a multi electrode array, before and after a macroporous overlayer had been deposited onto the surface. For the majority of the microlectrodes on the array the electrode surface was found to be increased by a factor of 5 to 6.

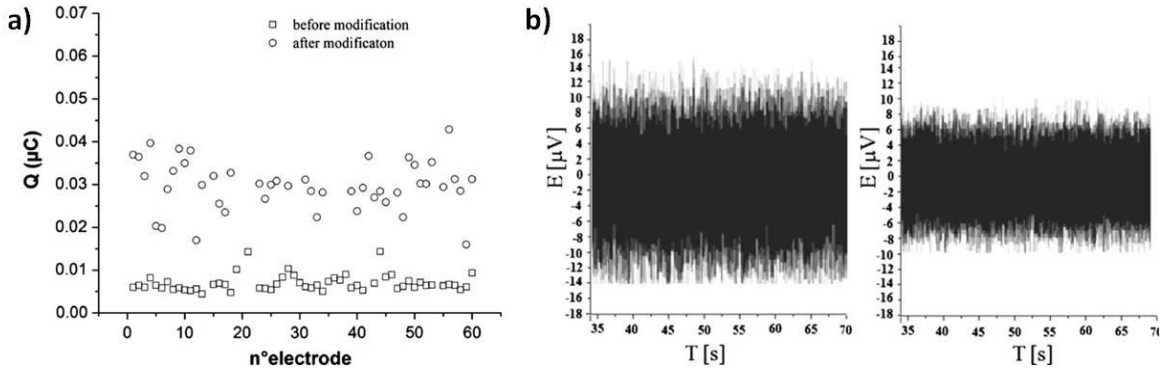

Figure 7.4: a) Charge associated with the gold oxide reduction peak obtained from CVs for macroporous microelectrodes (*after modification*) compared to smooth gold microelectrodes (*before modification*) on a MEA chip. b) Illustration of the reduction in noise level of a macroporous (right) compared to a smooth (left) gold microelectrode on a MEA. The microelectrode diameter was 30µm and the pore size 500nm.[482]

Although the primary goal of providing an electrode material with a defined porosity consists in increasing its active surface area, new functionalities in the field of neural engineering may also be achieved. The release profiles of nerve growth factor incorporated in macroporous PPy surfaces were considerably increased owing to the open pore structure, especially when electric stimuli were applied to macroporous conducting polymer films. [264] The performance in porous

MEAs may be further enhanced by increasing the pore density and hence the electroactive area in the deposited films. In colloidal templating one may simply use smaller spheres to reduce the pore size and increase the pore density in a given volume. However, the self-assembly of spheres smaller than a certain diameter (about 100nm) is more complicated.

A different approach to produce pores of smaller dimensions on an electrode surface involves the use of lyotropic liquid crystals as templates. Ordered mesoporous films can be formed when deposition of a material takes place around surfactant molecules arranged into a crystalline template structure. We used this strategy to further increase the active surface area by depositing soft-templated meso- instead of hard-templated macroporous films on the surface of the microelectrodes in MEAs. The principles of mesoporous film formation by lyotropic liquid crystal templating will be adressed in the following chapter.

7.2 Mesoporous films by lyotropic liquid crystal templating

Existing states of matter include solid, liquid and gaseous at ambiant temperature and pressure. In crystalline solids long range order is present established by strong ionic, metallic or covalent bonds. Due to weak intermolecular bonds molecules are still mobile in liquids and only a short range order is present. Liquid crystals (LCs) combine the properties of both, solids and liquids, with flow properties of ordinary liquids and the anisotropic physical parameters of crystals. LCs are thermodynamically stable and their phases are also called mesophase. Liquid crystals are divided into thermotropic and lyotropic LCs, depending on the origin of intermolecular interactions inducing ordering. In thermotropic LCs a phase transition in the compound is induced by a temperature change whereas lyotropic phases are sensible to both, temperature and concentration changes in the corresponding phase diagram of the system. The long range order together with the possibility to align nematic phases in thermotropic LCs by electric or magnetic fields is extremely useful for fabricating electronic displays (LCDs). But LCs are equally used for sensors, drug delivery vehicles, photonic band gap structures and optical elements such as adjustable lenses and lasers.[27, 485]

Lyotropic liquid crystals (LLCs) are formed in aqueous solutions containing surfactant molecules. The latter are amphiphilic, with a polar head group and a non-polar hydrocarbon tail. In water the polar part of the molecule is dissolved whereas the non-polar end shows affinity towards other hydrocarbon ends. Adding surfactant molecules to aqueous solutions first builds out a monolayer of molecules on the water surface with the polar groups pointing into and hydrocarbon tails sticking out of the water. This has been illustrated in Figure 2.9a) dealing with the transfer of such

molecular monolayers onto solid substrates using the LB technique. Since the available space at the air-liquid interface is restricted, additional molecules will be available in solution. Increasing the concentration of added surfactant brings the molecules closer together and micelles can be formed when a critical concentration (cmc) is reached, this process being illustrated in Figure 7.5. A balance is established between repulsive forces of the head groups and the force arising from the spatial confinement of the molecules due to the concentration increase. Depending on the nature of the head group anionic, cationic or nonionic surfactants can be distinguished.[27]

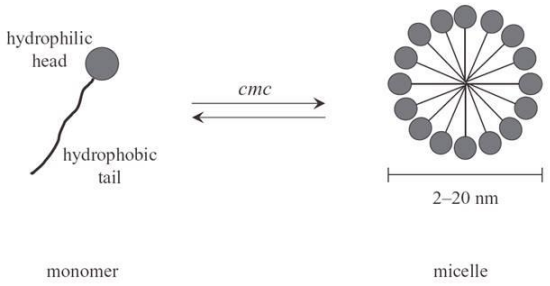

Figure 7.5: Scheme of the micelle formation, occurring when the critical micelle concentration (cmc) of surfactants in aqueous solutions is reached.

Further increase of surfactant concentration can lead to the formation of lyotropic liquid crystalline phases. The LLC phases of surfactants show long-range periodicity with a typical period ranging from 2 to 20 nm and exhibit a rich polymorphism of structures. In the phase diagram in Figure 7.6 different phases including micellar, hexagonal, cubic and lamellar are formed as a function of the concentration of nonionic surfactant in water and the temperature of the solution. When a precursor material is now mixed with one of the LLC phases the generation of nanostructured materials becomes possible. The surfactant acting as a template can be removed after the synthesis by calcination or a simple washing step. This approach first has been successfully applied to produce mesoporous silica by calcinating aluminosilicate gels in the presence of surfactants.[486] Since then many different organic and inorganic materials have successfully been mesostructured using this approach.[485, 487]

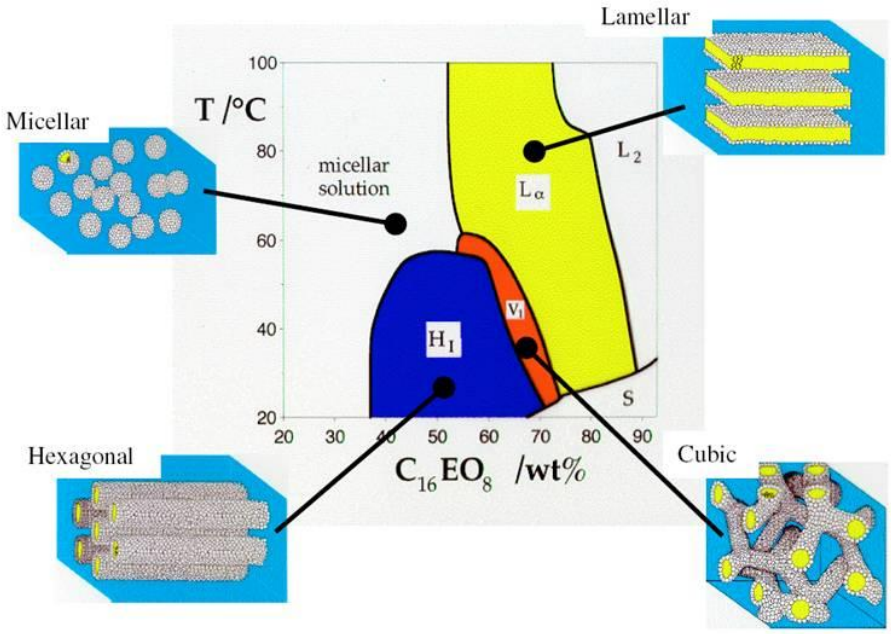

Figure 7.6: Phase diagram of $C_{16}EO_8$ mixed with water as a function of the temperature showing the most common phases in the lyotropic liquid crystalline media.[488]

The first metallic mesoporous structure produced from LLC templates was based on the chemical reduction of a platinum salt in the presence of surfactants, resulting in mesoporous colloidal Pt particles .[489, 490] Shortly after this, it has been reported that mesoporous platinum films also could be produced by electrochemical reduction of metal ions in the aqueous domains of the LLC template.[246] This was a remarkable finding as the mesoporous film deposits were not only flat, mechanically robust and shiny in appearance but most importantly, showed well ordered pores that were arranged perpendicular to the surface or under small angles to the surface normal. The driving force for the pore alignment is believed to be the applied electric field.[490] To date a wide range of mesoporous metal films can be electrochemically deposited from LLC templates including Co, Ni, Cu, Zn, Ru, Rh, Pd, Ag, Cd, Sn, Pt and Bi and alloys of these.[490, 491] However, not all of them showed a high degree of order in the final mesoporous structure. For some metals (e.g. gold) LLC templating did not lead to a mesoporous structure of the material. Besides metals also mesoporous conducting polymers[492] and prussian blue films[493] could be electrodeposited in this manner. A perpendicular pore alignment was also reported in mesoporous silica films that were electrodeposited by potential driven polycondensation of a silica sol.[494] The pore size in LLC templating can be adjusted in a range between 2 and 15nm by using surfactant molecules of different hydrocarbon chain lengths or the addition of hydrophobic additives.[246] The extremely high surface area of mesoporous materials makes them interesting candidates among others for applications in energy storage[495] (supercapacitors, batteries), energy conversion (fuel cells) and

sensors.[494, 496, 497] Here we used LLC templating to artificially increase the active surface area of the microelectrodes on the MEA by a mesoporous platium film deposit.

7.3 Characterization of unmodified MEAs

The MEAs that were used in this work were provided by the laboratory "Electronique, Systèmes de communication et Microsystèmes" (ESYCOM) in Paris (Lionel Rousseau). In order to highlight the influence of electrode diameter on intrinsic noise level, and further assess the benefit of mesoporous modifications, 56-channel MEAs with different electrode sizes (6, 8, 12, 16, 32, 64 µm) have been developed (see Figure 7.7a - c). The electrodes either were arranged in a 4×15 layout without corners, covering an area of 900×12600 μm^2 adapted to the geometry of embryonic hindbrain-spinal cord preparations, or in a 1×56 linear arrangement with an inter-electrode spacing of 150 µm. The different electrode sizes were produced from a metal layer of unique size (80 µm) covered by a silicon nitride insulation layer having an opening of variable size. These arrays were compatible with MultichannelSystems amplifier MEA1060 in order to be tested for neural recording.

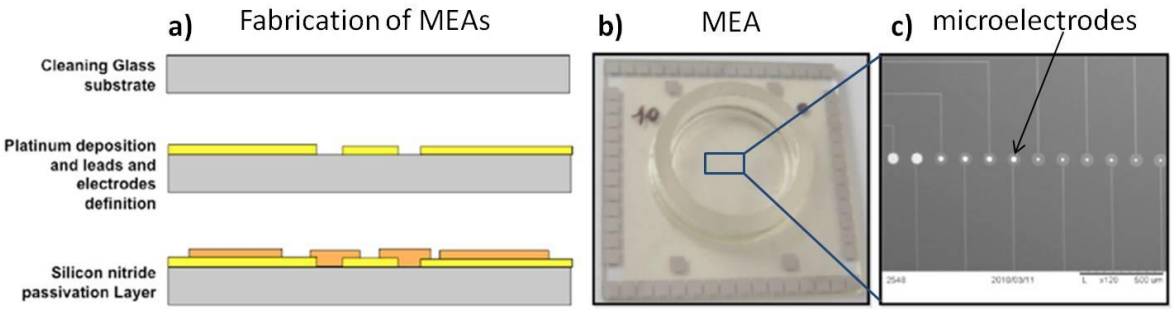

Figure 7.7: a) Microfabrication steps of the MEAs. b) Example of a MEA made on a glass substrate. c) Close-up view of microelectrodes of different sizes.

Figure 7.7a) illustrates the fabrication process of the MEAs using lithographic techniques. A detailed description of this can be found in the experimental section in chapter 9.1.5.1. Figure 7.7b) shows a digital image of such a MEA with platinum electrodes on the glass substrate. The microelectrodes are situated in the center of the ring and can be individually addressed by the metal pads at the border of the array thanks to the corresponding leads. Figure 7.7c) shows an example of resulting electrodes of different sizes on a silicon substrate. Here the electrode size

decreases from left to right (image showing 2×64µm, 4×32µm, 4×16µm and 2×12µm electrodes). All the tests and characterizations presented thereafter were performed on glass substrate MEAs.

We first assessed how the noise level of the microelectrodes depended on their diameter. To measure the intrinsic noise level of the electrodes, the electrical potential was recorded in physiological liquid (see experimental section in chapter 9.1.5.3). The standard deviation of the signal σ_s was then calculated over a 1 min recording period for each electrode of the array. Because this noise level was composed of both, the intrinsic noise level of the electrodes σ_e and the electronic noise level of the amplifiers σ_a, we assumed statistical independence of these two noise sources and estimated the intrinsic noise level of each electrode by using equation 7.2.

$$\sigma_e = \sqrt{\sigma_s^2 - \sigma_a^2} \qquad (7.2)$$

The electronic noise level of the amplifiers σ_a was measured with the amplifier inputs connected to the ground.

Figure 7.8a) shows an example of noise recording for different electrode sizes. It can be seen that the smaller the electrode, the higher the noise, with peak-to-peak amplitudes of typical measurements in the range of 40-60 µV for electrode diameters below 16 µm. This phenomenon is due to both the intrinsic thermal noise of the electrode and their higher sensitivity to environmental perturbations at high impedance.

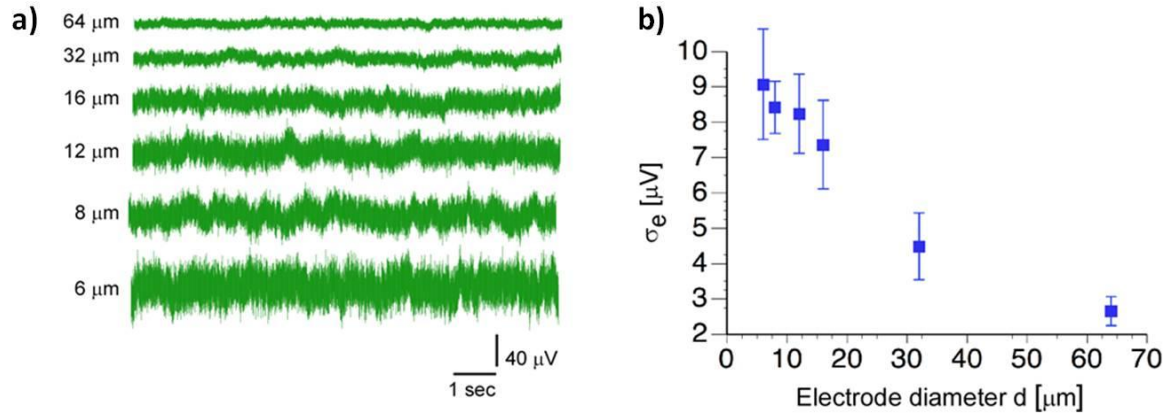

Figure 7.8: a) Example of background noise recording with electrodes of different sizes. b) Dependence of intrinsic electrode noise upon electrode diameter (average ± SD over 236 electrodes).

The strong increase of the noise level for smaller electrode sizes is problematic for the recording of neural activity, as the electrical signals originating from the electrogenic tissue often are too small to be clearly discriminated from the intrinsic noise of the electrode. [389, 390] Problems related to the thermal electrode noise have also been reported in other application fields of potentiostatic sensors, suggesting that this is a general problem encountered in microsensors.[497] The results of the noise measurement have further been quantified and are shown in Figure 7.8b). Plotting the intrinsic noise level as a function of the electrode diameter results in an inverse proportional relationship between these two parameters.

To further characterize the unmodified MEAs, the impedance of the microelectrodes was measured in physiological solution (see Chapter 9.1.5.4). Figure 7.9a) shows a plot of the impedance as a function of the electrode diameter. The impedance was found inversely proportional to the electrode diameter similarly as shown for the intrinsic noise. In the following, noise and impedance values were correlated for microelectrodes of different diameters and the experimental results were compared with the theoretical predictions shown in equation 7.1.[389, 390] Figure 7.9b) shows the noise level plotted as a function of the corresponding impedance for 63 electrodes. The electrode noise level was found to increase with the square root of the electrode impedance, which is in accordance with previous theoretical predictions.

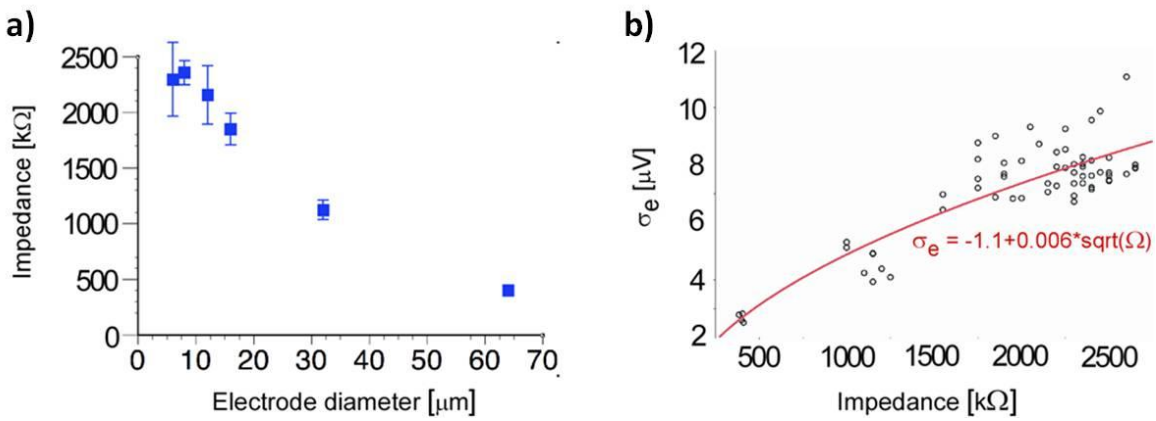

Figure 7.9: a) Dependence of electrode impedance (E = 0.3 V vs. Ag/AgCl and f = 1 kHz) on electrode diameter (n=65 electrodes). b) Square root dependence of intrinsic electrode noise on electrode impedance (n=63 electrodes) ($p<0.0001$).

The results shown here clearly indicate that the intrinsic noise depends strongly on the size or the geometric surface area of the microelectrodes. In order to increase the active surface area by keeping small overall dimensions, a mesoporous platinum overlayer is electrodeposited on the surface of the microelectrodes. This should significantly decrease the noise level, especially for microelectrodes with diameters smaller than 20µm.

7.4 Electroplating and electrochemical characterization of MEAs

Figure 7.10 outlines the key steps that were necessary to fabricate mesoporous microelectrodes on a MEA. A nanostructured metal film on the microelectrodes was obtained by electroplating a metal in the presence of lyotropic liquid crystalline phases, acting as a template.[246] Here, platinum ions that were dissolved in the aqueous domains of the liquid crystalline phases were electrochemically reduced. This resulted in a platinum deposit around the surfactant molecules that were arranged in a rod like configuration. Washing away the surfactant after the electroplating revealed an array of mesopores in the metal deposit. The mesoporous Pt film hence was an exact cast of the template structure.

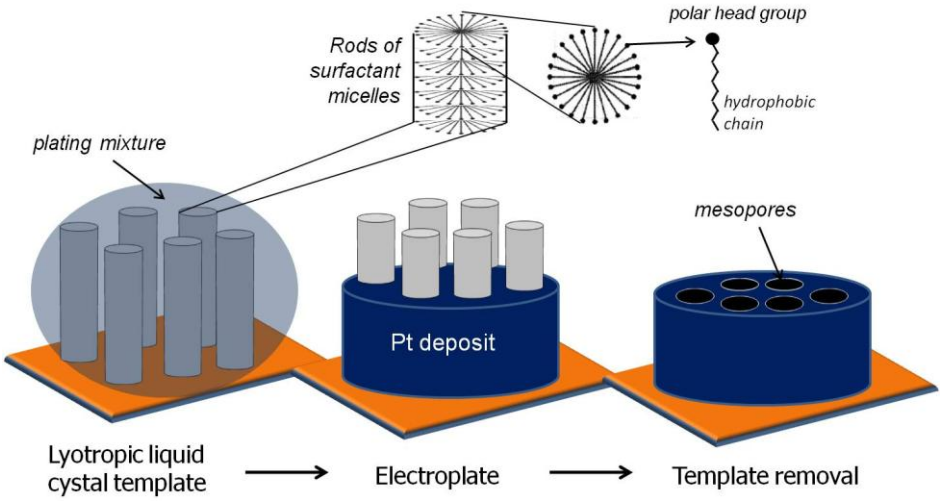

Figure 7.10: Illustration of the steps involved in the fabrication of mesoporous microelectrodes using lyotropic liquid crystal templating.

Details concerning the fabrication of the plating mixture composed of water, platinum salt and a nonionic surfactant in addition to the description of the subsequent electrodeposition onto the microelectrodes of the MEA can be found in chapter 9.1.5.2. As the plating mixture was highly viscous, owing to the high concentration of surfactant, care had to be taken to apply it to the electrodes in such a way that good physical contact is established between the electrode and the paste. The deposition of nanostructured platinum films could be either carried out simultaneously on all microelectrodes, or in separate deposition steps on single electrodes. The last option allowed to vary the applied charge density for the different electrodes on a single array and hence to examine the influence of film thickness on the properties of the modified electrodes.

Figure 7.11a) and b) show SEM images of a flat and a mesoporous 8-µm diameter microelectrode, respectively. The size of the mesopores (around 2 nm) is defined by the lyotropic liquid crystal

template used during the electrodeposition.[246] This pore size is too small to be resolved in SEM images, but nevertheless the global surface morphology of the electrodeposited film could be assessed at a lower resolution. Figure 7.11b) reveals a homogenous, very smooth platinum film. A slightly thicker deposit of platinum can be observed at the perimeter of the electrode originating from a more efficient radial diffusion occurring on microelectrodes. However for thin deposits, not exceeding an injected charge density of 2 C/cm^2 this phenomenon was not observed.

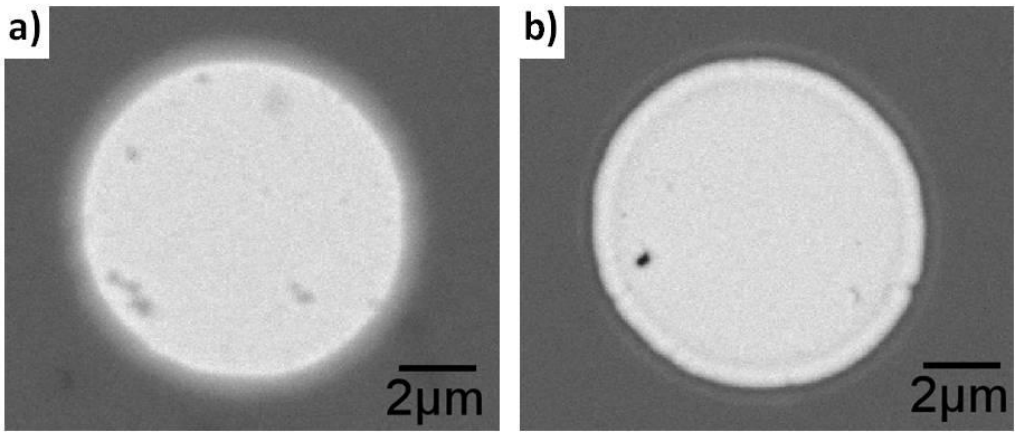

Figure 7.11: a) SEM image of a smooth platinum microelectrode on the MEA with a diameter of 8µm. b) The same microelectrode as in a) after deposition of a mesoporous platinum overlayer (applied charge density 8C/cm^2).

In order to compare flat with mesoporous microelectrodes, CV experiments were performed before and after electrodeposition. Cyclic voltammograms were recorded with a scan rate of 100 mV/s in 0.5 M sulfuric acid previously bubbled with nitrogen for 5min. Figure 7.12 shows typical CVs for 12-µm-diameter platinum microelectrodes with and without a nanostructured surface. The platinum oxide reduction current observed for the mesoporous electrode is more than one order of magnitude higher (×50) compared to the flat microelectrode. This increase is due to the well-ordered, highly accessible array of mesopores on the electrode surface.

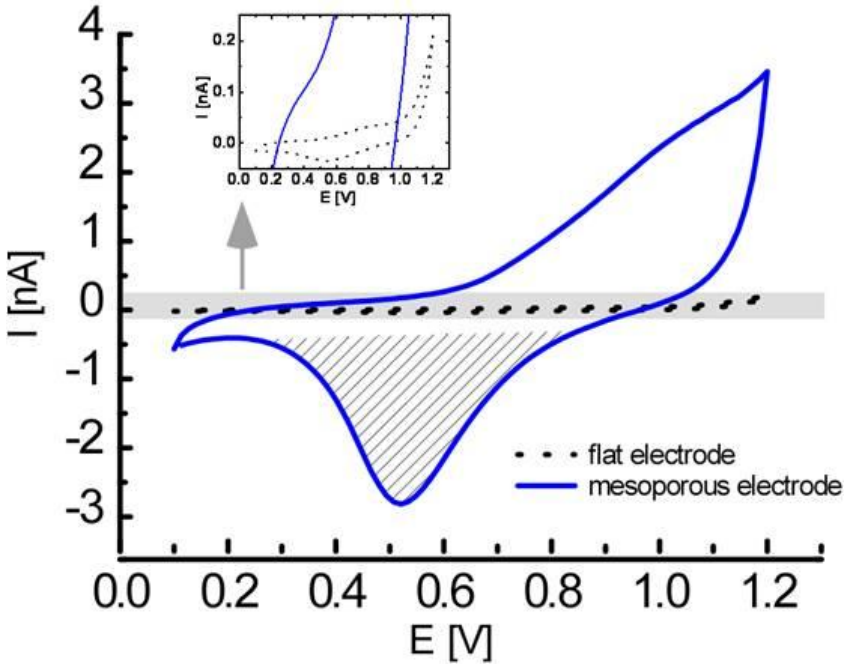

Figure 7.12 Electrochemical characterization. Comparison of the cyclic voltammograms obtained for a microelectrode (diameter: 12 µm) before (dashed line) and after (plain line) the deposition of a mesoporous platinum film on the surface. The inset zooms into the gray rectangle showing the CV of the non porous microelectrode in detail. Note the increased reduction peak of platinum oxide after porous modification (hashed area of the blue CV).

The results of the CV experiments confirm the successful deposition of mesoporous platinum films onto the surface of the microelectrodes leading to significantly increased active electrode areas.

7.5 Impedance and noise measurements with mesoporous MEAs

Impedance spectroscopy was performed (in the range 1-10000 Hz) to determine the decrease of impedance obtained by mesoporous modification (see chapter 9.1.5.4 for experimental details). Figure 7.13a) illustrates the frequency-dependent impedance amplitude of 12-µm diameter microelectrodes for different amounts of charge used for their nanostructuration. In theory, the higher the applied charge density, the thicker the mesoporous film, and thus the lower the impedance. We found that nanostructuration reduced the impedance by up to 2 orders of magnitude, the highest decrease being obtained at lower frequencies. Increasing the amount of charge used for the modification above 1 C/cm^2 improved electrode impedance only moderately. The mesoporous film behaves like the idealized de Levie model of a porous electrode. Each pore acts like a transmission line so that at low frequency the charging/discharging of the pore wall capacitance progresses deeper into the pore than at high frequency. Hence increasing film

thickness will have no effect beyond a certain value at a fixed frequency, because the innermost part of the pore will no longer contribute.[498]

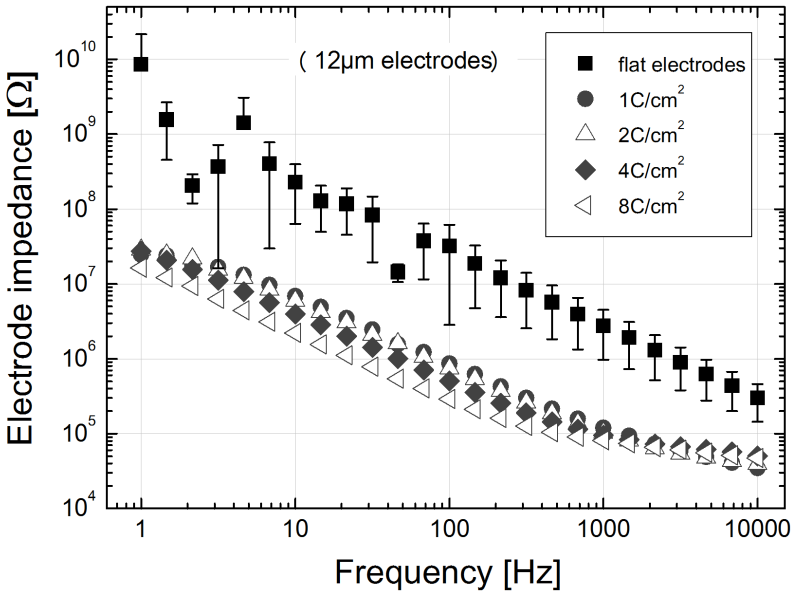

Figure 7.13: Impedance spectroscopy of flat versus mesoporous 12-µm-diameter microelectrodes modified using different charge densities.

Furthermore the impedance reduction for different electrode diameters was evaluated. This is shown in Figure 7.14 where the electrode impedance is plotted as a function of the applied charge density (which is proportional to film thickness) for different frequencies. For the 6- and 8-µm electrodes a similar trend is observed as in Figure 7.13, showing no significant decrease of the electrode impedance when the applied charge densities exceeds 1 C/cm^2. A reduction by a factor of 5-10 was generally obtained at all frequencies for the three diameters tested (6, 8, 12 microns), systematically with the strongest improvement (> 10) for 12 µm microelectrodes.

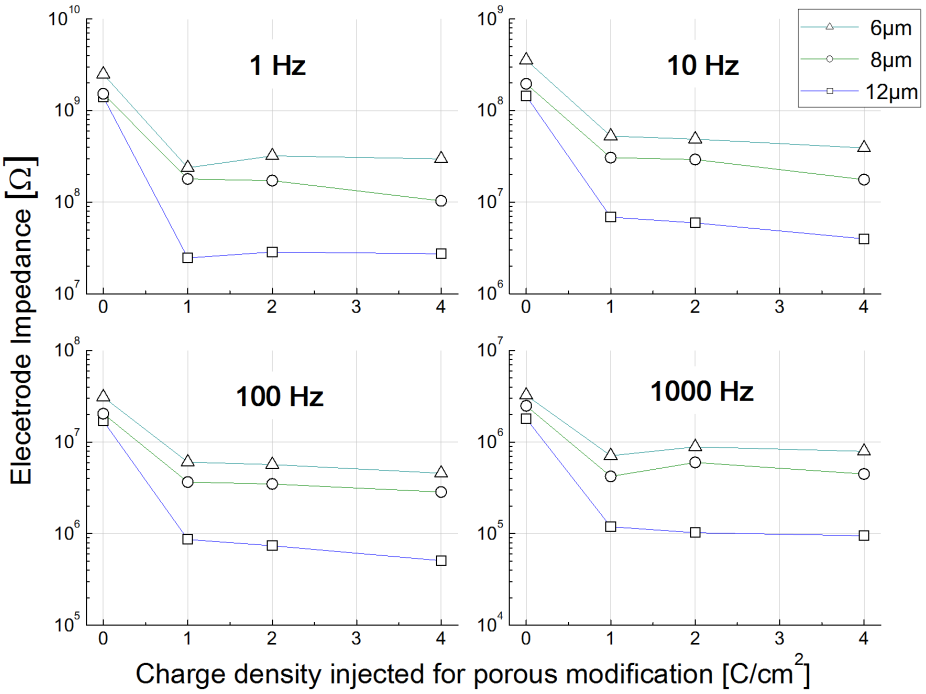

Figure 7.14: Influence of charge density on electrode impedance at 4 different frequencies for 3 electrode diameters. It can be seen that increasing charge density beyond 1 C/cm^2 only brings limited improvement of the impedance.

As expected from equation 7.1, decrease of the electrode impedance lowers also the noise level as shown in Figure 7.9b). In the following we therefore evaluated the improvement of the intrinsic noise level due to the mesoporous structuration of the electrode surface (details see section 9.1.5.3).

Figure 7.15a) shows an example of the noise signals recorded from flat and modified 12-µm diameter microelectrodes. A strong reduction of the noise level is observed for the microelectrode with a mesoporous platinum overlayer.

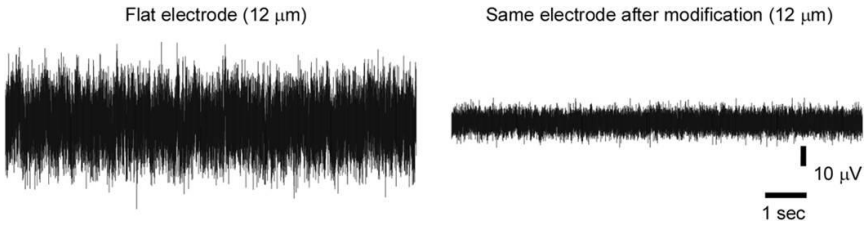

Figure 7.15: Example of the noise improvement for a 12-µm microelectrode (raw signals).

The quantitative evaluation of the noise level for the different electrode diameters is illustrated in Figure 7.16 as a function of the applied charge density. In accordance with the results obtained in the impedance measurements, no significant improvement was obtained by increasing the amount of charge injected beyond 1 C/cm^2. The lowest noise level was attained for the 12µm

mesoporous microelectrodes. The noise could also be significantly reduced for the microelectrodes with a diameter of 6 and 8µm.

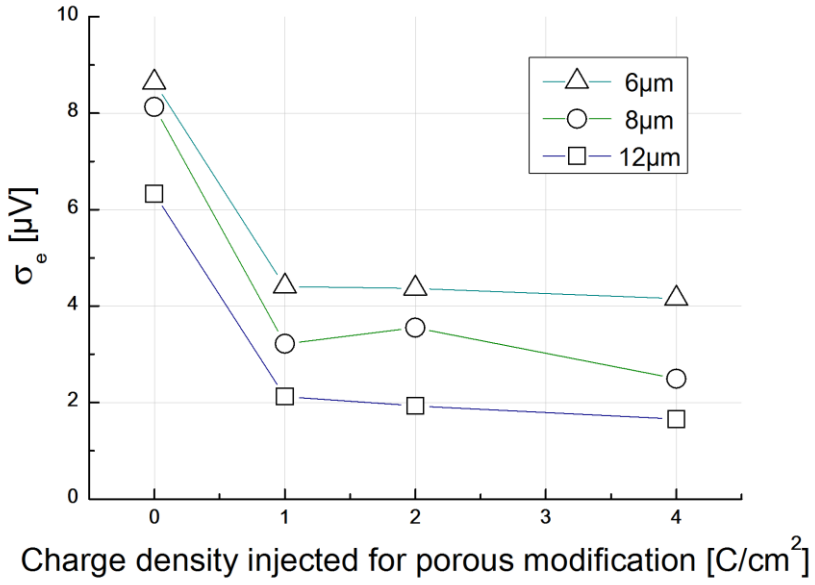

Figure 7.16: Example of noise improvement for 3 electrode diameters as a function of the charge density used for the mesoporous modification.

Finally, we tested the reproducibility of the noise improvement on an array composed of 56 12-µm microelectrodes that were modified with a charge of 4 C/cm^2.

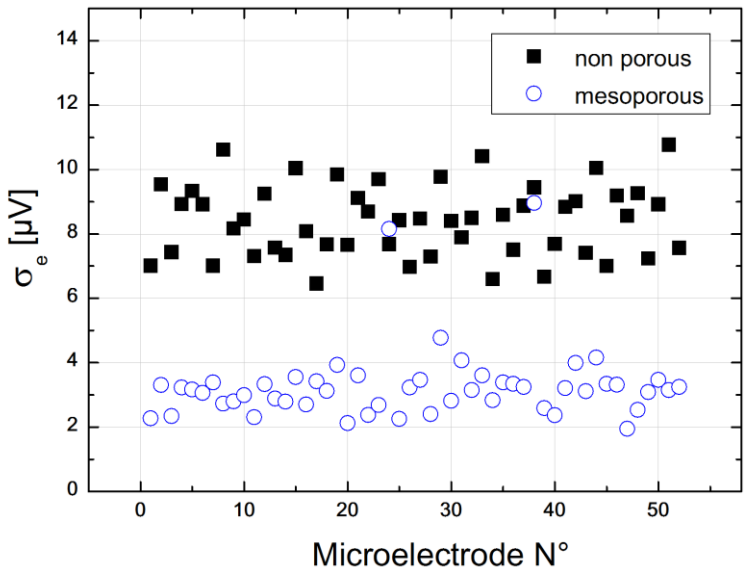

Figure 7.17: Improvement of microelectrode intrinsic noise across a whole array of 12-µm microelectrodes modified with a charge of 4 C/cm^2.

As shown in Figure 7.17, the noise improvement was homogenous across the array, decreasing from 8.4 ± 1.1 µV (mean ± SD) to 3.3 ± 1.2 µV, corresponding to an average reduction by a factor

of 2.7 ± 0.6.The most significant improvement of microelectrode performance was obtained for diameters of 12 microns, for which noise was reduced by roughly a factor of 3. As shown in Figure 7.16, the noise level of smaller microelectrodes could also be significantly reduced, although the improvement factor was slightly smaller. This may be understood in the light of a previous work detailing the influence of several parameters on electrodeposited mesoporous platinum films.[499] This study indeed showed that, when the size of the electrode is smaller than 200 µm, its roughness factor, which represents a measure for the gain of active surface area for a mesoporous compared to a smooth film, decreases for decreasing electrode size. This finding was attributed to lower efficiencies in the electrodeposition process when micro- instead of macroelectrodes were used. The fact that radial diffusion occurs more efficiently on microelectrodes can cause intermediate reaction products to diffuse away from the electrode surface before being reduced to solid platinum. The faradaic efficiency of the Pt deposition in this case varies with the size of the electrode and time and eventually because of the reduction of dissolved oxygen.[500] In the same regard, we observed during the electrodeposition experiments that a fixed amount of charge density was injected in less time into smaller microelectrodes, indicating that diffusion characteristics changed as a function of the microelectrode diameter. Nevertheless, the good reproducibility of the results obtained in different electrodeposition experiments provides evidence for the high degree of ordering of the lyotropic liquid crystal template, which is maintained in the final pore structure of the mesoporous film. It has been proposed by other authors to use mesoporous film deposits in order to improve the performance of microelectrode arrays. Mesoporous PEDOT showed improved electrical characteristics with respect to nodular PPy and PEDOT microelectrodes, but also a higher rate of cell death due to minute concentrations of remaining non-ionic surfactant. [501] Another work dealing with surfactant templated mesoporous platinum microelectrodes for a use in MEAs reported charge injection limits in the order of 3mC/cm^2 corresponding to 10-fold increase over smooth platinum surfaces. [502] However, no example for the recording of neuronal activity with such electrodes has been shown so far. Hence, in the following section, we will present the recording of neural activity in a biological tissue using mesoporous microelectrodes and compare the obtained results with those obtained for unmodified platinum microelectrodes.

7.6 Biological measurements with mesoporous MEAs

In order to show the benefits of the mesoporous structure deposited on the microelectrodes with respect to neural recording, spontaneous activity of an electrogenic tissue has been recorded with

a modified MEA. Figure 7.18a) shows the experimental setup used for the recording of neural activity. Similar to the noise recording, the potential was detected with respect to an Ag/AgCl reference electrode. Neural activity was recorded from a hindbrain-spinal cord of an embryonic mouse which was placed onto the microelectrodes of the MEA. Further experimental details can be found in chapter 9.1.5.5. Figure 7.18b) shows a view from below on the MEA containing the spinal cord fixed by a plastic net to ensure a tight contact with the microelectrodes.

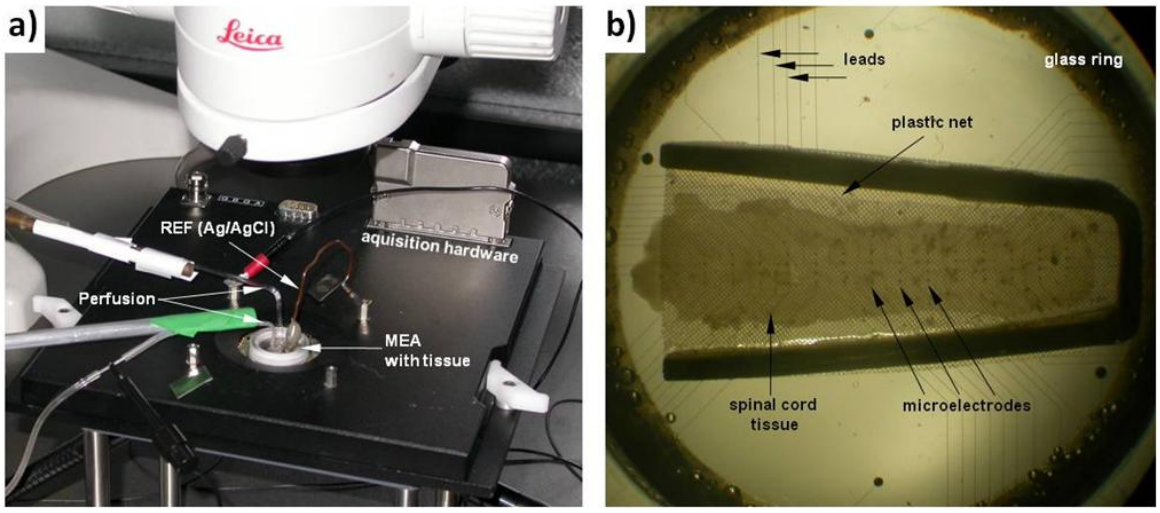

Figure 7.18 a) Optical photograph of the experimental setup used for the recording of neural activity. b) View from below on the area inside the glass ring of the MEA showing the spinal cord tissue, the plastic net ensuring tight contact between electrodes and tissue, the leads and the microelectrodes arranged in 4×15 layout.

Figure 7.19a) gives a closer view of the tissue placed on top of the microelectrodes. 12-µm diameter mesoporous platinum microelectrodes were used to record the rhythmic activity of the hindbrain-spinal cord preparations. As seen in Figure 7.19b), activity was composed of rostro-caudal waves originating in the hindbrain and propagating caudally along the spinal cord.[503] Figure 7.19c) shows a close-up view of two successive episodes recorded on 2 electrodes of the array. Each episode is composed of a local-field potential superimposed on a burst of spikes. Figure 7.19d) shows the same data segment after high-pass filtering (>200Hz), for which low-amplitude bursts of spikes can easily be seen. As illustrated in Figure 7.19e), these bursts would not have been visible using conventional 12-µm flat platinum microelectrodes.

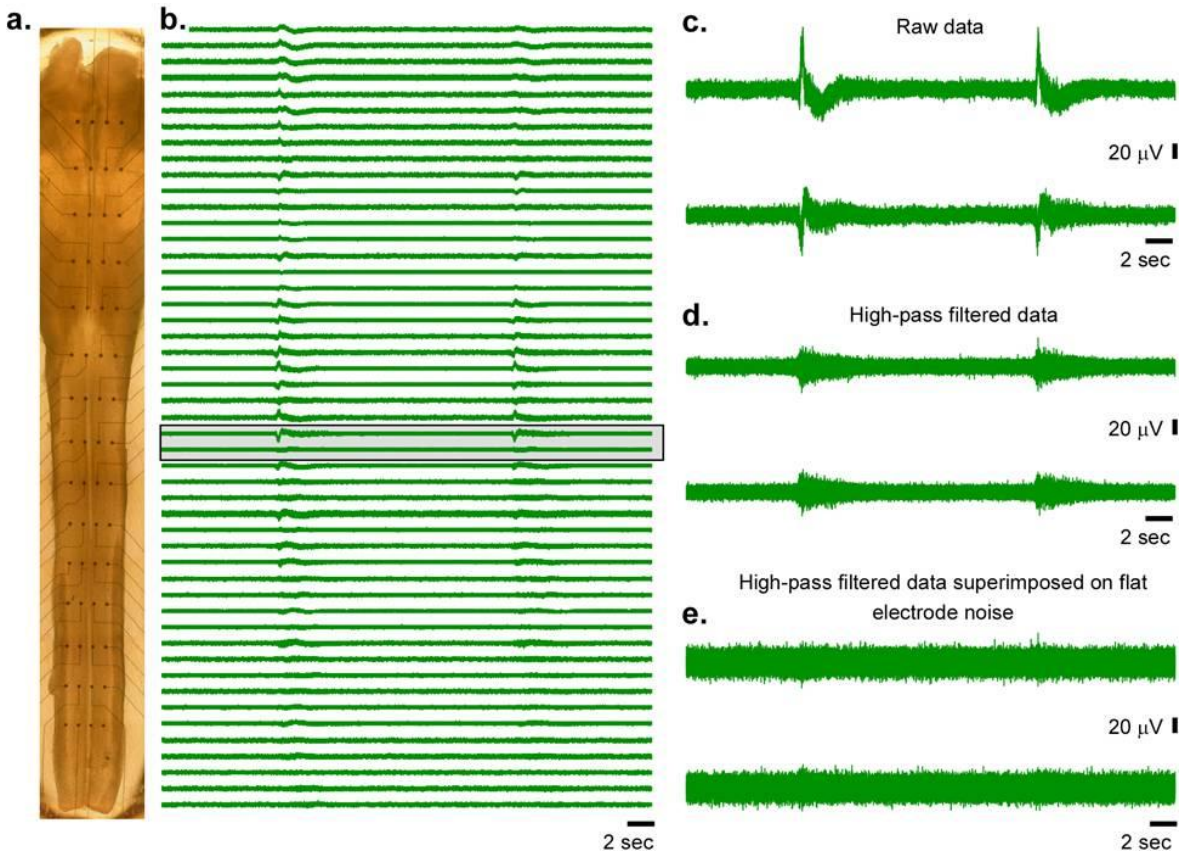

Figure 7.19 Low-noise recording of neural activity using mesoporous MEAs. a) Whole embryonic (E13.5) hindbrain-spinal cord preparation on a 4·15 mesoporous MEA. b) Example of array-wide recording of rhythmic activity in such a preparation showing two wave-like episodes. c) Close-up view of the raw signal corresponding to the 2 channels highlighted in b). Each episode is composed of a local field potential on which a burst of spikes is superimposed. d) Same signals as in c) after high-pass filtering showing only the bursts of spikes. e) Same signals as in d) but superimposed on the background noise of the same microelectrodes before mesoporous modification. This last panel shows that bursting activity would not have been detected with flat unmodified electrodes.

The mesoporous strategy thus offers an interesting alternative to other porous modifications (such as platinum black or carbon nanotubes), that have so far shown limited mechanical stability. Interestingly enough for end-users such as neuroscientists, modification of the microelectrodes can be achieved using a rather simple laboratory equipment (namely a voltage supply) from a chemical mixture quite easily prepared in the laboratory from commercially available chemicals.

8 Conclusion and Outlook

In the present work we employed template-assisted electrodeposition to produce new electrode materials with a highly controlled and ordered porosity. Besides their potential applications in various domains, they showed improved performance over non-porous electrodes in the context of the recording of neuronal activity using MEAs and the catalytic reduction of oxygen with cylindrical gold microwires. Our strategy for elaborating macroporous electrodes focused on colloidal crystal templating. The particular benefit of combining the Langmuir-Blodgett (LB) technique for the assembly of colloidal templates with electrodeposition for the subsequent infiltration of the templates consists in a very high level of control over the final architecture of macroporous electrodes. Besides controlling the number of sphere layers transferred on planar or cylindrical substrate geometries, the LB approach allowed to create a predefined sequence of layers with different particle sizes to be stacked at will within a colloidal template. Hence, in addition to templates composed of a single particle size, we generated colloidal crystals with on purpose integrated defects and gradients in terms of sphere size with a high structural integrity. During the infiltration of the templates with different metals or conducting polymers using amperometric electrodeposition we observed temporal current oscillations which were caused by a periodic variation of the electroactive area in the templates. The duration and the precision of the oscillating current signal was found to depend on the uniformity of the proceeding growth front of the electrodeposit and the organization of sphere layers in z-direction of the template. For example, templates of successive layers with increasing sphere diameters and a more progressive variation of the bead size in the different layers were more regular and resulted in more pronounced current transients. The current oscillations allowed us to follow the filling of the template with material and hence to precisely control the thickness of the macroporous electrodes.

The characterization by SEM revealed macroporous films of uniform thickness with interconnected pores on the surface of planar and cylindrical electrodes for both types of structures, composed of a single pore size or more complex architectures including integrated defect layers or pore size gradients. The active surface area of macroporous gold films could be determined from the gold-oxide stripping peak using CV and increased linearly with the number of pore layers on the electrode in accordance with geometrical considerations. We also found that the kinetics of the ion exchange with the electrolyte was enhanced in macroporous PPy compared to flat PPy films.

A miniaturization of the process could successfully be achieved by creating macroporous gold and PPy films on gold microwires with diameters between 25 and 250µm. The reduction of oxygen carried out on the gold microwires revealed higher catalytic currents combined with decreased overpotentials when macroporous instead of flat gold wires were used. This result is very promising with respect to potential applications of these porous wires in miniature biofuel cells or sensor devices. A further miniaturization of the device was proposed by generating a miniaturized electrochemical cell composed of two macroporous electrodes. This could be realized by electrodepositing a nickel film between two gold layers in a colloidal template, the former being selectively dissolved in acid. Owing to the control provided by the oscillating current signal the thickness of the macroporous electrodes as well as their respective distance can be precisely controlled. Using the stripping peak of the gold oxide reduction we showed that two independently addressable macroporous electrodes can be obtained. The concept of integrating two miniature porous electrodes in one single device may be employed to further reduce the overall dimensions in electrochemical cells as batteries or fuel cells by offering higher active electrode areas compared to devices with smooth electrodes. Future work should focus on improving the mechanical stability of the cell in order to prevent a short circuit of the two electrodes, especially after the dissolution of the colloidal template.

We also evaluated the possibility to deposit thin multilayer structures of two different materials in a colloidal monolayer in order to study the optical properties of the resulting material. Metal deposition on PPy films was strongly inhibited owing to the low and inhomogeneous conductivity in the polymer leading to less reproducible multilayer films with a rough surface structure. Amperometric deposition of alternating gold and nickel layers resulted in well defined and very smooth multilayer structures. The thickness of the individual layers could be controlled in the nanometer range by adapting the electrodeposition time. The current intensity was found to change for different deposited layers as a function of the position in the template. Either nickel layers or the colloidal template could be selectively dissolved. By comparing experimental and theoretically calculated reflectance spectra for gold/nickel multilayer samples several common features were found. The influence of different parameters including the sphere size, the number and thickness of the individual layers in the multilayer film etc. on the optical properties of the material will be examined in future work. This could enable to tailor materials offering interesting optical properties in the context of metamaterials.

Finally we used ordered mesoporous films deposited on the microelectrodes of microelectrode arrays (MEAs) to improve their performance with respect to neuronal recording. Small microelectrodes (typically <20µm) suffer from high noise levels limiting the recording sensitivity in

MEAs. It was found that the noise and the impedance strongly increase when the size of the microelectrode decreases confirming theoretical predictions. Thus we used lyotropic liquid crystalline phases as soft templates to deposit mesoporous platinum overlayers on the microelectrodes in order to artificially increase their active surface areas. The electrochemical characterization by CV confirmed the increase of the electrode area by almost two orders of magnitude for the mesoporous compared to the flat platinum film, leading to a decrease of the impedance by more than one order of magnitude and to a reduction of the noise by a factor of 2 to 3 depending on the diameter of the microelectrodes. With regard to the recording of neuronal activity we showed the utility of mesoporous film deposits by resolving neural signals on 12µm-electrodes which would have been hidden by the noise using flat platinum microelectrodes. Improved mechanical stability compared to other porous modification (e.g. platinum black or carbon nanotubes) combined with a high reproducibility are important characteristics of the mesoporous strategy. Besides the improvement with respect to the signal to noise ratio, demonstrated in this study, future work will also evaluate the performance of such nanostructured electrode arrays in the frame of neural stimulation, because the amount of injected charge should be in this case much higher for a given geometric electrode surface without damaging the electrode material.

9 Annex

9.1 Experimental section

9.1.1 Functionalization of silica spheres

The functionalization of the silica beads was carried out by adding a large amount of aminopropyltriethoxysilane directly into the nanoparticles dispersion. The amount of coupling agent was around 10 times greater than the amount necessary to cover the inorganic surface with a monolayer (the theoretical amount for such a coverage being nominally 2 molecules/nm^2). After it was left to react overnight, the mixture was held at 80°C for 1h to promote covalent bonding of the organosilane to the surface of the silica nanoparticles. The choice of aminopropyltriethoxysilane was driven by the necessity to avoid the aggregation of the silica particles either in solution before their spreading at the air–water interface or just after this step.

9.1.2 Langmuir-Blodgett experiments

9.1.2.1 Langmuir film formation

A dilute suspension of silica particles (ca. 10 mg per mL of a 80-20 v/v chloroform-ethanol mixture) was spread at the air-water interface of a Langmuir trough filled with double-distilled water. After solvent evaporation, the obtained Langmuir film was compressed stepwise (1 mN/m per 1 mN/m) until the increase of the surface pressure did not modify the area occupied by the particles at the interface. Transfer of a single layer of particles onto a clean glass slide was then carried out to verify the film quality.

9.1.2.2 Deposition of LB films onto planar substrates

Gold-coated glass slides were cut into small pieces with a surface between 3 and 4 cm^2 and used as substrates for the LB transfer. After cautious washing in several solvents (water, acetone and chloroform) to remove all possible contaminations from organic molecules, the pieces stayed in an aqueous cysteamine (Fluka) solution overnight to ensure a good hydrophilicity of the gold surface through the formation of a self-assembled monolayer. The slides were then used as substrates for the LB deposition, a computer-controlled dipping system allowing immersion and withdrawal through the interface. This procedure was automatically carried out several times, until the desired number of particle layers had been transferred.

9.1.3 Multilayers of different materials deposited in colloidal crystals

9.1.3.1 Optical characterization of metal multilayer samples

Simulations were performed with the finite-difference time-domain (FDTD) method, using MEEP, a freely available software package developed by Massachussets Institute of Technnology, with subpixel smoothing for increased accuracy. In all simulations, the colloidal monolayer has been represented by monodiperse spheres with a size of 1200nm arranged in a cubic face-centered lattice. The multilayer deposit was assumed to fill the monolayer up to a height of 1050nm, the thickness of each individual gold and nickel layer assumed to be 75nm. Refractive indices for silica and air were taken as 2.1 and 1.0, respectively, whereas for gold and nickel, they were determined from dispersion relations according to the Drude-Lorentz model using parameters given in the work from Rakic et al.[504]

The computational cell, in which the incoming wave propagates along the *z* direction, has been implemented with periodic boundary conditions in the *x* and *y* directions. The resolution of the grid has been refined such that the convergence of the results was ensured. To be in close agreement with the experimental conditions, the crystal was set on a substrate (with a dielectric constant of 2.3 on top of which a 200nm-thick gold layer was deposited) extending to the PMLs in the *z* direction.

9.1.4 Macroporous cylindrical microelectrodes

9.1.4.1 Langmuir film transfer on cylindrical gold microwires

Gold wires of various diameters (25, 50 and 250 µm) purchased from Goodfellow were cut in small pieces with a length between 2 and 3 cm and used as substrates for the LB transfer. After a cautious washing in several solvents (water, acetone and chloroform) to remove all possible contamination from organic molecules, the pieces stayed in an aqueous cysteamine (Fluka) solution overnight to ensure a good hydrophilicity of the gold surface. The small wires were then fixed with a scotch tape onto a glass support at one extremity and used for the LB deposition. A computer-controlled dipping system finally allows immersing the wires quickly through the interface before withdrawing them at a low speed (1 $mm.min^{-1}$) in order to deposit one single layer of particles during the upstroke. This procedure was automatically carried out several times, until the desired number of particle layers on the wires was reached (from 1 up to 100 layers).

9.1.4.2 Potentiostatic growth of gold and polypyrrole:

After the formation of the silica template, the gold wires were used as working electrodes in a typical three-electrode cell with a platinum or carbon grid as counter electrode and an Ag/AgCl electrode as reference. To ensure a homogeneous growth of the gold deposit, the counter electrode had a cylindrical shape and was placed symmetrically around the working electrode. A cyanide-free gold plating bath purchased from Metalor (ECF-60; gold concentration 10g.L^{-1}) was used as received for the metal deposition. A constant potential of -660mV was applied and the intensity of the faradaic current resulting from the Au ion reduction was measured with an Autolab PGSTAT 20 potentiosat (EcoChemie) system monitored by a PC running GPES 4.9 software.

9.1.5 **Measurements with MEAs**

9.1.5.1 Fabrication of MEAs (at ESYCOM, Paris)

First, an initial substrate consisting of either glass or a silicon wafer covered by a 500nm oxide layer is patterned with a metal layer defining the electrodes and their leads by a lift-off technique. For this purpose, the wafer is spin-coated with 2 µm of NLOF 2020 (Clariant) photoresist, which is further removed at specific locations by photolithography to define the geometry of the metal layer. Next, 50 nm of titanium and 150 nm of platinum are deposited over the whole wafer. The wafer is then placed in an ultrasonic bath with a dedicated remover AZ400 to remove the photoresist, leaving only the metal layer deposited directly on the initial substrate at the location of the electrodes and leads. In a second step, an insulation layer of silicon nitride is deposited by PECVD (Plasma Enhanced Chemical Vapor Deposition) over the whole wafer. This silicon nitride layer is then etched at the location of the electrodes. For this purpose, the wafer is protected by a NLOF photoresist film (2 µm), which is etched over the electrodes to define the different electrode sizes. Then, the silicon nitride is etched, using a plasma of SF6 gas at locations not protected by the photoresist (i.e. electrodes). NLOF is then removed. Finally, the wafer is cleaned and cut to separate the MEAs and an annular glass ring was glued with polydimethoxy silane (PDMS) to constitute a recording chamber around the electrodes.

9.1.5.2 Mesoporous modification of MEAs

The plating mixture consisted of a ternary system composed of 42wt% octaethylene glycol monododecyl ether ($C_{12}EO_8$, 98% purity, Sigma Aldrich), 29wt% hexachloroplatinic acid hydrate

(H_2PtCl_6 , 99.9% purity, Sigma Aldrich), and 29wt% Milli-Q reagent water (resistivity ≥ 18 MΩ cm). The components were mixed in a glass vial vigorously for several minutes at room temperature until a gel-like compound was obtained. The closed vial was then placed in a thermostated oven at ~40°C for 30 min to allow the mixture to homogenize. Subsequent mixing and heating steps were repeated until a homogeneous sample was obtained.

The viscous plating mixture was then applied simultaneously to all the microelectrodes on the MEA. An Ag/AgCl electrode and a platinum wire (diameter 1mm) were put into the plating mixture, to serve as reference and counter electrode, respectively. The microelectrodes of the MEA were the working electrodes. To reduce the platinum ions present in the plating mixture the potential was stepped from a value of +0,6 V to -0,1 V until the desired amount of charge had passed. In order to study the influence of the film thickness on the physical properties of the electrode, different amounts of charge ranging from 1 to 8 C/cm^2 were applied to single microelectrodes on the MEA. In some experiments electrodeposition was carried out simultaneously on all microelectrodes with a fixed value of charge. After the electrodeposition step the plating mixture was removed and the microelectrodes were rinsed with copious amounts of water to wash away the surfactant. To make sure that no surfactant remains in the pores, a piranha solution (be careful: dangerous solution), composed of 75vol% H_2SO_4 (95-98% H_2SO_4, Merck) and 25vol% hydrogen peroxide (H_2O_2, 30% solution, Fluka), was allowed to react with the microelectrodes for 10 min followed by a washing procedure with distilled water. Scanning electron micrographs of the electrodes were recorded with a Hitachi Tabletop Microscope TM-1000, using an accelerating voltage of 15 kV.

9.1.5.3 Thermal Noise

To measure the intrinsic noise level of the electrodes, the electrical potential was recorded for 1 minute in physiological liquid (in mM: 113 NaCl, 4.5 KCl, 2 $CaCl_2 2H_2O$, 1 $MgCl_2 6H_2O$, 25 $NaHCO_3$, 1 $NaH_2PO_4 H_2O$ and 11 D-glucose) between each of the 60 microelectrodes and an Ag/AgCl ground electrode pellet. Signals were 1100× amplified and bandpass filtered between 1 Hz and 3 kHz using MCS MEA1060-Up-BC filter amplifiers from MultichannelSystems (Reutlingen, Germany). Data were acquired at 10 kHz using two synchronized CED Power1401 AD converters and the Spike2 v6 software from Cambridge Electronic Design (Cambridge, England). The standard deviation of the signal σ_s was then calculated over a 1 min recording period for each electrode of the array. The electronic noise level of the amplifiers σ_a was measured with the amplifier inputs connected to the ground.

9.1.5.4 Impedance

Impedance measurements were performed in the same physiological liquid as that used for neural tissue recoding, using an Autolab PGSTAT 12 (EcoChemie, Metrohm) potentiostat equipped with a frequency response analyzer (FRA module). Measurements were recorded between 10 kHz and 1 Hz with an AC amplitude of 10 mV peak to peak and 6 points per frequency decades. The applied working potential during the measurement was maintained at 0.3V vs. Ag/AgCl.

9.1.5.5 Neural recordings

Neural recordings were obtained from whole embryonic mouse hindbrain-spinal cord preparations, as previously described.[503] In brief, E13.5 embryos were surgically removed from pregnant OF1 mice (Charles River Laboratories, L'Arbresle, France), previously killed by cervical dislocation. Embryos were decapitated and their whole spinal cord and hindbrain were dissected in the physiological liquid gassed with carbogen (95% O2, 5% CO2), meninges were removed, and the neural tube was opened along the rostro-caudal axis (open-book preparation) and then placed over the array of microelectrodes (4×15 layout) and superfused with physiological liquid, gassed with carbogen. A plastic net with small holes (70×70 μm^2) was laid on the neural tissue, in order to achieve a tight and uniform contact with the microelectrodes. Spontaneous rhythmic activity of this immature preparation was recorded for several hours at room temperature using the same apparatus as for the noise measurements.

9.2 Personal contribution of M. Heim to the different subtopics

Chapter II: Colloidal crystals

Based on previous reports in the literature, the Langmuir-Blodgett experiments for the assembly of colloidal crystals on samples with plane geometry have been performed by the candidate. Therefore colloidal silica particles were synthesized, surface functionalized and characterized by the candidate in collaboration with a post-doc, S. Reculusa.

Chapter III: Macroporous electrodes by infiltration of colloidal crystals

The possibility to control the film build-up due to oscillating current signals during the chronamperometric deposition into colloidal templates has been reported before. The observation of this phenomenon up to filling levels of 25 sphere layers is new and the candidate has also further extended the concept to platinum, nickel and polypyrrole. The electrochemical characterization of macroporous metal and conducting polymer samples was performed by the candidate. The active surface area was shown to increase linearly with the number of porous layers in macroporous gold electrodes, even for samples with a very high number of pore layers (up to 25).

Chapter IV: Macroporous materials with a gradient in pore diameter

The fabrication of colloidal templates with a planar defect and single-gradient structures as well as their optical characterization has been carried out by the candidate in collaboration with the post-doc. The more complex double-gradient template structures have been produced by the candidate using the LB technique by choosing an appropriate sequence of sphere size successions. The electrodeposition of PPy and gold into these templates together with the characterization of the resulting macroporous electrodes with different complex pore architectures in the SEM was done by the candidate.

Chapter V: Multilayer deposition of different materials in colloidal crystals

Templates composed of silica sphere monolayers have been assembled by the candidate using the LB technique. Alternate layers of different materials, either PPy and different metals or gold and nickel, have been electrodeposited into the templates by the candidate. The SEM characterization of the samples has been performed by the candidate, the optical characterization including the calculation of the theoretical spectra was done in collaboration with the post-doc.

Chapter VI: Catalytically active macroporous microelectrodes with cylindrical geometry

The deposition of colloidal templates on microwire substrates has been performed by the post-doc S. Reculusa. Electrodeposition experiments as well as the measurements for the determination of the active surface area and the catalytic activity of the microwires have been performed by the candidate in collaboration with the post-doc. The extension of the concept focusing on a miniaturized electrochemical cell has been undertaken by the candidate. All experiments including the electrodeposition of Au/Ni layers, the dissolution of the intermediate Ni-layer and the electrochemical characterization of the cell has been performed by the candidate. A slight modification of this approach enabled the candidate also to produce freestanding macroporous metallic films.

Chapter VII: Mesoporous microelectrodes on multielectrode arrays (MEAs) for low noise neuronal recording

Preliminary work showing promising results for the deposition of mesoporous films on microelectrodes of MEAs had been performed by a former PhD student, V. Urbanova. Based on this, electrodeposition of mesoporous platinum films on the microelectrodes of MEAs including the electrochemical characterization was performed by the candidate. In the same way the impedance and noise measurements were performed by the candidate. The test of the modified microelectrodes in neurobiological conditions was conducted by Dr. Blaise Yvert in collaboration with the candidate using an embryonic mouse spinal cord for the recording of spontaneous neuronal activity.

9.3 Publications and conference participations

9.3.1 Publications in peer-reviewed journals and patent applications

Reculusa, S.; Heim, M.; Gao, F.; Mano, N.; Ravaine, S.; Kuhn, A., "Design of catalytically active cylindrical and macroporous gold microelectrodes". *Adv. Funct. Mater.* **2011,** 21, 691-698.

Heim, M.; Reculusa, S.; Ravaine, S.; Kuhn, A., Engineering of complex macroporous materials through controlled electrodeposition in colloidal superstructures. *Adv. Funct. Mater.* **2012,** 22, 538-545.

Heim, M.; Yvert, B.; Kuhn, A., Nanostructuration strategies to enhance microelectrode array (MEA) performance for neuronal recording and stimulation. *Journal of Physiology-Paris*, DOI: 10.1016/j.jphysparis.2011.10.001.

Heim, M.; Urbanova, V.; Bouffier, L.; Mazzocco, C.; Rousseau, L.; Vytras, K.; Bartlett, P. N.; Kuhn, A.; Yvert, B., submitted.

Heim, M., Urbanova, V., Rousseau, L., Mazzocco, C., Kuhn, A., Yvert, B. (**2010**) Device to stimulate or record a signal to or from a living tissue. European Patent Application EP 10305609.9 and PCT application PCT/EP2011/059431 and PCT/EP2011/059431.

9.3.2 Conference participations

1. Surface Modification for Chemical and Biochemical Sensing (*SMCBS*), Cracow, Poland, 2009: M. Heim, P. Garrigue, S. Ravaine, N. Mano, A. Kuhn. **"**Electrochemical growth of alternating Metal/Polymer layers into a colloidal crystal template**",** Oral presentation (english)

2. XIIéme Colloque du Groupe Francais de Bioélectrochimie (*GFB*), Lacanau, France, 2010: M. Heim, V. Urbanová, F. Dubos, P.Garrigue, B.Yvert, K. Vytřas, A. Kuhn."Porous Microelectrode Arrays for Neurobiological Applications", Oral presentation (french)

3. Journée Scientifique de l'Institut des Sciences Moléculaires, Bordeaux, France, 2010: M. Heim, V. Urbanová, F. Dubos, P.Garrigue, B.Yvert, K. Vytřas, A. Kuhn." Porous Microelectrode Arrays for Neurobiological Applications ", Poster.

4. 61st Annual Meeting of the International Society of Electrochemistry (*ISE*), Nice, France, 2010: M. Heim, S. Reculusa, P. Garrigue, N. Mano, S. Ravaine , A. Kuhn."Synthesis and characterization of macroporous conducting polymers", Oral presentation (english)

5. 9th Spring Meeting of the International Society of Electrochemistry (*ISE*), Turku, Finnland, 2011: M. Heim, S. Reculusa, N. Mano, S. Ravaine , A. Kuhn. "Miniaturized cylindrical porous electrodes for sensing applications", Oral presentation (english)

6. Les Journées d' Electrochimie, Grenoble, France, 2011: M. Heim, S. Reculusa, N. Mano, S. Ravaine , A. Kuhn. "Conception d'électrodes macroporeuses avec une géométrie complexe", Oral presentation (french)

7. Journée Scientifique de l'Institut des Sciences Moléculaires, Bordeaux, France, 2011: M. Heim, S. Reculusa, N. Mano, S. Ravaine , A. Kuhn. "Conception d'électrodes macroporeuses avec une géométrie complexe", Oral presentation (french)

9.4 Remerciements

First of all I would like to thank all members of the jury committee for the evaluation of my thesis. In particular I would like to thank Prof. Orlin D. Velev and Prof. Jean-Christophe Lacroix for accepting the invitation to act as examiners (rapporteurs) in the jury.

Bei meinem Doktorvater Prof. Alexander Kuhn möchte ich mich dafür bedanken, dass er mir die Möglichkeit gegeben hat, auf einem äußerst interessanten und vielseitigen Thema zu arbeiten. Ich möchte mich bei ihm für eine exzellente Betreuung begleitet von Motivation, wissenschaftlicher Diskussion und Hilfestellung bedanken, die wesentliche Bausteine für die erfolgreiche Durchführung dieser Arbeit waren.

Je tiens également à remercier toutes les personnes avec lesquelles j'ai pu travailler durant ces trois ans. Stéphane Reculusa a contribué à la réussite d'une très grande partie des résultats présentés dans cette thèse. Pas seulement pour son support scientifique mais aussi linguistique je le remercie chaleureusement. Au même titre je voudrais remercier Serge Ravaine et Nicolas Mano pour leur soutien. Je remercie également toute l'équipe du CNIC et en particulier Blaise Yvert pour une collaboration dans une atmosphère extrêmement agréable. En tant que "correspondant allemand" j'ai pu y profiter de l'hospitalité à la française.

Je souhaite aussi remercier les personnes qui m'ont soutenu au quotidien pendant ces trois ans. Un grand merci à toute l'équipe du NSYSA pour cette atmosphère extraordinaire presque familiale. Je voudrais spécialement dire MERCI à Gabriel qui m'a beaucoup motivé et aidé dans des discussions ainsi que par sa façon de travailler. Je remercie également Yémima, Milena, Lisa, Lea, Laurent Le Henaff, Catherine, Hélène, Salem, Suresh, Jerôme, Nina et Zahra pour cette ambiance amicale dans le laboratoire ou en dehors. Je voudrais aussi remercier les anciens membres du laboratoire pour leur bon accueil, en particulier Christophe, Emelie, Veronika, Jennifer, Emeline, Emmanuel et Frédérique. Je tiens aussi à remercier Dodzi, Laurent Bouffier, Stéphane Arbault, Neso, Valérie, Isabelle, Véronique, Aline, Sandra et Bertrand. Merci à Patrick pour son aide précieux surtout au début mais aussi tout au long de ma thèse et d'avoir supporté le "Boucher de Bavière" aux matchs de foot.

En outre je remercie les personnes ayant contribué de proche ou de loin à la réussite de ce travail. Merci beaucoup à Lionel Rousseau pour la fabrication des MEAs. Merci à Beatrice Agricole et Jean-François pour m'avoir confié tous les secrets de la technique de Langmuir-Blodgett ainsi que la fourniture de billes de silice. Je remercie aussi Mme Sellier et M. Martineau au CREMEM pour

les séances de microscopie électroniques. Finalement je voudrais remercier mes colocataires ainsi que ma famille pour tout leur soutien, spécialement précieux dans des périodes comme l'écriture de ce manuscrit ainsi que la soutenance de thèse.

10 References

1. D. Linden and T. B. Reddy, *Handbook of Batteries*, **2002**, McGraw-Hill, New York.
2. A. Wieckowski and J. Norskov, *Fuel Cell Science: Theory, Fundamentals, and Biocatalysis*, **2010**, John Wiley & Sons, Hoboken, New Jersey.
3. J. Wang, *Analytical electrochemistry*, **2006**, John Wiley & Sons, Hoboken, New Jersey.
4. P. Gründler, *Chemical sensors: an introduction for scientists and engineers*, **2007**, Springer, Berlin.
5. A. S. Arico, P. Bruce, B. Scrosati, J.-M. Tarascon and W. van Schalkwijk, *Nat Mater.*, **2005**, 4, 366-377.
6. Y.-G. Guo, J.-S. Hu and L.-J. Wan, *Adv. Mater.*, **2008**, 20, 2878-2887.
7. J. Heinze, *Angew. Chem. Int. Ed.*, **1993**, 32, 1268-1288.
8. A. Schulte and W. Schuhmann, *Angew. Chem. Int. Ed.*, **2007**, 46, 8760-8777.
9. C. Amatore, S. Arbault, Y. Chen, C. Crozatier, F. Lemaître and Y. Verchier, *Angew. Chem. Int. Ed.*, **2006**, 45, 4000-4003.
10. A. Walcarius, *Anal. Bioanal.Chem.*, **2010**, 396, 261-272.
11. C. R. Martin, *Science*, **1994**, 266, 1961-1966.
12. Z. Zhang, Y. Wang, Z. Qi, W. Zhang, J. Qin and J. Frenzel, *J. Phys. Chem. C*, **2009**, 113, 12629-12636.
13. F. Marlow, Muldarisnur, P. Sharifi, R. Brinkmann and C. Mendive, *Angew. Chem. Int. Ed.*, **2009**, 48, 6212-6233.
14. D. J. Norris, E. G. Arlinghaus, L. Meng, R. Heiny and L. E. Scriven, *Adv. Mater.*, **2004**, 16, 1393-1399.
15. P. Ni, P. Dong, B. Cheng, X. Li and D. Zhang, *Adv. Mater.*, **2001**, 13, 437-441.
16. V. K. LaMer and R. H. Dinegar, *J. Am. Chem. Soc.*, **1950**, 72, 4847-4854.
17. Y. Xia, B. Gates, Y. Yin and Y. Lu, *Adv. Mater.*, **2000**, 12, 693-713.
18. W. Stöber, A. Fink and E. Bohn, *J. Colloid Interface Sci.*, **1968**, 26, 62-69.
19. H. Giesche, *J. Eur. Ceram. Soc.*, **1994**, 14, 189-204.
20. C. G. Tan, B. D. Bowen and N. Epstein, *J. Colloid Interface Sci.*, **1987**, 118, 290-293.
21. K. Nozawa, H. Gailhanou, L. Raison, P. Panizza, H. Ushiki, E. Sellier, J. P. Delville and M. H. Delville, *Langmuir*, **2004**, 21, 1516-1523.
22. G. H. Bogush, M. A. Tracy and C. F. Zukoski Iv, *J. Non-Cryst. Solids*, **1988**, 104, 95-106.
23. G. Tolnai, F. Csempesz, M. Kabai-Faix, E. Kálmán, Z. Keresztes, A. L. Kovács, J. J. Ramsden and Z. Hórvölgyi, *Langmuir*, **2001**, 17, 2683-2687.
24. Z. Wu, H. Han, W. Han, B. Kim, K. H. Ahn and K. Lee, *Langmuir*, **2007**, 23, 7799-7803.
25. S. Reculusa, P. Massé and S. Ravaine, *J. Colloid Interface Sci.*, **2004**, 279, 471-478.
26. G. M. Whitesides and B. Grzybowski, *Science*, **2002**, 295, 2418-2421.

27. Y. S. Lee, *Self-Assembly and Nanotechnology - A Force Balance Approach*, **2008**, John Wiley & Sons, Hoboken, New Jersey.

28. J. F. Galisteo-López, M. Ibisate, R. Sapienza, L. S. Froufe-Pérez, Á. Blanco and C. López, *Adv. Mater.*, **2011**, 23, 30-69.

29. F. Li, D. P. Josephson and A. Stein, *Angew. Chem. Int. Ed.*, **2011**, 50, 360-388.

30. R. Mayoral, J. Requena, J. S. Moya, C. López, A. Cintas, H. Miguez, F. Meseguer, L. Vázquez, M. Holgado and Á. Blanco, *Adv. Mater.*, **1997**, 9, 257-260.

31. H. Miguez, F. Meseguer, C. Lopez, A. Mifsud, J. S. Moya and L. Vazquez, *Langmuir*, **1997**, 13, 6009-6011.

32. L. V. Woodcock, *Nature*, **1997**, 385, 141-143.

33. K. E. Davis, W. B. Russel and W. J. Glantschnig, *J. Chem. Soc., Faraday Trans.*, **1991**, 87, 411-424.

34. V. M. Shelekhina, O. A. Prokhorov, P. A. Vityaz, A. P. Stupak, S. V. Gaponenko and N. V. Gaponenko, *Synth. Met.*, **2001**, 124, 137-139.

35. M. Holgado, F. Garcia-Santamaria, A. Blanco, M. Ibisate, A. Cintas, H. Miguez, C. J. Serna, C. Molpeceres, J. Requena, A. Mifsud, F. Meseguer and C. López, *Langmuir*, **1999**, 15, 4701-4704.

36. A. van Blaaderen, R. Ruel and P. Wiltzius, *Nature*, **1997**, 385, 321-324.

37. O. Vickreva, O. Kalinina and E. Kumacheva, *Adv. Mater.*, **2000**, 12, 110-112.

38. C. D. Dushkin, G. S. Lazarov, S. N. Kotsev, H. Yoshimura and K. Nagayama, *Colloid. Polym. Sci.*, **1999**, 277, 914-930.

39. M. Müller, R. Zentel, T. Maka, S. G. Romanov and C. M. Sotomayor Torres, *Adv. Mater.*, **2000**, 12, 1499-1503.

40. N. Denkov, O. Velev, P. Kralchevski, I. Ivanov, H. Yoshimura and K. Nagayama, *Langmuir*, **1992**, 8, 3183-3190.

41. Q. Yan, Z. Zhou and X. S. Zhao, *Langmuir*, **2005**, 21, 3158-3164.

42. Y. Li, T. Kunitake and S. Fujikawa, *Colloids Surf., A*, **2006**, 275, 209-217.

43. P. Jiang, J. F. Bertone, K. S. Hwang and V. L. Colvin, *Chem. Mater.*, **1999**, 11, 2132-2140.

44. Y. A. Vlasov, X.-Z. Bo, J. C. Sturm and D. J. Norris, *Nature*, **2001**, 414, 289-293.

45. S. Wong, V. Kitaev and G. A. Ozin, *J. Am. Chem. Soc.*, **2003**, 125, 15589-15598.

46. S. M. Yang, H. Míguez and G. A. Ozin, *Adv. Funct. Mater.*, **2002**, 12, 425-431.

47. Y. H. Ye, F. LeBlanc, A. Haché and V. V. Truong, *Appl. Phys. Lett.*, **2001**, 78, 52-54.

48. M. A. McLachlan, N. P. Johnson, R. M. D. L. Rue and D. W. McComb, *J. Mater. Chem.*, **2004**, 14, 144-150.

49. A. Hartsuiker and W. L. Vos, *Langmuir*, **2008**, 24, 4670-4675.

50. S.-L. Kuai, X.-F. Hu, A. Haché and V.-V. Truong, *J. Cryst. Growth*, **2004**, 267, 317-324.

51. F. Piret and B. L. Su, *Chem. Phys. Lett.*, **2008**, 457, 376-380.

52. J. Zhang, H. Liu, Z. Wang and N. Ming, *J. Appl. Phys.*, **2008**, 103, 013517-013520.

53. V. Kitaev and G. A. Ozin, *Adv. Mater.*, **2003**, 15, 75-78.

54. S. H. Im, M. H. Kim and O. O. Park, *Chem. Mater.*, **2003**, 15, 1797-1802.

55. A. S. Dimitrov and K. Nagayama, *Langmuir*, **1996**, 12, 1303-1311.

56. Z.-Z. Gu, A. Fujishima and O. Sato, *Chem. Mater.*, **2002**, 14, 760-765.

57. B. Griesebock, M. Egen and R. Zentel, *Chem. Mater.*, **2002**, 14, 4023-4025.

58. L. K. Teh, N. K. Tan, C. C. Wong and S. Li, *Appl. Phys. A*, **2005**, 81, 1399-1404.

59. C. Jin, M. A. McLachlan, D. W. McComb, R. M. De La Rue and N. P. Johnson, *Nano Lett.*, **2005**, 5, 2646-2650.

60. O. D. Velev and K. H. Bhatt, *Soft Matter*, **2006**, 2, 738-750.

61. K. Hasegawa, H. Nishimori, M. Tatsumisago and T. Minami, *Journal of Materials Science*, **1998**, 33, 1095-1098.

62. R. J. Kershner, J. W. Bullard and M. J. Cima, *J. Colloid Interface Sci.*, **2004**, 278, 146-154.

63. M. Giersig and P. Mulvaney, *Langmuir*, **1993**, 9, 3408-3413.

64. A. L. Rogach, N. A. Kotov, D. S. Koktysh, J. W. Ostrander and G. A. Ragoisha, *Chem. Mater.*, **2000**, 12, 2721-2726.

65. M. Böhmer, *Langmuir*, **1996**, 12, 5747-5750.

66. M. Trau, D. A. Saville and I. A. Aksay, *Science*, **1996**, 272, 706-709.

67. M. Trau, D. A. Saville and I. A. Aksay, *Langmuir*, **1997**, 13, 6375-6381.

68. Y. Solomentsev, M. Böhmer and J. L. Anderson, *Langmuir*, **1997**, 13, 6058-6068.

69. N. V. Dziomkina, M. A. Hempenius and G. J. Vancso, *Polymer*, **2009**, 50, 5713-5719.

70. P. Richetti, J. Prost and P. Barois, *J. Physique Lett.*, **1984**, 45, 1137-1143.

71. S.-R. Yeh, M. Seul and B. I. Shraiman, *Nature*, **1997**, 386, 57-59.

72. T. Gong, D. T. Wu and D. W. M. Marr, *Langmuir*, **2002**, 18, 10064-10067.

73. K.-Q. Zhang and X. Y. Liu, *Nature*, **2004**, 429, 739-743.

74. A. S. Negi, K. Sengupta and A. K. Sood, *Langmuir*, **2005**, 21, 11623-11627.

75. T. H. Zhang and X. Y. Liu, *Appl. Phys. Lett.*, **2006**, 89, 261914.

76. Y. Liu, R.-G. Xie and X.-Y. Liu, *Appl. Phys. Lett.*, **2007**, 91, 063105-063103.

77. S. O. Lumsdon, E. W. Kaler, J. P. Williams and O. D. Velev, *Appl. Phys. Lett.*, **2003**, 82, 949-951.

78. S. O. Lumsdon, E. W. Kaler and O. D. Velev, *Langmuir*, **2004**, 20, 2108-2116.

79. A. Yethiraj, J. H. J. Thijssen, A. Wouterse and A. van Blaaderen, *Adv. Mater.*, **2004**, 16, 596-600.

80. R. C. Hayward, D. A. Saville and I. A. Aksay, *Nature*, **2000**, 404, 56-59.

81. R. C. Bailey, K. J. Stevenson and J. T. Hupp, *Adv. Mater.*, **2000**, 12, 1930-1934.

82. R. Xie and X.-Y. Liu, *Adv. Funct. Mater.*, **2008**, 18, 802-809.

83. W. M. Choi and O. O. Park, *Nanotechnology*, **2006**, 17, 325.

84. R. Xie and X.-Y. Liu, *J. Am. Chem. Soc.*, **2009**, 131, 4976-4982.

85. I. Langmuir, *J. Am. Chem. Soc.*, **1917**, 39, 1848-1906.

86. K. B. Blodgett, *J. Am. Chem. Soc.*, **1935**, 57, 1007-1022.

87. I. I. I. D. H. McCullough and S. L. Regen, *Chem. Commun.*, **2004**, 2787-2791.

88. C. Zoski, G, ed., *Handbook of electrochemistry*, **2007**, Elsevier, Amsterdam.

89. M. Bardosova, F. C. Dillon, M. E. Pemble, I. M. Povey and R. H. Tredgold, *J. Colloid Interface Sci.*, **2009**, 333, 816.

90. M. Bardosova, M. E. Pemble, I. M. Povey and R. H. Tredgold, *Adv. Mater.*, **2010**, 22, 3104-3124.

91. B. van Duffel, R. H. A. Ras, F. C. De Schryver and R. A. Schoonheydt, *J. Mater. Chem.*, **2001**, 11, 3333-3336.

92. K. Muramatsu, M. Takahashi, K. Tajima and K. Kobayashi, *J. Colloid Interface Sci.*, **2001**, 242, 127-132.

93. M. Szekeres, O. Kamalin, R. A. Schoonheydt, K. Wostyn, K. Clays, A. Persoons and I. Dekany, *J. Mater. Chem.*, **2002**, 12, 3268-3274.

94. M. Bardosova, P. Hodge, L. Pach, M. E. Pemble, V. Smatko, R. H. Tredgold and D. Whitehead, *Thin Solid Films*, **2003**, 437, 276-279.

95. S. Reculusa and S. Ravaine, *Chem. Mater.*, **2003**, 15, 598-605.

96. S. G. Romanov, M. Bardosova, M. Pemble and C. M. S. Torres, *Appl. Phys. Lett.*, **2006**, 89, 043105-043103.

97. M. E. Pemble, M. Bardosova, I. M. Povey, R. H. Tredgold and D. Whitehead, *Physica B*, **2007**, 394, 233-237.

98. S. G. Romanov, M. Bardosova, D. E. Whitehead, I. M. Povey, M. Pemble and C. M. S. Torres, *Appl. Phys. Lett.*, **2007**, 90, 133101.

99. Y. Li, W. Cai and G. Duan, *Chem. Mater.*, **2007**, 20, 615-624.

100. G. Zhang and D. Wang, *Chemistry - An Asian Journal*, **2009**, 4, 236-245.

101. X. Wang, S. M. Husson, X. Qian and S. R. Wickramasinghe, *Mater. Lett.*, **2009**, 63, 1981-1983.

102. H.-L. Li, W. Dong, H.-J. Bongard and F. Marlow, *J. Phys. Chem. B*, **2005**, 109, 9939-9945.

103. S. H. Park, D. Qin and Y. Xia, *Adv. Mater.*, **1998**, 10, 1028-1032.

104. P. Jiang and M. J. McFarland, *J. Am. Chem. Soc.*, **2004**, 126, 13778-13786.

105. A. Mihi, M. Ocaña and H. Míguez, *Adv. Mater.*, **2006**, 18, 2244-2249.

106. R. M. Amos, J. G. Rarity, P. R. Tapster, T. J. Shepherd and S. C. Kitson, *Physical Review E*, **2000**, 61, 2929.

107. C. E. Finlayson, P. Spahn, D. R. E. Snoswell, G. Yates, A. Kontogeorgos, A. I. Haines, G. P. Hellmann and J. J. Baumberg, *Adv. Mater.*, **2011**, 23, 1540-1544.

108. O. L. J. Pursiainen, J. J. Baumberg, H. Winkler, B. Viel, P. Spahn and T. Ruhl, *Adv. Mater.*, **2008**, 20, 1484-1487.

109. Y. Yin and Y. Xia, *J. Am. Chem. Soc.*, **2003**, 125, 2048-2049.

110. Z. Zheng, K. Gao, Y. Luo, D. Li, Q. Meng, Y. Wang and D. Zhang, *J. Am. Chem. Soc.*, **2008**, 130, 9785-9789.

111. V. Rastogi, S. Melle, O. G. Calderón, A. A. García, M. Marquez and O. D. Velev, *Adv. Mater.*, **2008**, 20, 4263-4268.

112. O. D. Velev, B. G. Prevo and K. H. Bhatt, *Nature*, **2003**, 426, 515-516.

113. J. R. Millman, K. H. Bhatt, B. G. Prevo and O. D. Velev, *Nat Mater.*, **2005**, 4, 98-102.

114. H. Míguez, C. López, F. Meseguer, A. Blanco, L. Vázquez, R. Mayoral, M. Ocaña, V. Fornés and A. Mifsud, *Photonic crystal properties of packed submicrometric SiO2 spheres*, **1997**, AIP.

115. M. Gonçalves, J. Brás and R. Almeida, *Journal of Sol-Gel Science and Technology*, **2007**, 42, 135-143.

116. G. I. N. Waterhouse and M. R. Waterland, *Polyhedron*, **2007**, 26, 356-368.

117. E. Yablonovitch, *Phys. Rev. Lett.*, **1987**, 58, 2059.

118. S. John, *Phys. Rev. Lett.*, **1987**, 58, 2486.

119. F. Meseguer, *Colloids Surf., A*, **2005**, 270-271, 1-7.

120. J. D. Joannopoulos, P. R. Villeneuve and S. Fan, *Nature*, **1997**, 386, 143-149.

121. J. M. Lourtioz, *Photonic crystals - Towards nanoscale photonic devices*, **2008**, Springer Heidelberg.

122. J. D. Joannopoulos, S. G. Johnson, J. N. Winn and R. D. Meade, *Photonic crystals - Molding the flow of light*, **2008**, Princeton University Press, New Jersey

123. E. Yablonovitch, T. J. Gmitter and K. M. Leung, *Phys. Rev. Lett.*, **1991**, 67, 2295.

124. C. Cuisin, A. Chelnokov, D. Decanini, D. Peyrade, Y. Chen and J. M. Lourtioz, *Opt. Quantum Electron.*, **2002**, 34, 13-26.

125. S. Y. Lin, J. G. Fleming, D. L. Hetherington, B. K. Smith, R. Biswas, K. M. Ho, M. M. Sigalas, W. Zubrzycki, S. R. Kurtz and J. Bur, *Nature*, **1998**, 394, 251-253.

126. K. M. Ho, C. T. Chan, C. M. Soukoulis, R. Biswas and M. Sigalas, *Solid State Commun.*, **1994**, 89, 413-416.

127. J. G. Fleming and S.-Y. Lin, *Opt. Lett.*, **1999**, 24, 49-51.

128. S. Noda, K. Tomoda, N. Yamamoto and A. Chutinan, *Science*, **2000**, 289, 604-606.

129. S. Ogawa, M. Imada, S. Yoshimoto, M. Okano and S. Noda, *Science*, **2004**, 305, 227-229.

130. Z. Y. Li and Z. Q. Zhang, *Adv. Mater.*, **2001**, 13, 433-436.

131. M. Maldovan and E. L. Thomas, *Nat Mater.*, **2004**, 3, 593-600.

132. H. S. Sözüer, J. W. Haus and R. Inguva, *Phys. Rev. B: Condens. Matter*, **1992**, 45, 13962.

133. H. S. Sözüer and J. W. Haus, *J. Opt. Soc. Am. B*, **1993**, 10, 296-302.

134. A. Blanco, E. Chomski, S. Grabtchak, M. Ibisate, S. John, S. W. Leonard, C. Lopez, F. Meseguer, H. Miguez, J. P. Mondia, G. A. Ozin, O. Toader and H. M. van Driel, *Nature*, **2000**, 405, 437-440.

135. Q. Yan, Z. Zhou, X. S. Zhao and S. J. Chua, *Adv. Mater.*, **2005**, 17, 1917-1920.

136. Y. Jun, C. A. Leatherdale and D. J. Norris, *Adv. Mater.*, **2005**, 17, 1908-1911.

137. Q. Yan, L. Wang and X. S. Zhao, *Adv. Funct. Mater.*, **2007**, 17, 3695-3706.

138. Q. Yan, A. Chen, S. J. Chua and X. S. Zhao, *Adv. Mater.*, **2005**, 17, 2849-2853.

139. R. Pozas, A. Mihi, M. Ocaña and H. Míguez, *Adv. Mater.*, **2006**, 18, 1183-1187.

140. N. Tétreault, A. C. Arsenault, A. Mihi, S. Wong, V. Kitaev, I. Manners, H. Miguez and G. A. Ozin, *Adv. Mater.*, **2005**, 17, 1912-1916.

141. P. Massé, S. Reculusa, K. Clays and S. Ravaine, *Chem. Phys. Lett.*, **2006**, 422, 251-255.

142. J.-F. Dechézelles, P. Massé, E. Cloutet, H. Cramail and S. Ravaine, *Colloids Surf., A*, **2009**, 343, 8.

143. T. Ding, K. Song, K. Clays and C.-H. Tung, *Langmuir*, **2009**, 26, 4535-4539.

144. W. Lee, S. A. Pruzinsky and P. V. Braun, *Adv. Mater.*, **2002**, 14, 271-274.

145. S. A. Rinne, F. Garcia-Santamaria and P. V. Braun, *Nat. Photonics*, **2008**, 2, 52-56.

146. W. Cai and V. M. Shalaev, *Optical Metamaterials: Fundamentals and Applications*, **2010**, Springer, Berlin.

147. http://imagico.de/pov/metamaterials.html.

148. V. G. Veselago, *Soviet Physics Uspekhi*, **1968**, 10, 509.

149. D. R. Smith, W. J. Padilla, D. C. Vier, S. C. Nemat-Nasser and S. Schultz, *Phys. Rev. Lett.*, **2000**, 84, 4184.

150. V. M. Shalaev, *Nat. Photonics*, **2007**, 1, 41-48.

151. C. M. Soukoulis and M. Wegener, *Nat. Photonics*, **2011**, 5, 523-530.

152. C. Enkrich, M. Wegener, S. Linden, S. Burger, L. Zschiedrich, F. Schmidt, J. F. Zhou, T. Koschny and C. M. Soukoulis, *Phys. Rev. Lett.*, **2005**, 95, 203901.

153. N. Liu, H. Guo, L. Fu, S. Kaiser, H. Schweizer and H. Giessen, *Nat Mater.*, **2008**, 7, 31.

154. V. M. Shalaev, W. Cai, U. K. Chettiar, H.-K. Yuan, A. K. Sarychev, V. P. Drachev and A. V. Kildishev, *Opt. Lett.*, **2005**, 30, 3356-3358.

155. S. Zhang, W. Fan, N. C. Panoiu, K. J. Malloy, R. M. Osgood and S. R. J. Brueck, *Phys. Rev. Lett.*, **2005**, 95, 137404.

156. S. Zhang, W. Fan, K. J. Malloy, S. R. J. Brueck, N. C. Panoiu and R. M. Osgood, *J. Opt. Soc. Am. B*, **2006**, 23, 434-438.

157. J. Yao, Z. Liu, Y. Liu, Y. Wang, C. Sun, G. Bartal, A. M. Stacy and X. Zhang, *Science*, **2008**, 321, 930.

158. G. Dolling, C. Enkrich, M. Wegener, C. M. Soukoulis and S. Linden, *Opt. Lett.*, **2006**, 31, 1800-1802.

159. S. Zhang, W. Fan, K. J. Malloy, S. R. Brueck, N. C. Panoiu and R. M. Osgood, *Opt. Express*, **2005**, 13, 4922-4930.

160. J. Valentine, S. Zhang, T. Zentgraf, E. Ulin-Avila, D. A. Genov, G. Bartal and X. Zhang, *Nature*, **2008**, 455, 376.

161. C. García-Meca, R. Ortuño, F. J. Rodríguez-Fortuño, J. Martí and A. Martínez, *Opt. Lett.*, **2009**, 34, 1603-1605.

162. S. Xiao, U. K. Chettiar, A. V. Kildishev, V. P. Drachev and V. M. Shalaev, *Opt. Lett.*, **2009**, 34, 3478-3480.

163. J. Zhou, T. Koschny, M. Kafesaki and C. M. Soukoulis, *Phys. Rev. B: Condens. Matter*, **2009**, 80, 035109.

164. J. Fischer, G. von Freymann and M. Wegener, *Adv. Mater.*, **2010**, 22, 3578-3582.

165. D. Chanda, K. Shigeta, S. Gupta, T. Cain, A. Carlson, A. Mihi, A. J. Baca, G. R. Bogart, P. Braun and J. A. Rogers, *Nat. Nano*, **2011**, 6, 402-407.

166. S. Xiao, V. P. Drachev, A. V. Kildishev, X. Ni, U. K. Chettiar, H.-K. Yuan and V. M. Shalaev, *Nature*, **2010**, 466, 735-738.

167. J. B. Pendry, *Phys. Rev. Lett.*, **2000**, 85, 3966.

168. N. Fang, H. Lee, C. Sun and X. Zhang, *Science*, **2005**, 308, 534-537.

169. T. Taubner, D. Korobkin, Y. Urzhumov, G. Shvets and R. Hillenbrand, *Science*, **2006**, 313, 1595.

170. U. Leonhardt, *Science*, **2006**, 312, 1777-1780.

171. J. B. Pendry, D. Schurig and D. R. Smith, *Science*, **2006**, 312, 1780-1782.

172. D. Schurig, J. J. Mock, B. J. Justice, S. A. Cummer, J. B. Pendry, A. F. Starr and D. R. Smith, *Science*, **2006**, 314, 977-980.

173. L. H. Gabrielli, J. Cardenas, C. B. Poitras and M. Lipson, *Nat. Photonics*, **2009**, 3, 461-463.

174. J. Valentine, J. Li, T. Zentgraf, G. Bartal and X. Zhang, *Nat Mater.*, **2009**, 8, 568-571.

175. T. Ergin, N. Stenger, P. Brenner, J. B. Pendry and M. Wegener, *Science*, **2010**, 328, 337-339.

176. R. Liu, C. Ji, J. J. Mock, J. Y. Chin, T. J. Cui and D. R. Smith, *Science*, **2009**, 323, 366-369.

177. A. Cho, *Science*, **2010**, 328, 1621.

178. R. Fenollosa and F. Meseguer, *Adv. Mater.*, **2003**, 15, 1282-1285.

179. A. Stein, F. Li and N. R. Denny, *Chem. Mater.*, **2007**, 20, 649-666.

180. W. Dong, H. Bongard, B. Tesche and F. Marlow, *Adv. Mater.*, **2002**, 14, 1457-1460.

181. F. Marlow and W. Dong, *ChemPhysChem*, **2003**, 4, 549-554.

182. P. Jiang, *Angew. Chem. Int. Ed.*, **2004**, 43, 5625-5628.

183. A. A. Zakhidov, R. H. Baughman, Z. Iqbal, C. Cui, I. Khayrullin, S. O. Dantas, J. Marti and V. G. Ralchenko, *Science*, **1998**, 282, 897-901.

184. J. S. King, E. Graugnard and C. J. Summers, *Adv. Mater.*, **2005**, 17, 1010-1013.

185. S. Reculusa, B. Agricole, A. Derré, M. Couzi, E. Sellier, S. Ravaine and P. Delhaès, *Adv. Mater.*, **2006**, 18, 1705-1708.

186. H. Miguez, N. Tetreault, B. Hatton, S. M. Yang, D. Perovic and G. A. Ozin, *Chem. Commun.*, **2002**, 2736-2737.

187. E. Palacios-Lidón, J. F. Galisteo-López, B. H. Juárez and C. López, *Adv. Mater.*, **2004**, 16, 341-345.

188. A. Rugge, J. S. Becker, R. G. Gordon and S. H. Tolbert, *Nano Lett.*, **2003**, 3, 1293-1297.

189. J. S. King, D. P. Gaillot, E. Graugnard and C. J. Summers, *Adv. Mater.*, **2006**, 18, 1063-1067.

190. B. T. Holland, C. F. Blanford and A. Stein, *Science*, **1998**, 281, 538-540.

191. J. E. G. J. Wijnhoven and W. L. Vos, *Science*, **1998**, 281, 802-804.

192. Y. Cao, Y. Wang, Y. Zhu, H. Chen, Z. Li, J. Ding and Y. Chi, *Superlattices Microstruct.*, **2006**, 40, 155-160.

193. Z. Zhong, Y. Yin, B. Gates and Y. Xia, *Adv. Mater.*, **2000**, 12, 206-209.

194. J. P. Bosco, K. Sasaki, M. Sadakane, W. Ueda and J. G. Chen, *Chem. Mater.*, **2009**, 22, 966-973.

195. Y. Ma, J. F. Chen, Y. Ren and X. Tao, *Colloids Surf., A*, **2010**, 370, 129-135.

196. P. Jiang, K. S. Hwang, D. M. Mittleman, J. F. Bertone and V. L. Colvin, *J. Am. Chem. Soc.*, **1999**, 121, 11630-11637.

197. S. H. Park and Y. Xia, *Adv. Mater.*, **1998**, 10, 1045-1048.

198. S. A. Johnson, P. J. Ollivier and T. E. Mallouk, *Science*, **1999**, 283, 963.

199. H. Míguez, F. Meseguer, C. López, F. López-Tejeira and J. Sánchez-Dehesa, *Adv. Mater.*, **2001**, 13, 393-396.

200. D. P. Puzzo, A. C. Arsenault, I. Manners and G. A. Ozin, *Angew. Chem. Int. Ed.*, **2009**, 48, 943-947.

201. F. Yan and W. A. Goedel, *Adv. Mater.*, **2004**, 16, 911-915.

202. P. V. Braun, R. W. Zehner, C. A. White, M. K. Weldon, C. Kloc, S. S. Patel and P. Wiltzius, *Adv. Mater.*, **2001**, 13, 721-724.

203. O. D. Velev, P. M. Tessier, A. M. Lenhoff and E. W. Kaler, *Nature*, **1999**, 401, 548-548.

204. E. Arsenault, N. Soheilnia and G. A. Ozin, *ACS Nano*, **2011**, 5, 2984-2988.

205. G. Subramanian, V. N. Manoharan, J. D. Thorne and D. J. Pine, *Adv. Mater.*, **1999**, 11, 1261-1265.

206. P. M. Tessier, O. D. Velev, A. T. Kalambur, A. M. Lenhoff, J. F. Rabolt and E. W. Kaler, *Adv. Mater.*, **2001**, 13, 396-400.

207. D. Wang, J. Li, C. T. Chan, V. Salgueiriño-Maceira, L. M. Liz-Marzán, S. Romanov and F. Caruso, *Small*, **2005**, 1, 122-130.

208. Y. Zhao, X. Zhao, J. Hu, M. Xu, W. Zhao, L. Sun, C. Zhu, H. Xu and Z. Gu, *Adv. Mater.*, **2009**, 21, 569-572.

209. N. Sapoletova, T. Makarevich, K. Napolskii, E. Mishina, A. Eliseev, A. van Etteger, T. Rasing and G. Tsirlina, *Phys. Chem. Chem. Phys.*, **2010**, 12, 15414-15422.

210. L. Santos, P. Martin, J. Ghilane, P.-C. Lacaze, H. Randriamahazaka, L. M. Abrantes and J.-C. Lacroix, *Electrochem. Commun.*, **2010**, 12, 872-875.

211. X. Meng, R. Al-Salman, J. Zhao, N. Borissenko, Y. Li and F. Endres, *Angew. Chem. Int. Ed.*, **2009**, 48, 2703-2707.

212. P. N. Bartlett, P. R. Birkin, M. A. Ghanem and C.-S. Toh, *J. Mater. Chem.*, **2001**, 11, 849-853.

213. P. Jiang, J. Cizeron, J. F. Bertone and V. L. Colvin, *J. Am. Chem. Soc.*, **1999**, 121, 7957-7958.

214. P. N. Bartlett, P. R. Birkin and M. A. Ghanem, *Chem. Commun.*, **2000**, 1671-1672.

215. P. N. Bartlett, J. J. Baumberg, P. R. Birkin, M. A. Ghanem and M. C. Netti, *Chem. Mater.*, **2002**, 14, 2199-2208.

216. S. Ben-Ali, D. A. Cook, S. A. G. Evans, A. Thienpont, P. N. Bartlett and A. Kuhn, *Electrochem. Commun.*, **2003**, 5, 747-751.

217. R. Szamocki, S. Reculusa, S. Ravaine, P. N. Bartlett, A. Kuhn and R. Hempelmann, *Angew. Chem. Int. Ed.*, **2006**, 45, 1317-1321.

218. R. Szamocki, A. Velichko, C. Holzapfel, F. Mücklich, S. Ravaine, P. Garrigue, N. Sojic, R. Hempelmann and A. Kuhn, *Anal. Chem.*, **2007**, 79, 533-539.

219. A. Altube, Á. Blanco and C. López, *Mater. Lett.*, **2008**, 62, 2677-2680.

220. P. N. Bartlett, J. J. Baumberg, S. Coyle and M. E. Abdelsalam, *Faraday Discuss.*, **2004**, 125, 117-132.

221. T. Sumida, Y. Wada, T. Kitamura and S. Yanagida, *Langmuir*, **2002**, 18, 3886-3894.

222. P. N. Bartlett, M. A. Ghanem, I. S. El Hallag, P. de Groot and A. Zhukov, *J. Mater. Chem.*, **2003**, 13, 2596-2602.

223. Y.-W. Chung, I.-C. Leu, J.-H. Lee, J.-H. Yen and M.-H. Hon, *J. Electrochem. Soc.*, **2007**, 154, E77-E83.

224. Y. Hao, F. Q. Zhu, C. L. Chien and P. C. Searson, *J. Electrochem. Soc.*, **2007**, 154, D65-D69.

225. X. Yu, Y. J. Lee, R. Furstenberg, J. O. White and P. V. Braun, *Adv. Mater.*, **2007**, 19, 1689-1692.

226. H. Zhang, X. Yu and P. V. Braun, *Nat. Nano*, **2011**, 6, 277-281.

227. V. Urbanová, M. Bartoš, K. Vytřas and A. Kuhn, *Electroanalysis*, **2010**, 22, 1524-1530.

228. V. Urbanová, K. Vytras and A. Kuhn, *Electrochem. Commun.*, **2010**, 12, 114-117.

229. T. Sumida, Y. Wada, T. Kitamura and S. Yanagida, *Chem. Commun.*, **2000**, 1613-1614.

230. T. Cassagneau and F. Caruso, *Adv. Mater.*, **2002**, 14, 34-38.

231. S. Tian, J. Wang, U. Jonas and W. Knoll, *Chem. Mater.*, **2005**, 17, 5726-5730.

232. P. V. Braun and P. Wiltzius, *Nature*, **1999**, 402, 603-604.

233. T. Sumida, Y. Wada, T. Kitamura and S. Yanagida, *Chem. Lett.*, **2001**, 30, 38-39.

234. Y. Yang, H. Yan, Z. Fu, B. Yang, J. Zuo and S. Fu, *Solid State Commun.*, **2006**, 139, 218-221.

235. T. Sumida, Y. Wada, T. Kitamura and S. Yanagida, *Chem. Lett.*, **2002**, 31, 180-181.

236. P. N. Bartlett, T. Dunford and M. A. Ghanem, *J. Mater. Chem.*, **2002**, 12, 3130-3135.

237. J. Hu, M. Abdelsalam, P. Bartlett, R. Cole, Y. Sugawara, J. Baumberg, S. Mahajan and G. Denuault, *J. Mater. Chem.*, **2009**, 19, 3855-3858.

238. J. Lenz, V. Trieu, R. Hempelmann and A. Kuhn, *Electroanalysis*, **2011**, 23, 1186-1192.

239. T. M. Benedetti, V. R. Goncales, D. F. S. Petri, S. I. C. De Torresi and R. M. Torresi, *J. Braz. Chem. Soc.*, **2010**, 21, 1704-1709.

240. Y. F. Yuan, X. H. Xia, J. B. Wu, Y. B. Chen, J. L. Yang and S. Y. Guo, *Electrochim. Acta*, **2011**, 56, 1208-1212.

241. V. R. Goncales, R. P. Salvador, M. R. Alcantara and S. I. C. d. Torresi, *J. Electrochem. Soc.*, **2008**, 155, K140-K145.

242. R. Szamocki, A. Velichko, F. Mücklich, S. Reculusa, S. Ravaine, S. Neugebauer, W. Schuhmann, R. Hempelmann and A. Kuhn, *Electrochem. Commun.*, **2007**, 9, 2121-2127.

243. K. S. Choi, E. W. McFarland and G. D. Stucky, *Adv. Mater.*, **2003**, 15, 2018-2021.

244. R. Szamocki, *Synthèse Contrôllée d'électrodes macroporeuses pour des applications électrocatalytiques*, Phd thesis, **2006**, University Bordeaux I / Universität des Saarlandes, Bordeaux / Saarbrücken.

245. S. Trasatti and O. A. Petrii, *J. Electroanal. Chem.*, **1992**, 327, 353-376.

246. G. S. Attard, P. N. Bartlett, N. R. B. Coleman, J. M. Elliott, J. R. Owen and J. H. Wang, *Science*, **1997**, 278, 838-840.

247. H. Yamada, H. Nakamura, F. Nakahara, I. Moriguchi and T. Kudo, *J. Phys. Chem. C*, **2006**, 111, 227-233.

248. Y. Yamauchi and K. Kuroda, *Electrochem. Commun.*, **2006**, 8, 1677-1682.

249. B. Zhao and M. M. Collinson, *Chem. Mater.*, **2010**, 22, 4312-4319.

250. M. Singh, P. K. Kathuroju and N. Jampana, *Sens. Actuators, B*, **2009**, 143, 430-443.

251. E. Smela, *Adv. Mater.*, **1999**, 11, 1343-1345.

252. M. R. Gandhi, P. Murray, G. M. Spinks and G. G. Wallace, *Synth. Met.*, **1995**, 73, 247-256.

253. T. F. Otero and M. T. Cortés, *Adv. Mater.*, **2003**, 15, 279-282.

254. E. Smela, *Adv. Mater.*, **2003**, 15, 481-494.

255. W. Sun and X. Chen, *J. Power Sources*, **2009**, 193, 924.

256. U. Lange, N. V. Roznyatovskaya and V. M. Mirsky, *Anal. Chim. Acta*, **2008**, 614, 1.

257. A. Malinauskas, *Synth. Met.*, **1999**, 107, 75.

258. V. G. Khomenko, V. Z. Barsukov and A. S. Katashinskii, *Electrochim. Acta*, **2005**, 50, 1675.

259. R. A. Green, N. H. Lovell, G. G. Wallace and L. A. Poole-Warren, *Biomaterials*, **2008**, 29, 3393-3399.

260. A. Mollahosseini and E. Noroozian, *Synth. Met.*, **2009**, 159, 1247-1254.

261. T. Cassagneau and F. Caruso, *Adv. Mater.*, **2002**, 14, 1629-1633.

262. W. Qian, Z.-Z. Gu, A. Fujishima and O. Sato, *Langmuir*, **2002**, 18, 4526-4529.

263. C. Y. Kuo, S. Y. Lu, S. Chen, M. Bernards and S. Jiang, *Sens. Actuators, B*, **2007**, 124, 452-458.

264. G. Kang, R. B. Borgens and Y. Cho, *Langmuir*, **2011**, 27, 6179-6184.

265. L. Zhao, L. Tong, C. Li, Z. Gu and G. Shi, *J. Mater. Chem.*, **2009**, 19, 1653-1658.

266. L. Xu, J. Wang, Y. Song and L. Jiang, *Chem. Mater.*, **2008**, 20, 3554-3556.

267. G. G. Wallace, G. M. Spinks and L. A. P. Kane-Maguire, *Conductive electroactive polymers: intelligent polymer systems*, **2009**, CRC Press, Boca Raton.

268. S. Ghosh, G. A. Bowmaker, R. P. Cooney and J. M. Seakins, *Synth. Met.*, **1998**, 95, 63.

269. T. A. Skotheim and J. R. Reynolds, *Handbook of conducting polymers*, **2007**, CRC, Boca Raton.

270. E. A. Bazzaoui, S. Aeiyach and P. C. Lacaze, *Synth. Met.*, **1996**, 83, 159-165.

271. Y. Z. Wang, R. G. Sun, D. K. Wang, T. M. Swager and A. J. Epstein, *Appl. Phys. Lett.*, **1999**, 74, 2593-2595.

272. J. Ge and Y. Yin, *Angew. Chem. Int. Ed.*, **2011**, 50, 1492-1522.

273. J. Shin, P. V. Braun and W. Lee, *Sens. Actuators, B*, **2010**, 150, 183-190.

274. Y. Takeoka and M. Watanabe, *Langmuir*, **2003**, 19, 9104-9106.

275. D. Nakayama, Y. Takeoka, M. Watanabe and K. Kataoka, *Angew. Chem. Int. Ed.*, **2003**, 42, 4197-4200.

276. J. M. Weissman, H. B. Sunkara, A. S. Tse and S. A. Asher, *Science*, **1996**, 274, 959-963.

277. N. Griffete, H. Frederich, A. Maitre, M. M. Chehimi, S. Ravaine and C. Mangeney, *J. Mater. Chem.*, **2011**, 21, 13052-13055.

278. J. Zhou, C. Q. Sun, K. Pita, Y. L. Lam, Y. Zhou, S. L. Ng, C. H. Kam, L. T. Li and Z. L. Gui, *Appl. Phys. Lett.*, **2001**, 78, 661-663.

279. A. C. Arsenault, V. Kitaev, I. Manners, G. A. Ozin, A. Mihi and H. Miguez, *J. Mater. Chem.*, **2005**, 15, 133-138.

280. E. Tian, J. Wang, Y. Zheng, Y. Song, L. Jiang and D. Zhu, *J. Mater. Chem.*, **2008**, 18, 1116-1122.

281. K.-U. Jeong, J.-H. Jang, C. Y. Koh, M. J. Graham, K.-Y. Jin, S.-J. Park, C. Nah, M.-H. Lee, S. Z. D. Cheng and E. L. Thomas, *J. Mater. Chem.*, **2009**, 19, 1956-1959.

282. J. H. Holtz and S. A. Asher, *Nature*, **1997**, 389, 829-832.

283. K. Lee and S. A. Asher, *J. Am. Chem. Soc.*, **2000**, 122, 9534-9537.

284. J. H. Holtz, J. S. W. Holtz, C. H. Munro and S. A. Asher, *Anal. Chem.*, **1998**, 70, 780-791.

285. V. L. Alexeev, A. C. Sharma, A. V. Goponenko, S. Das, I. K. Lednev, C. S. Wilcox, D. N. Finegold and S. A. Asher, *Anal. Chem.*, **2003**, 75, 2316-2323.

286. Y.-J. Lee, S. A. Pruzinsky and P. V. Braun, *Langmuir*, **2004**, 20, 3096-3106.

287. K. Sumioka, H. Kayashima and T. Tsutsui, *Adv. Mater.*, **2002**, 14, 1284-1286.

288. S. H. Foulger, P. Jiang, A. Lattam, D. W. Smith, J. Ballato, D. E. Dausch, S. Grego and B. R. Stoner, *Adv. Mater.*, **2003**, 15, 685-689.

289. A. C. Arsenault, T. J. Clark, G. von Freymann, L. Cademartiri, R. Sapienza, J. Bertolotti, E. Vekris, S. Wong, V. Kitaev, I. Manners, R. Z. Wang, S. John, D. Wiersma and G. A. Ozin, *Nat Mater.*, **2006**, 5, 179-184.

290. G. A. Ozin and A. C. Arsenault, *Mater. Today*, **2008**, 11, 44-51.

291. J. R. Lawrence, Y. Ying, P. Jiang and S. H. Foulger, *Adv. Mater.*, **2006**, 18, 300-303.

292. B. Li, J. Zhou, L. Li, X. J. Wang, X. H. Liu and J. Zi, *Appl. Phys. Lett.*, **2003**, 83, 4704-4706.

293. A. C. Arsenault, D. P. Puzzo, I. Manners and G. A. Ozin, *Nat. Photonics*, **2007**, 1, 468-472.

294. J. Ge, Y. Hu and Y. Yin, *Angew. Chem. Int. Ed.*, **2007**, 46, 7428-7431.

295. J. Ge and Y. Yin, *Adv. Mater.*, **2008**, 20, 3485-3491.

296. H. Fudouzi and Y. Xia, *Adv. Mater.*, **2003**, 15, 892-896.

297. P. Jiang, D. W. Smith, J. M. Ballato and S. H. Foulger, *Adv. Mater.*, **2005**, 17, 179-184.

298. J. Ge, J. Goebl, L. He, Z. Lu and Y. Yin, *Adv. Mater.*, **2009**, 21, 4259-4264.

299. S. Nishimura, N. Abrams, B. A. Lewis, L. I. Halaoui, T. E. Mallouk, K. D. Benkstein, J. van de Lagemaat and A. J. Frank, *J. Am. Chem. Soc.*, **2003**, 125, 6306-6310.

300. L. I. Halaoui, N. M. Abrams and T. E. Mallouk, *J. Phys. Chem. B*, **2005**, 109, 6334-6342.

301. S. Guldin, S. Hüttner, M. Kolle, M. E. Welland, P. Müller-Buschbaum, R. H. Friend, U. Steiner and N. Tetreault, *Nano Lett.*, **2010**, 10, 2303-2309.

302. A. Mihi and H. Miguez, *J. Phys. Chem. B*, **2005**, 109, 15968-15976.

303. H. A. Atwater and A. Polman, *Nat Mater.*, **2010**, 9, 205-213.

304. R. M. Cole, J. J. Baumberg, F. J. Garcia de Abajo, S. Mahajan, M. Abdelsalam and P. N. Bartlett, *Nano Lett.*, **2007**, 7, 2094-2100.

305. D. M. Kuncicky, B. G. Prevo and O. D. Velev, *J. Mater. Chem.*, **2006**, 16, 1207-1211.

306. M. E. Abdelsalam, P. N. Bartlett, T. Kelf and J. Baumberg, *Langmuir*, **2005**, 21, 1753-1757.

307. P. M. Tessier, O. D. Velev, A. T. Kalambur, J. F. Rabolt, A. M. Lenhoff and E. W. Kaler, *J. Am. Chem. Soc.*, **2000**, 122, 9554-9555.

308. S. Mahajan, J. Richardson, T. Brown and P. N. Bartlett, *J. Am. Chem. Soc.*, **2008**, 130, 15589-15601.

309. D. K. Corrigan, N. Gale, T. Brown and P. N. Bartlett, *Angew. Chem. Int. Ed.*, **2010**, 49, 5917-5920.

310. T. V. Teperik, F. J. Garcia de Abajo, A. G. Borisov, M. Abdelsalam, P. N. Bartlett, Y. Sugawara and J. J. Baumberg, *Nat. Photonics*, **2008**, 2, 299-301.

311. B. Gates, Y. Yin and Y. Xia, *Chem. Mater.*, **1999**, 11, 2827-2836.

312. X. Wang, S. M. Husson, X. Qian and S. R. Wickramasinghe, *J. Membr. Sci.*, **2010**, 365, 302-310.

313. S. Ben-Ali, D. A. Cook, P. N. Bartlett and A. Kuhn, *J. Electroanal. Chem.*, **2005**, 579, 181-187.

314. Y. Bon Saint Côme, H. Lalo, Z. Wang, M. Etienne, J. Gajdzik, G.-W. Kohring, A. Walcarius, R. Hempelmann and A. Kuhn, *Langmuir*, accepted.

315. T. Cassagneau and F. Caruso, *Adv. Mater.*, **2002**, 14, 1837-1841.

316. J.-D. Qiu, H.-Z. Peng, R.-P. Liang and M. Xiong, *Electroanalysis*, **2007**, 19, 1201-1206.

317. X. Chen, Y. Wang, J. Zhou, W. Yan, X. Li and J.-J. Zhu, *Anal. Chem.*, **2008**, 80, 2133-2140.

318. J. Zhou, H. Huang, J. Xuan, J. Zhang and J. J. Zhu, *Biosens. Bioelectron.*, **2010**, 26, 834-840.

319. X. Yang, Y. Jin, Y. Zhu, L. Tang and C. Li, *J. Electrochem. Soc.*, **2008**, 155, J23-J25.

320. H.-J. Liu, W.-J. Cui, L.-H. Jin, C.-X. Wang and Y.-Y. Xia, *J. Mater. Chem.*, **2009**, 19, 3661-3667.

321. M. Nakayama, T. Kanaya and R. Inoue, *Electrochem. Commun.*, **2007**, 9, 1154-1158.

322. J.-H. Kim, S. H. Kang, K. Zhu, J. Y. Kim, N. R. Neale and A. J. Frank, *Chem. Commun.*, **2011**, 47, 5214-5216.

323. S.-W. Woo, K. Dokko, H. Nakano and K. Kanamura, *J. Power Sources*, **2009**, 190, 596-600.

324. N. S. Ergang, J. C. Lytle, K. T. Lee, S. M. Oh, W. H. Smyrl and A. Stein, *Adv. Mater.*, **2006**, 18, 1750-1753.

325. N. S. Ergang, M. A. Fierke, Z. Wang, W. H. Smyrl and A. Stein, *J. Electrochem. Soc.*, **2007**, 154, A1135-A1139.

326. P. G. Bruce, B. Scrosati and J.-M. Tarascon, *Angew. Chem. Int. Ed.*, **2008**, 47, 2930-2946.

327. P. Jiang, G. N. Ostojic, R. Narat, D. M. Mittleman and V. L. Colvin, *Adv. Mater.*, **2001**, 13, 389-393.

328. Q. Yan, X. S. Zhao and Z. Zhou, *J. Cryst. Growth*, **2006**, 288, 205-208.

329. F. Fleischhaker, A. C. Arsenault, Z. Wang, V. Kitaev, F. C. Peiris, G. von Freymann, I. Manners, R. Zentel and G. A. Ozin, *Adv. Mater.*, **2005**, 17, 2455-2458.

330. J. Li, L. Xue, Z. Wang and Y. Han, *Colloid. Polym. Sci.*, **2007**, 285, 1037-1041.

331. G. Von Freymann, S. John, V. Kitaev and G. A. Ozin, *Adv. Mater.*, **2005**, 17, 1273-1276.

332. K. Wostyn, Y. Zhao, G. de Schaetzen, L. Hellemans, N. Matsuda, K. Clays and A. Persoons, *Langmuir*, **2003**, 19, 4465-4468.

333. Y. Zhao, K. Wostyn, G. De Schaetzen, K. Clays, L. Hellemans, A. Persoons, M. Szekeres and R. A. Schoonheydt, *Appl. Phys. Lett.*, **2003**, 82, 3764-3766.

334. P. Massé, S. Reculusa and S. Ravaine, *Colloids Surf., A*, **2006**, 284-285, 229-233.

335. J. F. Dechézelles, G. Mialon, T. Gacoin, C. Barthou, C. Schwob, A. Maître, R. A. L. Vallée, H. Cramail and S. Ravaine, *Colloids Surf., A*, **2011**, 373, 1-5.

336. A. Deák, B. Bancsi, A. L. Tóth, A. L. Kovács and Z. Hórvölgyi, *Colloids Surf., A*, **2006**, 278, 10-16.

337. F. García-Santamaría, M. Ibisate, I. Rodríguez, F. Meseguer and C. López, *Adv. Mater.*, **2003**, 15, 788-792.

338. J. S. King, D. Heineman, E. Graugnard and C. J. Summers, *Appl. Surf. Sci.*, **2005**, 244, 511-516.

339. J. S. King, E. Graugnard and C. J. Summers, *Appl. Phys. Lett.*, **2006**, 88.

340. P. Lodahl, A. Floris van Driel, I. S. Nikolaev, A. Irman, K. Overgaag, D. Vanmaekelbergh and W. L. Vos, *Nature*, **2004**, 430, 654-657.

341. V. Tsakova, *J. Solid State Electrochem.*, **2008**, 12, 1421.

342. R. M. Hernandez, L. Richter, S. Semancik, S. Stranick and T. E. Mallouk, *Chem. Mater.*, **2004**, 16, 3431.

343. S. Park, S.-W. Chung and C. A. Mirkin, *J. Am. Chem. Soc.*, **2004**, 126, 11772.

344. S. Park, J.-H. Lim, S.-W. Chung and C. A. Mirkin, *Science*, **2004**, 303, 348-351.

345. Y. Jyoko, S. Kashiwabara, Y. Hayashi and W. Schwarzacher, *Electrochem. Solid-State Lett.*, **1999**, 2, 67-69.

346. M. Monev and et al., *J. Phys. Condens. Matter*, **1999**, 11, 10033.

347. K. H. Lee, G. H. Kim and W. Y. Jeung, *Electrochem. Commun.*, **2004**, 6, 115-119.

348. L. Péter, Q. Liu, Z. Kerner and I. Bakonyi, *Electrochim. Acta*, **2004**, 49, 1513-1526.

349. K. Leistner, S. Fähler, H. Schlörb and L. Schultz, *Electrochem. Commun.*, **2006**, 8, 916-920.

350. J. Zhang, Y. Li, X. Zhang and B. Yang, *Adv. Mater.*, **2010**, 22, 4249-4269.

351. A. Plettl, F. Enderle, M. Saitner, A. Manzke, C. Pfahler, S. Wiedemann and P. Ziemann, *Adv. Funct. Mater.*, **2009**, 19, 3279-3284.

352. J. J. Kim, Y. Li, E. J. Lee and S. O. Cho, *Langmuir*, **2011**, 27, 2334-2339.

353. J. Hur and Y.-Y. Won, *Soft Matter*, **2008**, 4, 1261-1269.

354. C. Liu, F. Li, L.-P. Ma and H.-M. Cheng, *Adv. Mater.*, **2010**, 22, E28-E62.

355. V. Müller, M. Rasp, J. Rathouský, B. Schütz, M. Niederberger and D. Fattakhova-Rohlfing, *Small*, **2010**, 6, 633-637.

356. M. M. Dimos and G. J. Blanchard, *J. Phys. Chem. C*, **2010**, 114, 6019-6026.

357. A. Heller, *Phys. Chem. Chem. Phys.*, **2004**, 6, 209-216.

358. A. Heller, *Anal. Bioanal.Chem.*, **2006**, 385, 469-473.

359. S. T. Singleton, J. J. O'Dea and J. Osteryoung, *Anal. Chem.*, **1989**, 61, 1211-1215.

360. M. M. Murphy, J. J. O'Dea and J. Osteryoung, *Anal. Chem.*, **1991**, 63, 2743-2750.

361. P. Salaün and C. M. G. van den Berg, *Anal. Chem.*, **2006**, 78, 5052-5060.

362. L. Fink and D. Mandler, *J. Electroanal. Chem.*, **2010**, 649, 153-158.

363. J. Wang, N. Foster, S. Armalis, D. Larson, A. Zirino and K. Olsen, *Anal. Chim. Acta*, **1995**, 310, 223-231.

364. H. Huiliang, D. Jagner and L. Renman, *Anal. Chim. Acta*, **1987**, 201, 1-9.

365. J. H. Moon, S. Kim, G.-R. Yi, Y.-H. Lee and S.-M. Yang, *Langmuir*, **2004**, 20, 2033-2035.

366. S. Hu, Y. Men, S. V. Roth, R. Gehrke and J. Rieger, *Langmuir*, **2008**, 24, 1617-1620.

367. J. H. Song and I. Kretzschmar, *Langmuir*, **2008**, 24, 10616-10620.

368. J. H. Moon, G.-R. Yi and S.-M. Yang, *J. Colloid Interface Sci.*, **2005**, 287, 173.

369. C. H. Lai, Y. J. Huang, P. W. Wu and L. Y. Chen, *J. Electrochem. Soc.*, **2010**, 157.

370. R. Zeis, T. Lei, K. Sieradzki, J. Snyder and J. Erlebacher, *J. Catal.*, **2008**, 253, 132-138.

371. L. Deng, F. Wang, H. Chen, L. Shang, L. Wang, T. Wang and S. Dong, *Biosens. Bioelectron.*, **2008**, 24, 329-333.

372. A. Zebda, L. Renaud, M. Cretin, F. Pichot, C. Innocent, R. Ferrigno and S. Tingry, *Electrochem. Commun.*, **2009**, 11, 592-595.

373. M. Kotobuki, H. Munakata and K. Kanamura, *J. Power Sources*, **2011**, 196, 6947-6950.

374. C. A. Thomas, P. A. Springer, G. E. Loeb, Y. Berwald-Netter and L. M. Okun, *Exp. Cell. Res.*, **1972**, 74, 61-66.

375. D. A. Robinson, *Proceedings of the IEEE*, **1968**, 56, 1065-1071.

376. G. W. Gross, A. N. Williams and J. H. Lucas, *J. Neurosci. Methods*, **1982**, 5, 13-22.

377. D. J. Anderson, K. Najafi, S. J. Tanghe, D. A. Evans, K. L. Levy, J. F. Hetke, X. Xue, J. J. Zappia and K. D. Wise, *IEEE Trans. Biomed. Eng.*, **1989**, 36, 693-704.

378. E. M. Maynard, C. T. Nordhausen and R. A. Normann, *Electroen. Clin. Neuro.*, **1997**, 102, 228-239.

379. U. Egert, B. Schlosshauer, S. Fennrich, W. Nisch, M. Fejtl, T. Knott, T. Müller and H. Hämmerle, *Brain Res. Protoc.*, **1998**, 2, 229-242.

380. Q. Bai, K. D. Wise and D. J. Anderson, *IEEE Trans. Biomed. Eng.*, **2000**, 47, 281-289.

381. J. Csicsvari, D. A. Henze, B. Jamieson, K. D. Harris, A. Sirota, P. Barthó, K. D. Wise and G. Buzsáki, *J. Neurophysiol.*, **2003**, 90, 1314-1323.

382. D. Heck, *J. Neurosci. Methods*, **1995**, 58, 81-87.

383. L. Berdondini, K. Imfeld, A. Maccione, M. Tedesco, S. Neukom, M. Koudelka-Hep and S. Martinoia, *Lab Chip*, **2009**, 9, 2644-2651.

384. M. Hutzler, A. Lambacher, B. Eversmann, M. Jenkner, R. Thewes and P. Fromherz, *J. Neurophysiol.*, **2006**, 96, 1638-1645.

385. U. Frey, U. Egert, F. Heer, S. Hafizovic and A. Hierlemann, *Biosens. Bioelectron.*, **2009**, 24, 2191-2198.

386. G. Charvet, et al., *Biosens. Bioelectron.*, 25, 1889-1896.

387. S. F. Cogan, *Annu. Rev. Biomed. Eng.*, **2008**, 10, 275-309.

388. J. B. Johnson, *Physical Review*, **1928**, 32, 97.

389. M. O. Heuschkel, M. Fejtl, M. Raggenbass, D. Bertrand and P. Renaud, *J. Neurosci. Methods*, **2002**, 114, 135-148.

390. R. C. Gesteland, B. Howland, J. Y. Lettvin and W. H. Pitts, *Proceedings of the IRE*, **1959**, 47, 1856-1862.

391. G. T. A. Kovacs, eds. D. A. Stenger and T. M. McKenna, **1994**, Academic Press, London UK, p. 121.

392. D. R. Merrill, M. Bikson and J. G. R. Jefferys, *J. Neurosci. Methods*, **2005**, 141, 171-198.

393. D. B. McCreery, W. F. Agnew, T. G. H. Yuen and L. Bullara, *IEEE Trans. Biomed. Eng.*, **1990**, 37, 996-1001.

394. C. Haberler, F. Alesch, P. R. Mazal, P. Pilz, K. Jellinger, M. M. Pinter, J. A. Hainfellner and H. Budka, *Ann. Neurol.*, **2000**, 48, 372-376.

395. A. M. Kuncel and W. M. Grill, *Clinical Neurophysiology*, **2004**, 115, 2431-2441.

396. L. S. Robblee and T. L. Rose, in *Neural protheses: fundamental studies*, eds. W. F. Agnew and D. B. McCreery, **1990**, Prentice Hall, Englewood Cliffs, New Jersey, pp. 25-66.

397. D. L. Guyton and F. T. Hambrecht, *Science*, **1973**, 181, 74-76.

398. D. Guyton and F. Terry Hambrecht, *Med. Biol. Eng. Comput*, **1974**, 12, 613-620.

399. P. Walter and K. Heimann, *Graefe's Archive for Clinical and Experimental Ophthalmology*, **2000**, 238, 315-318.

400. H. Hämmerle, K. Kobuch, K. Kohler, W. Nisch, H. Sachs and M. Stelzle, *Biomaterials*, **2002**, 23, 797-804.

401. T. L. Rose, E. M. Kelliher and L. S. Robblee, *J. Neurosci. Methods*, **1985**, 12, 181-193.

402. M. Janders, U. Egert, M. Stelzle and W. Nisch, in *Engineering in Medicine and Biology Society, 1996. Bridging Disciplines for Biomedicine. Proceedings of the 18th Annual International Conference of the IEEE*, 1996, pp. 245-247 vol.241.

403. A. Norlin, J. Pan and C. Leygraf, *J. Electrochem. Soc.*, **2005**, 152, J7-J15.

404. A. Jackson, J. Mavoori and E. E. Fetz, *Nature*, **2006**, 444, 56-60.

405. S. B. Brummer and M. J. Turner, *IEEE Trans. Biomed. Eng.*, **1977**, BME-24, 440-443.

406. E. Slavcheva, R. Vitushinsky, W. Mokwa and U. Schnakenberg, *J. Electrochem. Soc.*, **2004**, 151, E226-E237.

407. X. Beebe and T. L. Rose, *IEEE Trans. Biomed. Eng.*, **1988**, 35, 494-495.

408. J. S. Foos and S. M. Erker, *J. Electrochem. Soc.*, **1986**, 133, 1983-1984.

409. T. Nyberg, A. Shimada and K. Torimitsu, *J. Neurosci. Methods*, **2007**, 160, 16-25.

410. X. Cui, J. F. Hetke, J. A. Wiler, D. J. Anderson and D. C. Martin, *Sens. Actuators, A*, **2001**, 93, 8-18.

411. X. Cui and D. C. Martin, *Sens. Actuators, A*, **2003**, 103, 384.

412. X. Cui and D. C. Martin, *Sens. Actuators, B*, **2003**, 89, 92-102.

413. X. Cui, J. Wiler, M. Dzaman, R. A. Altschuler and D. C. Martin, *Biomaterials*, **2003**, 24, 777-787.

414. H. Yamato, M. Ohwa and W. Wernet, *J. Electroanal. Chem.*, **1995**, 397, 163-170.

415. N. A. Kotov, et al., *Adv. Mater.*, **2009**, 21, 3970-4004.

416. S. Sirivisoot, R. Pareta and J. T. Webster, *Nanotechnology*, **2011**, 22, 085101.

417. M. R. Abidian, D. H. Kim and D. C. Martin, *Adv. Mater.*, **2006**, 18, 405-409.

418. X. Zhang, S. Prasad, S. Niyogi, A. Morgan, M. Ozkan and C. S. Ozkan, *Sens. Actuators, B*, **2005**, 106, 843-850.

419. V. Lehmann and H. Foll, *J. Electrochem. Soc.*, **1990**, 137, 653-659.

420. V. Bucher, M. Graf, M. Stelzle and W. Nisch, *Biosens. Bioelectron.*, **1999**, 14, 639-649.

421. A. M. Feltham and M. Spiro, *Chem. Rev.*, **1971**, 71, 177-193.

422. W. G. Regehr, J. Pine and D. B. Rutledge, *IEEE Trans. Biomed. Eng.*, **1988**, 35, 1023-1032.

423. G. T. A. Kovacs, C. W. Storment, M. Halks-Miller, C. R. Belczynski, Jr., C. C. D. Santina, E. R. Lewis and N. I. Maluf, *IEEE Trans. Biomed. Eng.*, **1994**, 41, 567-577.

424. D. A. Borkholder, J. Bao, N. I. Maluf, E. R. Perl and G. T. A. Kovacs, *J. Neurosci. Methods*, **1997**, 77, 61-66.

425. S. Jun, M. Hynd, K. Smith, J. Song, J. Turner, W. Shain and S. Kim, *Med. Biol. Eng. Comput*, **2007**, 45, 1015-1021.

426. C. A. Marrese, *Anal. Chem.*, **1987**, 59, 217-218.

427. S. Arcot Desai, J. D. Rolston, L. Guo and S. M. Potter, *Front. Neuroeng.*, **2010**, 3.

428. P. Seung-Joon and et al., *J. Micromech. Microeng.*, **2003**, 13, 373.

429. T. Akin, K. Najafi, R. H. Smoke and R. M. Bradley, *IEEE Trans. Biomed. Eng.*, **1994**, 41, 305-313.

430. A. Blau, C. Ziegler, M. Heyer, F. Endres, G. Schwitzgebel, T. Matthies, T. Stieglitz, J. U. Meyer and W. Göpel, *Biosens. Bioelectron.*, **1997**, 12, 883-892.

431. J. D. Weiland, D. J. Anderson and M. S. Humayun, *IEEE Trans. Biomed. Eng.*, **2002**, 49, 1574-1579.

432. B. Wessling, A. Besmehn, W. Mokwa and U. Schnakenberg, *J. Electrochem. Soc.*, **2007**, 154, F83-F89.

433. B. Wessling, W. Mokwa and U. Schnakenberg, *J. Electrochem. Soc.*, **2008**, 155, F61-F65.

434. S. Negi, R. Bhandari, L. Rieth and F. Solzbacher, *Sens. Actuators, B*, **2009**, 137, 370-378.

435. A. Van Ooyen, G. Topalov, G. Ganske, W. Mokwa and U. Schnakenberg, *J. Micromech. Microeng.*, **2009**, 19.

436. R. Fröhlich, A. Rpzany, J. Riedmüller, A. Bolz and M. Schaldach, *J. Mater. Sci. - Mater. Med.*, **1996**, 7, 393-397.

437. R. D. Meyer, S. F. Cogan, T. H. Nguyen and R. D. Rauh, *IEEE Trans. Neural Syst. Rehabil. Eng.*, **2001**, 9, 2-11.

438. S. C. Mailley, M. Hyland, P. Mailley, J. M. McLaughlin and E. T. McAdams, *Mater. Sci. Eng. C*, **2002**, 21, 167-175.

439. Y. Lu, T. Wang, Z. Cai, Y. Cao, H. Yang and Y. Y. Duan, *Sens. Actuators, B*, **2009**, 137, 334-339.

440. K. S. Kang and J. L. Shay, *J. Electrochem. Soc.*, **1983**, 130, 766-769.

441. B. Wessling, W. Mokwa and U. Schnakenberg, *J. Micromech. Microeng.*, **2006**, 16, S142-S148.

442. S. Negi, R. Bhandari, L. Rieth, R. Van Wagenen and F. Solzbacher, *J. Neurosci. Methods*, **2010**, 186, 8-17.

443. S. F. Cogan, J. Ehrlich, T. D. Plante, A. Smirnov, D. B. Shire, M. Gingerich and J. F. Rizzo, *J. Biomed. Mater. Res.*, **2009**, 89, 353-361.

444. D. J. Comstock, S. T. Christensen, J. W. Elam, M. J. Pellin and M. C. Hersam, *Electrochem. Commun.*, **2010**, 12, 1543-1546.

445. C. M. Voge and J. P. Stegemann, *J. Neural Eng.*, **2011**, 8, 011001.

446. V. Lovat, D. Pantarotto, L. Lagostena, B. Cacciari, M. Grandolfo, M. Righi, G. Spalluto, M. Prato and L. Ballerini, *Nano Lett.*, **2005**, 5, 1107-1110.

447. A. Mazzatenta, M. Giugliano, S. Campidelli, L. Gambazzi, L. Businaro, H. Markram, M. Prato and L. Ballerini, *J. Neurosci.*, **2007**, 27, 6931-6936.

448. A. O. Fung, C. Tsiokos, O. Paydar, L. H. Chen, S. Jin, Y. Wang and J. W. Judy, *Nano Lett.*, **2010**, 10, 4321-4327.

449. H.-C. Su, C.-M. Lin, S.-J. Yen, Y.-C. Chen, C.-H. Chen, S.-R. Yeh, W. Fang, H. Chen, D.-J. Yao, Y.-C. Chang and T.-R. Yew, *Biosens. Bioelectron.*, **2010**, 26, 220-227.

450. T. Gabay and et al., *Nanotechnology*, **2007**, 18, 035201.

451. T. D. B. Nguyen-Vu, H. Chen, A. M. Cassell, R. Andrews, M. Meyyappan and J. Li, *Small*, **2006**, 2, 89-94.

452. K. Wang, H. A. Fishman, H. Dai and J. S. Harris, *Nano Lett.*, **2006**, 6, 2043-2048.

453. T. D. B. Nguyen-Vu, H. Chen, A. M. Cassell, R. J. Andrews, M. Meyyappan and J. Li, *IEEE Trans. Biomed. Eng*, **2007**, 54, 1121-1128.

454. Z. Yu, T. E. McKnight, M. N. Ericson, A. V. Melechko, M. L. Simpson and B. Morrison, *Nano Lett.*, **2007**, 7, 2188-2195.

455. E. W. Keefer, B. R. Botterman, M. I. Romero, A. F. Rossi and G. W. Gross, *Nat. Nano*, **2008**, 3, 434-439.

456. P. Li, X. Lim, Y. Zhu, T. Yu, C.-K. Ong, Z. Shen, A. T.-S. Wee and C.-H. Sow, *J. Phys. Chem. B*, **2007**, 111, 1672-1678.

457. C.-H. Chen and et al., *Nanotechnology*, **2010**, 21, 485501.

458. M. Hughes, M. S. P. Shaffer, A. C. Renouf, C. Singh, G. Z. Chen, D. J. Fray and A. H. Windle, *Adv. Mater.*, **2002**, 14, 382-385.

459. M. Hughes, G. Z. Chen, M. S. P. Shaffer, D. J. Fray and A. H. Windle, *Chem. Mater.*, **2002**, 14, 1610-1613.

460. Y. Lu, T. Li, X. Zhao, M. Li, Y. Cao, H. Yang and Y. Y. Duan, *Biomaterials*, **2010**, 31, 5169-5181.

461. R. Green, C. Williams, N. Lovell and L. Poole-Warren, *J. Mater. Sci. - Mater. Med.*, **2008**, 19, 1625-1629.

462. H. Chen, L. Guo, A. R. Ferhan and D.-H. Kim, *J. Phys. Chem. C*, **2011**, 115, 5492-5499.

463. E. Jan, J. L. Hendricks, V. Husaini, S. M. Richardson-Burns, A. Sereno, D. C. Martin and N. A. Kotov, *Nano Lett.*, **2009**, 9, 4012-4018.

464. M. R. Abidian, J. M. Corey, D. R. Kipke and D. C. Martin, *Small*, **2010**, 6, 421-429.

465. C. E. Schmidt, V. R. Shastri, J. P. Vacanti and R. Langer, *Proc. Natl. Acad. Sci. U.S.A.*, **1997**, 94, 8948-8953.

466. A. Kotwal and C. E. Schmidt, *Biomaterials*, **2001**, 22, 1055-1064.

467. W. R. Stauffer and X. T. Cui, *Biomaterials*, **2006**, 27, 2405-2413.

468. X. Cui, V. A. Lee, Y. Raphael, J. A. Wiler, J. F. Hetke, D. J. Anderson and D. C. Martin, *J. Biomed. Mater. Res. B*, **2001**, 56, 261-272.

469. D. H. Kim, S. M. Richardson-Burns, J. L. Hendricks, C. Sequera and D. C. Martin, *Adv. Funct. Mater.*, **2007**, 17, 79-86.

470. S. M. Richardson-Burns, J. L. Hendricks, B. Foster, L. K. Povlich, D.-H. Kim and D. C. Martin, *Biomaterials*, **2007**, 28, 1539-1552.

471. S. M. Richardson-Burns, J. L. Hendricks and D. C. Martin, *J. Neural Eng.*, **2007**, 4, L6-L13.

472. K. A. Ludwig and et al., *J. Neural Eng.*, **2011**, 8, 014001.

473. R. Wadhwa, C. F. Lagenaur and X. T. Cui, *J. Controlled Release*, **2006**, 110, 531-541.

474. K. A. Ludwig, J. D. Uram, J. Yang, D. C. Martin and D. R. Kipke, *J. Neural Eng.*, **2006**, 3, 59-70.

475. M. R. Abidian, K. A. Ludwig, T. C. Marzullo, D. C. Martin and D. R. Kipke, *Adv. Mater.*, **2009**, 21, 3764-3770.

476. K. Deligkaris, T. S. Tadele, W. Olthuis and A. van den Berg, *Sens. Actuators, B*, **2010**, 147, 765-774.

477. S. Ghosh and O. Inganäs, *Adv. Mater.*, **1999**, 11, 1214-1218.

478. T. Nyberg, O. Inganäs and H. Jerregård, *Biomed. Microdevices*, **2002**, 4, 43-52.

479. D.-H. Kim, M. Abidian and D. C. Martin, *J. Biomed. Mater. Res.*, **2004**, 71A, 577-585.

480. M. R. Abidian and D. C. Martin, *Adv. Funct. Mater.*, **2009**, 19, 573-585.

481. D. H. Kim, J. A. Wiler, D. J. Anderson, D. R. Kipke and D. C. Martin, *Acta Biomater.*, **2010**, 6, 57-62.

482. V. Urbanová, Y. Li, K. Vytras, B. Yvert and A. Kuhn, *J. Electroanal. Chem.*, **2011**, 656, 91-95.

483. J. Yang and D. C. Martin, *Sens. Actuators, B*, **2004**, 101, 133-142.

484. J. Yang and D. C. Martin, *Sens. Actuators, A*, **2004**, 113, 204-211.

485. C. Wang and et al., *Sci. Technol. Adv. Mater.*, **2009**, 10, 023001.

486. C. T. Kresge, M. E. Leonowicz, W. J. Roth, J. C. Vartuli and J. S. Beck, *Nature*, **1992**, 359, 710-712.

487. J. Y. Ying, C. P. Mehnert and M. S. Wong, *Angew. Chem. Int. Ed.*, **1999**, 38, 56-77.

488. P. N. Bartlett, *The Electrochemical Society Interface*, **Winter 2004**, 13, 28.

489. G. S. Attard, J. M. Corker, C. G. Göltner, S. Henke and R. H. Templer, *Angew. Chem. Int. Ed.*, **1997**, 36, 1315-1317.

490. Y. Yamauchi and K. Kuroda, *Chem. Asian J.*, **2008**, 3, 664-676.

491. G. S. Attard, S. A. A. Leclerc, S. Maniguet, A. E. Russell, I. Nandhakumar and P. N. Bartlett, *Chem. Mater.*, **2001**, 13, 1444.

492. J. F. Hulvat and S. I. Stupp, *Angew. Chem. Int. Ed.*, **2003**, 42, 778-781.

493. A. A. Karyakin, E. A. Puganova, I. A. Budashov, I. N. Kurochkin, E. E. Karyakina, V. A. Levchenko, V. N. Matveyenko and S. D. Varfolomeyev, *Anal. Chem.*, **2003**, 76, 474-478.

494. A. Walcarius, E. Sibottier, M. Etienne and J. Ghanbaja, *Nat Mater.*, **2007**, 6, 602-608.

495. P. A. Nelson and J. R. Owen, *J. Electrochem. Soc.*, **2003**, 150, A1313-A1317.

496. S. Park, T. D. Chung and H. C. Kim, *Anal. Chem.*, **2003**, 75, 3046-3049.

497. T. Imokawa, K.-J. Williams and G. Denuault, *Anal. Chem.*, **2005**, 78, 265-271.

498. J. M. Elliott and J. R. Owen, *Phys. Chem. Chem. Phys.*, **2000**, 2, 5653-5659.

499. J. M. Elliott, G. S. Attard, P. N. Bartlett, N. R. B. Coleman, D. A. S. Merckel and J. R. Owen, *Chem. Mater.*, **1999**, 11, 3602-3609.

500. B. Gollas, J. M. Elliott and P. N. Bartlett, *Electrochim. Acta*, **2000**, 45, 3711-3724.

501. J. Yang, D. H. Kim, J. L. Hendricks, M. Leach, R. Northey and D. C. Martin, *Acta Biomater.*, **2005**, 1, 125-136.

502. S. Park, Y. J. Song, H. Boo and T. D. Chung, *J. Phys. Chem. C*, **2010**, 114, 8721-8726.

503. B. Yvert, C. Mazzocco, S. Joucla, A. Langla and P. Meyrand, *J. Neurosci.*, **2011**, 31, 8832-8840.

504. A. D. Rakic, A. B. Djurisic, J. M. Elazar and M. L. Majewski, *Appl. Opt.*, **1998**, 37, 5271-5283.